Mathematical and Computational Modelling of Tissue Engineered Bone in a Hydrostatic Bioreactor

Katherine H. L. Leonard
Jesus College

Computational Biology, Department of Computer Science, University of Oxford.

Hilary Term, 2014

This thesis is submitted to the Department of Computer Science, University of Oxford, for the degree of Doctor of Philosophy. This thesis is entirely my own work, and, except where indicated, describes my own research.

Abstract

In vitro tissue engineering is a method for developing living and functional tissues external to the body, often within a device called a bioreactor to control the chemical and mechanical environment. However, the quality of bone tissue engineered products is currently inadequate for clinical use as the implant cannot bear weight. In an effort to improve the quality of the construct, hydrostatic pressure, the pressure in a fluid at equilibrium that is required to balance the force exerted by the weight of the fluid above, has been investigated as a mechanical stimulus for promoting extracellular matrix deposition and mineralisation within bone tissue. Thus far, little research has been performed into understanding the response of bone tissue cells to mechanical stimulation.

In this thesis we investigate an *in vitro* bone tissue engineering experimental setup, whereby human mesenchymal stem cells are seeded within a collagen gel and cultured in a hydrostatic pressure bioreactor. In collaboration with experimentalists a suite of mathematical models of increasing complexity is developed and appropriate numerical methods are used to simulate these models. Each of the models investigates different aspects of the experimental setup, from focusing on global quantities of interest through to investigating their detailed local spatial distribution. The aim of this work is to increase understanding of the underlying physical processes which drive the growth and development of the construct, and identify which factors contribute to the highly heterogeneous spatial distribution of the mineralised extracellular matrix seen experimentally.

The first model considered is a purely temporal model, where the evolution of cells, solid substrate, which accounts for the initial collagen scaffold and deposited extracellular matrix along with attendant mineralisation, and fluid in response to the applied pressure are examined. We demonstrate that including the history of the mechanical loading of cells is important in determining the quantity of deposited substrate. The second and third models extend this non–spatial model, and examine biochemically and biomechanically–induced spatial patterning separately. The first of these spatial models demonstrates that nutrient diffusion along with nutrient–dependent mass transfer terms qualitatively reproduces the heterogeneous spatial effects seen experimentally. The second multiphase model is used to investigate whether the magnitude of the shear stresses generated by fluid flow, can qualitatively explain the heterogeneous mineralisation seen in the experiments. Numerical simulations reveal that the spatial distribution of the fluid shear stress magnitude is highly heterogeneous, which could be related to the spatial heterogeneity in the mineralisation seen experimentally.

Acknowledgements

There are many people to thank who have supported me over the course of my doctoral research, not all of whom I can include individually here.

Firstly, I would like to say a huge thank you to my supervisors; Ozzy, Jon and Sarah, without whose help this thesis would not exist. Thank you for all the guidance and discussions, throughout the course of my thesis research. In particular, thank you for all the support and advice provided during the writing-up stages.

Thank you to my experimental collaborators – particularly to James and Yvonne for answering so many questions, Alicia for her valuable insights, and Josh for running the experiments.

In addition, I thank the Doctoral Training Centre for their support and faith in me, and especially in offering me a funded place despite illness.

A big thank you to my parents for their limitless help and advice over all the years. Also to my siblings Anne and Hugh, and close friend Vasi.

An meine deutsche Familie, Sigrid, Sebastian und Julia, vielen Dank für alles.

Zu guter Letzt möchte ich mich noch bei meinem Freund Christian bedanken, der immer für mich da ist. Für sein großartiges Korrekturlesen. Dafür, dass er meine Verrücktheiten hinnimmt und immer an mich glaubt.

Contents

Chapter 1

Tissue engineering of bone

In this chapter we give the background to the subjects discussed in this thesis and review existing literature in these areas, before introducing the research contained in this thesis. The chapter is split into four sections. The first section (Section 1.1) covers the biological background. This includes the biology and structure of bone, and a background to the field of tissue engineering. In addition, we review the existing studies into the effects of hydrostatic pressure on bone tissue development. The second section (Section 1.2) covers the mathematical background, including related mathematical models and existing theoretical studies into tissue engineering, and specifically bone tissue engineering. The third section (Section 1.3) covers the methods that have been used to obtain a solution to the equations describing the mathematical models of biological tissues. Finally, Section 1.4 uses the earlier sections of this chapter to motivate the research presented in the remainder of this thesis.

1.1 Biological background

The biological literature review is organised into four sections. The first covers the biology of bone (Section 1.1.1) and the second section reviews aspects of tissue engineering relevant to this thesis (Section 1.1.2). The third and fourth sections cover the effects of shear stress and

hydrostatic pressure on bone tissue (Sections 1.1.3 and 1.1.4 respectively).

1.1.1 The biology of bone

Bone is an essential structure in the mammalian body with many important functions. Its strength and rigidity provides protection for vital organs *e.g.* the rib cage for the heart and lungs, and the skull for the brain. As part of the musculoskeletal system the skeleton acts as a framework, giving shape to the body, and allows movement through the attachment of muscles, ligaments and tendons acting across joints. In addition, bone provides storage for minerals and is the site of blood cell production. The adult human skeleton consists of 213 bones [Buck and Dumanian, 2012a], which may be classified into four main types: long bones (such as the femur), short bones (such as the patella), flat bones (such as the skull) and irregular bones (such as the vertebrae) [Clarke, 2008].

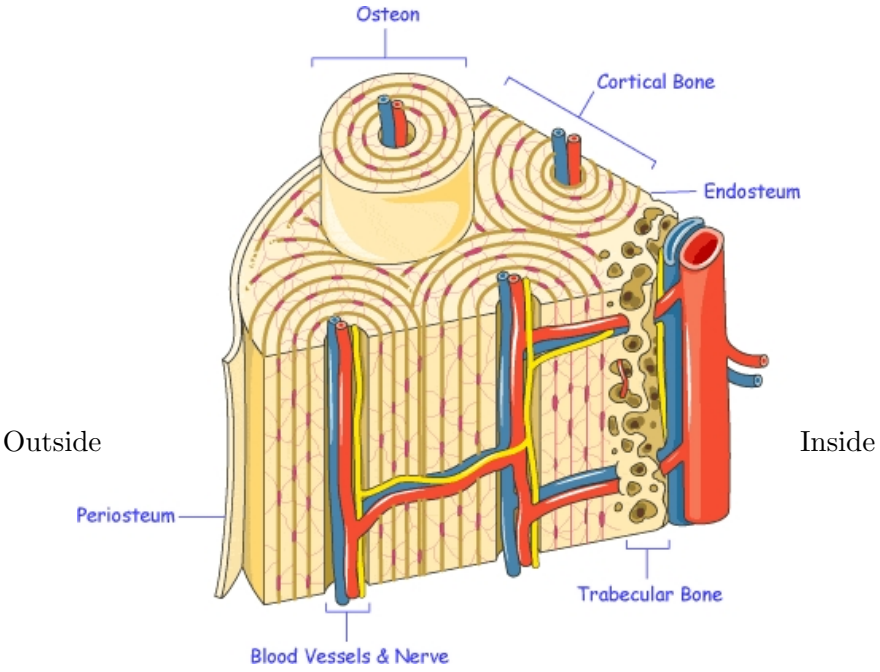

Figure 1.1: A segment from a typical long bone showing the positions of cortical and trabecular bone, and the locations of the osteons. Reproduced with permission from `www.iofbonehealth.org`.

There are two main types of bone tissue: *compact* or *cortical* bone; and *cancellous* or *trabecular* bone. The former is very dense and, therefore, strong, with a porosity of 5 – 10% [Doblaré *et al.*, 2004], whereas the latter is much more porous (50 – 95% porosity), with an open or spongy structure due to connected trabeculae. These trabeculae are little rods or beams of bone in

between which lies bone marrow. Within the body cancellous/trabecular bone is usually surrounded by a layer of cortical/compact bone for protection and strength, as shown in Figure 1.1. The mature adult human skeleton consists of 80% compact and 20% trabecular bone [Buck and Dumanian, 2012a], although the exact ratio varies according to the position of the bone within the body [Clarke, 2008].

Bone consists of three main components: mineralised bone matrix, cells and bone fluid. Bone marrow is also found at the centre of some bones, and houses the production of blood cells. The bone extracellular matrix (ECM) itself consists mainly of collagen type I. The matrix gives bone its structure and the ability to withstand tensile forces [Doblaré *et al.*, 2004, Clarke, 2008, Buck and Dumanian, 2012a]. Mineralisation of the bone matrix is the process by which soluble inorganic ions, mainly in the form of hydroxyapatite [Buck and Dumanian, 2012a], are converted into solids [Clarke, 2008] and gives bone its ability to withstand compressive forces. The inorganic minerals give bone strength, making it a stiff material that can bear weight. Together, bone matrix and mineralised ions make up 95% of the dry weight of bone tissue [Johnson *et al.*, 2011]. Furthermore, calcium and other ions need to be balanced within the body and bone provides storage for these, allowing the body to control levels within blood and other tissues. The fluid that is located in the pores of the intratrabecular space is a mixture including bone marrow and fat. Other liquid within bone tissue, in which occurs the diffusion of nutrients from blood vessels to cells, has a significantly lower viscosity than bone marrow [Cowin and Doty, 2007]. Bone tissue is highly vascularised so that no part of the tissue is more than 200 – 300 μm from its blood supply [Buck and Dumanian, 2012a].

In order to be both as strong and as light as possible, bone tissue adapts in response to mechanical forces throughout an individual's life. This process, known as *remodelling*, is achieved by the coordination of several cell types, including osteocytes, osteoblasts, osteoclasts and osteoprogenitor cells (precursors to osteoblasts). Remodelling not only allows bone to adapt to mechanical forces, but also to replace any microfractures, microdamage, or old bone [Clarke, 2008, Doblaré *et al.*, 2004]. In addition, it allows the body to regulate mineral homoeostasis. Osteoblasts deposit new bone, while osteoclasts absorb old bone. The work of these different cells in healthy adult animals is balanced at a rate which replaces around 2 – 3% of the skeleton per year until there is a gradual loss of bone mass due to ageing [Turner, 1998]. Imbalanced

activity between the different cell types can lead to diseases such as osteoporosis [Chen *et al.*, 2010]. A more detailed review of the remodelling process can be found in Clarke [2008].

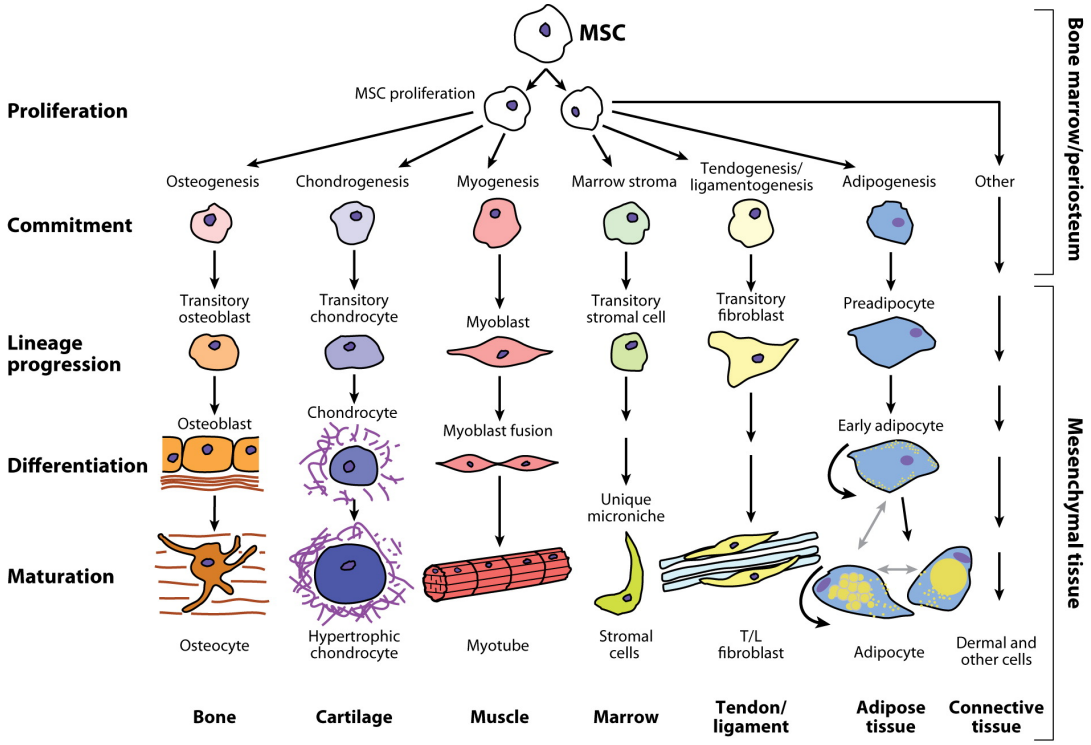

AR Singer NG, Caplan AI. 2011.
Annu. Rev. Pathol. Mech. Dis. 6:457–78

Figure 1.2: Hypothesis of the possible differentiation lines for mesenchymal stem cells (MSCs), which can differentiate into a number of different cell types. Reproduced with permission from Singer and Caplan [2011].

Osteoblasts arise from mesenchymal stem cells (MSCs) through differentiation, as illustrated in Figure 1.2. After bone formation is complete, osteoblasts have several different fates. About 50% undergo apoptosis [Johnson *et al.*, 2011]. Others become bone–lining cells, mature into osteocytes, or return to being osteoprogenitor cells (de–differentiation) [Buck and Dumanian, 2012a]. Osteocytes are terminally differentiated osteoblasts, as illustrated in Figure 1.2, which become embedded in lacunae (a term for a space in the bone containing an osteocyte) within the ECM and develop finger–like projections of the cytoplasm, called *processes*, which connect them to other osteocytes. Osteocytes make up 90% of all bone cells [Buck and Dumanian, 2012a] and are known to sense changes in fluid flow caused by loading, as shown in Figure 1.3 [Chen *et al.*, 2010, Mullender *et al.*, 2004]. During extended bed rest osteocyte numbers decrease and bone mass is lost [Rauh *et al.*, 2011], which indicates that mechanical stimulation is essential for

the regulation of bone tissue. Osteoclasts are thought to be derived from haematopoietic stem cells, the stem cells that differentiate into blood and immune cells, and to be differentiated from mononuclear phagocytes, a type of white blood cell capable of ingesting and destroying particles and microbes foreign to the body, which fuse together to form multinucleated preosteoclasts, the precursors to osteoclasts.

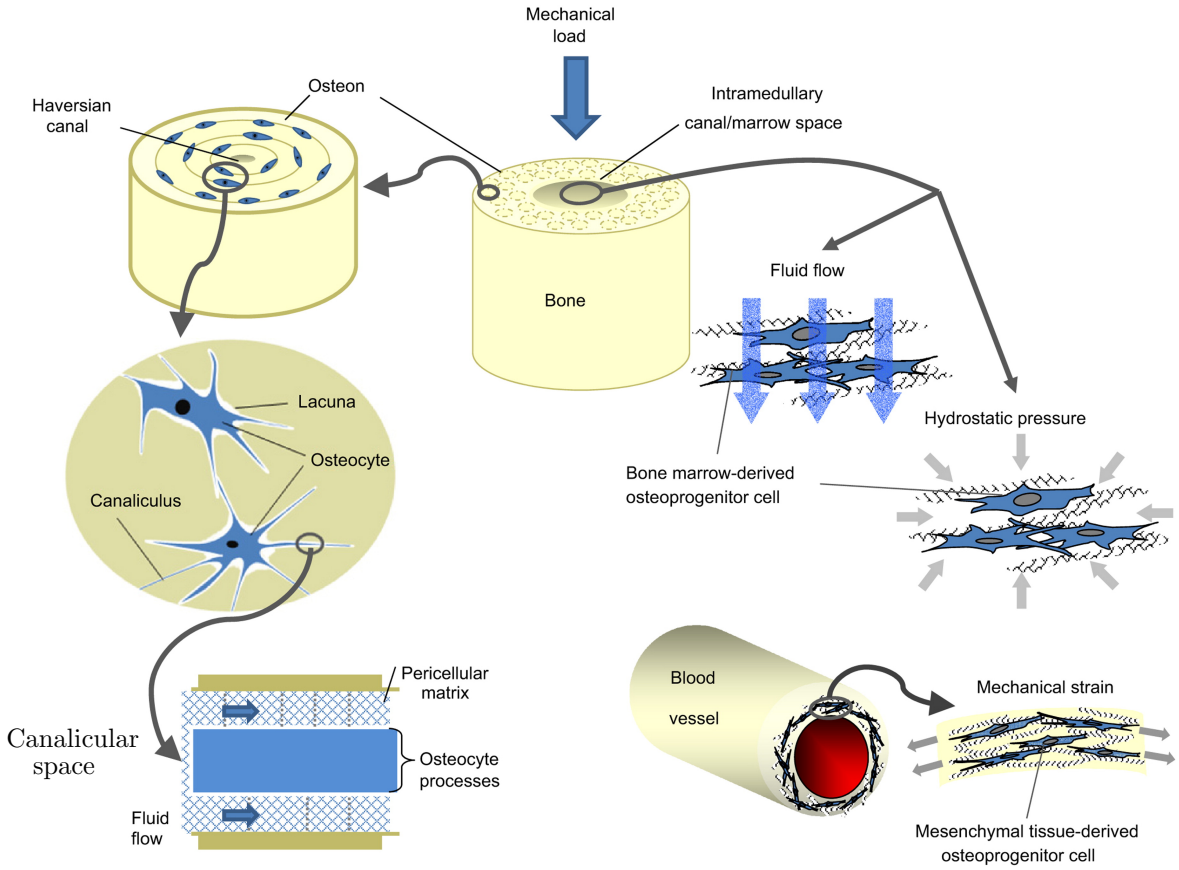

Figure 1.3: A schematic to show the organisation and positioning of different cell types within bone and the physiological forces they experience, reproduced with permission from Chen *et al.* [2010]. The left hand side of the diagram indicates the hierarchical structure of bone tissue, whereas the right hand side shows the mechanical forces that osteoprogenitor cells experience in bone tissue. Osteoprogenitor cells are also found in other mesenchymal tissues, such as blood vessels, where they experience mechanical strains.

The main structural unit in cortical bone is an osteon, which is cylindrical in shape, as shown in Figure 1.1. Osteons contain a central channel called a Haversian canal, containing blood vessels and nerves, and they are important as they contain passageways, or canaliculi, in which lie the osteocytic processes, connecting the osteocytes within their lacunae. Mechanobiology is the study of how cells and tissues respond to mechanical forces. Mechanobiological research indicates that osteocytes are the main mechanosensors within bone tissue and regulate os-

teoblast and osteoclast activity through signalling molecules and direct contact [Chen *et al.*, 2010, Klein-Nulend *et al.*, 2005]. Hydrostatic pressure and changes in fluid flow also affect the osteoprogenitor cells, which are precursors to osteoblasts, and are located in the marrow space, as illustrated in Figure 1.3. Studies suggest that osteoprogenitor cells have varying degrees of response to mechanical signals depending on their degree of differentiation [Chen *et al.*, 2010].

Regeneration and repair of bone tissue

Bone is generally able to repair by regeneration without the formation of scar tissue and, unlike other tissues, it returns to its normal shape and strength after trauma provided there is good alignment of the fractured ends. The bone regeneration process post–trauma is a complex mechanism, and beyond the scope of this literature review, but details may be found in Buck and Dumanian [2012b] and Geris *et al.* [2009]. In essence, the ends of the fractured or cut bone have to be fairly closely aligned in order for new bone to bridge the gap between them and create a union which matures and strengthens over time. Small gaps between the two bone ends can be bridged by new bone growth, but there is a critical size to the defect, which is defined as a gap no more than two and a half times the radius of the bone [Schroeder and Mosheiff, 2011]; smaller than the critical size, healing normally occurs, but larger and the gap cannot be bridged.

There are many cases where bone repair post–trauma fails and surgical intervention is needed. Such cases include situations where the quantity of bone required is beyond the body's capability to generate, such as critical size defects occurring after bone loss, for example, due to accidental trauma or tumour resection. The correction of skeletal abnormalities, such as bone lengthening, is limited by the critical size gap [Dimitriou *et al.*, 2011]. Surgical intervention is also needed when a problem has occurred with the normal repair process and there has been non–union or delayed union [Dimitriou *et al.*, 2011]. There are currently several standard surgical options available for such cases: autologous bone grafting, allogenic bone grafting and prosthetic implants. Autologous bone grafting, where the transplant is taken from the same person, has the advantage that there is a reduced risk of rejection and infection when compared to other methods. However, the amount of bone that can be harvested from the donor site is limited [Dimitriou *et al.*, 2011], the process is painful, two surgical procedures are needed

and the risk of complications is high [Schroeder and Mosheiff, 2011]. Allogenic bone grafting, where the transplant is taken from another individual of the same species, does not have the same size limitations but there can be problems with rejection and infection. Prostheses have the disadvantage that they do not integrate into the surrounding tissue and more than 30% of patients need a revision within seven years [Schroeder and Mosheiff, 2011]. Another method is to use distraction osteogenesis, where the two ends of the bone are moved apart gradually, which allows the regeneration of bone between the two ends, to lengthen the bone. However, this process is painful and takes a long time [Schroeder and Mosheiff, 2011]. Further information on the advantages and disadvantages of the current surgical methods within a clinical setting can be found in Buck and Dumanian [2012b] and O'Keefe and Mao [2011]. Tissue engineering is an alternative method of producing bone tissue implants and is free from some of the risks and disadvantages mentioned above.

1.1.2 Tissue engineering

Definitions of the term *tissue engineering* vary according to the context in which the term is used. Rose and Oreffo [2002] define it as "the application of scientific principles to the design, construction, modification and growth of living tissues using biomaterials, cells and factors, alone or in combination". Orlando *et al.* [2011] distinguish between *regenerative medicine* and *tissue engineering*. They define the former as "a field in the health sciences that aims to replace or regenerate human cells, tissues or organs to restore or establish normal function", and the latter as "manufacturing body parts *ex vivo*, by seeding cells on or into a supporting scaffold". Within this thesis we are specifically interested in cells seeded on or into a scaffold and grown *in vitro* within a bioreactor, with the goal of producing clinically useful bone tissue implants. The term *construct* is often used to describe the combination of scaffold, cells, attendant ECM and fluid, to distinguish it from the culture medium in which it lies. This literature review will mainly focus on the need for, and background to, engineered bone tissue. An historic overview and discussion on the current position of regenerative medicine can be found in Orlando *et al.* [2011].

In the remainder of this section we focus on the need for tissue engineering, the bioreactors, the scaffolds and the cells used in tissue engineering, and finally the cell seeding process.

The need for tissue engineering

With advances in medicine and increased life expectancy, failure of organs and tissues as a consequence of injury, disease or age, is increasing the demand for donor tissues and organs. This upsurge in demand is not being met by an increase in the number of donated organs and there is a chronic shortage. Currently around 1000 people per year die in the UK waiting for donor organs[a].

Autogenic transplantation has limitations in terms of quantity and can only be used for certain tissues, such as skin and bone. Complications can arise with allogenic organ or tissue transplantation; not all are successful and there is a risk of rejection. The recipient must take immunosuppressants to ensure that his or her body does not recognise the donor organ or tissue as foreign and this can result in immunodeficiency and susceptibility to other diseases. Xenographic transplantations, where the donor and recipient are from different species, also have severe limitations including the possibility of infection and disease.

Tissue engineered products often use autologous cells, removing the problems associated with rejection and the need for immunosuppressants. In addition they are living and so able to integrate into the host tissue, resulting in a better functioning tissue. This is especially important in children as the tissue engineered implant can develop along with the child and so does not need replacing as the child grows [Orlando *et al.*, 2011]. Tissue engineered products can also be used for drug trials, reducing the need for animal experimentation [Martin, 2004].

There are several different approaches to tissue engineering. These can be broadly divided into *in vitro* approaches, where the construct is developed external to the body in a device known as a bioreactor and then implanted, and *in vivo* approaches, which use the body as a bioreactor. *In vivo* approaches include the use of non–living scaffolds, injection of stem cells and gene–therapy, and have shown some success [O'Keefe and Mao, 2011, Boccaccio *et al.*, 2011, Johnson *et al.*, 2011]. *In vitro* approaches include the use of organ–derived ECM scaffolds, obtained by decellularisation of organs and reseeding with appropriate stem or progenitor cells [Badylak *et al.*, 2011, Orlando *et al.*, 2011]. This method, while forming a functioning tissue, avoids rejection and the need for immunosuppressants. The ECM remains mostly intact during

[a]This data was taken from `www.organdonation.nhs.uk`.

decellularisation, with associated growth factors and blood vessel structure preserved. By this means, it provides an environment for the self–organisation and differentiation of cells needed to create a functioning tissue. There are several hurdles still to be overcome with this type of tissue engineering strategy [Badylak *et al.*, 2011], including problems with an insufficiency of donor tissues and organs which can be decellularised. Hence, significant research has been invested in the use of non–organ–derived scaffolds [Wong *et al.*, 2010] as used in the experiments described in this thesis.

Currently clinical success of tissue engineered implants is limited. The barriers to using tissue engineered bone products within the clinical situation are reviewed in Salter *et al.* [2012]. Vascularisation of tissue engineered products is a significant challenge, and constructs are currently limited by size [Johnson *et al.*, 2011]. Success has been limited to small, simple and avascular tissues such as blood vessels, bladder, cartilage, trachea and skin [Orlando *et al.*, 2011, Wong *et al.*, 2010].

Bioreactors used in tissue engineering

A bioreactor can be defined as any device which allows a particular chemical or biological process to be controlled and monitored, and can include a wide variety of different vessels. Within tissue engineering the use of a bioreactor allows precise control of the biophysical and biochemical environment experienced by the construct during growth. It also can be used to stimulate mechanosensitive tissues, such as bone, so they develop properly. Bespoke bioreactors are often built for the particular experimental procedure of interest, but several bioreactors are now available commercially [Rauh *et al.*, 2011, El Haj and Cartmell, 2010, Yeatts and Fisher, 2011]. Furthermore, many bioreactors are fitted with sensors to provide measurements of certain quantities of interest as the tissue develops, for example oxygen probes or pH sensors. This is especially important for the automation of the experimental process [Yeatts and Fisher, 2011], which is needed if tissue engineering is to be used in clinical applications. Different cell cultures sourced from different people will develop at different rates, and monitoring the progression of the growth of the construct, in order to determine when it is ready for implantation, will be essential [Martin, 2004]. Tissue engineering studies using a bioreactor are particularly useful for advancing understanding of cell behaviour in a three–dimensional environment, as the develop-

ing construct can be observed and monitored when subject to a specific type of stimulation in a controlled setting [Lee *et al.*, 2011].

The size of an avascular construct is limited, as diffusion is the only transport mechanism in the absence of perfused flow. A construct larger than 1 mm in diameter grown in static culture will normally result in a necrotic core, consisting of cells that have undergone premature death, and a proliferating rim [Martin, 2004]. This effect is increased in tissue engineered bone constructs as the cells at the rim of the construct produce more ECM, reducing pore size and, thus, reducing mass transport to the centre of the construct [Yeatts and Fisher, 2011]. Ensuring an adequate delivery of nutrients required for growth, such as oxygen, glucose and growth factors, and removal of waste products is essential for the growth of a tissue. As mentioned in Section 1.1.1, bone is highly vascular so that no part of the tissue is far away from its blood supply [Johnson *et al.*, 2011], ensuring sufficient nutrient delivery and waste product removal. A variety of bioreactors have been developed to increase mass transfer to the centre of the construct via advective transport so that larger constructs can be grown. These include the spinner flask, the rotating vessel, perfusion and the hollow fibre bioreactors, described in the next paragraph.

Figure 1.4(a) shows the spinner flask, where the cell–seeded scaffolds are suspended in the culture medium and a magnetic stirring mechanism is used to keep the fluid mixed. The advantages of this system include ease of implementation, but the disadvantages include the lack of adequate mass transport to the centre of larger scaffolds and a non–uniform end product. The rotating vessel, an example of which is sketched in Figure 1.4(b), consists of two cylinders, with the space in between filled with culture medium and the scaffolds. The advantages again include ease of implementation, but the disadvantages include an inhomogeneous end product and scaffolds that are free to move and can, consequently, collide [El Haj and Cartmell, 2010, Martin, 2004]. With perfusion bioreactor systems, a typical sketch of which is shown in Figure 1.4(c), the fresh culture medium is pumped through the scaffold within a sealed container. These have proved to be more effective than the spinner flask and rotation vessels in increasing mass transport to the centre of the scaffold. However, the perfusion bioreactor is more complex to set up than the rotating vessel and spinner flask bioreactors, and the construct needs to be tightly sealed so that the culture medium cannot flow around it, as this results in inhomogeneous tissue growth.

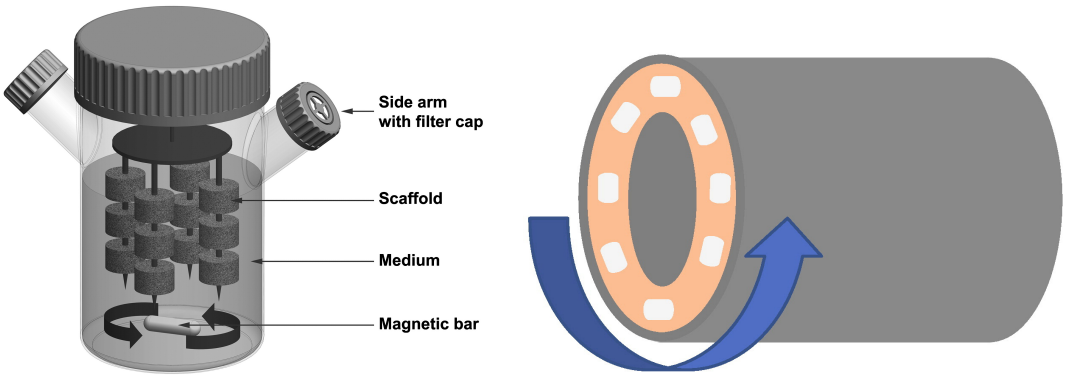

(a) Spinner flask

(b) Rotating vessel

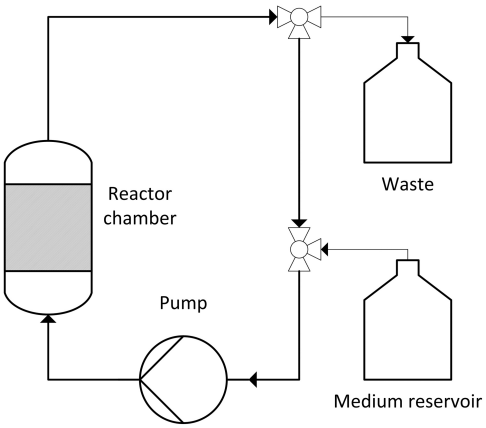

(c) Perfusion bioreactor

Figure 1.4: Sketches of bioreactors designed to increase mass transport. Figure (a), reproduced with permission from Rauh *et al.* [2011], shows a spinner flask bioreactor. Figure (b), reproduced with permission from Yeatts and Fisher [2011], shows an example rotating vessel bioreactor. Figure (c), reproduced with permission from Rauh *et al.* [2011], shows the setup of a typical perfusion bioreactor.

As a consequence, the potential choices of scaffold geometry are limited. In addition, perfusion systems have been shown to be particularly effective in bone tissue engineering as the flow through the porous scaffold results in the cells in the scaffold experiencing shear stresses, further discussed in Section 1.1.3. Hollow fibre bioreactors, a sketch of which is shown in Figure 1.5, consists of a bundle of cylindrical porous fibres, each surrounded by an extra–capillary space in which the cells are cultured [Ellis and Chaudhuri, 2007, Morgan *et al.*, 2007, Martin, 2004]. Culture medium flows through the lumen of the porous fibres with an experimentally controllable inlet velocity. Some hollow fibre bioreactors also include an extra–capillary space port which allows fluid to enter into or exit from the extra–capillary space directly. The membrane in between the fibre and the extra–capillary space allows for the advective and diffusive transport of nutrients and waste products. These bioreactors have a large membrane surface area in

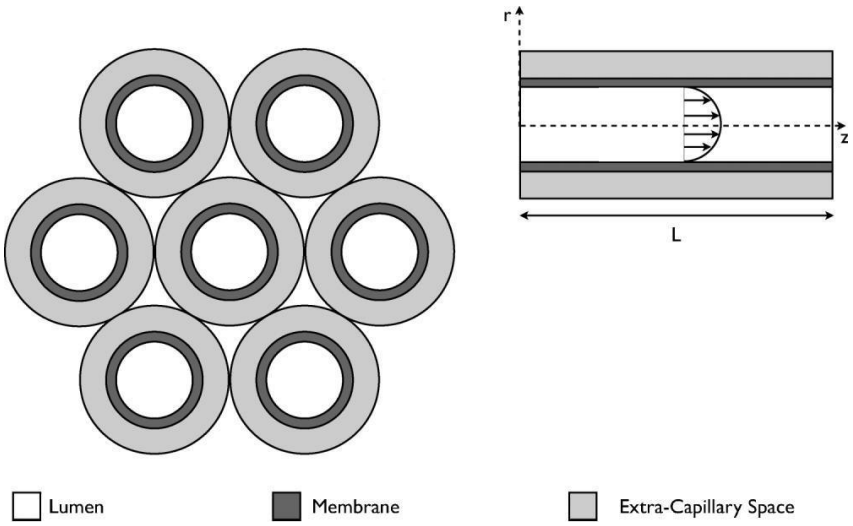

Figure 1.5: Sketch to indicate the setup of a hollow fibre bioreactor, reproduced with permission from Shipley *et al.* [2011]. The diagram on the left hand side indicates a cross section through the bundle of cylindrical fibres, while the diagram on the right hand side indicates the flow through the length of one of the fibres. Some experimental setups also include an extra–capillary space port (not shown on this diagram), to allow fluid to enter or exit directly into or from the extra–capillary space.

relation to fluid volume, and have been shown to significantly increase mass transport over other three–dimensional tissue culture methods, without imparting high shear stresses on cells. This is because the use of the membrane allows for a different rate of flow in the lumen from that in the extra–capillary space, so that the cells are protected from the high flow rate in the lumen. Currently, however, only small quantities of tissue have been produced.

Bone tissue experiences a variety of different mechanical loading *in vivo*, including bending, shear, compression and torsion [Basso and Heersche, 2002, Rauh *et al.*, 2011, El Haj and Cartmell, 2010]. Bone tissue grown *in vitro* within a bioreactor with mechanical stimulation shows better viability and improved quality when compared to those developed without stimulus [Yeatts and Fisher, 2011]. As a result a range of bioreactor systems have been designed to reproduce the mechanical stimuli encountered *in vivo* in order to encourage the development of the growing construct into that of bone tissue. These bioreactors include the hydrostatic pressure bioreactor, four point bending device, compression systems and magnetic force bioreactor, discussed below [Rauh *et al.*, 2011, El Haj and Cartmell, 2010, Cartmell and El Haj, 2005]. A bioreactor can either apply the mechanical stimuli directly to the cells or to their surrounding environment [El Haj and Cartmell, 2010]. An example of the former is the magnetic

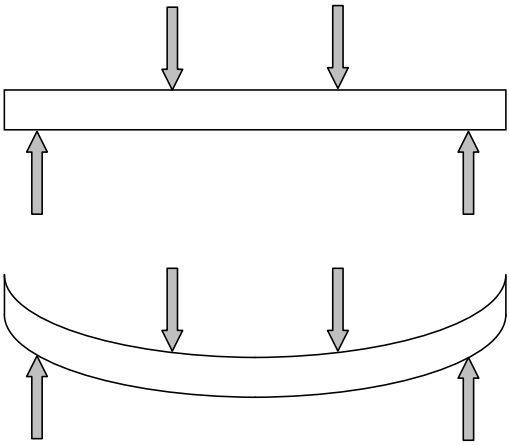

Figure 1.6: Schematic to illustrate the setup in a four-point bending bioreactor device. The top schematic shows a beam before the four points of load are applied. The lower schematic illustrates the beam after loading has been applied, causing the beam to bend. This bending applies a strain to a monolayer of cells placed on the beam (not shown).

force bioreactor, whereas examples of the latter include the spinner flask, perfusion and hydrostatic bioreactors. A number of bioreactors have been designed to combine different mechanical stimuli [El Haj and Cartmell, 2010]; for example Orr and Burg [2008] designed a bioreactor to combine both perfusion and hydrostatic pressure.

Hydrostatic pressure bioreactor devices provide mechanical stimulation by delivering compressed air to the developing construct. Sometimes a membrane is used in a hydrostatic pressure bioreactor in order to minimise the fluctuation in the concentration of the dissolved gases in the air delivered during pressure changes [Eggum and Hunter, 2008]. The effects of hydrostatic pressure on bone–producing cells, and studies investigating its use, are discussed further in Section 1.1.4.

The four–point bending device, as illustrated in Figure 1.6, applies strain to a monolayer which is placed on a beam affixed at either end. As a load is applied, the centre of the beam is displaced downwards, causing it to bend. Although monolayer studies can give some idea of cell response to different mechanical stimuli, for us to fully understand cellular response *in vivo* cells need to be studied in their natural three–dimensional environment.

Compression systems encompass a variety of different bioreactors, which involve compressing the developing construct by the use of a piston [Cartmell and El Haj, 2005]. In the magnetic force bioreactor, biocompatible magnetic nanoparticles attached directly to the cells experience

a magnetic field. Their movement, under the magnetic field exerted by the bioreactor, imparts stress directly to the cell membrane. Further information on bioreactors used in the production of engineered bone tissue are reviewed in Rauh *et al.* [2011], El Haj and Cartmell [2010], Cartmell and El Haj [2005] and Yeatts and Fisher [2011]. These include past studies and the advantages and disadvantages of each system.

In this thesis we focus on a hydrostatic pressure bioreactor used by our experimental collaborators in this thesis [Henstock *et al.*, 2013], and discuss the particular system under consideration further in Chapter 2.

Scaffolds used in tissue engineering

Within tissue engineering applications, the scaffold acts as a template to which the seeded cells can adhere. Biodegradable scaffolds are normally used, with the aim of ensuring that the scaffold degrades at the same rate as the ECM is deposited, so that it is eventually completely replaced by ECM [Yeatts and Fisher, 2011]. A wide variety of materials have been used to make scaffolds for tissue engineering applications. These include natural polymers, such as collagen and alginate, and synthetic polymers such as polylactic acid (PLA), polyglycolic acid (PGA) and polylactic–co–glycolic acid (PLGA). Ceramics and bioactive glass have also been used [Salter *et al.*, 2012]. Each material has its associated advantages and disadvantages, and there has not, as yet, been any one "perfect" scaffold designed. Furthermore, biochemically enhanced scaffolds have been investigated, where the scaffold has been modified to encourage cell attachment, proliferation, migration or differentiation [Johnson *et al.*, 2011, Salter *et al.*, 2012].

For the clinical application of tissue engineered bone, a scaffold needs to be chosen such that it [Johnson *et al.*, 2011]:

1. can be sterilised, to remove the risk of infection;
2. is biocompatible, so that an immune response in the host is not induced;
3. is osteoconductive, so that bone–producing cells can attach and proliferate;
4. is osteointegrative, so that it can integrate into the host bone tissue upon implantation;

and

5. is osteoinductive, so that, by transferring mechanical stimuli to the cells, undifferentiated cells are encouraged to differentiate into bone–producing cells.

In addition, a scaffold with a microstructure that allows for the movement of cells and the transport of nutrients, and which can withstand the mechanical loading to which it is subjected upon implantation, is essential [Yeatts and Fisher, 2011]. The above conditions often produce conflicting design constraints; for example a more porous scaffold increases mass transport and cellular in–growth, but decreases mechanical stability.

Scaffolds can be manufactured to take on specific shapes required for implantation, although some bioreactors, for example the perfusion bioreactor, are currently unable to accommodate irregular shapes [El Haj and Cartmell, 2010].

Cells used in tissue engineering

MSCs are used in the experiments performed by our experimental collaborators, as detailed in Chapter 2, which are described by the mathematical models developed in this thesis. They are multipotent stem cells.

Stem cells are cells with the ability to proliferate and self–renew, producing progeny cells, while also having the ability to differentiate into one or more different cell types. There is a hierarchy of different types of cells with these properties. Totipotent cells can differentiate into all cell types of the organism, and, in mammals, exist only in the zygote. Pluripotent stem cells, such as embryonic stem cells, have the ability to differentiate into any one of the three germ layers [Wong *et al.*, 2010, Badylak *et al.*, 2011], whereas multipotent stem cells have the ability to differentiate into more than one different cell type within a particular germ layer. Progenitor cells are further along the path of differentiation than stem cells. They have the ability to replicate, albeit a limited number of times, while being able to differentiate further. MSCs are defined as multipotent, as they can differentiate into multiple cell tissue types, including bone, cartilage, muscle and fat, as illustrated in Figure 1.2. MSCs can be found in multiple tissue types and locations within the adult human body.

Stem cells reside in a particular niche environment, where they maintain their "stem"–ness, and can replicate indefinitely. It is only when they move away from this environment that they differentiate according to the biochemical and mechanical stimuli they receive. The biochemistry controlling stem and progenitor cell differentiation is well understood. In contrast, the mechanobiology of stem cells, and how they respond to the mechanical microenvironments that cause them to differentiate down a particular pathway, is still not fully understood [Lee *et al.*, 2011].

Often stem cells and progenitor cells are used in regenerative medicine due to their proliferative potential. However, there are problems with acquiring enough cells of sufficient quality for use in regenerative medicine, especially with older patients [Dimitriou *et al.*, 2011]. In addition there are issues with expanding the stem cell population *ex vivo* safely, without microbe contamination or malignancy [O'Keefe and Mao, 2011, Schroeder and Mosheiff, 2011]. Thus, research is being carried out into alternative methods for extracting and growing stem and progenitor cells [Dimitriou *et al.*, 2011].

For bone tissue engineering a mixture of osteoblasts and osteoclasts is sometimes used so that the construct has the ability to remodel [El Haj and Cartmell, 2010]. This is less usual than seeding the scaffold with stem cells or osteoprogenitor cells, because bone growth, as opposed to bone remodelling, is desired in the early stages of tissue development. After implantation osteoclasts will migrate from the surrounding bone tissue into the implant and then remodelling can occur.

Due to the limited availability of osteoblasts and the difficulties with obtaining and expanding stem cell populations, many tissue engineering experimental studies have made use of osteoblast or osteocyte–type cell lines, for example in Liu *et al.* [2010] and Gardinier *et al.* [2009]. These cell lines have been developed purely for *in vitro* experimental use and are usually originally derived from malignant cells. This gives them good proliferative ability, suiting experimental laboratory work [Czekanska *et al.*, 2012]. Their use also does not have the ethical issues associated with using samples from animals or humans.

Cell seeding

Cell seeding is the process by which the cells are initially introduced onto or into the porous scaffold. The initial cell density and the spatial distribution of the cells are important factors in the quality of the end product. There are two main methods for cell seeding. The first is *static*, where cells are injected into, or placed onto, the scaffold before it enters the bioreactor. The second is *dynamic*, where the scaffold is introduced to the cells in suspension in the culture medium in the bioreactor, to enable flow–enhanced seeding. Bioreactors such as the perfusion and stirring flask devices have been used to increase the effectiveness of the dynamic seeding process over the static process [Martin, 2004, Yeatts and Fisher, 2011].

1.1.3 Cell response to shear stress

Physiological mechanical loading *in vivo* causes fluid flow in the lacunae, as illustrated in Figure 1.3, and it is hypothesised that the shear stresses this flow generates are sensed by the osteocytes, which then regulate osteoblastic and osteoclastic activity [Chen *et al.*, 2010]. A number of studies have investigated the effects of fluid–mediated shear stress on bone–producing cells, and there are several reviews in this field [McCoy and O'Brien, 2010, Yeatts and Fisher, 2011, Riddle and Donahue, 2009]. As studies to date have used perfused fluid flow to investigate the effects of shear stress, there is a question mark over whether results can be attributed to shear stress in isolation, or are also due to the increase in mass transport. However, studies have indicated that shear stresses induce osteogenesis, enhance MSC and osteoblast proliferation, encourage osteoblast differentiation and increase mineralisation [McCoy and O'Brien, 2010, Yeatts and Fisher, 2011]. It is estimated that shear stresses causing osteogenesis *in vivo* are within the ranges 0.8 – 3 Pa [McCoy and O'Brien, 2010, Yeatts and Fisher, 2011]. However, human MSCs in three–dimensional *in vitro* culture have been recorded as responding to shear stresses within the ranges 10^{-4} – 1.2 Pa [McCoy and O'Brien, 2010]. Very high shear stresses have been shown to be inhibitory, and if the flow rate of the culture medium is too high it can cause damage to the cells or wash the cells off the scaffold.

1.1.4 Cell response to hydrostatic pressure

Hydrostatic pressure is defined as the pressure in a fluid at equilibrium that is required to balance the force exerted by the weight of the fluid above. When stimulating growth in a bioreactor, cyclical or dynamic pressure is usually applied because it is physiologically more realistic than a constant applied pressure, and has been shown to produce constructs with more of an osteogenic phenotype, and consequently more of the characteristics of bone tissue [Basso and Heersche, 2002, Roelofsen *et al.*, 1995]. Often the words *cyclic*, *intermittent*, *dynamic* are added to emphasise the fact that the applied stimulus varies with time.

It is well documented that hydrostatic pressure stimulation promotes cellular differentiation down the chondrogenic lineage to form cartilaginous tissues [Elder and Athanasiou, 2009]. However, the effects of hydrostatic pressure on bone cells and the resultant effect on the bone tissue composition has received much less attention and is not well understood [Chen *et al.*, 2010, Liu *et al.*, 2010, Hess *et al.*, 2010]. It has, however, been suggested that hydrostatic pressure is important in the stimulation and regulation of bone growth and remodelling [Basso and Heersche, 2002, Chen *et al.*, 2010]. As discussed in Section 1.1.1 and indicated in Figure 1.3, hydrostatic pressure is experienced by cells residing in the marrow space, and the physiological pressure within the lacunar–canalicular system, in which the osteocytes are embedded, has been estimated computationally to reach up to 2230 kPa [Zhang *et al.*, 1998]. As, to the author's knowledge, no review exists of the effects of hydrostatic pressure on bone tissue, this section aims to give the reader an overview of the biological literature pertaining to this subject.

Apoptosis of mammalian cells can occur at pressures from 100 – 200 megapascals (MPa), with higher pressures causing necrotic death [Rivalain *et al.*, 2010]. High hydrostatic pressure has been used as a method of sterilisation of foods as it effectively kills micro–organisms without altering the structure and, as a consequence, the taste and texture of the food. Moreover, high hydrostatic pressure may be of use in killing tumour cells without damaging the structure and mechanical function of the tissue [Diehl *et al.*, 2008]. Therefore, this method is currently being investigated for use in bone tumour surgery [Diehl *et al.*, 2008]. Cancerous tissues could, for example, be removed from the patient, subjected to high hydrostatic pressures, and then re–implanted. In this way the structure of the tissue would be retained and could act as a

scaffold without containing malignant cells. However, the pressures exerted by the bioreactor used for the experiments presented within this thesis are within physiologically normal loading ranges (less than 400 kPa), and orders of magnitude below the ranges that cause damage to mammalian cells. Thus, neither pressure–induced apoptosis nor necrosis is considered in the mathematical models developed within this thesis.

A variety of studies have been performed to investigate the effects of hydrostatic pressure on bone tissue. However, it is difficult to draw conclusions due to the variety of different experimental conditions used. Existing studies into the effects of hydrostatic pressure have used multiple cell types (osteoblasts [Roelofsen *et al.*, 1995, Nagatomi *et al.*, 2001, 2003, Takai *et al.*, 2004], osteoclasts [Klein-Nulend *et al.*, 1990], osteoprogenitor cells [Roelofsen *et al.*, 1995], fibroblasts [Nagatomi *et al.*, 2001, Orr and Burg, 2008], endothelial cells [Nagatomi *et al.*, 2001], stromal cells [Eggum and Hunter, 2008], mesenchymal stem cells [Hess *et al.*, 2010, Kim *et al.*, 2007], co–cultures [Liu *et al.*, 2009] and cell lines [Liu *et al.*, 2010, Gardinier *et al.*, 2009]), sourced from different animals of different ages on a variety of substrates. A large proportion of existing studies have included research into the effects of hydrostatic pressure on monolayers [Nagatomi *et al.*, 2001, 2003, Eggum and Hunter, 2008, Liu *et al.*, 2009, 2010, Gardinier *et al.*, 2009]. However, it is questionable whether experimental results from monolayers are useful when considering three–dimensional tissue cultures [Mullender *et al.*, 2004, Elder and Athanasiou, 2009, Swartz and Fleury, 2007]. In addition, experimental conditions, such as loading frequency, magnitude and duration of the applied hydrostatic pressure vary widely from paper to paper. Furthermore, Gardinier *et al.* [2009], Kim *et al.* [2007] and Orr and Burg [2008] also included the effects of fluid flow into their studies. Some of the results are contradictory or inconclusive, for example, Klein-Nulend *et al.* [1990] found that osteoclastic activity was reduced following the application of hydrostatic pressure stimulation, whereas the results of Liu *et al.* [2009] indicated that hydrostatic pressure promotes the development of osteoclasts and those of Liu *et al.* [2010] indicated increased osteoclast activity. However, overall, results do indicate that dynamic hydrostatic pressure has a positive influence on bone development; it has been shown that hydrostatic pressure stimulation causes increased intracellular concentration of calcium ions [Liu *et al.*, 2010], increased bone formation [Henstock *et al.*, 2013], increased matrix mineralisation [Roelofsen *et al.*, 1995], increased osteoblast proliferation [Nagatomi *et al.*, 2001]

and function [Takai *et al.*, 2004], increased collagen and calcium content [Nagatomi *et al.*, 2003], and decreased levels of osteocyte apoptosis [Liu *et al.*, 2010]. In addition, Nagatomi *et al.* [2001, 2003] and Hess *et al.* [2010] demonstrated a delay in response to hydrostatic pressure and Hess *et al.* [2010] demonstrated that the timing of application of pressure was important. Further research is needed to clarify the effects of hydrostatic pressure on bone tissue.

1.2 Mathematical modelling

There are a large number of factors to consider when engineering a tissue–scaffold construct. To create a functional piece of tissue a number of complex and interacting processes that occur naturally within the body during development and growth need to be reproduced. In addition, biological systems show complexity on a wide variety of temporal and spatial scales. Hence, mathematical modelling and numerical simulation are invaluable tools for studying such intricate systems [Díaz-Zuccarini and Lawford, 2010, Sengers *et al.*, 2007b].

Experimental techniques are expensive and time consuming, and the amount of information they can provide is limited [Sengers *et al.*, 2007b]. For example, oxygen concentration can be measured outside the developing tissue, but to get an idea of how it varies through the construct probes need to be inserted into the tissue, giving information only at discrete spatial points. This invasive procedure may also affect the biological processes that are taking place. Another example would be obtaining information about scaffold porosity and cell numbers, yielding information at discrete temporal points. But, as the construct is damaged during the process of retrieving this information, many experimental repetitions are required which is both expensive and time consuming. On the other hand computational simulation of a calibrated mathematical model can be used to give continuous spatial and temporal information. It may also be used to predict other quantities of interest which are not experimentally obtainable, such as the pressures, strains and stresses to which the developing construct is subjected.

Mathematical modelling does have its limitations and cannot be used in isolation: assumptions need to be made, the effects of which on the conclusions drawn may be unclear; parameterisation of a model is often difficult and many parameters cannot be estimated directly; analytical solutions to the governing equations do not usually exist, and numerical techniques need to be

used in order to achieve an approximate solution; not all the mechanisms of the underlying system or process can be included into a model because the model would then become too complex either to be able to solve (analytically or numerically) or from which to draw useful conclusions.

Two approaches to mathematical modelling are discrete modelling and continuum modelling. For discrete modelling individual units are tracked. Within the modelling of biological tissues discrete models are useful for understanding the micro–environment around the cells and can incorporate, for example, subcellular phenomena. However, one of the limitations of discrete models is that, as the number of units increases, simulation becomes impractical due to excessive computational demands. Another approach, continuum modelling, is more appropriate when considering the dynamics of the system as a whole. Properties are averaged over representative volumes in a systematic manner, allowing differential equations to be derived. However, estimating parameter values for continuum models can be difficult [Kapellos *et al.*, 2010] and the approach becomes invalid if the population number is small, or either the processes of interest or experimental results are on the scale of the individual units. In addition to purely discrete or continuum approaches, a further approach that is emerging is advanced multiscale modelling, which combines the advantages of the two approaches above. This allows, for example, details from the microscale to be included without numerical implementation becoming excessively computationally demanding [Díaz-Zuccarini and Lawford, 2010]. Tissue engineering examples using multiscale models include Shipley *et al.* [2009] and Sanz-Herrera *et al.* [2009, 2008].

Mathematical modelling of tissue engineering is a relatively new field. Due to the similarities of the processes, the majority of models are based on existing mathematical models of biological tissue growth. There are few mathematical models specific to *in vitro* bone tissue engineering, where the construct is developed within a bioreactor, and none, to the author's knowledge, of tissue engineered bone within a hydrostatic bioreactor. There are a number of reviews covering the different areas of interest [Doblaré *et al.*, 2004, Díaz-Zuccarini and Lawford, 2010, Sengers *et al.*, 2007b, Boccaccio *et al.*, 2011, MacArthur, 2004, Gerhard *et al.*, 2009, Geris *et al.*, 2009, 2010]. The review of O'Dea *et al.* [2012], which examines continuum mathematical models of tissue engineering, is particularly applicable to this work. In addition to reviewing existing mathematical models of tissue engineering in Section 1.2.2, the author also refers to related

mathematical models in the next section, exploring work that could provide valuable ideas.

1.2.1 Mathematical models of related systems

Before discussing previous mathematical models of tissue engineering, we discuss related mathematical models including tumour modelling, transport mechanics and multiphase models that are relevant to the models that are developed in this thesis.

Tumour growth

Due to the life–threatening nature of malignant tumours, their growth and spread have been the subject of significant research [Byrne *et al.*, 2006, Byrne, 2010, Lowengrub *et al.*, 2010, Rejniak and McCawley, 2010, Roose *et al.*, 2007]. However, understanding of the exact processes involved and the methods of treatment is still limited due to the complexity of these diseases [Quaranta *et al.*, 2005].

Tumour growth occurs in several distinct stages. The first of these is avascular growth, where the collection of abnormal cells is small enough that diffusion from the surrounding normal tissue is adequate to supply cells with the nutrients required. Exponential growth occurs initially, but an avascular tumour's maximum size is limited to a diameter of approximately two millimetres as cells further away from the boundary are starved of nutrients and, consequently, undergo necrotic death. This results in a layered structure, with a contracting necrotic core, a proliferating outer rim, and a layer of quiescent cells in between. To continue growing past this diffusion–controlled limit the tumour must acquire its own vasculature. It can be seen that there are several similarities between the avascular stage of tumour growth and the *in vitro* development of engineered tissues. Because of this, many mathematical models describing the growth of engineered tissues are built on mathematical models for describing the avascular phase of tumour growth.

Transport mechanisms

The spatial movement of cells and nutrients within tissue growth is highly important. Within continuum mathematical models of the growth of tissues, two transport mechanisms, diffusive and advective transport, are mainly used in order to describe the spatial movement of substances and particles. Diffusion describes the stochastic motion of a particle, whereas advection describes movement according to a local velocity field.

In general, the spatio–temporal evolution of a particle may be described by

$$\frac{\partial X}{\partial t} + \nabla \cdot (X\mathbf{v}) = f(X) + \nabla \cdot (\mathbf{D}(X, \mathbf{x}, t)\nabla X)\,. \tag{1.1}$$

Here $X(\mathbf{x}, t)$ represents the density of the species under consideration at the spatial point $\mathbf{x}$ and time $t \geq 0$, which could be the concentration of a nutrient in solution or the population of a cell colony. The term $\nabla \cdot (X\mathbf{v})$ describes spatial movement due to advection, where $\mathbf{v}$ is a vector describing local flow, and the term $\nabla \cdot (\mathbf{D}(X, \mathbf{x}, t)\nabla X)$ describes spatial movement due to diffusion where $\mathbf{D}(X, \mathbf{x}, t)$ is the diffusion coefficient matrix. The term $f(X)$ encompasses other local spatio–temporal changes in the density of X. For example, if X were to represent a cell population, $f(X)$ may represent cell birth or cell death processes. A separate equation to describe the velocity flow field, $\mathbf{v}$, in order to close the system of equations is required. Within the mathematical modelling of tissue growth, the Stokes equations and the Darcy flow law are two popular choices to describe the local velocity flow field.

The Navier–Stokes equations describe the flow of a viscous, Newtonian fluid [Acheson, 1990]. Many existing models of biological tissue growth have assumed that cells and fluid may be represented as viscous fluids and so have described their movement using the Navier–Stokes equations. Incompressibility is often assumed in order to simplify the system of equations. Furthermore, assuming a small Reynolds number (the ratio of inertial to viscous forces), which is an assumption that is often used when modelling biological media [Truskey, 2009, Astanin and Preziosi, 2008], inertial terms may be ignored and the Navier–Stokes equations can be reduced to Stokes flow [Ockendon and Ockendon, 1995, Acheson, 1990].

Another popular fluid flow model is Darcy's law, which states that the velocity of a fluid through

a porous medium is proportional to the pressure gradient. It was originally empirically derived by examination of water flow through sand in the 19th century by Henry Darcy. It has since been mathematically derived via homogenisation of the incompressible Navier–Stokes equations [Whitaker, 1986, Neuman, 1977]. Darcy's law has been used to describe the movement of cells and fluid through the ECM in tumour modelling [Byrne and Chaplain, 1997, Roose, 2003]. However, the validity of this assumption has been questioned as, within a tumour, the ECM cannot be readily identified as a porous material. In tissue engineering problems the scaffold is porous. It is, therefore, more appropriate to model fluid flow through the scaffold using Darcy's law [Wilson *et al.*, 2007]. The Brinkman equations, which have also been used in tissue growth mathematical models, are an extension to Darcy flow, and incorporate the effects of macroscale viscosity [Swartz and Fleury, 2007]. They allow for the inclusion of a no–slip boundary condition.

In cases where either diffusive transport or advective transport is the dominant mechanism, the appropriate term may be ignored, to give

$$\frac{\partial X}{\partial t} = f(X) + \nabla \cdot (\mathbf{D}(X, \mathbf{x}, t)\nabla X)\,, \tag{1.2}$$

or

$$\frac{\partial X}{\partial t} + \nabla \cdot (X\mathbf{v}) = f(X), \tag{1.3}$$

respectively. Furthermore, the assumption that the diffusion coefficient is a scalar constant is often used due to lack of detailed experimental information and to simplify the system of equations.

Multiphase models

Multiphase models, or mixture models, have been successfully used in a wide variety of applied mathematical applications to model a mixture consisting of two or more distinct and separate *phases*. A simple example is rain falling through air: these two substances are chemically distinct and can be viewed as a mixture. In these models each of the phases has a *volume fraction*, which sum to unity at each spatial point. Multiphase models are popular for modelling tissues, which can be viewed as a mixture of different phases or constituents; for example cells, ECM, scaffold

and interstitial fluid. The advantages of this framework are multiple: each constituent can have its own velocity, material and mechanical properties, production and removal rates; it is easy to include additional phases and assumptions on the structure of the tissue do not need to be made [Cogan and Guy, 2010]; inclusion of the diffusion of chemicals in solution is straightforward; it is possible to include reactions amongst these chemicals and to allow for particles with electrical charge [Ateshian, 2007, Sun *et al.*, 1999, Lai *et al.*, 1991]. Consequently, mixture theory has been used in modelling a variety of different biological applications including cell motility [Cogan and Guy, 2010], tumour growth [Breward *et al.*, 2002, 2003, Franks and King, 2003, Byrne and Preziosi, 2003, Preziosi and Tosin, 2009, Hubbard and Byrne, 2013], biofilms [Cogan and Guy, 2010], soft tissues [Simon, 1992] and tissue engineering [Lemon *et al.*, 2006, Lemon and King, 2007a,b, Sengers *et al.*, 2004, O'Dea *et al.*, 2008, 2010, Osborne *et al.*, 2010, O'Dea *et al.*, 2013]. Using the multiphase framework, different fluid flow models can be used for each phase, for example Stokes flow [Franks *et al.*, 2003a,b, Franks and King, 2003, Breward *et al.*, 2002, Byrne *et al.*, 2003] or Darcy flow [Byrne and Chaplain, 1997, Roose, 2003]. Lemon *et al.* [2006] were the first to present a general multiphase framework for use in modelling tissue growth, with the particular application of modelling the growth and development of *in vitro* engineered tissues. A number of further mathematical models of tissue engineering have built on the work of Lemon *et al.* [2006], including Lemon and King [2007a,b], O'Dea *et al.* [2008, 2010], Osborne *et al.* [2010], O'Dea *et al.* [2013] and the model presented in Chapters 5 – 7.

1.2.2 Mathematical models of tissue engineering

The number of mathematical models built specifically to study engineered bone tissue is limited. Many existing tissue engineering models are built in such a way that they either do not specify a particular tissue application or they can be applied to multiple tissue types, for example Coletti *et al.* [2006], Lemon *et al.* [2006], Wilson *et al.* [2007] and Shakeel *et al.* [2013]. Such models could be applied to bone tissue with suitable parameterisation. In the following we review existing mathematical models of tissue engineering and examine their features.

Cell movement

Cells are responsible for depositing and maintaining their ECM environment. Consequently, the cell distribution within the construct is highly influential on the end product quality of the construct [Sengers *et al.*, 2009]. Thus, an understanding of cell movement and dynamics is important. Many theoretical tissue engineering studies have focused on describing cell movement through porous scaffolds and these mathematical studies help increase understanding about the dynamics of tissue growth and development and can be used to guide initial cell seeding and bioreactor design.

Assuming that advective transport is negligible, Equation (1.2) has been used in many tissue engineering studies to describe the spatio–temporal evolution of a population of cells. One such example is Fisher's equation (also known as the Fisher–Kolmogoroff equation) [Murray, 2002], which represents cellular proliferation by logistic growth and cellular migration by diffusion. This was used by Sengers *et al.* [2007a] to describe the spreading of human bone marrow cells and an osteoblast–type line in two spatial dimensions, with results comparing well to experimental data. It was also used by Sengers *et al.* [2009] to model the initial stages of human bone marrow stromal cell three–dimensional spreading and by Shakeel *et al.* [2013] to model the cell population in a perfusion bioreactor.

Models of the form given by Equation (1.3) have been especially popular in modelling cell distributions in perfusion and hollow fibre bioreactors. For example Wilson *et al.* [2007] assume cells move through advective transport mechanisms only in order to model the movement through a homogeneous porous scaffold. Furthermore, Lemon *et al.* [2006] used linear stability theory to demonstrate that either aggregative or diffusive cell behaviour can be predicted by such a model, dependent on the size of the cell growth rate. Travelling wave behaviour of the cells moving through the scaffold was predicted using such a model by Lemon and King [2007a,b]. In particular, Lemon and King [2007b] demonstrated that both forward and backward–moving waves were possible when nutrient were assumed to be in plentiful supply.

To date, tissue engineering studies have tended not to use both advective and diffusive transport mechanism to describe the movement of cells, arguing that either one or the other is the dominant mechanism and the other may be neglected. Although both transport mechanism

are included in the equations describing the spatio–temporal evolution of cells in O'Dea *et al.* [2008, 2010], the diffusion term is only added in order to aid numerical solution rather than to describe cell movement. However, equations of the form given by Equation (1.1) have been used to describe the spatio–temporal distribution of a nutrient or nutrients in solution in several theoretical tissue engineering studies.

An example of a discrete model that has been used to describe the movement of cells in tissue engineering applications is cellular automaton. Sengers *et al.* [2007a] used this model to argue that the assumption that osteoblast–type line and human bone marrow stromal cells were immobile did not reproduce experimental results, and that cell motility is an important factor in cell spreading. Cheng *et al.* [2006] included the effects of cell motility in their cellular automaton study, as well as the effects of contact inhibition, which is often not included in continuum models, and several other aspects of cell behaviour, including different migration states, variable cell cycle length and a waiting time after cell collisions allowing for the "stickiness" of the cells and propensity of the population to form cell aggregates.

An understanding of cell movement through a scaffold enables studies to examine and contrast methods of cell seeding. For example, in Lemon and King [2007a] two methods of initial cell seeding were considered (see Section 1.1.2 for further details of the cell seeding process): static seeding, where cells were placed in one region of the scaffold, and dynamic seeding, where cells were placed throughout the central region of the scaffold. At large times both seeding strategies predicted the same cell density, indicating that for long experiments the spatial distribution in the construct is independent of the initial seeding strategy used. Cheng *et al.* [2006] used their model to compare the effectiveness of two initial cell seeding strategies: uniform seeding; and an initial configuration where there was a cylindrical–shaped "wound" area devoid of cells in the centre of the domain. Cheng *et al.* [2006] used numerical simulations to demonstrate that, depending on seeding strategy, the speed of tissue growth can be enhanced by the cellular migration speed. It was concluded that additional growth factors could be added in order to increase the tissue growth rate. Seven different seeding strategies were considered in Shakeel *et al.* [2013], and it was demonstrated that although a uniform seeding strategy results in the highest initial cell growth rate, in order to achieve the largest number of cells over the timeframe and the most uniform final cell distribution, it is best to seed away from the flow inlet so as not

to block the nutrient source. Carlier *et al.* [2011] used their model to determine which seeding strategy resulted in the greatest bone formation. In order to maximise bone formation it was demonstrated that a low MSC density seeding strategy needed a low rate of calcium release, whereas a high MSC seeding density needed a high rate of calcium release. It was determined that seeding with a high density of MSCs was a better overall strategy.

Even though the spatial distribution of cells are known to be highly important in the end product quality during tissue growth, several existing theoretical studies in tissue engineering ignore spatio–temporal changes in cell numbers in order to simplify the model so as to examine other effects, for example mass transport. Shipley *et al.* [2010] model the transport of water through a hollow fibre bioreactor in the absence of any cells, and Sengers *et al.* [2004], Shipley *et al.* [2009] and Shipley and Waters [2012] assume a constant cell population so that the processes of cell birth and death are ignored. Whittaker *et al.* [2009] assume the initial cell population number doubles through the experimental time period.

Cell populations

Progenitor or stem cells are often used in tissue engineering applications due to their proliferation potential, as discussed in Section 1.1.2. As a result, the construct will contain more than one cell type, often with different degrees of differentiation and different properties. Most of the previous models discussed have assumed one population of cells. However, this assumption may not be sufficiently accurate if the characteristics of the different cells vary widely. Carlier *et al.* [2011] considered two separate cell populations: osteoblasts and MSCs. Delay differential equations were used, so as to allow for the time taken for cell differentiation and maturation of an osteoblast cell. These were modelled as delays of 10 days and 3 days respectively, and it was assumed that only mature osteoblast cells could deposit collagen. A small delay was also included in the growth factor removal. These effects are often modelled as occurring instantaneously in other theoretical studies and including the time delay is more biologically realistic. Lemon *et al.* [2007], in order to consider the competition between the cells and the ECM for space, developed an ordinary differential equation (ODE) model for two different cell populations. Applicable either to bone or cartilage tissue, the evolution of the volume fractions of undifferentiated human MSCs, differentiated human MSCs and ECM was considered through

time in an inert scaffold in this work. Undifferentiated cells changed into differentiated cells at a given rate and only differentiated cells were modelled as secreting ECM. The ECM was modelled as both stimulating cell growth, through being a source of growth factors, while also limiting cellular growth due to competition for space. The system of equations was solved exactly and experimental data was used to parameterise the model under both normal and low oxygen conditions. The theoretical model was shown to reproduce a similar shape to experimental results for the total quantity of stem cells, showing lag, log and then stationary growth phases.

Mass transport

Due to the problems of mass transport to the centre of the scaffold, as discussed in Section 1.1.2, a large number of theoretical studies have focused on modelling nutrient concentrations within the developing construct. These studies can drive bioreactor and experiment design to ensure adequate mass transport to the developing tissue construct.

Tissue growth requires the supply of a number of nutrients, for example oxygen, glucose and growth factors, and the removal of several waste products, for example lactate and carbon dioxide. However, the majority of mathematical models consider the concentration of one nutrient, often chosen to be oxygen, which is assumed to be rate–limiting in order to simplify the model [Lemon and King, 2007a, Lewis *et al.*, 2005, Coletti *et al.*, 2006, Shakeel *et al.*, 2013, Shipley *et al.*, 2011]. In their study, Shipley and Waters [2012] modelled the concentration of oxygen and the waste product lactate, and the spatio–temporal distribution of oxygen, lactate and glucose were considered in Shipley *et al.* [2009].

The majority of theoretical tissue engineering studies assume that nutrient and waste product transport occurs by both advection and diffusion. The spatial distribution of concentration of the substance(s) is represented by equations of the form given by Equation (1.1), where X now represents the concentration of the nutrient or waste product under consideration [Lemon and King, 2007a, Coletti *et al.*, 2006, Shakeel *et al.*, 2013, Shipley *et al.*, 2009, Shipley and Waters, 2012]. The role of advective transport is especially important to consider when there is perfused flow, such as in the perfusion and hollow fibre bioreactor systems. In contrast, Lewis *et al.* [2005] use the diffusion equation, Equation (1.2), to represent the oxygen concentration with a linear

cell uptake term in a setup where there is no perfused flow and so oxygen transport is purely diffusive.

A Michaelis–Menten uptake term is often used to describe the cell uptake of the nutrient(s) under consideration. This was originally derived to describe the kinetics of an enzyme reaction [Murray, 2002]. Coletti *et al.* [2006] used such a term to describe the cell uptake of oxygen and predicted that higher oxygen concentrations in the surrounding culture medium resulted in better oxygenation in the centre of the scaffold, but that even when the oxygen concentration external to the construct was maximal, the concentrations in the centre of the scaffold were too low for cell survival. Furthermore, Coletti *et al.* [2006] demonstrated the importance of having the construct fit tightly in a perfusion bioreactor to prevent preferential flow occurring at the sides of the construct which was predicted to cause a heterogeneous cell distribution. Shipley *et al.* [2011] and Shipley and Waters [2012] also used Michaelis–Menten uptake terms in order to determine the optimal experimentally variable parameters for a hollow fibre bioreactor to ensure adequate nutrient delivery and waste product removal to the growing tissue. Lewis *et al.* [2005] considered both a Michaelis–Menten and a linear cell uptake term for oxygen, and concluded that the linear term described the experimental data better than a Michaelis–Menten term. Due to this, Shipley *et al.* [2009] also used a linear uptake term in their study.

Mechanotransduction

Bone is a mechanosensitive tissue. The inclusion of the effects of mechanical loading on cell growth and ECM deposition in mathematical models is of importance in understanding the development of mechanosensitive tissues.

Mechanoregulatory algorithms are hypotheses that predict the type of tissue formation (for example, bone, cartilage and connective tissue) under different mechanical stimulation types and magnitudes *in vivo*. Recent reviews on the subject may be found in Isaksson [2012] and Boccaccio *et al.* [2011]. Isaksson *et al.* [2006] compare the different algorithms with *in vivo* experimental results, but with limited success. In addition there is a question mark over whether these algorithms are valid for tissue engineering studies *in vitro* [Khayyeri *et al.*, 2009].

In order to describe the growth of a mechanosensitive tissue within a perfusion bioreactor, O'Dea

et al. [2008] restricted the multiphase model developed by Lemon *et al.* [2006] to two phases: a cellular phase, consisting of cells and attendant ECM; and a culture medium phase. The bioreactor represented by a two–dimensional channel and two different mechanotransduction–mediated growth regimes were postulated to demonstrate the effects of cell density–dependent and pressure–dependent growth on the resultant tissue composition. O'Dea *et al.* [2010] extended this work to include a third phase representing a rigid, porous and inert scaffold. This allowed interactions between the cellular and the scaffold phases to be included. Intraphase forces and interphase traction were also included in order to account for contact inhibition forces between cells. Uniform growth and the two mechanotransduction driven growth functions presented in O'Dea *et al.* [2008] were considered along with a third form of mechanotransduction driven tissue growth, shear stress–dependent growth. Results showed that the size of the parameters describing cell aggregation and repulsion, which controlled the interactions between the cells and between the cells and the scaffold, could alter how the colony is predicted to populate the scaffold.

In order to investigate the effects of fluid mediated shear stresses in a perfusion bioreactor, Shakeel *et al.* [2013] modified the shear stress–dependent growth term, postulated by O'Dea *et al.* [2010], and also included the effects of shear stress–dependent nutrient uptake. Results demonstrated that high flow rates caused high shear stresses, which at certain values inhibited cell growth. O'Dea *et al.* [2013] extended the work of O'Dea *et al.* [2010] and Osborne *et al.* [2010] in order to consider the effects of scaffold variation upon the composition of a mechanosensitive tissue. It was shown that inhomogeneities in the scaffold result in inhomogeneous cell proliferation and ECM deposition.

1.3 Solution methods

We now review the solution methods used to solve the equations governing the mathematical models introduced in Section 1.2, and in particular, for solving the systems of equations that will be used later in this thesis. In the following, we first focus on the analytical methods in Section 1.3.1 before discussing numerical methods in Section 1.3.2.

1.3.1 Analytical methods

Very few mathematical models are described by equations with explicit analytical solutions. Analytical techniques are often used systematically to simplify the governing equations or to identify the qualitative behaviour of the system of equations.

Phase plane analysis can be used for systems of ODEs in order to give an idea of the dynamics of the system and stability of critical points [Kreyszig, 2000]. These will be utilised in this thesis to make qualitative predictions of an ODE model in Chapter 3.

Nondimensionalisation allows assessment of the importance of the terms in the governing equations and terms that are less important may be neglected, simplifying the model [Fowler, 1997]. For example, when modelling fluids, the assumption that the Reynolds number (the ratio of inertial to viscous forces) or the Péclet number (the ratio of advective transport to diffusive transport rate) are very much smaller, or very much greater than one, is often made, justifying neglecting specific transport processes under certain conditions. Methods which have exploited the geometry of the experimental setup in order to reduce the spatial dimension have also been used; for example, O'Dea *et al.* [2010], Shipley *et al.* [2011] and Shipley *et al.* [2010] appeal to the small aspect ratio of their bioreactors (perfusion and hollow fibre bioreactors), and Wilson *et al.* [2007] assume radial symmetric construct growth to give analytical expressions for quantities of interest in order to verify their two–dimensional numerical results. However, Osborne *et al.* [2010] demonstrated that, although the long–wavelength limit analytical reduction presented in O'Dea *et al.* [2010] provided a good approximation when the total yield was examined even when the aspect ratio of the channel was not that small, two–dimensional spatial variation can occur which is not detected by the analytical reduction. For example, at least two spatial dimensions are needed in order to accurately represent fluid shear stress, and, therefore, capture the effects of shear stress mediated mechanotransduction mechanisms.

1.3.2 Numerical methods

As the complexity of the mathematical model increases, the ability to solve the governing equations analytically decreases, and numerical techniques are often needed to compute the approximate solution to the mathematical model. The expression *numerical solution* is often

used (and this term is employed in this thesis) although it should be noted that the result is really an approximation to the analytical solution. Finite element methods (FEMs) are often used to give numerical solutions to the systems of equations. An important distinction must be made between FEMs, as used in this thesis, and finite element models. The former is a numerical method which can be used to give approximate solutions to partial differential equations (PDEs). The second is a modelling approach, where the domain is first discretised into a mesh before applying a model at each element, often using computer aided design and off–the–shelf software [Boccaccio *et al.*, 2011]. The advantage of the former is that the model and numerical method are independent. Consequently, analytical techniques may be used to verify the numerical solution. Further details of the differences between the two can be found in Boccaccio *et al.* [2011].

Finite difference methods are another grid–based method that can be used to solve systems of PDEs. The advantages of FEMs over finite difference methods include the fact that FEMs can handle complex and non–regular geometries and that Neumann boundary conditions are systematically discretised even for nonlinear problems.

Both Osborne and Whiteley [2010] and Hubbard and Byrne [2013] outline general methods to solve a multiphase model with an arbitrary number of viscous phases. In both cases, continuous Galerkin FEMs are used to solve the conservation of momentum equations. Osborne and Whiteley [2010] approximate the hyperbolic term in the conservation of mass equations using the method of characteristics, and includes an artificial diffusion term to stabilise the numerical scheme and resolve a sharp interface. In contrast, Hubbard and Byrne [2013] solve the hyperbolic conservation of mass equations using a conservative upwind finite volume scheme, which removes the need to add an artificial diffusion term.

1.4 Thesis overview

Although engineering artificial bone tissue is a promising method of creating implants, current tissue engineered bone products fall short in terms of mechanical integrity and biological qualities in comparison with actual bone. As yet, no engineered bone implant has been able to match, or improve upon, the biochemical and mechanical qualities of bone grafts.

Mathematical models, and numerical simulations based on these models, are extremely useful tools in increasing the understanding of complex systems such as biological tissues and in aiding the design of experiments, as we have described in Section 1.2. It is the combination of experimental, mathematical and computational methods that will hopefully allow the production of tissue engineered bone products that are of a sufficient size and quality to be clinically useful, mass produced, and affordable.

The aim of this thesis is to develop and investigate mathematical models of tissue engineered bone growth. Our particular focus is on an experimental setup used by our experimental collaborators where bone–producing cells are introduced into collagen gel and grown *in vitro* within a hydrostatic bioreactor. These collaborators are in the experimental group headed by Professor Alicia El Haj at the Institute for Science and Technology in Medicine (ISTM), part of the University of Keele. We formulate a suite of models of the experimental system, and scientific computing is used to provide an approximation to the exact solution of the underlying equations governing the mathematical model.

Preliminary experimental work by our collaborators indicates that intermittent cyclical hydrostatic pressure (intermittent oscillating pressure applied to the fluid in which the scaffold sits) produces a denser and more mineralised bone tissue engineered product than constant atmospheric pressure. The hypothesis is that cyclic hydrostatic pressure stimulates cells to differentiate down the osteogenic pathway. Within this thesis, a suite of three continuum models of increasing complexity are developed. The first model aims to quantitatively describe the temporal evolution of the experimental system under consideration. The second and third models examine the qualitative effect of nutrient transport and mechanical factors on the spatial distribution of the quantities of interest in the construct respectively. These models are then used to investigate specific questions of interest, such as those given below.

- Given that bone–producing cells respond to elevated levels of hydrostatic pressure by increasing mineralisation, are the effects of the cell memory of the loading history important?
- Does the loading strategy influence the spatial distribution of cells and ECM deposition and mineralisation?

- What factors, biochemical or biomechanical, contribute to the heterogeneous spatial distribution of mineralisation seen experimentally?

The remainder of this thesis is structured as follows. In Chapter 2 we summarise the methods used by our experimental collaborators at the ISTM, the data obtained from the *in vitro* experiments, and the conversion of these into mathematical relationships that are used in the remainder of the thesis.

In Chapter 3 we introduce a time–dependent model. The development of the tissue construct in a hydrostatic bioreactor is examined in the form of a system of ODEs. The model is used to predict that it is highly important to include the cell history of loading to which it has been subjected in order to accurately predict levels of solid substrate deposition. Spatial effects are included in Chapter 4, where the construct only is modelled as a fixed domain, with cellular movement being represented as a diffusive process, to investigate biochemically–induced spatial patterning. It is predicted that, when the concentration of a diffusible nutrient and nutrient–dependent growth are introduced, the results qualitatively reproduce the heterogeneous spatial distribution in the solid phase seen experimentally.

In order to consider the effects of fluid flows and examine the spatial patterning induced by biomechanical effects, Chapter 5 presents a multiphase model which extends the work of Osborne *et al.* [2010], O'Dea *et al.* [2010] and O'Dea *et al.* [2013] to the hydrostatic bioreactor experimental setup. Here both the construct and the surrounding culture medium are considered, as opposed to just the construct as in previous chapters, and nutrients are assumed to be well perfused in the fluid phase. The cell and fluid phases are assumed to behave as viscous fluids, while a solid substrate phase representing the initial scaffold, ECM and mineralisation, is modelled as a solid. In Chapter 6 we demonstrate that flow is driven through two terms representing cell–cell and cell–substrate interactions, which are functions of the constituent phase volume fractions and their spatial gradients. In order to investigate the effects of these forcing terms on the quantities of interest, the velocity and pressure solution and its dependence on variations in parameter values and initial conditions, at the initial time point is investigated. The work is extended in Chapter 7 to consider time–dependent numerical simulations and the spatio–temporal evolution of the constituent phase volume fractions and associated fluid shear stress magnitudes is examined. We demonstrate that, as time evolves, the predicted fluid shear

stresses become higher in mean and maximal magnitude under stimulated than under control conditions. Furthermore, we illustrate that the form of the initial conditions, describing the shape and position of the construct in the well, does not significantly affect the average quantity of cells and substrate over time but does have a significant effect on the standard deviation of these phases, and both the average and standard deviation of the the fluid shear stress magnitudes as time evolves.

Finally, conclusions are drawn in Chapter 8 and areas for future work are also discussed.

Appendix A includes a discussion on the computational methods used in this thesis, and Appendix B details additional initial conditions used in Chapter 7. Appendix C includes, for reference, a list of abbreviations, a description of the mathematical notation and a list of nomenclature used in this thesis.

Chapter 2

Experimental methods

The aim of this chapter is to give the background to the techniques used by our experimental collaborators at the Institute for Science and Technology in Medicine at the University of Keele. These experiments test the hypothesis that intermittent cyclic hydrostatic pressure stimulation produces a denser, more mineralised construct than constant atmospheric pressure. Furthermore, we detail appropriate modelling assumptions and identify dependent variables of interest. This allows us, in Chapters 3 – 7, to develop mathematical models to represent the experiments.

***Disclaimer**: the experimental methods, Section 2.1, and the data and images in Figures 2.2 and 2.5 – 2.9 describe and present the work that was carried out by our experimental collaborators at the ISTM and are not part of the work performed by the author. They form the basis from which the mathematical models presented in this thesis are developed. The remainder of the chapter, including a conversion of the setup and data into mathematical terms, were performed by the author.*

2.1 Experimental methods

In vitro experiments were performed by our collaborators, in a similar manner to that outlined in Henstock *et al.* [2013], as follows. Collagen type I hydrogels, purified from the tendons of rat tails, were chosen as the scaffold material for these experiments due to their biocompati-

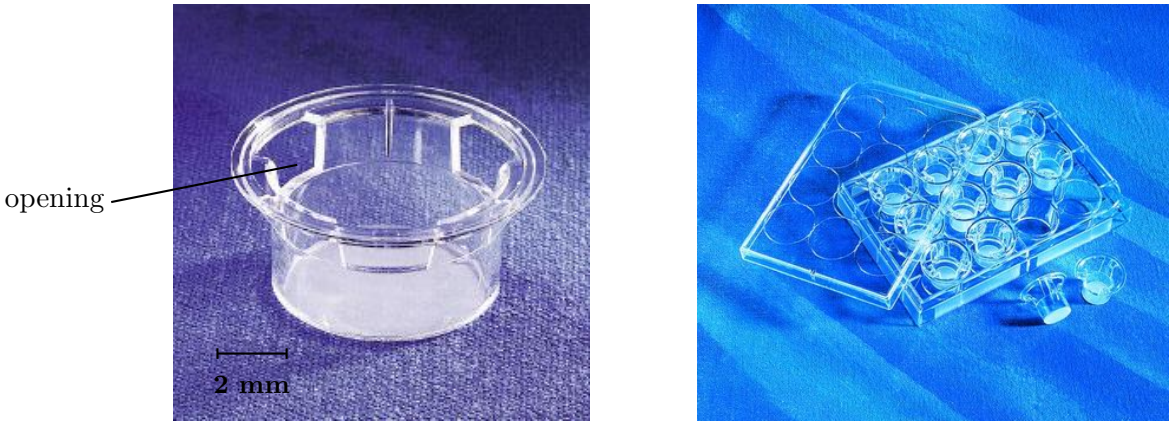

(a) Transwell insert (b) A 12–well plate

Figure 2.1: Pictures illustrating (a) the polyester (polyethylene terephthalate) membrane transwell–clear insert with the three side wall openings and (b) a 12–well plate holding the inserts. Both pictures are reproduced from the Corning Life Sciences catalogue with permission.

ble, osteoconductive and osteointegrative properties. In order to make the gels, the collagen was diluted to the required concentration from the original stock concentration of 10 mg/ml (produced by BD Biosciences) to which adult human MSCs (produced by Lonza, sourced from adult humans via iliac crest bone marrow aspiration) were added in suspension. In order to reduce donor–specific variability, cells from the same donor were used where possible. The required volume of the gel was then pipetted onto a fully permeable microporous membrane of a sterile polyester (polyethylene terephthalate) transwell–clear insert (produced by Corning Life Sciences) as shown in Figure 2.1(a). Each transwell insert holding a construct was placed into an individual well in a 12–well plate as shown in Figure 2.1(b). The wells were then filled with osteogenic culture medium so as to submerge the collagen gel. The culture medium consisted of a variety of nutrients and growth hormones to encourage osteogenic differentiation and prevent the growth of pathogens. Henstock *et al.* [2013] detail the precise components of the culture medium and further details of the experimental methods. The gels were allowed to settle for 24 hours, during which time the cells adhered to the collagen and caused it to contract into a ruffled ball shape which then relaxed into a roughly hemispherical shape. The hemispherical shape formed is thought to be due to the attachment of the cells to the microporous membrane of the transwell insert. The shape of the gels did not change significantly over the course of the experiment, and Figure 2.2 shows micro computerised technology (μCT) imaging of a gel at day 14 to illustrate the shape. The transwell insert can be completely removed from the

Figure 2.2: μCT scan a of sample collagen gel after 14 days of growth showing a roughly hemispherical shape. The shape did not significantly change over the course of the experiment. This gel was produced by seeding 20,000 human mesenchymal stem cells in 300 μl of 5 mg/ml of collagen suspension. Courtesy of the ISTM, the University of Keele.

well without disturbing the developing construct which allowed the media to be refreshed when desired. Our collaborators performed this procedure once a day, on weekdays only. At the same time the three side wall openings, shown in Figure 2.1(a), allow exchange of media and the diffusion of nutrients and waste products to the region of culture medium above the construct, while the membrane allows flow of media through the base of the insert. During the course of the experiment the constructs were kept at a constant temperature of 37 °C with 5% carbon dioxide in the surrounding gas.

In the initial run of experiments, gels of initial volume 300 μl, with collagen concentrations of 0.5 mg/ml containing approximately 20,000 cells, were prepared. *Control* samples were kept at constant atmospheric pressure throughout the experiment. *Stimulated* samples received one hour of cyclic pressure loading per weekday, and otherwise experienced constant atmospheric pressure. This was achieved by placing the well plate in the bioreactor for the duration of cyclic loading. The hydrostatic pressure bioreactor is a custom–made device, produced in collaboration between the ISTM and Tissue Growth Technologies. It comprises a sealed vessel and a machine capable of compressing incubated air above a 12–well plate. The compression of the gas phase is controlled by a computer, allowing for precise regulation of the frequency and amplitude of the pressure applied. Further details on the bioreactor equipment may be found in Henstock *et al.* [2013].

We now provide a quantitative description of the experimental setup.

Table 2.1: Dimensional spatial values for each individual well.

Description of variable	**Mathematical notation**	**Dimensional value**
Radius of well	R	8.13 mm
Height of surface of culture medium	H	17.0 mm
Height of support insert membrane above base of well	s_h	2.9 mm

2.2 Mathematical description of experimental setup and data

2.2.1 Domain

We represent an individual well as cylindrical in shape with the hemispherical cell–scaffold construct sitting on the permeable membrane of the transwell insert and submerged in culture medium, as shown in Figure 2.3. We construct a domain, Ω, in three–dimensional Cartesian

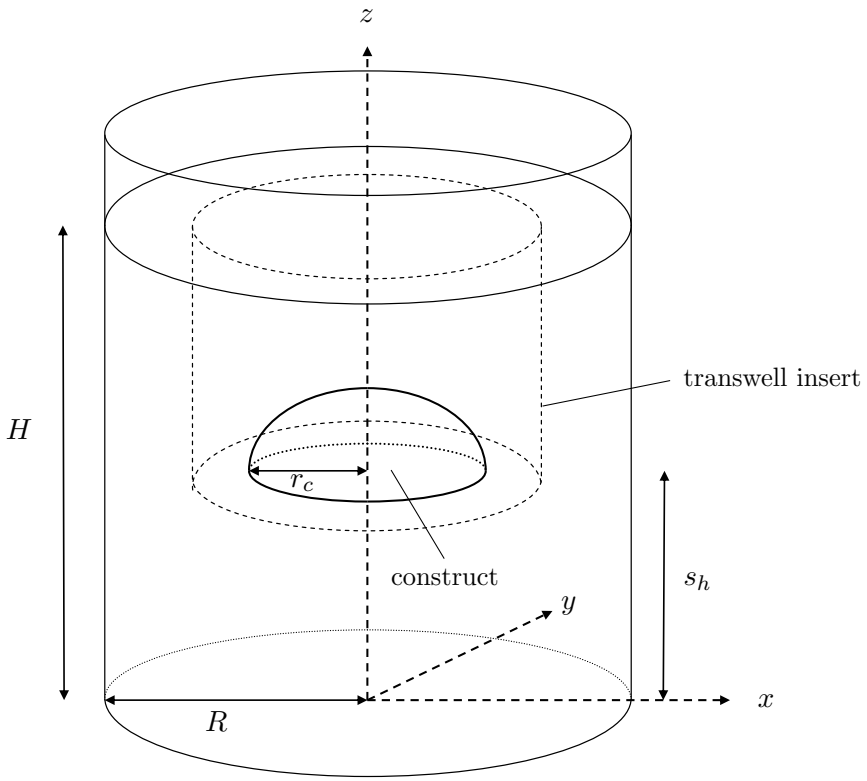

Figure 2.3: Sketch of an individual well, with the position of the construct and the transwell insert indicated by dashed lines. Here H is the height of the culture medium within the well, R is the radius of the well, s_h is the height of the base of the construct above the base of the well and r_c is the radius of the hemispherical construct. The radius of the construct varies according to the initial collagen concentration, and its dimensional value is discussed in Section 2.2.3. The dashed arrows indicate the coordinate axes. This schematic is not to scale.

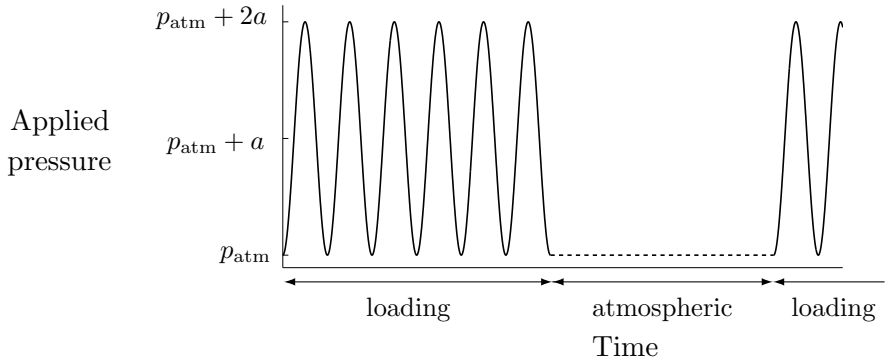

Figure 2.4: Intermittent cyclic applied pressure, as described by Equation (2.2). Here p_{atm} is atmospheric pressure and a is the amplitude of the cyclic loading. The horizontal axis represents time (not to scale) and the vertical axis represents the pressure applied by the bioreactor. The dashed line indicates a continuation of atmospheric pressure.

coordinates with the origin at the centre of the base of the well, given by

$$\Omega = \{(x, y, z) \in \mathbb{R}^3 : x^2 + y^2 \leq R^2, 0 \leq z \leq H\}. \tag{2.1}$$

We ignore the impermeable walls of the transwell insert, as the construct is not in contact with the walls, and is much smaller than the diameter of the transwell insert. Other quantities of interest, such as the height of the culture medium and the radius of the well are shown in Figure 2.3, with Table 2.1 giving the description and dimensional values of the variables describing the geometric domain.

2.2.2 Loading

In the stimulated experiments, an *intermittent cyclic* loading strategy is employed. This is sinusoidal when the construct is in the bioreactor. When the constructs are not in the bioreactor they experience atmospheric pressure. The pressure applied to the surface of the culture medium during the experiments, denoted by $p_{\text{app}}(t)$, where $t \geq 0$ is time, is described by

$$p_{\text{app}}(t) = \begin{cases} p_{\text{atm}} + a\left(1 - \cos\left(2\pi\omega t\right)\right) & \text{if the construct is in the bioreactor,} \\ p_{\text{atm}} & \text{otherwise,} \end{cases} \tag{2.2}$$

where p_{atm} is atmospheric pressure, ω is the frequency and a is the amplitude of the cyclic loading. Note that control samples are subjected to constant atmospheric pressure and spend no time in the bioreactor. This intermittent cyclic loading regime is illustrated in Figure 2.4. The current experimental strategy is to place the stimulated samples in the bioreactor under hydrostatic loading during weekdays for one hour but not at the weekend and we assume that the stimulated specimens enter the bioreactor at the same time each weekday.

2.2.3 Data

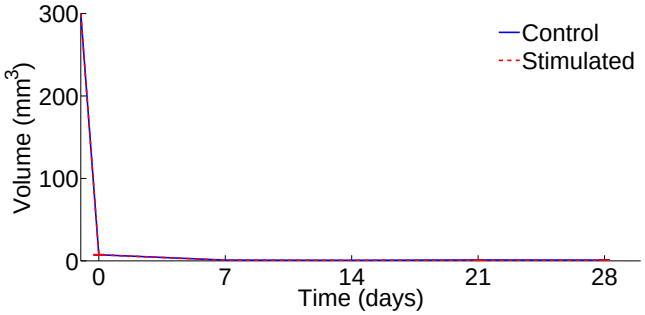

(a) Initial 24 hours included

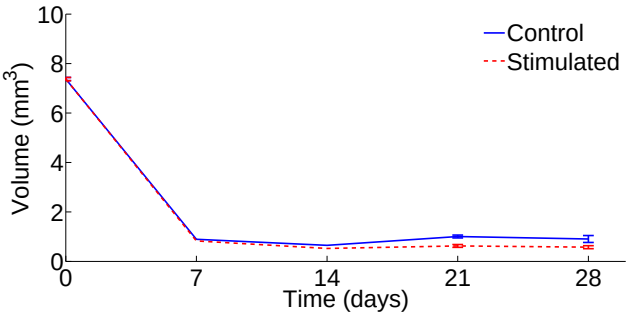

(b) Without initial 24 hours

Figure 2.5: Graphs showing how the average gel volumes vary over time. The day on which the gel was made, "day -1", is included in (a) to show the degree of contraction over the initial 24 hours. The mathematical models start at "day 0" once the gels have settled, and (b) shows the average gel volume from this time point onwards. The bars at days 21 and 28 indicate the standard error. Data courtesy of the ISTM, the University of Keele.

μCT is used to image and analyse the gels at two separate density thresholds which are measured by a linear attenuation coefficient. The lower threshold captures all of the construct material, whereas the higher threshold only captures the mineralised parts.

Figure 2.5 shows the evolution of the total gel volume and Figure 2.6 shows the evolution of the mineralised volume fraction (the mineralised volume divided by the volume of the whole

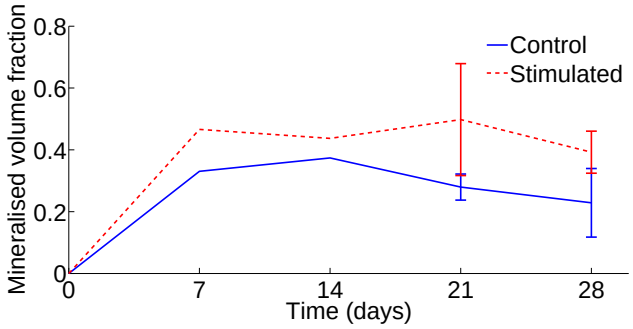

(a) Average gel mineralised volume

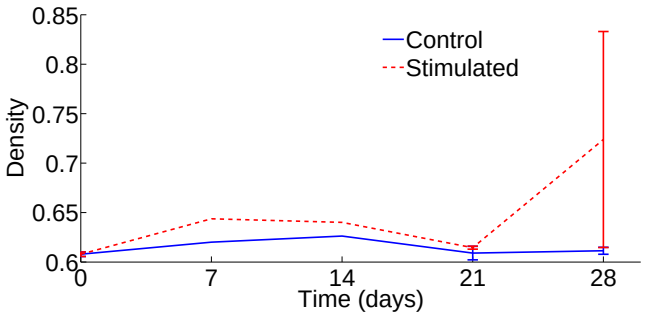

(b) Average gel densities

Figure 2.6: Graphs showing how (a) the average gel mineralised volume fraction and (b) the average gel density vary over time. The vertical axis in (b) represents density measured by a linear attenuation coefficient. The bars at days 21 and 28 indicate the standard error. Data courtesy of the ISTM, the University of Keele.

gel) and the density of the gels over the course of the experiment. For clarity "day -1" is the day the collagen gels are made, so that the experimental run starts on "day 0" after the gels have contracted. Figure 2.5(a) includes "day -1" so the degree of volume contraction over the first 24 hours may be visualised, whereas Figure 2.5(b) shows the gel volumes from "day 0", so that the change of volume of the gel over the experimental time period of interest can be seen. The lines for the volume of the constructs experiencing stimulated and control (non–stimulated) loading conditions through time are very similar, indicating that the gels under stimulated and control loading conditions contract at roughly the same rate, and have a similar volume over the duration of the experiment. It should be noted that, once analysed in the μCT scanner, the gels are discarded and just one gel each was evaluated at days 7 and 14 and four gels each at days 0, 21 and 28. Therefore, days 0, 21 and 28 record an average value and a standard error, whereas days 7 and 14 record just one value.

Previous experimental work, as discussed in Section 1.1.4, indicates that bone–producing cells respond to dynamic hydrostatic pressure loading by increasing the quantity of ECM deposi-

tion and mineralisation. The results presented here support this, with the stimulated samples showing increased mineralisation (Figure 2.6(a)) and increased density (Figure 2.6(b)) over the control samples. It has also been shown in preliminary experimental runs and previous work that intermittent applications of static high pressure gave similar results to control loading conditions in terms of mineralised volume fraction and density [Henstock *et al.*, 2013].

We note that the data presented here are not statistically significant (to a 5% significance level) due to the low number of repeats. However, a statistically significant increase in the mineralised volume fraction and in the density of the stimulated samples, to a 5% significance level, over controls samples has been demonstrated over a shorter timescale and when matrigel™ was used as a scaffold material. Our experimental collaborators are going to repeat the experiments presented here for a larger number of gels. In the absence of this data, we proceed with the results presented above.

Initial cell and collagen quantities

From the experimental data it is possible to extract the initial volumes for the cells, collagen and total gel to give the initial conditions for use in the mathematical models developed in this thesis.

To determine the initial volume of cells, we assume that human MSCs are spherical in shape in suspension, with an average radius of 15.25 μm [Furlani *et al.*, 2009], and further assume that the volume of a cell does not change from when it is in suspension to when it adheres to the collagen gel. Denoting the initial number of seeded cells by N_0, and assuming that there is no cellular proliferation or death within the initial 24 hours during which time the cells are adhering to the scaffold[a], the initial volume of cells can be roughly calculated as

$$\frac{4}{3}N_0\pi 0.01525^3 \text{ mm}^3.$$

Assuming that the density of the collagen is 1.35 g cm^{-3} [Podrazký and Sedmerová, 1966] enables us to calculate the initial volume of collagen used to make the gels. With the above

[a] An experiment performed by our experimental collaborators at the ISTM compared cell numbers before and after the collagen gel contracted. This showed that there was not a significant difference in cell numbers, indicating that there is little or no cell proliferation during the first 24 hours.

Table 2.2: The initial volumes of collagen and cells and the average volumes of the construct to 2 d.p.

Initial volume (mm^3)		Weighted average volume (mm^3)		
collagen	cells	control gels	stimulated gels	combined
0.11	0.30	1.51	1.23	1.37

data, for $N_0 = 20000$ cells seeded in a 300 μl suspension of collagen at a concentration of 0.5 mg/ml as practised experimentally, the initial volumes for the cells and collagen are given in Table 2.2.

Figure 2.5(a) illustrates a very large loss of construct volume over the first 24 hours. The two lines, representing the volume of the gels under control and stimulated loading conditions, are indistinguishable indicating that contraction is independent of the loading conditions. From Figure 2.5(b) it can be seen that, although there is still contraction occurring during the first seven days of the experimental timeframe, it is much smaller in magnitude than over the first 24 hours. The above justifies the assumption that the gels have contracted by "day 0" and that the total volume of both the stimulated and control gels (including any bone fluid or culture medium contained within the pores of the construct matrix) remain equal and constant throughout time after this. For the purposes of evaluating the initial conditions for the mathematical models, we take a weighted (by the number of gels) average volume from the data at days 0, 7, 14, 21 and 28 for both stimulated and control gels to determine the initial construct volume, and this is given in Table 2.2.

Spatial effects are included in Chapters 4 – 7. In order to calculate the initial conditions for the constituent phases we assume a perfectly hemispherical construct with volume $V_0 = 2/3\pi r_c^3$, where r_c is the radius in mm. Using a total construct volume of 1.37 mm^3 from Table 2.2, rearranging yields the radius of the gels to be

$$r_c = 0.8681 \text{ mm}. \tag{2.3}$$

Imaging analyses at day 0, reproduced in Figure 2.7, indicate that the cell distribution after contraction is homogeneous. Figure 2.7(a) shows a picture of the whole construct and Figure 2.7(b) shows fluorescent imaging of the whole construct, where the individual cells appear

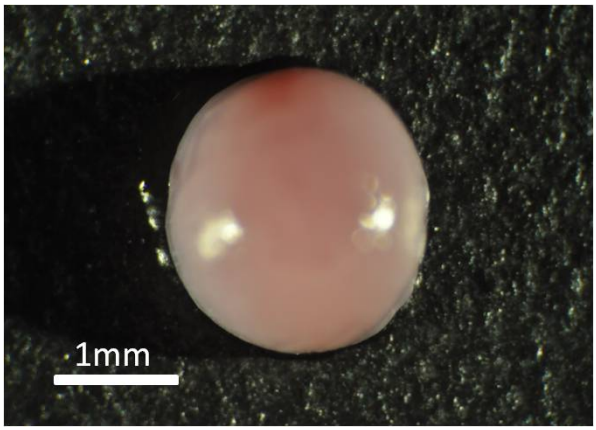

(a) Brightfield image

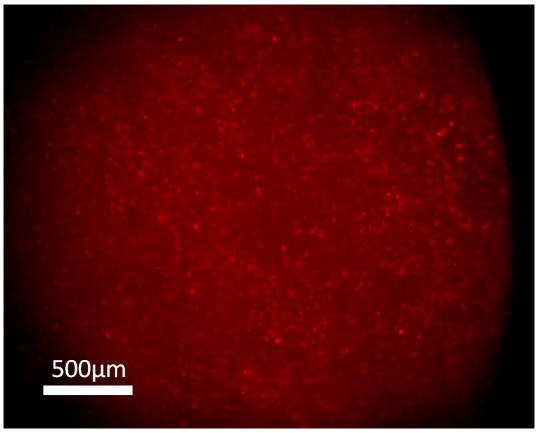

(b) Fluorescent PKH26 cell tracker

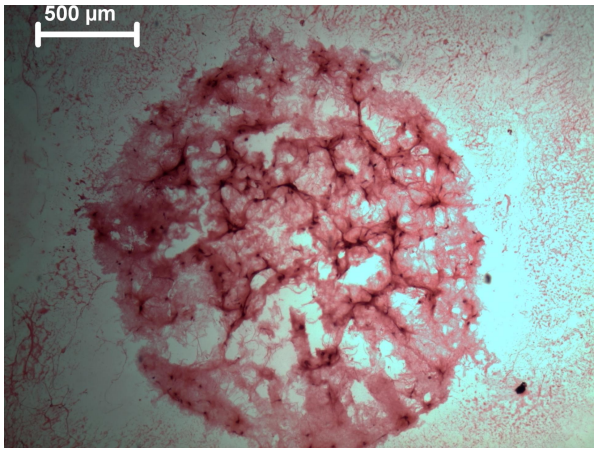

(c) 15μm slice stained with Haematoxylin and Eosin

Figure 2.7: Imaging analyses of a collagen gel at day 0 for 40,000 MSCs in 0.5 mg/ml collagen gel. Figure (a) shows the whole gel from above. Figure (b) shows the gel from above with the cells stained with a fluorescent dye so that they show up as red dots. Figure (c) shows a slice of the gel stained with Haematoxylin and Eosin showing the cell nuclei and cytoplasm, which appear as blue and pink respectively. Courtesy of the ISTM, the University of Keele.

as red dots. A 15 μm slice through the centre of the gel stained with Haematoxylin and Eosin in order to illustrate cell morphology is shown in Figure 2.7(c). The cytoplasm and the nucleus of the cells appear pink and blue in colour respectively. Figures 2.7(b) and (c) show no clear patterning in cell distribution, for example more cells located towards the centre of the construct or more at the periphery of the gel. These figures justify assuming an initially homogeneous cell distribution in Chapter 4.

In order to understand the spatial distribution of the collagen in the construct after contraction μCT was performed, and is reproduced in Figure 2.8. Each picture shows the results at a particular density threshold, with the density threshold increasing from left to right and top to

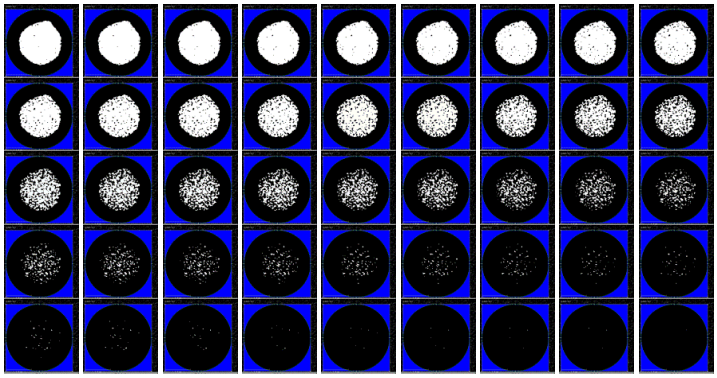

Figure 2.8: Images showing successive increase of the density threshold in μCT (left to right, top to bottom) of the collagen–cell construct at day 0, which is 1.6 mm in diameter. White indicates matter above the density threshold and black indicates matter below the density threshold. The black rim around the gel is air. As the density threshold is increased less of the construct can be visualised. Imaging data are for 40,000 MSCs seeded in a collagen of initial concentration 0.5 mg/ml. Courtesy of the ISTM, the University of Keele.

bottom. This justifies an initial homogeneous collagen distribution in Chapter 4.

Model parameterisation

The initial scaffold consists of collagen type I only and ECM is predominately collagen based. It is not experimentally possible to distinguish between the initial collagen scaffold and collagen that is deposited in the form of ECM by the cells over the course of the experiment. Rather than modelling the scaffold and ECM as separate phases, we consider the evolution of the total amount of mineralised collagen, known as the "substrate" phase. We assume that the cells spend the first 24 hours of the experiment contracting the gel and differentiating, and that they do not deposit any ECM in this time, so that the initial volume of the substrate is equivalent to the initial volume of the collagen, as given in Table 2.2. We further assume that cells do not show a preference in binding to the secreted ECM as opposed to the rat–derived collagen which comprises the initial scaffold.

In order to parameterise the mathematical models in this thesis, we make the assumption that any increase in the substrate volume fraction from the initial time point can be represented by the mineralised volume fraction. This is measured experimentally with μCT analysis as the volume of material with a density above a higher threshold (assumed to capture mineralised portions of the gel only) divided by the volume of material at a lower threshold (which

is assumed to capture all the material). This assumption is equivalent to assuming only mineralisation of the existing collagen scaffold, and no ECM deposition, takes place during the experimental timeframe. In discussion with experimentalists, it is thought that the quantity of ECM deposition is very small in comparison to mineralisation, justifying this assumption.

The average mineralised volume fraction of the gels at days 21 and 28 is given in Table 2.3. There is a decrease in the average mineralised volume fraction between days 21 and 28 for both the control and stimulated samples. To represent this, we include the effects of substrate degradation in our mathematical models, and this is discussed further in Chapter 3. Although gel density information is also available, as displayed in Figure 2.6(b), we do not use these data to parameterise the mathematical models. This is because it is implicit in our assumptions during the development of our mathematical models that all phases have the same density.

Table 2.3: The average volume fraction of the gels that is mineralised for days 21 and 28. We make the assumption that any increase in volume fraction of the solid phase can be represented by an increase in mineralisation.

	21 days	28 days
Control	0.2796	0.2286
Stimulated	0.4979	0.3924

In contrast to the spatially homogeneous initial distribution of the solid phase, image analysis reveals that the spatial distribution of the mineralisation becomes heterogeneous with time. Figure 2.9 shows the construct at day 14 from a similar experimental setup stained in such a way that calcium appears red. It is found that, as the experiment progresses, a rim of mineralisation is seen at the periphery of the construct, which appears dark red. This does not extend into the centre of the construct, which is pink due to the colour of the gel. This occurs under both loading regimes, but is more pronounced under the stimulated loading conditions. Such a heterogeneous spatial distribution in the mineralisation produces an ineffective tissue engineered bone construct.

2.3 Close of chapter

In this chapter we have presented the experiments that the mathematical models developed in this thesis intend to describe. Furthermore, we have discussed a conversion of the experimental

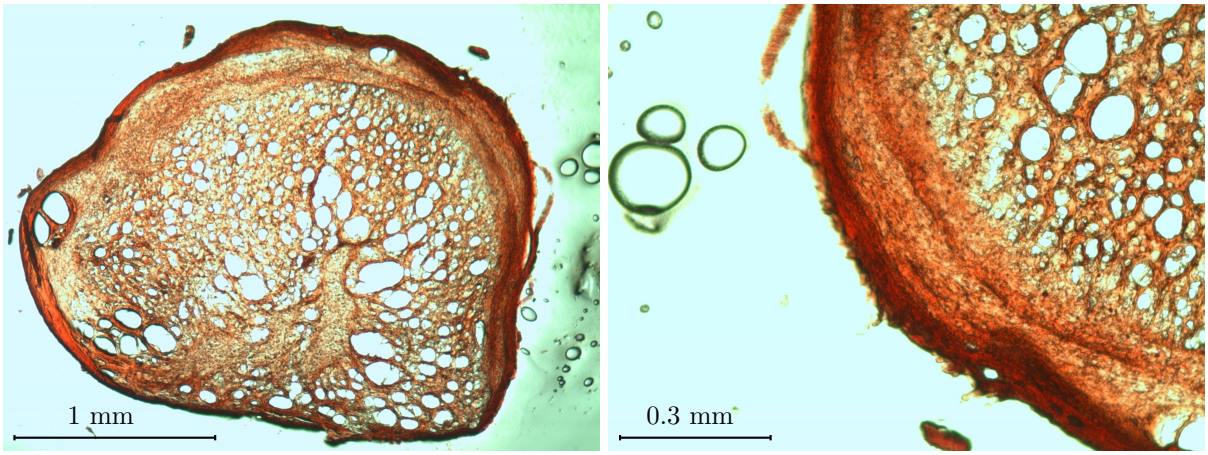

(a) Full sized image (b) Magnification of the edge

Figure 2.9: A histological slice stained with Alizarin red staining. This turns calcium red and illustrates the type of spatial distribution in the mineralisation seen at day 14. This particular experimental setup was of a matrigel^{TM} seeded with chick bone cells under intermittent cyclic loading. The experimental setup of human MSCs seeded in collagen gels produces a similar result. Courtesy of the ISTM, the University of Keele and reproduced from Reinwald *et al.* [2014] with permission.

setup and data into mathematical quantities, along with the assumptions made to allow us to do this. Further modelling assumptions are made during the course of the thesis as the models are developed and these assumptions are discussed when they are first made. We now proceed, in the following chapters, to develop a suite of mathematical models with increasing complexity in order to describe the experiments and address the questions posed in Section 1.4. In particular we wish to elucidate the factors which cause the rim of mineralisation to form experimentally, as shown in Figure 2.9, and determine the experimental conditions that would result in a higher quality construct, with increased mineralisation and with this mineralisation being more spatially homogeneous.

Chapter 3

A temporally–dependent model

In this chapter we develop a time–dependent model for the evolution of the cells, the substrate and the fluid. The model includes the effects of cell birth, cell death, substrate deposition and substrate degradation. Two hypotheses for the form of the substrate deposition rate, which are dependent on the pressure exerted on the surface of the culture medium, are tested, and the model is parameterised using the experimental data introduced in Chapter 2. Previous research and preliminary experiments indicate that stimulation by hydrostatic pressure increases substrate deposition and mineralisation. In order to represent this, for the first hypothesis, in Section 3.1, we model the substrate deposition as a switch function dependent on the current pressure, where the rate of deposition increases when the applied pressure is above a threshold value. However, it is found that, in comparison to experimental data, this overestimates the quantity of the substrate deposited when the construct is subjected to longer durations of elevated pressure. The effects of the pressure loading history are included, in Section 3.2, in a revised hypothesis where the substrate deposition rate decays exponentially with the time the pressure has been above the threshold. Numerical results are shown to agree quantitatively with the experimental data. The calibrated model is then used, in Section 3.3, to optimise the experimentally variable conditions, so as to produce the best quality implant within the experimental timeframe.

3.1 Mathematical model of bone tissue growth

We consider a time–dependent ODE model, where we determine the evolution of the volume fraction of three separate phases. We assume that all the material in the construct is either part of a cell phase, a *substrate phase* (encompassing collagen from the initial scaffold and deposited ECM along with any mineralisation), or a fluid phase. The volume fractions of these phases are represented by $\theta_C(t)$, $\theta_J(t)$ and $\theta_W(t)$ respectively, with $\theta_k(t) \in [0,1]$ for $k = C, J, W$, where $t \geq 0$ is time. Although there will be multiple cell populations present due to the differentiation of the MSCs with which the scaffold is seeded, as depicted in Figure 1.2, the different cell types are difficult to characterise without invasive techniques. Consequently, we consider one population of cells with volume fraction $\theta_C(t)$. Assuming that all the volume is accounted for we have

$$\theta_C(t) + \theta_J(t) + \theta_W(t) = 1, \tag{3.1}$$

also called the *no voids condition*. We assume that the concentration of nutrients required for cell proliferation, such as oxygen and glucose, are proportional to the volume fraction of the fluid phase. We model cell proliferation to be proportional to the substrate volume fraction, because cells need to attach to the substrate in order to proliferate [Schwartz and Assoian, 2001, McCoy and O'Brien, 2010], and the quantity of nutrients, proportional to the volume fraction of the fluid phase. This gives

$$\frac{\mathrm{d}\theta_C}{\mathrm{d}t} = k_b \theta_J \theta_W \theta_C - k_d \theta_C, \tag{3.2}$$

where $k_b > 0$ is the cell proliferation (birth) rate and $k_d > 0$ is the cell apoptosis (death) rate. Here the first term on the right hand side of the equation, $k_b \theta_J \theta_W \theta_C$, models the rate of cell proliferation and the second term, $-k_d \theta_C$, models the rate of cell death [Murray, 2002]. The pressures exerted by the bioreactor are not high enough to cause pressure–dependent apoptosis and so this effect is not included in the model.

Changes in substrate volume fraction through time are modelled as occurring due to substrate deposition and degradation. We model both processes as mechanisms modulated by cells, with the substrate deposition rate dependent on the current pressure. In addition we assume that

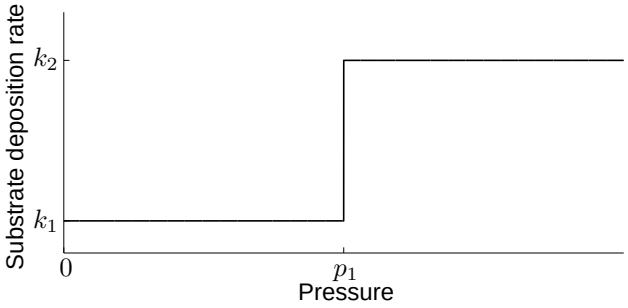

Figure 3.1: Sketch of the substrate deposition rate given by Equation (3.4), where the vertical axis represents the substrate deposition rate, $k_p\left(p(t)\right)$, and the horizontal axis represents the current pressure, $p(t)$. The threshold pressure value between the lower substrate deposition rate of k_1 and the higher rate of k_2 is given by $p(t) = p_1$.

cells require nutrients, dissolved in the fluid phase, to produce the substrate, so that

$$\frac{\mathrm{d}\theta_J}{\mathrm{d}t} = k_p\left(p(t)\right)\theta_C\theta_W - k_{jd}\theta_J\theta_C, \tag{3.3}$$

where $p(t)$ is the local pressure at time t, $k_p\left(p(t)\right) > 0$ is the rate of substrate deposition by the cells and $k_{jd} \geq 0$ is the rate at which the cells degrade the substrate. The first term on the right hand side of the equation, $k_p\left(p(t)\right)\theta_C\theta_W$, represents substrate deposition, and the second term, $-k_{jd}\theta_J\theta_C$, represents substrate degradation by the cells through hydrolysis. Note that we ignore the natural degradation of the substrate as this is on a much longer timescale than the timescales of substrate deposition and active substrate degradation[a]. The fluid volume fraction at time t, $\theta_W(t)$, is obtained through the no voids condition, Equation (3.1).

We now need to prescribe the functional form of the substrate deposition rate, $k_p\left(p(t)\right)$. We assume that there exists a pressure threshold, p_1, above which the cellular pathway controlling substrate deposition is amplified and the rate of substrate deposition is enhanced. We first model the substrate deposition rate by a switch function, in a similar fashion to pressure–dependent growth in O'Dea *et al.* [2010], given by

$$k_p\left(p(t)\right) = \begin{cases} k_1 & \text{if } p(t) < p_1, \\ k_2 & \text{if } p(t) \geq p_1, \end{cases} \tag{3.4}$$

where $k_2 > k_1$, and $k_1 > 0$, as shown in Figure 3.1. The pressures exerted by the bioreactor are

[a]This was suggested as a result of communication with our experimental collaborators.

within physiological normal ranges, and so we assume not high enough to limit substrate deposition, and so this mechanism is not included into our model. The data presented in Chapter 2, previous work discussed Section 1.1.4, and preliminary experiments, suggest that a developing bone construct responds to a higher applied pressure by increasing substrate deposition. Consequently, we assume that the threshold pressure value, p_1, lies within the experimental range, so that $p_1 > p_{\text{atm}}$. We further assume that the pressure experienced within the construct is the same as the pressure applied to the surface of the culture medium, so that

$$p(t) = \begin{cases} p_{\text{atm}} + a\left(1 - \cos\left(2\pi\omega t\right)\right) & \text{if the construct is in the bioreactor,} \\ p_{\text{atm}} & \text{otherwise,} \end{cases} \tag{3.5}$$

where p_{atm} is atmospheric pressure, a is the amplitude and ω is the frequency of the cyclic loading.

3.1.1 Initial conditions

Chapter 2 details the conversion of the experimental data into initial quantities. The initial conditions in general are given by $\theta_C(0) = \dfrac{C_0}{V_0}$ and $\theta_J(0) = \dfrac{J_0}{V_0}$, where V_0 is the weighted average volume of the construct and C_0 and J_0 are the initial volume of cells and collagen respectively. By Table 2.2, the initial conditions are given by

$$\theta_C(0) = \frac{0.11}{1.37}, \qquad \theta_J(0) = \frac{0.3}{1.37}. \tag{3.6}$$

3.1.2 Parameters

We make the assumption that the parameters k_b, k_d, k_1, k_2, p_1, k_{jd}, and their dimensionless equivalents, are constant and independent of both space and time. Following discussion with our experimental collaborators we assume that the rate of cell birth, k_b, is one per day. The rate of cell death, k_d, is roughly equivalent to osteoblast apoptosis, which from Jilka *et al.* [1998] we take to be 0.6% of cell birth. The lower rate of substrate deposition (for pressures below the threshold p_1), k_1, is taken to be 57% of cell birth [Flanagan and Nichols, 1969].

Further parameters that are inputs to the system are guided by the current experimental set

Table 3.1: Dimensional parameters obtained from literature and the experimental setup.

Parameter	**Value**	**Reference/origin**
k_b	1 day^{-1}	Discussion with experimental collaborators
k_d	$0.006k_b$	Jilka *et al.* [1998]
k_1	$0.57k_b$	Flanagan and Nichols [1969]
a	140 kPa	Current experimental input
ω	1 Hz	Current experimental input

up. Table 3.1 details the values of the known dimensional parameters and the origin of this information. The remaining parameters, k_{jd}, k_2 and p_1, are unknown and we obtain these by parameter fitting. This is achieved by a comparison of the experimental data presented in Chapter 2 with the numerical results from the mathematical model in Section 3.1.5.

3.1.3 Nondimensionalisation

Noting that θ_k for $k = C, J, W$ are dimensionless, we nondimensionalise the remaining variables as follows:

$$t = \frac{\hat{t}}{k_b}, \qquad p = p_0\hat{p} + p_{\text{atm}}, \tag{3.7}$$

where the caret is used to indicate the dimensionless variable and we set $p_0 = 1$ kPa. Although a choice of $p_0 = a$ kPa may initially seem more appropriate, we choose $p_0 = 1$ kPa in order to facilitate optimisation of the amplitude of loading in Section 3.3. The pressures applied by the bioreactor are of the order kPa and so this is an appropriate pressure scaling.

The dimensionless equations corresponding to Equations (3.2) and (3.3) respectively, on dropping carets, are

$$\frac{\mathrm{d}\theta_C}{\mathrm{d}t} = (\theta_J\theta_W - K_d)\,\theta_C, \tag{3.8}$$

$$\frac{\mathrm{d}\theta_J}{\mathrm{d}t} = K_p\,(p(t))\,\theta_C\theta_W - K_{jd}\theta_J\theta_C, \tag{3.9}$$

where $K_d = \dfrac{k_d}{k_b}$, $K_p = \dfrac{k_p}{k_b}$ and $K_{jd} = \dfrac{k_{jd}}{k_b}$ and $K_d > 0$, $K_p > 0$ and $K_{jd} \geq 0$. The substrate

deposition rate is given by

$$K_p\left(p(t)\right) = \begin{cases} K_1 & \text{if } p(t) < P_1, \\ K_2 & \text{if } p(t) \geq P_1, \end{cases} \tag{3.10}$$

where $K_1 = \dfrac{k_1}{k_b}$, $K_2 = \dfrac{k_2}{k_b}$ with $K_2 > K_1 > 0$ and $P_1 = \dfrac{p_1 - p_{\text{atm}}}{p_0}$ with $P_1 > 0$ are constants. The dimensionless equation describing the current pressure, obtained from Equation (3.5), is given by

$$p(t) = \begin{cases} A\left(1 - \cos\left(2\pi\Upsilon t\right)\right) & \text{if the construct is in the bioreactor,} \\ 0 & \text{otherwise,} \end{cases} \tag{3.11}$$

where $\Upsilon = \dfrac{\omega}{k_b}$ and $A = \dfrac{a}{p_0}$.

In summary, the dimensionless model is given by Equations (3.1), (3.8) and (3.9) with the substrate deposition rate given by the switch function in Equation (3.10). Pressure depends on the loading strategy used and, for the strategy currently practised experimentally, is given by Equation (3.11). Initial conditions remain unchanged from Equation (3.6).

3.1.4 Constant applied pressure

Using Equation (3.1) to eliminate θ_W, the above system given by Equations (3.1), (3.8) and (3.9) can be described by two coupled ODEs:

$$\frac{\mathrm{d}\theta_C}{\mathrm{d}t} = \left(\theta_J(1 - \theta_C - \theta_J) - K_d\right)\theta_C, \tag{3.12}$$

$$\frac{\mathrm{d}\theta_J}{\mathrm{d}t} = \left(K_p\left(p(t)\right)\left(1 - \theta_C - \theta_J\right) - K_{jd}\theta_J\right)\theta_C. \tag{3.13}$$

Let us consider the experimental conditions of constant applied pressure, so that $p(t) = p_A$ for all $t \geq 0$. In this case the substrate deposition rate, Equation (3.10), is constant through time. Writing $K_p = K_p(p_A) = \text{constant}$, we can locate the equilibrium points and classify their local stability via phase plane analysis.

Nullclines

To identify the equilibrium points, we first find the nullclines for the system given by Equations (3.12) and (3.13). The nullclines for $\frac{\mathrm{d}\theta_C}{\mathrm{d}t} = 0$ are given by

$$\theta_C = 0, \tag{3.14}$$

$$(1 - \theta_J - \theta_C)\theta_J = K_d, \tag{3.15}$$

where Equation (3.15) is a quadratic equation in θ_J, with real solutions[b] for $0 \leq \theta_C \leq 1 - 2\sqrt{K_d}$ given by

$$\theta_J = \frac{1 - \theta_C \pm \sqrt{(\theta_C - 1)^2 - 4K_d}}{2}. \tag{3.16}$$

The nullclines for $\frac{\mathrm{d}\theta_J}{\mathrm{d}t} = 0$ are given by

$$\theta_C = 0, \tag{3.17}$$

$$K_p(1 - \theta_J - \theta_C) = K_{jd}\theta_J, \tag{3.18}$$

and the possible equilibrium states are as follows.

1. The line $\theta_C = 0$ is a line of equilibrium points for all parameters, as Equations (3.14) and (3.17) are identical.

2. The equilibrium point, which occurs at the intersection of Equations (3.15) and (3.18), given by

$$(\theta_C, \theta_J) = \left(1 - \left(\gamma + \frac{1}{\gamma}\right)\sqrt{K_d}, \gamma\sqrt{K_d}\right), \tag{3.19}$$

with $\theta_W = \frac{\sqrt{K_d}}{\gamma}$, where

$$K_p = \gamma^2 K_{jd}, \qquad \text{for } \gamma > 0. \tag{3.20}$$

By the conditions $\theta_C, \theta_J \in [0, 1]$, the restrictions $\frac{1}{\gamma} \geq \sqrt{K_d} > 0$ and $\frac{\gamma}{(\gamma^2 + 1)} \geq \sqrt{K_d} > 0$ must hold. As $\frac{(1 + \gamma^2)}{\gamma} = \frac{1}{\gamma} + \gamma > \gamma$, the equilibrium point given by Equation (3.19)

[b] There also exists real solutions for $\theta_C \geq 1 + 2\sqrt{K_d}$. However, we also have the conditions $\theta_C \in [0, 1]$ and $K_d > 0$ and so this inequality cannot occur.

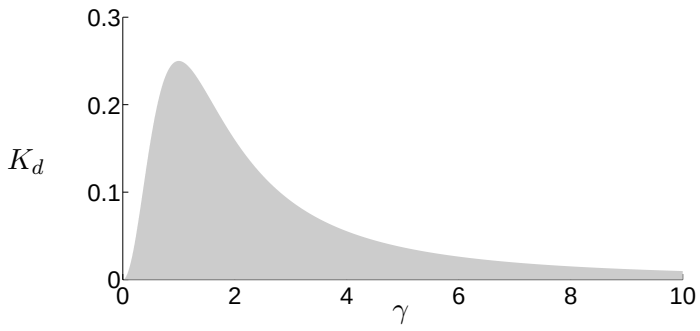

Figure 3.2: The shaded region indicates the parameter sets for which the non–zero equilibrium point, given by Equation (3.21), exists, where γ is defined in Equation (3.20).

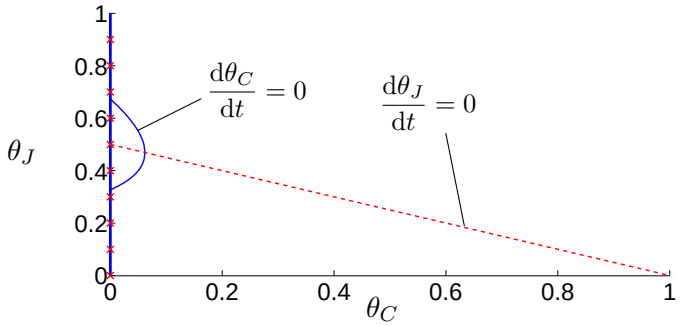

Figure 3.3: The nullclines for the system given by Equations (3.12) and (3.13) with constant applied pressure, and the parameters $K_d = 0.22$, $K_p = 0.6$ and $K_{jd} = 0.6$ for $\theta_C, \theta_J \in [0, 1]$. The blue solid lines indicate the $\dfrac{\mathrm{d}\theta_C}{\mathrm{d}t} = 0$ nullclines and the red dashed lines indicated the $\dfrac{\mathrm{d}\theta_J}{\mathrm{d}t} = 0$ nullclines. Crosses are used instead of a dashed line when both the nullclines are coincident, along the line $\theta_C = 0$.

exists when

$$\frac{\gamma}{\gamma^2 + 1} \geq \sqrt{K_d}, \tag{3.21}$$

with $K_d > 0$ already imposed. This region is shown for $\gamma \in (0, 10]$ in Figure 3.2.

The nullclines given by Equations (3.14) – (3.18) are sketched in Figure 3.3 for the non–zero parameters $K_d = 0.22$, $K_p = 0.6$ and $K_{jd} = 0.6$. Blue solid lines indicate the $\dfrac{\mathrm{d}\theta_C}{\mathrm{d}t} = 0$ nullclines, and red dashed lines indicate the $\dfrac{\mathrm{d}\theta_J}{\mathrm{d}t} = 0$ nullclines. Red crosses over a solid blue line are used when $\dfrac{\mathrm{d}\theta_C}{\mathrm{d}t} = \dfrac{\mathrm{d}\theta_J}{\mathrm{d}t} = 0$ so that the two nullclines are coincident. The equilibrium point given by Equation (3.19) exists at the intersection of the parabola given by Equation (3.15) and the straight line given by Equation (3.18) in Figure 3.3.

Stability analysis

Linearising around the equilibrium point (θ_C^*, θ_J^*), where an asterisk is used to denote the value of the dependent variable at equilibrium, the stability of the above equilibrium points is considered. We write

$$\theta_C = \theta_C^* + \epsilon\tilde{\theta}_C + \ldots, \qquad \theta_J = \theta_J^* + \epsilon\tilde{\theta}_J + \ldots, \tag{3.22}$$

where $0 < \epsilon \ll 1$ is sufficiently small that quadratic and higher order terms may be neglected. Substituting the expansions given by Equation (3.22) into Equations (3.12) and (3.13), after ignoring terms in ϵ of order two or higher and simplifying, gives

$$\frac{\mathrm{d}\tilde{\theta}_C}{\mathrm{d}t} = \tilde{\theta}_J(1-\theta_C^*-\theta_J^*)\theta_C^* + (\theta_J^*(1-\theta_C^*-\theta_J^*) - K_d)\,\tilde{\theta}_C - \theta_J^*\theta_C^*(\tilde{\theta}_J + \tilde{\theta}_C), \tag{3.23}$$

$$\frac{\mathrm{d}\tilde{\theta}_J}{\mathrm{d}t} = (K_p(1-\theta_C^*-\theta_J^*) - K_{jd}\theta_J^*)\,\tilde{\theta}_C - \Big(K_p(\tilde{\theta}_J + \tilde{\theta}_C) + K_{jd}\tilde{\theta}_J\Big)\,\theta_C^*. \tag{3.24}$$

We consider now the stability of the equilibrium points.

1. Along the line of equilibrium points given by $\theta_C^* = 0$, Equations (3.23) and (3.24) give

$$\frac{\mathrm{d}}{\mathrm{d}t}\begin{pmatrix}\tilde{\theta}_C\\ \tilde{\theta}_J\end{pmatrix} = \begin{pmatrix}\theta_J^*(1-\theta_J^*) - K_d\\ K_p(1-\theta_J^*) - K_{jd}\theta_J^*\end{pmatrix}\tilde{\theta}_C, \tag{3.25}$$

   and note that in this case the right hand side is independent of $\tilde{\theta}_J$. We seek solutions of the form

$$\begin{pmatrix}\tilde{\theta}_C\\ \tilde{\theta}_J\end{pmatrix} = \begin{pmatrix}v_1\\ v_2\end{pmatrix}e^{\lambda t}, \tag{3.26}$$

   for constant v_1, v_2. Substituting Equation (3.26) into Equation (3.25) yields

$$\begin{pmatrix}\theta_J^*(1-\theta_J^*) - K_d - \lambda & 0\\ K_p(1-\theta_J^*) - K_{jd}\theta_J^* & -\lambda\end{pmatrix}\begin{pmatrix}v_1\\ v_2\end{pmatrix} = \mathbf{0}, \tag{3.27}$$

   and non–trivial solutions occur when λ satisfies $\lambda\,(\lambda - (\theta_J^*(1-\theta_J^*) - K_d)) = 0$. The eigen-

values, λ, and corresponding eigenvectors, $\mathbf{v} = (v_1, v_2)^{\mathrm{T}}$, are given by

$$\begin{aligned} \lambda &= 0, & \mathbf{v} &\propto \begin{pmatrix} 0 \\ 1 \end{pmatrix}, \\ \lambda &= \theta_J^*(1-\theta_J^*) - K_d, & \mathbf{v} &\propto \begin{pmatrix} \theta_J^*(1-\theta_J^*) - K_d \\ K_p(1-\theta_J^*) - K_{jd}\theta_J^* \end{pmatrix}. \end{aligned} \tag{3.28}$$

Solving Equation (3.25), and substituting into Equation (3.22), after simplification, gives

$$\theta_C(t) = \tilde{\epsilon} e^{\left(\theta_J^*(1-\theta_J^*) - K_d\right)t} + \mathcal{O}(\tilde{\epsilon}^2), \tag{3.29}$$

$$\theta_J(t) = \theta_J^* + \tilde{\epsilon}\frac{K_p(1-\theta_J^*) - K_{jd}\theta_J^*}{\theta_J^*(1-\theta_J^*) - K_d} e^{\left(\theta_J^*(1-\theta_J^*) - K_d\right)t} + \mathcal{O}(\tilde{\epsilon}^2), \tag{3.30}$$

where $\tilde{\epsilon} = A_1\epsilon$ for some constant A_1. So if $\theta_J^*(1-\theta_J^*) - K_d < 0$, then $\lim_{t\to\infty} \theta_C = 0$, and trajectories are stable. However, if $\theta_J^*(1-\theta_J^*) - K_d > 0$, then trajectories are unstable as t gets large and positive, so that solutions move away from the equilibrium point and the linearised system is no longer valid.

In the small region around the line of equilibrium points given by $\theta_C^* = 0$, for which the expansion given by Equation (3.22) is valid, the trajectory is given by solving Equation (3.25) directly for $\tilde{\theta}_C$, $\tilde{\theta}_J$ by eliminating t. This yields

$$\theta_C = \frac{\theta_J^*(1-\theta_J^*) - K_d}{K_p(1-\theta_J^*) - K_{jd}\theta_J^*}(\theta_J - \theta_J^*). \tag{3.31}$$

2. At the equilibrium point given by Equation (3.19), after manipulation, Equations (3.23) and (3.24) give

$$\frac{\mathrm{d}}{\mathrm{d}t}\begin{pmatrix} \tilde{\theta}_C \\ \tilde{\theta}_J \end{pmatrix} = \left(1 - \left(\gamma + \frac{1}{\gamma}\right)\sqrt{K_d}\right)\begin{pmatrix} -\sqrt{K_d}\gamma & \frac{\sqrt{K_d}}{\gamma}(1-\gamma^2) \\ -K_{jd}\gamma^2 & -K_{jd}(\gamma^2+1) \end{pmatrix}\begin{pmatrix} \tilde{\theta}_C \\ \tilde{\theta}_J \end{pmatrix}. \tag{3.32}$$

For a given parameter set this can be solved analytically by seeking solutions of the form given by Equation (3.26). It can also be shown that the point given by Equation (3.19), when it exists (i.e. the inequality given by Equation (3.21) holds), is always locally stable for $\gamma, K_d > 0$.

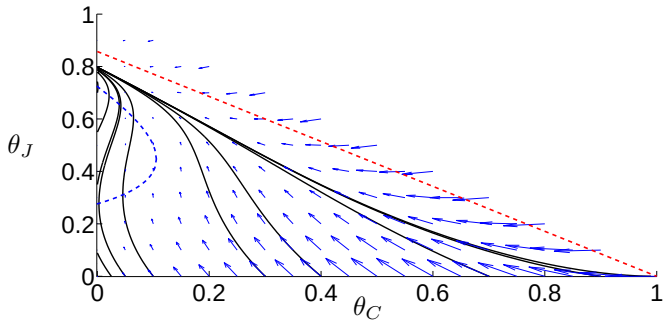

(a) $K_d = 0.2$, $K_p = 0.6$ and $K_{jd} = 0.1$.

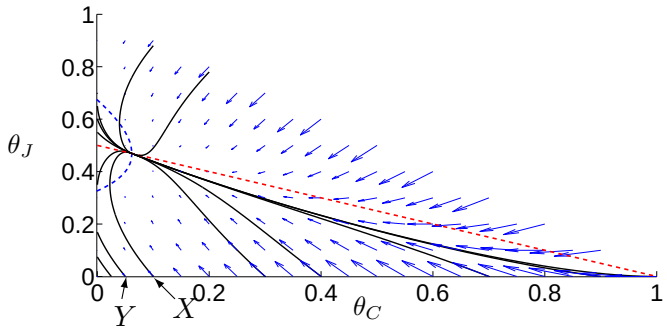

(b) $K_{jd} = 0.6$, $K_p = 0.6$ and $K_d = 0.22$, $(\theta_C, \theta_J) \in [0, 1] \times [0, 1]$

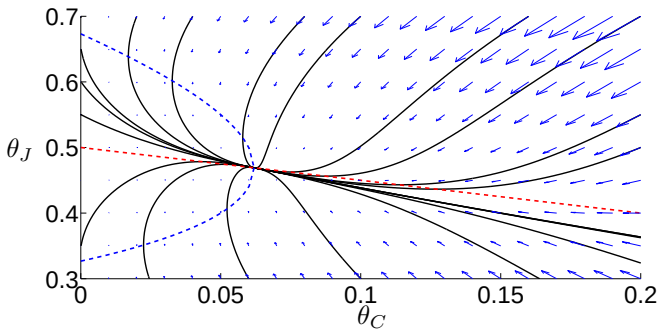

(c) $K_{jd} = 0.6$, $K_p = 0.6$ and $K_d = 0.22$, $(\theta_C, \theta_J) \in [0, 0.2] \times [0.3, 0.7]$

Figure 3.4: Phase plane portraits for the system given by Equations (3.12) and (3.13), for constant applied pressure, with $K_d = 0.2$, $K_p = 0.6$ and $K_{jd} = 0.1$ in (a), and $K_{jd} = 0.6$, $K_p = 0.6$ and $K_d = 0.22$ in (b) and (c). Figure (c) shows the region around the non–zero equilibrium point in (b) in more detail. The blue dashed lines indicates the $\dfrac{\mathrm{d}\theta_C}{\mathrm{d}t} = 0$ nullclines given by Equation (3.15) and the red dashed lines indicates the $\dfrac{\mathrm{d}\theta_J}{\mathrm{d}t} = 0$ nullclines given by Equation (3.18). The two nullclines in (b) and (c) intersect at the stable equilibrium point given by Equation (3.19). Black solid lines indicate trajectories and the small blue arrows show the direction of trajectories, with their size proportional to the rate of change of the solution. The initial conditions for the trajectories are chosen for illustrative purposes. As the trajectories approach the line $\theta_C^* = 0$, they can be described by Equation (3.31). The X and Y in (b) illustrate the initial conditions $(0.1, 10^{-4})$ and $(0.05, 10^{-4})$, for which trajectories go to the non–zero equilibrium point given by Equation (3.19) and the line of equilibrium points $\theta_C^* = 0$ respectively.

Phase plane portraits for constant pressure, illustrating the above two situations, are shown in Figure 3.4. Figure 3.4(a) shows a phase plane portrait with the parameters $K_d = 0.2$, $K_p = 0.6$ and $K_{jd} = 0.1$, where the inequality given by Equation (3.21) is not satisfied, and so $\theta_C^* = 0$ is a line of stable equilibrium points. Figures 3.4(b) and (c) show a phase plane portrait with the parameters $K_d = 0.22$, $K_p = 0.6$ and $K_{jd} = 0.6$, for which the inequality given by Equation (3.21) is satisfied and so the equilibrium point is given by Equation (3.19). It can be seen in Figure 3.4(b) that the global stability of the system for the case where the inequality given by Equation (3.21) is satisfied can depend on the initial values of the volume fractions for the cell and the substrate phases (and by the no voids conditions, Equation (3.1), the fluid phase). For example, with the parameters $K_d = 0.22$, $K_p = 0.6$ and $K_{jd} = 0.6$, trajectories with the initial conditions $(\theta_C(0), \theta_J(0)) = (0.1, 10^{-4})$ (indicated in Figure 3.4(b) by an X) approach the non–zero equilibrium point given by Equation (3.19). However, for the initial condition of $(\theta_C(0), \theta_J(0)) = (0.05, 10^{-4})$ (indicated in Figure 3.4(b) by a Y), solutions are attracted to the line of equilibrium points given by $\theta_C^* = 0$, so that all cells die in the long–term.

From the stability analysis carried out in this section, for a constant applied pressure regime and given the parameters K_d, K_p and K_{jd}, we can predict the equilibrium state the system attains at large times. If the parameters lie within the region given by Equation (3.21), trajectories either approach the point given by Equation (3.19), or the line $\theta_C^* = 0$, depending on the initial conditions. Otherwise, if the parameters do not lie within the region given by Equation (3.21), the line $\theta_C^* = 0$ is the only stable equilibrium point, and so all the cells will die in the long term.

When a loading regime is applied such that pressure moves through the threshold, the rate of substrate deposition changes from $K_p = K_1$ to $K_p = K_2$ or vice versa. As stability analysis gives us the equilibrium points in both of these cases, it is likely that specimens that experience cyclic loading will oscillate between the equilibrium values of the system for the two parameter sets ($K_p = K_1$ for one set, and $K_p = K_2$ for the other). We demonstrate, in Section 3.1.5, that this is indeed the case.

Table 3.2: Parameters obtained from literature and determined by the experimental setup. All parameters are dimensionless except for the temporal scaling parameter, k_b.

Parameters describing rates					
K_d	=	0.006	K_1	=	0.57
Loading parameters					
Υ	=	$24 \times 60 \times 60$	A	=	140
Temporal scaling					
k_b	=	$(60 \times 60 \times 24)^{-1}$ s^{-1}			

3.1.5 Time–dependant applied pressure

Relaxing the assumption that the applied pressure is constant, we calculate the numerical solution of the system of equations for the cases where the applied pressure depends on time as given by Equation (3.11).

Parameterisation of the model

As discussed in Chapter 2, we assume that the average volume fraction of mineralisation obtained from the *in vitro* experiments, Table 2.3, is equal to the increase in the volume fraction of the substrate phase ($\theta_J(t) - \theta_J(0)$ at time $t \geq 0$).

The values for the substrate degradation rate, K_{jd}, the pressure threshold, P_1, and the substrate deposition rate for pressures above the threshold, K_2, are not known and are not directly experimentally measurable as mentioned in Section 3.1.2. We estimate the value of these parameters by comparing the results of the mathematical model to experimental data. We first consider control loading conditions, so that applied pressure is always below the threshold, and the parameters K_2 and P_1 do not need to be known. Using the dimensionless versions of the parameters given in Table 3.1 and detailed in Table 3.2, minimisation of the sum of the squared errors between the numerical results and the experimental results for control specimens, at days 21 and 28, yields $K_{jd} = 0.12$, as is shown in Figure 3.5.

It should be noted that the constructs are seeded with human MSCs and, consequently, that no osteoclasts will be present as these cells originate from a different cell lineage. Osteoclasts

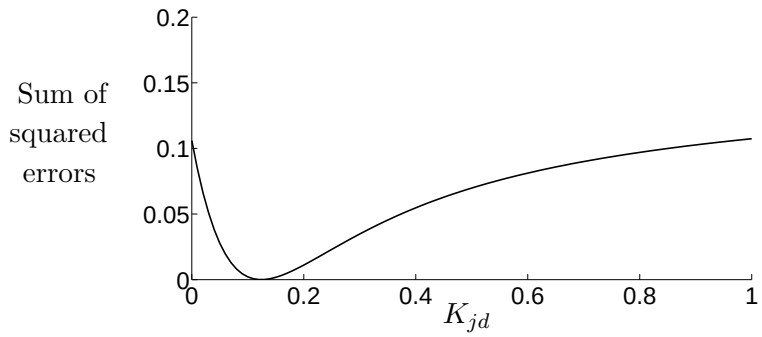

Figure 3.5: The sum of the squared errors between the numerical and experimental results for days 21 and 28 under control conditions, for a varying dimensionless substrate degradation rate, $K_{jd} \in [0, 1]$. Other parameters are given in Table 3.2. A value of $K_{jd} = 0.12$ minimises this error and so we choose this value for the dimensionless substrate degradation rate.

are the cells that degrade mineralised ECM (see Section 1.1.1). However, osteoblasts, which originate from the MSC line, are thought to be able to hydrolyse collagen [Parikka *et al.*, 2005] so that they can move through the matrix. Accordingly, a small but non–zero ratio of the substrate degradation to cell birth rate seems reasonable.

In order to estimate the values of $P_1 > 0$ and $K_2 > K_1$ a parameter sweep is performed over $(P_1, K_2) \in [10, 280] \times [0.6, 180]$, comparing numerical results of the mathematical model against experimental data for the gels under intermittent cyclic loading conditions. The surface of the sum of the squared errors between numerical and experimental results for days 21 and 28 is shown in Figure 3.6. Examining this figure we can infer that, for these particular experimental conditions, there is a relationship between P_1 and K_2 that minimises the sum of the squared errors. Denoting the average dimensionless substrate over each cycle of sinusoidal loading by κ, we have

$$K_2 = \frac{\kappa\Upsilon - K_1}{1 - \pi^{-1} \arccos\left(1 - \frac{P_1}{A}\right)} + K_1, \tag{3.33}$$

which, for $\kappa = 5.06 \times 10^{-4}$, describes the line along which the sum of the squared errors are minimised, and is indicated by a black dashed line in Figure 3.6. In the absence of experimental results under different amplitudes and frequencies of loading, we choose the parameters which minimise the global error, given by $P_1 = 210$ and $K_2 = 130$. The intermittent cyclic loading strategy used by our experimental collaborators with this choice of pressure threshold is plotted in Figure 3.7 and illustrates the proportion of time the pressure is above the threshold under this loading strategy.

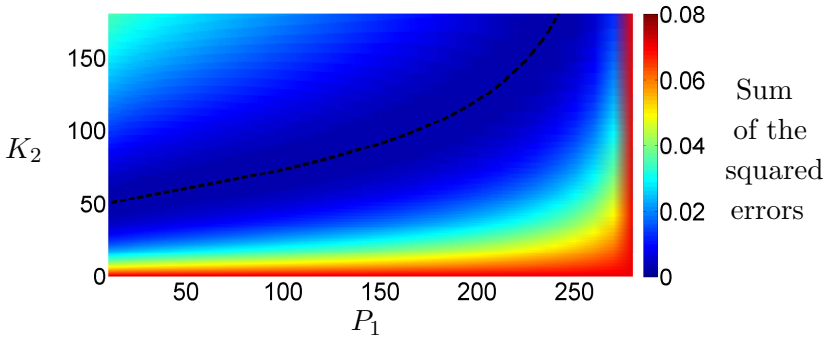

Figure 3.6: Sum of the squared errors between the numerical results and the experimental data for the gels subjected to intermittent cyclic hydrostatic pressure stimulation, for the parameters $(P_1, K_2) \in [10, 280] \times [0.6, 180]$. Other parameters are given in Table 3.2 with $K_{jd} = 0.12$. The dashed black line shows the line of best fit that minimises the sum of the squared errors, given by Equation (3.33) with κ equal to 5.06×10^{-4}.

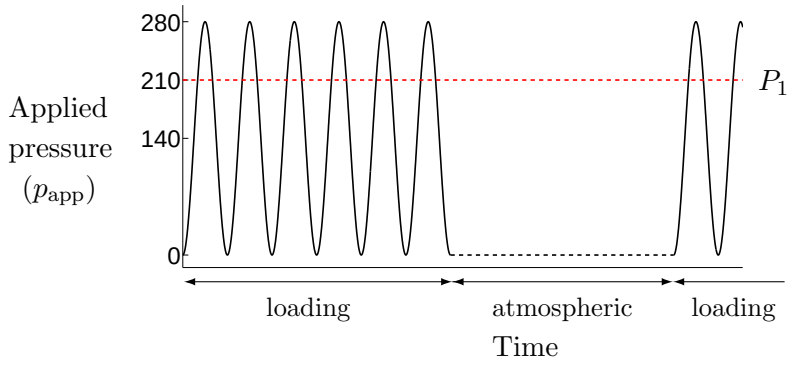

Figure 3.7: The intermittent cyclic loading regime with an amplitude of 140 kPa as currently practised. The pressure threshold at $P_1 = 210$ is indicated by the dashed red line, which equates to a dimensional threshold value of 210 kPa above atmospheric pressure. As in Figure 2.4, the horizontal axis represents time (not to scale) and the vertical axis represents the pressure applied by the bioreactor, p_{app}. The blue dashed line indicates a continuation of the loading regime.

Table 3.3: Parameters, obtained from literature and guided by the experimental setup as given in Table 3.2, and from comparing numerical results from the mathematical model to experimental data in Section 3.1.5. All parameters are dimensionless except for the temporal scaling parameter, k_b.

Parameters describing rates					
K_d	=	0.006	K_{jd}	=	0.12
K_1	=	0.57	K_2	=	130
P_1	=	210			
Loading parameters					
Υ	=	$24 \times 60 \times 60$	A	=	140
Temporal scaling					
k_b	=	$(60 \times 60 \times 24)^{-1}$ s^{-1}			

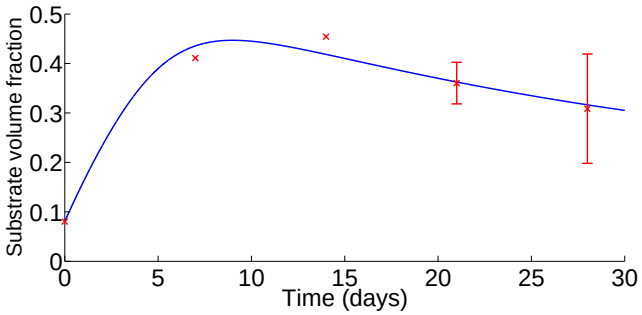

(a) Control loading regime

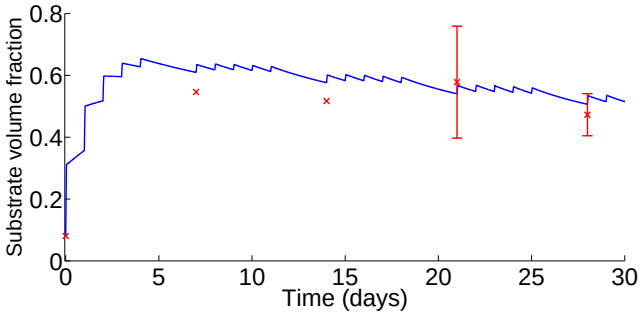

(b) Stimulated loading regime

Figure 3.8: Comparison of the results from numerical simulation to the experimental data for the (a) control and (b) stimulated loading regimes. Parameters are given in Table 3.3. The blue lines shows numerical results from the mathematical model and the red crosses show the experimental results with the bars indicating the standard error when available.

Using the parameters given in Table 3.3, Figure 3.8 compares the theoretical results from the mathematical model obtained by numerical simulation against the experimental data. It can be seen that the fit is good. The blue line, representing numerical results, is within the standard error of the experimental data for both days 21 and 28, as we would expect. In addition, the numerical results of the mathematical model reproduce similar results for the substrate volume fraction at days 7 and 14.

Numerical results

Using the parameters detailed in Table 3.3, we can use the mathematical model to simulate expected experimental results for any given initial conditions under any loading regime. To test that the model yields sensible results, we consider and compare the theoretical behaviour of the system under four different loading regimes for the initial conditions given by Equation (3.6). These are:

- *constant atmospheric pressure*, the control conditions,
- *intermittent cyclic loading*, the stimulated loading regime used experimentally, with cyclic loading for one hour a day at a frequency and amplitude of 1 Hz and 140 kPa respectively, and otherwise atmospheric pressure, as given by Equation (3.5),
- *constant elevated pressure* (high enough that applied pressure is above the threshold, but far below the magnitude needed to cause damage to cells),
- elevated pressure applied for one hour a day, and atmospheric pressure otherwise, which we call *intermittent elevated pressure*.

Although the regimes of applying intermittent elevated and constant elevated pressure are not currently practised experimentally, we include them here for comparison, and to make predictions of possible outcomes that could be tested experimentally. Figure 3.9 shows the numerical results for the two loading regimes where applied pressure is constant in time: constant atmospheric and constant elevated pressure. For these two loading regimes the stability analysis performed in Section 3.1.4 is valid. As the inequality given by Equation (3.21) holds for $K_p = K_1$ with the parameters given in Table 3.3, the solution approaches the equilibrium point given by

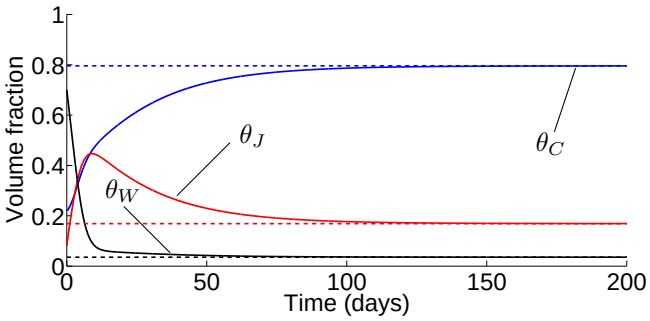

(a) Constant atmospheric pressure

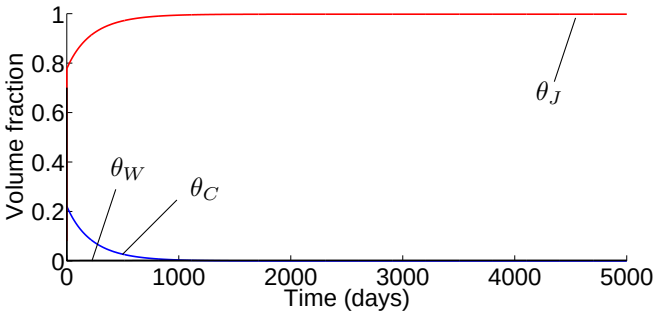

(b) Constant elevated pressure, long timescale

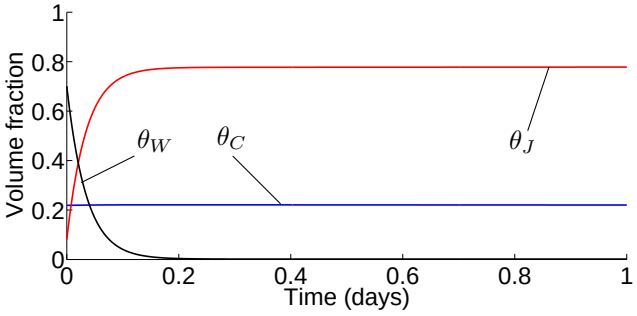

(c) Constant elevated pressure, short timescale

Figure 3.9: Numerical results for the loading regimes with constant applied pressure. Figure (a) shows results under control loading conditions and Figures (b) and (c) show results for loading conditions of constant elevated pressure at 300 kPa above atmospheric pressure. Parameters are given in Table 3.3 and initial conditions are given by Equation (3.6). The blue, red and black lines indicate the volume fractions of the cell phase, the substrate phase and the fluid phase receptively. The solid lines indicate the numerical solution, and the dashed lines in (a) indicate the position of the equilibrium point given by Equation (3.19) for $K_p = K_1$. The black line indicating the fluid phase volume fraction cannot be distinguished from the time axis in (b), and so (c) shows (b) on a much shorter timescale, so that the initial rapid change in the constituent phase volume fractions can be seen.

Equation (3.19) in the long term under constant atmospheric pressure. Numerical results agree with this, as may be seen in Figure 3.9(a). In this figure, the dashed lines show the position of the equilibrium point given by Equation (3.19), and the solid lines show the numerical solution. However, when $K_p = K_2$, the inequality given by Equation (3.21) does not hold for the parameters given in Table 3.3. Consequently, from the analysis in Section 3.1.4, we know that the solution approaches the equilibrium point given by $\theta_C^* = 0$. This is confirmed by numerical results for constant elevated pressure, as may be seen in Figure 3.10(b). We note that, for this parameter set and these initial conditions, the substrate and fluid volume fractions approach values of 1 and 0 respectively in the long term. Figure 3.9(c) shows the numerical results under the loading regime of constant elevated pressure on a short timescale (1 day). Examination of this figure shows that there is an initial rapid change of the constituent phase volume fractions under the constant elevated pressure loading regime, due to the high value of K_p. It then takes a significant length of time before equilibrium is reached, Figure 3.9(b). This is because the fluid phase volume fraction, θ_W, quickly becomes very small, and so by Equations (3.8) and (3.9) the rates of cell birth and substrate deposition are almost negligible. Consequently, change over time is driven by cell death and substrate degradation and these rates are small especially when θ_C gets small. Hence, it takes a long time for the system to reach equilibrium.

Figure 3.10 shows the numerical results for the loading regimes of intermittent cyclic loading and intermittent elevated pressure. At large times, the numerical solutions of under both these regimes settle to quasi–equilibria, where a repeating pattern around a long term average may be seen. The dashed lines in Figures 3.10(a) and (b) indicate the position of the point given by Equation (3.19) for $K_p = K_1$, and, therefore, the equilibrium under control conditions in the long term. We note that, in both cases, the long term averages stabilise to values between those indicated by the dashed lines and $(\theta_C^*, \theta_J^*, \theta_W^*) = (0, 1, 0)$ (the equilibrium point of the system under the constant elevated pressure loading regime as can be seen from examining Figure 3.9(b)). This is expected as discussed at the end of Section 3.1.4. The timings of the applications of loadings are clear in Figure 3.10 due to the sharp increase in substrate volume fraction. A schematic of the cyclic loading with the threshold indicated is reproduced in Figure 3.7.

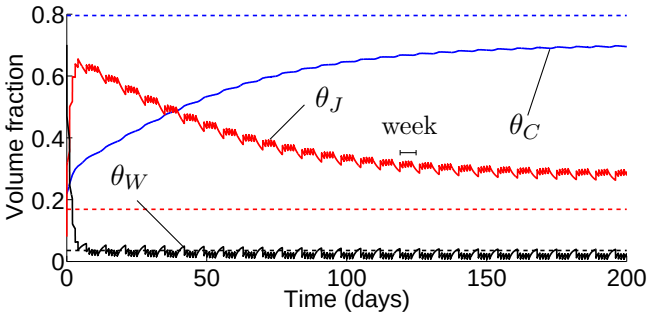

(a) Intermittent cyclic loading

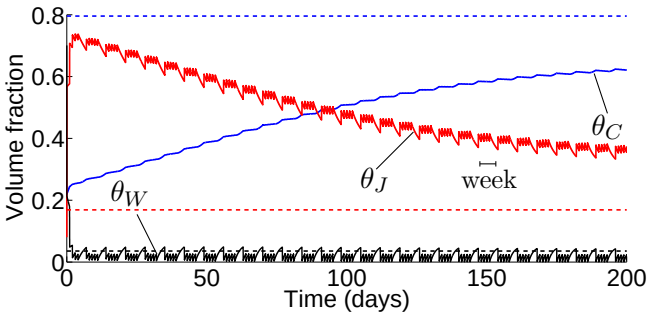

(b) Intermittent elevated pressure

Figure 3.10: Numerical results for the loading regimes where the applied pressure is dependent on time. Figure (a) shows the results under the intermittent cyclic loading regime, where the applied pressure is given by Equation (3.5), and Figure (b) shows the results under the intermittent elevated pressure loading regime, where the applied pressure is at 300 kPa above atmospheric while the construct is in the bioreactor (for one hour per weekday) and at atmospheric pressure the remainder of the time. Parameters are given in Table 3.3 with the initial conditions given by Equation (3.6). The blue, red and black lines indicate the volume fractions of the cell, substrate and fluid phases respectively. The solid lines indicate the numerical solution and the dashed lines indicate the positions of the equilibrium points given by Equation (3.19) for $K_p = K_1$. The length of a week is indicated.

The percentage increase in substrate volume fraction for the intermittent cyclic, constant elevated and intermittent elevated pressure loading regimes over control conditions is shown in Table 3.4. This compares the effectiveness of the different loading strategies. According to the results displayed in Table 3.4, the best loading strategy to increase substrate quantity, and, consequently, produce a more "bone–like" tissue engineered product over control conditions, is constant elevated pressure. The regime of intermittent elevated pressure is less effective, and intermittent cyclic loading is predicted to be the least effective loading regime of these three over the control loading conditions. This is also clear from inspecting Figure 3.11, which compares the theoretical substrate volume fraction during the experimental time period under the four loading strategies. These results contradict experimental evidence. As discussed in

Table 3.4: Theoretical percentage increase in the substrate volume fraction for samples subjected to the given loading regimes over control (constant atmospheric pressure) loading conditions. Parameters are given in Table 3.3 and initial conditions are given by Equation (3.6).

Loading regime	**Time** (days)	**Percentage increase in substrate volume fraction over control specimens (2 d.p.)**
Intermittent cyclic loading	7	39.96 %
	14	37.74 %
	21	49.06 %
	28	60.09 %
	Long term average	63.52 %
Intermittent elevated pressure	7	57.36 %
	14	59.09 %
	21	78.06 %
	28	97.61 %
	Long term average	93.87 %
Constant elevated pressure	7	80.51 %
	14	89.79 %
	21	121.13 %
	28	155.67 %
	Long term equilibrium	491.25 %

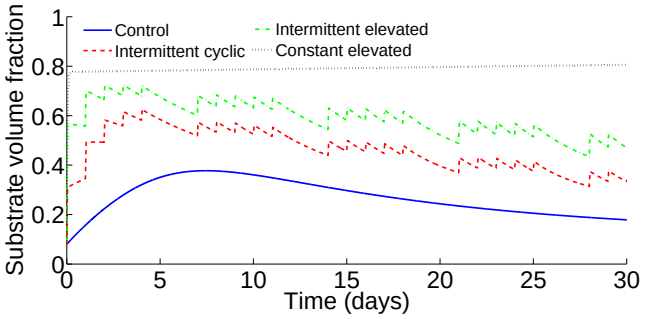

Figure 3.11: The theoretical substrate volume fraction under the four different loading regimes considered: control, intermittent cyclic, intermittent elevated and constant elevated, over the experimental timeframe. Parameters are given in Table 3.3 and initial conditions are given by Equation (3.6).

Chapter 2, previous experimental work suggests that both intermittent elevated and constant elevated pressure loading regimes yield similar results as the samples experiencing constant atmospheric pressure. In particular, the quantity of substrate deposition predicted by the model for samples under constant elevated pressure is biologically unrealistic.

It is known that dynamic simulation is needed to encourage the differentiation of cells towards a bone phenotype [Turner, 1998, Klein-Nulend *et al.*, 2005]. Following discussion with our experimental collaborators we now theorise that the bone–producing cells (either osteoblasts or their mechanosensors, osteocytes) have a memory for the loading they receive. This could be due to, for example, a saturation of ion channels and further experimental work is needed in order to investigate the subcellular response to hydrostatic pressure loading. Motivated by this, we include the additional effects of cell memory within the model and we test this hypothesis in the next section.

3.2 Including cell memory into the model

As in Section 3.1, we assume that there is a pressure threshold, p_1, above which the cellular pathway controlling substrate deposition is amplified, with the modification that the strength of this amplification decreases with the length of time for which the pressure has been above this threshold. This represents how the cells become accustomed to their loading conditions. In fact cell response to loading is much more complex and it is thought that it includes many relaxation times, with different decay rates, and the effect of diminishing returns and recovery periods. In the absence of more detailed biological information and parameters we represent the cell response by one simple decay rate which depends on the length of time for which the cell is in the stimulated state. Let t_1 be the last time that the applied pressure was equal to the threshold pressure (where the applied pressure had a positive gradient with respect to time):

$$t_1(t) = \max\left\{T : p(T) = p_1, \frac{\mathrm{d}p}{\mathrm{d}t}\Big|_{t=T} > 0\right\}, \tag{3.34}$$

as illustrated in Figure 3.12, with $t_1(0) = 0$. We assume that the cell memory is reset when the

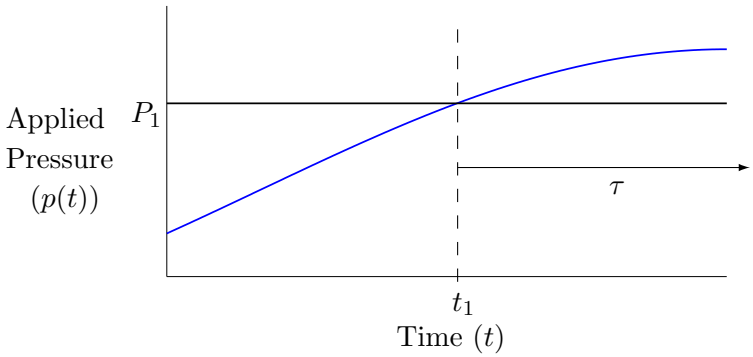

Figure 3.12: Sketch to illustrate where t_1, as defined in Equation (3.34), lies. The variable τ, given by Equation (3.35), is also indicated. The horizontal axis represents time, and the vertical axis represents pressure. The blue line illustrates how the applied pressure evolves with time, and the black horizontal line indicates the position of the pressure threshold.

pressure drops below the threshold and we define

$$\tau(t) = \begin{cases} t - t_1, & \text{if } p(t) \geq p_1, \\ 0 & \text{otherwise,} \end{cases} \tag{3.35}$$

where τ is the time elapsed since the last time the applied pressure passed through the pressure threshold with a increasing gradient, with $p(\tilde{t}) \geq p_1$ for all $\tilde{t} \in [t_1, t_1 + \tau]$. The above changes to the model may be introduced by modifying the substrate deposition, previously given by Equation (3.4), to

$$k_p\left(t, p(t)\right) = \begin{cases} k_1, & \text{if } p(t) < p_1, \\ k_1 + (k_3 - k_1)\exp\left(-\frac{\tau}{\alpha}\right), & \text{if } p(t) \geq p_1, \end{cases} \tag{3.36}$$

where $\alpha > 0$ is a measure of the length of time in seconds that it takes for cells to become desensitised to pressures above the threshold value and is assumed to be constant, and $k_3 > k_1 > 0$ is the initial rate of substrate deposition for $p \geq p_1$ at the instant $t = t_1$ so that $\tau = 0$. The functional form given by Equation (3.36) is plotted in Figure 3.13 for three different values of α, where the positions of t_1 and τ are indicated on Figure 3.13(a). It can be seen from Figure 3.13 that an increased value of α corresponds to a slower decay rate. Note that, if the applied pressure is above the threshold for the duration of the experiment, so that $p(t) > p_1 \ \forall t \geq 0$, τ will be equivalent to t, the length of time for which the experiment has been elapsing.

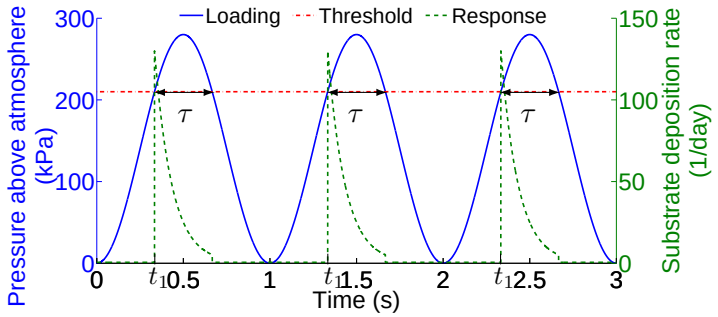

(a) $\alpha = 0.1$ seconds

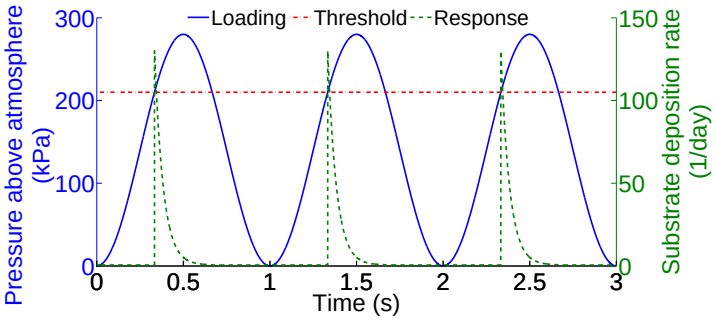

(b) $\alpha = 0.05$ seconds

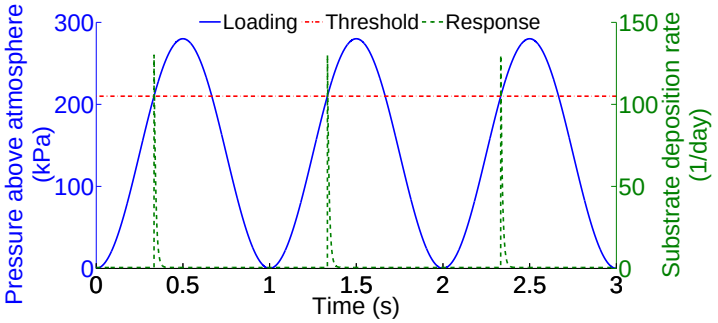

(c) $\alpha = 0.01$ seconds

Figure 3.13: Sketches to illustrate how the substrate deposition rate, $k_p(t, p(t))$, varies for cyclical loading for different values of α. The parameters describing the applied pressure are set as practised experimentally: $\omega = 1$ Hz, $a = 140$ kPa. Additionally, for illustration, we use similar paramters as in Section 3.1, and set $p_1 = p_{\text{atm}} + 210$ kPa, $k_1 = 0.57$ day^{-1} and $k_3 = 130$ day^{-1}. The left hand vertical axis (coloured blue) represents applied pressure above atmospheric pressure in kPa (loading). The right hand vertical axis (coloured green) is the substrate deposition rate, k_p, measured in day^{-1} (the response). The horizontal axis represents time, measured in seconds. The red horizontal dot–dashed line indicates the pressure threshold, p_1.

Nondimensionalisation is performed as in Section 3.1.3. Denoting dimensionless variables by a caret and writing $\hat{\tau} = \dfrac{\tau}{k_b}$, yields Equations (3.1), (3.8) and (3.9) with

$$K_p\left(\hat{t}, \hat{p}(\hat{t})\right) = \begin{cases} K_1, & \text{if } \hat{p}(\hat{t}) < P_1, \\ K_1 + (K_3 - K_1)\exp\left(-\frac{\hat{\tau}}{\hat{\alpha}}\right), & \text{if } \hat{p}(\hat{t}) \geq P_1, \end{cases} \tag{3.37}$$

where $K_1 = \dfrac{k_1}{k_b}$ and $P_1 = \dfrac{p_1 - p_{\text{atm}}}{p_0}$ as in Section 3.1.3, and both $K_3 = \dfrac{k_3}{k_b}$ and $\hat{\alpha} = \alpha k_b$ are dimensionless. As before pressure is given by Equation (3.11) and the initial conditions are given by Equation (3.6). We note that k_3 is not the same parameter as k_2 in Section 3.1, and, as a consequence, K_3 and K_2 are different. In addition, both k_3 and α, and so K_3 and $\hat{\alpha}$, are not directly experimentally measurable. Consequently, these parameters are estimated by fitting numerical results of the mathematical model to experimental data in Section 3.2.1. All other parameters are kept as in Table 3.3 unless otherwise stated. We now drop the caret notation and keep variables dimensionless unless otherwise stated.

We note that Equation (3.37) is identical to Equation (3.10) for $p(t) < P_1$. As a consequence, for pressures below the threshold, this modified model behaves in the same way as our original model in Section 3.1. However, the behaviour of the substrate deposition rate is altered as soon as $p(\tilde{t}) \geq P_1$ at some time $\tilde{t}$. As a consequence, the stability analysis from Section 3.1.4 holds for situations when applied pressure is constantly below the threshold, so that $K_p = K_1$ for all time. However, the stability analysis for constant applied pressures above the threshold no longer applies.

For $\alpha \ll \tau$, the term $(K_3 - K_1)\exp\left(-\dfrac{\tau}{\alpha}\right)$ approaches zero and, consequently, the rate of substrate deposition given by Equation (3.37) approaches K_1. Therefore, we predict that, for loading regimes where the applied pressure remains above the threshold for longer periods (*e.g.* the intermittent elevated and constant elevated loading regimes), trajectories of the system will approach the equilibrium points for constant applied pressure for $K_p = K_1$ as given in Section 3.1.4. For an applied pressure regime of cyclic loading, as long as the amplitude is sufficiently high such that the pressure exceeds the threshold at some time, the applied pressure will frequently equal the threshold pressure value. In this case cell memory, measured by τ, will be reset regularly. For this loading regime we expect that the volume fractions will approach

values between those given by stability analysis for $K_p = K_1$ and for $K_p = K_3$, with the exact values depending on the size of α and the frequency, amplitude and the duration of loading. Consequently, we expect the resultant behaviour of the system of equations under intermittent cyclic stimulation to be similar to the quasi–equilibrium behaviour as seen in Figure 3.10(a) and discussed in Section 3.1.5. This is indeed found to be the case.

3.2.1 Numerical scheme

Euler methods are used to discretise time and the numerical solutions are found by proceeding through time, where a variable timestep size is used. This means that the largest timestep is used when the construct is at constant atmospheric pressure, a smaller timestep is used during the loading period when pressure is below the threshold in order to capture the fast oscillations of the applied pressure, and the smallest timestep is used when the applied pressure is above the threshold and the exponential in Equation (3.37) is important, in order to capture the effect of the decay in K_p. Denoting the timestep size at the j^{th} timestep by $(\Delta t)_j$, we use

$$(\Delta t)_j = \begin{cases} (\Delta t)_h, & \text{if } p(t_j) \geq P_1, \\ (\Delta t)_m, & \text{if } p(t_j) < P_1 \text{ and the construct is in the bioreactor,} \\ (\Delta t)_l, & \text{otherwise,} \end{cases} \tag{3.38}$$

where $(\Delta t)_h \leq (\Delta t)_m \leq (\Delta t)_l$. It is known *a priori* where the periods of loading are and, consequently, where smaller timestep sizes are needed. Further details relating to numerical implementation are given in Appendix A.

Parameterisation

As this modified model behaves in the same manner as the original model in Section 3.1 for pressures below the threshold, $p(t) < P_1$, we use the same associated parameters (k_b, K_1, K_d and K_{jd}) as given in Table 3.3. In addition, we assume that the pressure threshold, P_1, is the same as before, so that $P_1 = 210$.

In order to estimate values for α and K_3 we perform a parameter sweep over the region $\alpha > 0$

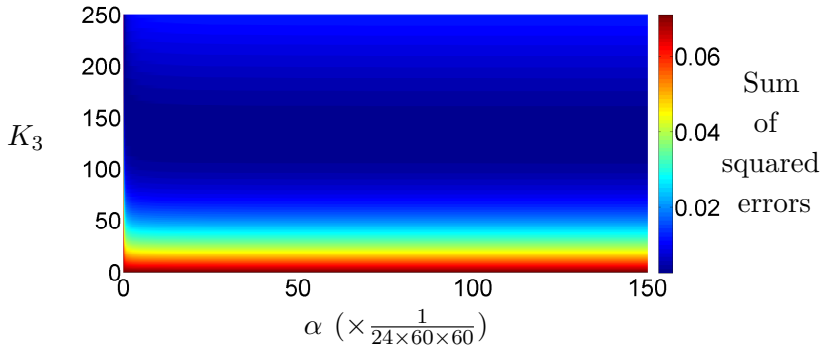

(a) Intermittent cyclic loading

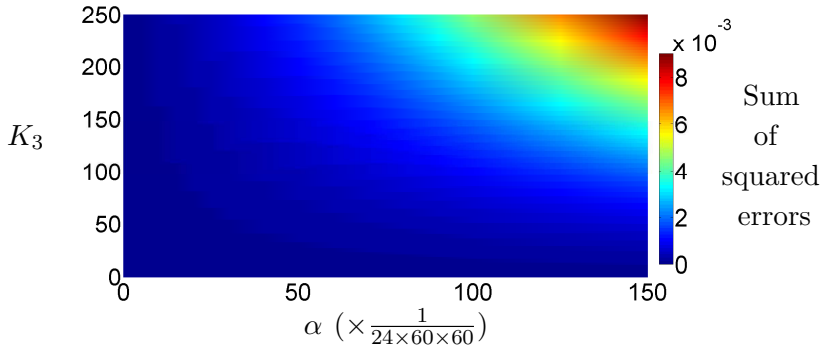

(b) Intermittent elevated pressure

Figure 3.14: The sum of the squared errors between the numerical results and experimental data on days 21 and 28 for $(\alpha, K_3) \in \left[\frac{10^{-1}}{24\times60\times60}, \frac{150}{24\times60\times60}\right] \times [0.6, 250]$. Other parameters are given in Table 3.3. Figure (a) shows the sum of the squared errors between the theoretical and experimental results for the intermittent cyclic loading regime. Figure (b) shows the sum of the squared errors between the theoretical results for the intermittent elevated pressure loading regime and the experimental results from the control specimens. Note that the α axis has been rescaled by a factor of $(24 \times 60 \times 60)^{-1}$ for ease of viewing.

and $K_3 > K_1$ for the values $(\alpha, K_3) \in \left[\frac{10^{-1}}{24\times60\times60}, \frac{150}{24\times60\times60}\right] \times [0.6, 250]$. The sum of the squared errors between numerical results from the mathematical model and the experimental data on days 21 and 28 is shown in Figure 3.14(a). We note that previous experiments indicated that intermittent elevated loading gave the same results as controls [Henstock *et al.*, 2013]. To ensure that the mathematical model behaves suitably when the construct is exposed to pressures above the threshold for longer periods, such as the intermittent elevated and constant elevated pressure loading regimes, we compare the numerical results from the mathematical model for intermittent elevated pressure against the experimental results for control specimens. The sum of the squared errors on days 21 and 28 is shown in Figure 3.14(b). If we were just to minimise the sum of the squared errors for the surface in Figure 3.14(a) then a high value for

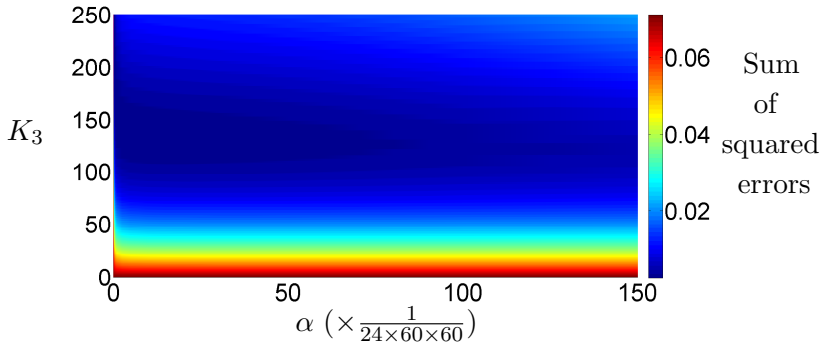

Figure 3.15: The sum of the two surfaces in Figure 3.14, being the sum of the squared errors between the numerical results and experimental data on days 21 and 28 comparing the numerical results against experimental data for intermittent cyclic loading, and the numerical results for intermittent elevated pressure loading regime against control experimental data for $(\alpha, K_3) \in \left[\frac{10^{-1}}{24\times60\times60}, \frac{150}{24\times60\times60}\right] \times [0.6, 250]$. Other parameters are given in Table 3.3. Note that the α axis has been rescaled by a factor of $(24\times60\times60)^{-1}$ for ease of viewing.

α would be chosen, corresponding to a slow decay rate. The model would then overestimate the substrate volume fraction for longer periods of loading where the pressure is above the threshold, as was the case in our original model in Section 3.1. By using the sum of surfaces in Figures 3.14(a) and (b) we aim to find the pair α, K_3 such that the model behaves suitably in situations where applied pressure is above the threshold for both short and long durations. The sum of the two surfaces is shown in Figure 3.15, and the error is minimised for the parameters $\alpha = \frac{0.25}{(24\times60\times60)}$ and $K_3 = 231.3$. This predicts that the length of the cell memory is very short and on the order of deciseconds (1 decisecond is equivalent to 10^{-1} seconds). However, the ratio of τ to α is of order 1 for the current stimulated loading strategy, as expected. From now on we use these values for K_3 and α, so that the parameters are given by Table 3.5.

Figure 3.16 compares the numerical results from the theoretical mathematical model, using the parameters in Table 3.5, with experimental data. It may be seen in Figure 3.16 that the fit of the mathematical model to the experimental data is very good, and in particular at days 7 and 14 (the data from these two data points were not used in the parameterisation due to there being only one measurement).

Table 3.5: Parameters for the model with loading history. All parameters are dimensionless, except for the temporal scaling parameter, k_b.

Parameters describing rates	**Physical meaning**	**Origin**
$K_d = 0.006$	Cell death rate	Literature [Jilka *et al.*, 1998]
$K_{jd} = 0.12$	Substrate degradation rate	Parameter fit, Section 3.1.5
$K_1 = 0.57$	Substrate deposition rate at atmospheric pressure	Literature [Flanagan and Nichols, 1969]
$K_3 = 231.3$	Substrate deposition rate at the instance the applied pressure moves above the threshold	Parameter fit, Section 3.2.1
$P_1 = 210$	Pressure threshold	Parameter fit, Section 3.1.5
$\alpha = \frac{0.25}{24 \times 60 \times 60}$	Cell memory of loading decay rate	Parameter fit, Section 3.2.1

Loading parameters	**Physical meaning**	**Origin**
$\Upsilon = 24 \times 60 \times 60$	Frequency of cyclic loading	Current experimental input
$A = 140$	Amplitude of cyclic loading	Current experimental input

Parameters relating to numerical method		
$(\Delta t)_l = 10^{-5}$	$(\Delta t)_m = 10^{-6}$	$(\Delta t)_h = 10^{-8}$

Temporal scaling
$k_b = (60 \times 60 \times 24)^{-1}\ \mathrm{s}^{-1}$

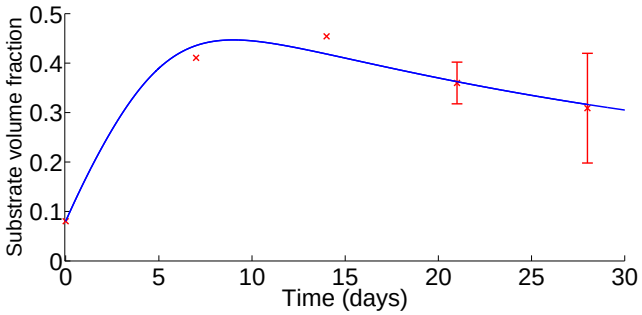

(a) Control loading conditions

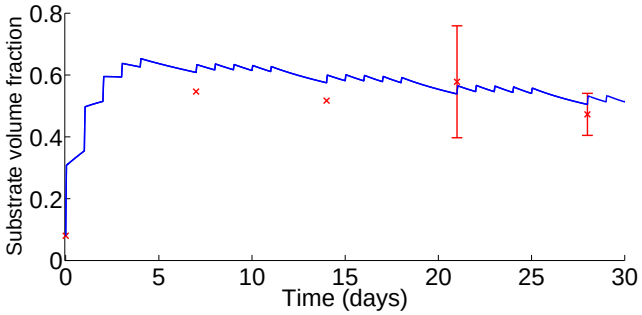

(b) Stimulated loading conditions

Figure 3.16: Comparison of results from numerical simulations to experimental data under the (a) control and (b) and stimulated loading regimes. Parameters are given in Table 3.5 and the initial conditions are given by Equation (3.6). The horizontal axis represents dimensional time, in days, and the vertical axis represents the substrate volume fraction. The blue lines show the numerical results from the mathematical model, and the red crosses show the experimental data, with the bars indicating the standard error when available.

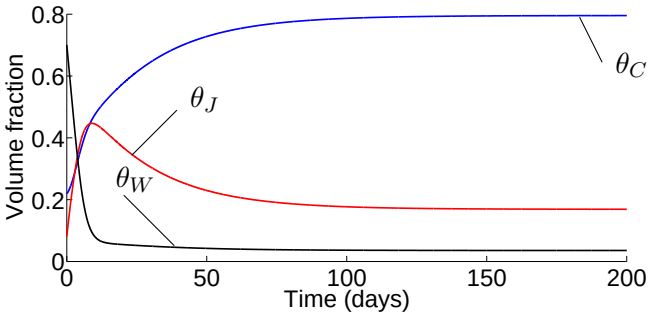

(a) Control

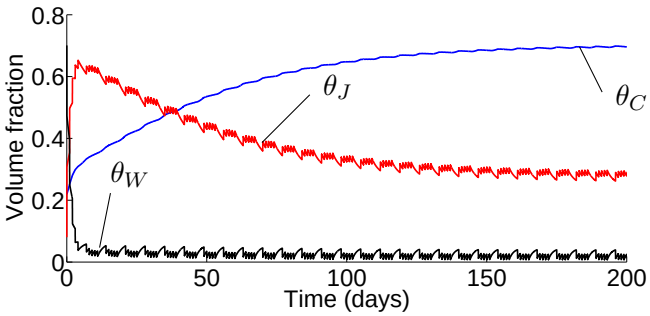

(b) Stimulated

Figure 3.17: Numerical results for the mathematical model with loading history included, so that the substrate deposition rate is given by Equation (3.37), under control (constant atmospheric) and stimulated (intermittent cyclic) loading conditions in (a) and (b) respectively. Parameters are given in Table 3.5 and the initial conditions are given by Equation (3.6). The blue, red and black lines indicate the volume fractions of the cell, the substrate and the fluid phases respectively.

Numerical results

In a similar manner to Section 3.1.5 we use the parameters found in the previous section, and given in Table 3.5, to simulate expected results using the theoretical mathematical model with the substrate deposition rate given by Equation (3.37). We consider the four different loading strategies, as detailed in Section 3.1.5, for the initial conditions given by Equation (3.6).

Figure 3.17 shows the numerical results for initial conditions given by Equation (3.6) under the constant atmospheric and intermittent cyclic loading regimes. The results for the intermittent elevated and constant elevated loading regimes are not displayed as these are visually indistinguishable from the results with constant atmospheric pressure shown in Figure 3.17(a).

Table 3.6 gives the predicted percentage increase in the substrate volume fraction of the various loading regimes over control conditions. It can be seen that, in contrast to Table 3.4, results agree with experiments. The loading regimes of constant elevated and intermittent elevated

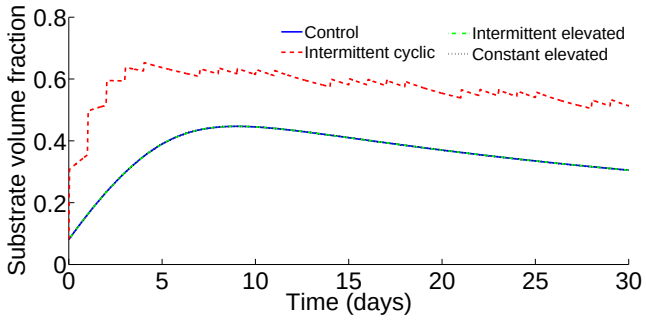

Figure 3.18: A comparison of the theoretical substrate volume fraction under the four different loading regimes considered for the model with history where the substrate deposition rate is given by Equation (3.36). Parameters are given in Table 3.5 and initial conditions are given by Equation (3.6). The lines representing the control, intermittent elevated and constant elevated loading regimes are indistinguishable.

pressure show very little increase in substrate volume fraction over control specimens in the current experimental timeframe of 28 days. This may also be seen by inspecting Figure 3.18, which compares the theoretical substrate volume fraction during the experimental timeframe for the four different loading strategies. In comparison to the equivalent results for the model without memory, in Figure 3.11, it can be seen that the intermittent elevated and constant elevated loading conditions give very similar results to the samples under control conditions. The same is seen experimentally. These results indicate that the substrate deposition rate given by Equation (3.36) gives more accurate results than our original model, which used Equation (3.4) as the substrate deposition rate.

We note that the cell volume fraction, θ_C, in Figure 3.17 equilibrates to a relatively high number, higher than one might expect experimentally. However, without experimental data on cell numbers it is not possible to suggest a better value. Procedures to give an idea of cell numbers could be performed in future work. This would help us to validate the model and is discussed further in Section 3.4.

3.3 Optimising experimental conditions

Now that the mathematical model is parameterised and has been demonstrate to represent substrate deposition behaviour under strategies where the pressure remains above the threshold for long periods, it may be used to give predictions and to optimise the experimentally

Table 3.6: Theoretical percentage increase in the substrate volume fraction for samples subjected to the given loading regimes over control (constant atmospheric pressure) loading conditions for the model with history where the substrate deposition rate is given by Equation (3.36). Parameters are given in Table 3.5 and initial conditions are given by Equation (3.6).

Loading regime	**Time** (days)	**Percentage increase in substrate volume fraction over control specimens (2 d.p.)**
Intermittent cyclic loading	7	39.68 %
	14	37.41 %
	21	48.64 %
	28	59.54 %
	Long term average	65.27 %
Intermittent elevated pressure	7	0.04 %
	14	0.02 %
	21	0.03 %
	28	0.05 %
	Long term equilibrium	0.05 %
Constant elevated pressure	7	0.00 %
	14	-0.00 %
	21	-0.00 %
	28	-0.00 %
	Long term equilibrium	0.00 %

variable parameters. The aim is to find the particular experimental conditions, such as initial quantities and loading strategy, that produce the most "bone–like" construct. As discussed previously this is related to the quantity of mineralised ECM. Thus, we seek the input parameters that give the maximal increase in substrate volume fraction at the experimental end point for the stimulated constructs in comparison to those experiencing control conditions (*i.e.* $\max\left(\theta_J^{\text{stimulated}}(t) - \theta_J^{\text{control}}(t)\right)$ at $t = 28$ days). In order to enable easy comparison of the experimental values we convert back into dimensional variables for this section unless otherwise stated.

We can consider varying both the initial quantities and the loading conditions used. With respect to the loading conditions, some experimentally variable inputs that could be altered are detailed in Figure 3.19 and include:

- the type of waveform for the stimulated conditions, currently cyclic loading;
  - the amplitude of the cyclic loading, a, currently 140 kPa;
  - the frequency of the cyclic loading, ω, currently 1 Hz;

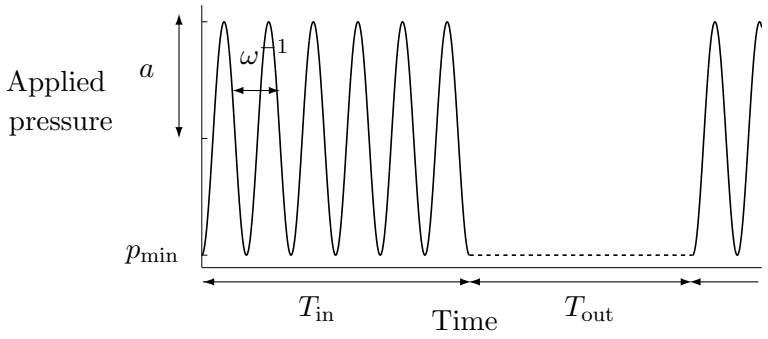

Figure 3.19: Intermittent cyclic loading strategy illustrating some of the experimentally changeable parameters.

- the length of the applications of loading in the bioreactor, T_{in} in Figure 3.19, currently one hour;
- the length of the resting periods at constant atmospheric pressure, T_{out} in Figure 3.19, currently 23 hours each weekday and the whole of the weekend;
- the lowest applied pressure in the bioreactor, $p_{\min}$ in Figure 3.19, currently atmospheric pressure; and
- the total length of the experiment, currently 28 days.

The current experimental process is manually intensive and so we do not consider varying the timings of the applications each day and keep these at the same fixed time each weekday. Optimising for the duration of the loading periods, T_{in} in Figure 3.19, with all other parameters fixed, would suggest that the construct is constantly in the bioreactor under cyclic loading. However, this is not biologically realistic and is discussed further in Section 3.4. Consequently, we keep the timings and the length of duration of the loading sessions as practised experimentally. If the experimental process were to be automated in future, the effect of the timing of the loading applications could be considered. As the model is dependent on the two times for which applied pressure equals the threshold, and the length of time between these two, we do not investigate the effects of different waveforms. A different waveform with an applied pressure intersecting the pressure threshold at the same time points would yield the same results. In addition we keep the total length of the experiment fixed at 28 days, and keep $p_{\min} = p_{\text{atm}}$ for convenience.

In the following sections we consider the effect of altering the initial volume fractions of cells

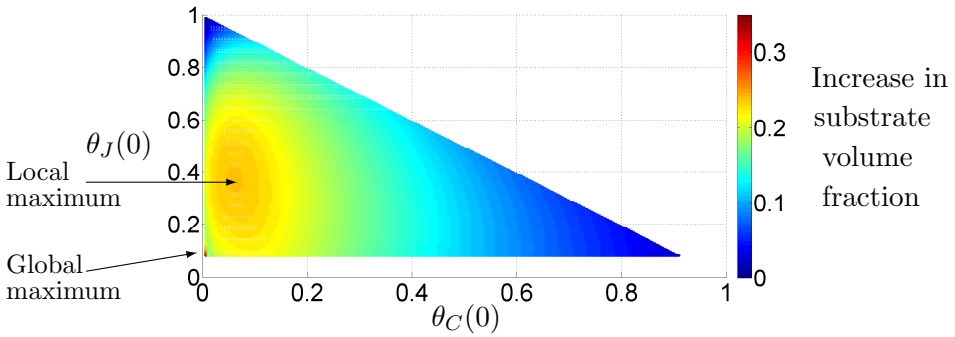

Figure 3.20: The theoretical increase in the substrate volume fraction at day 28 of the samples under stimulated over control loading conditions, for different initial conditions for the cell and substrate volume fractions such that $(\theta_C(0), \theta_J(0)) \in [0.005, 1] \times [0.08, 1]$, with $\theta_C(0) + \theta_J(0) \leq 1$ by definition. All other parameters are given in Table 3.5.

and collagen (note that, given these, the initial fluid volume fraction is implicit by the no voids condition, Equation (3.1)), the amplitude and the frequency of the cyclic loading individually in Sections 3.3.1, 3.3.2 and 3.3.3 respectively. We assume that, for the reasons discussed above, all other conditions are the same as currently practised experimentally.

3.3.1 Initial seeding strategy

We first consider the optimal initial conditions for cells and collagen, while keeping other conditions as practised experimentally. Seeding with no cells is not of experimental interest and would result in a static system. From Section 3.1.4 we know that $\theta_C = 0$ is a stable equilibrium point, and so that if $\theta_C(0) = 0$, $\dfrac{\mathrm{d}\theta_C}{\mathrm{d}t} = \dfrac{\mathrm{d}\theta_J}{\mathrm{d}t} = 0$ for all time. In addition we want to ensure that the initial substrate volume fraction is structurally feasible and is not so low that the gel collapses. Following discussion with our experimental collaborators the gels used in the experiments described in Chapter 2 were on the lower end of the range for a cohesive gel and our collaborators at the ISTM would not suggest using any lower concentration of collagen in order to form the constructs. Given this we us suppose that $\theta_J(0) = 0.080$ (3 d.p.), the initial condition for the substrate volume fraction given by Equation (3.6), is the lowest initial substrate volume fraction possible for a cohesive gel. Restricting $\theta_J(0) \geq 0.080$ and $\theta_C(0) > 0$, we consider the optimal initial conditions according to the mathematical model. Figure 3.20 shows the increase in the substrate volume fraction for samples under stimulated over control loading conditions at day 28 for the possible initial conditions $\theta_C(0)$ and $\theta_J(0)$. From this we suggest

using the initial conditions given by $(\theta_C(0), \theta_J(0)) = (0.095, 0.350)$ (3 d.p.) which relates to a local maximum in Figure 3.20. Although there exists a higher global maximum in Figure 3.20 at the point $(\theta_C(0), \theta_J(0)) = (0.003, 0.080)$ (3 d.p.), this set of initial conditions corresponds to a very small ridge in the surface of Figure 3.20 and, consequently, would be hard to achieve experimentally with any accuracy. We also note that this initial cell volume fraction equates to approximately 274 cells and that in this case the continuum modelling assumption may not be accurate.

3.3.2 Amplitude

We now consider the optimal amplitude of cyclic loading, while keeping other conditions as experimentally practised and using the initial conditions given by Equation (3.6).

Figure 3.21 shows the increase in the substrate volume fraction at day 28 for samples experiencing intermittent cyclic loading, as given by Equation (3.11), for varying amplitude over controls. When $a < \frac{p_1}{2}$, the pressure experienced by the developing construct under the stimulated loading regime never reaches the threshold pressure value. In this cases $k_p = k_1$ for all time by Equation (3.36) and so the intermittent cyclic loading regime has the same effect on the constructs as constant atmospheric pressure. This is shown as a zero increase in Figure 3.21 for $a < 105$ kPa. As the amplitude increases for $a > \frac{p_1}{2}$, more time of each oscillation has

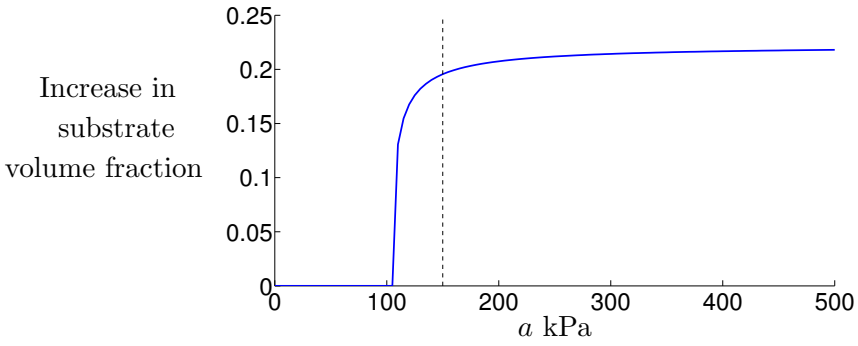

Figure 3.21: The increase in the substrate volume fraction at day 28 of samples under stimulated over control loading conditions for different amplitudes, a, of cyclic loading, as given in Equation (3.5). All other parameters are kept as in Table 3.5, with the initial conditions given by Equation (3.6). The dashed line at $a = 150$ kPa indicates the maximum amplitude that can be applied in the current experimental setup.

a pressure greater than the threshold, as illustrated in Figure 3.22. The length of time that

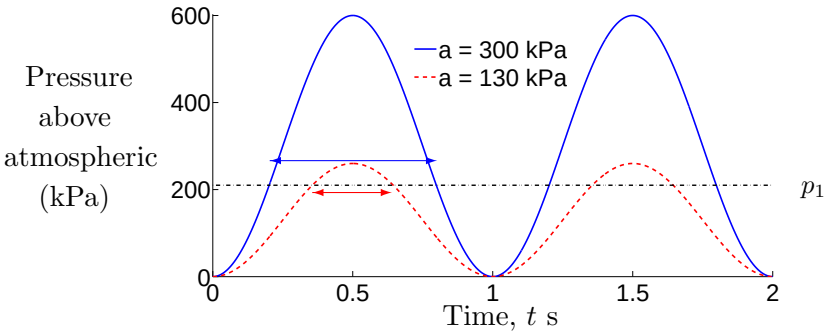

Figure 3.22: Graph demonstrating that the larger the amplitude of the cyclic loading, the longer the time the applied pressure is above the threshold value, as indicated by the length of the arrows. The blue solid and dashed red lines show cyclic loading given by Equation (3.5) with $\omega = 1$ Hz for $a = 300$ kPa and $a = 130$ kPa respectively. The black dash–dotted line shows the position of the pressure threshold, $p_1 = p_{\text{atm}} + 210$ kPa.

the cells are depositing substrate at a higher rate, consequently, increases. However, due to the exponential factor in Equation (3.37), this increased effect is limited as the length of time above the pressure threshold increases. It can be seen from Figure 3.21 that increasing the amplitude above a value of about $a = 200$ kPa does not result in a significant increase in the substrate volume fraction of the construct, and that using an amplitude of 500 kPa in comparison to 300 kPa results in only a 0.0038 increase in the substrate volume fraction of the construct at day 28 under stimulated loading conditions. Producing this increased amplitude will have associated costs and there are limits to what the bioreactor machinery can manage. The maximum pressure that the bioreactor can currently apply is 300 kPa above atmospheric pressure. As a result, keeping all other parameters as in Table 3.5 with the initial conditions given by Equation (3.6), we suggest using an amplitude of 150 kPa during the periods of cyclic loading.

3.3.3 Frequency

We now investigate the optimal frequency of the cyclic loading while keeping other conditions as practised experimentally and using the initial conditions given by Equation (3.6). Figure 3.23 shows the increase in the substrate volume fraction for samples experiencing intermittent cyclic loading over controls, for a varying frequency, ω, of cyclic loading at day 28.

When $\omega = 0$, Equation (3.5) yields that $p(t) = p_{\text{atm}}$ for all time. Consequently, there is no

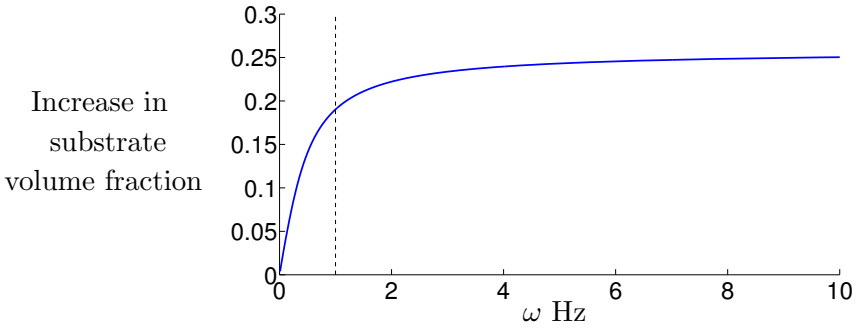

Figure 3.23: The increase in substrate volume fraction at day 28 of samples under intermittent cyclic loading over constant atmospheric pressure, for different frequencies, ω, of cyclic loading. All other parameters are given in Table 3.5 with initial conditions given by Equation (3.6). The dashed line at $\omega = 1$ Hz indicates the maximum frequency which can be applied in the current experimental setup.

difference between the stimulated and control loading conditions. For small non–zero frequencies of cyclic loading, increasing the frequency results in a substantial increase in the substrate volume fraction of the samples under stimulated in comparison to control loading conditions. However, as the frequency increases, the rate of the increase in the substrate volume fraction of samples under stimulated loading conditions decreases. When the frequency is very small, the number of oscillations in a given time window is less than for a higher frequency and, consequently, the number of times the cell memory is reset is lower. This is illustrated in Figure 3.24. As frequency increases there are more oscillations within a given length of time, the cell memory is reset more often, and so the average value of k_p is higher. However, the maximum frequency the current bioreactor setup can apply is 1 Hz and so we suggest keeping the frequency at 1 Hz as currently practised experimentally, while keeping all other parameters as in Table 3.5 for the initial conditions given by Equation (3.6). As for the amplitude, our current model suggests that increasing the frequency will give ever increasing gains, even if very marginal. This is because, currently, we have not included time or delay for the cells to respond to the pressure they experience.

3.4 Conclusion and discussion

We have presented a mathematical model with temporal dependence to describe the growth of a tissue engineered bone construct consisting of a collagen scaffold seeded with human MSCs

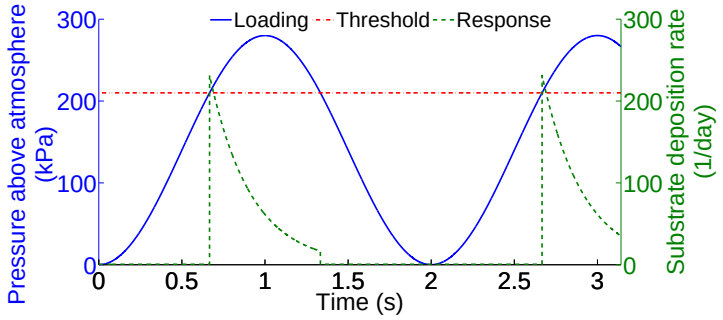

(a) $\omega = 0.5\ Hz$

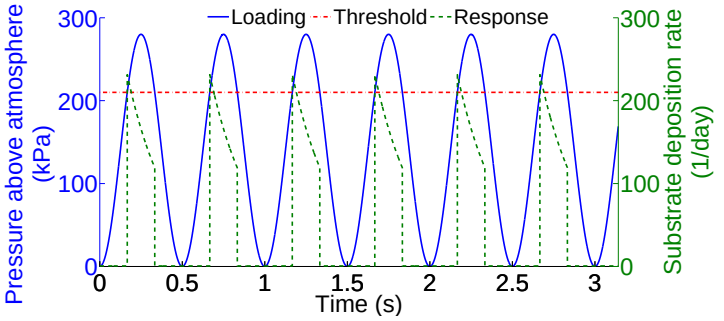

(b) $\omega = 2\ Hz$

Figure 3.24: Figures demonstrating that increasing the frequency of loading for fixed $\alpha = 0.25$ s results in a higher average value of k_p over a fixed time window. Here, the blue solid line represents the cyclic applied pressure exerted by the bioreactor (loading), the red dash–dotted line shows the pressure threshold value, and the green dashed line shows the substrate deposition rate (response).

and submerged in culture medium under hydrostatic pressure stimulation. The evolution of a phase representing bone–producing cells, a solid "substrate" phase representing the collagen scaffold and mineralised ECM, and a fluid phase are considered through time. The effects of cell proliferation, cell death, substrate deposition and substrate degradation are included, where the substrate deposition rate is modelled as a function dependent on the pressure exerted by the bioreactor.

We initially hypothesise that the substrate deposition rate can be represented by a switch function, as given by Equation (3.4), where bone–producing cells deposit substrate at a lower rate for pressures below a certain threshold, and at a higher rate for pressures above this threshold. The equilibrium points are found and stability analysis is performed for constant applied pressure. It is shown that two possible equilibrium states exist: a state where all the cells die out in the long term, and a state for which cells, substrate and fluid are all present in the long term, which only exists for certain parameter sets where Equation (3.21) is fulfilled.

The model is parameterised using experimental data from our collaborators at the ISTM. The model fits experimental data well for samples under control and stimulated loading conditions, as shown in Figure 3.8. In contrast, when the constructs are exposed to elevated pressures for a length of time, the model overestimates the quantity of substrate, as can be seen in Table 3.4. Accordingly the model is modified, in Section 3.2, to include an exponential decay term in the substrate deposition rate in order to account for the cell memory of the history of loading. Parameterising the mathematical model using experimental data yields the rate of exponential decay to be equivalent to 0.25 seconds. As may be seen in Table 3.6, the modified form of the substrate deposition rate adequately predicts the quantity of substrate formation when the constructs are exposed to longer durations of elevated pressure. The fit to experimental data may be seen in Figure 3.16. Thus, in Chapters 4 – 7 we use the model with cell memory.

The parameterised model is used to optimise the experimentally variable conditions in Section 3.3. We suggest using $(\theta_C(0), \theta_J(0)) = (0.095, 0.350)$ (3 d.p.) as the initial conditions for our mathematical model. It can be seen from Figure 3.20 that this point corresponds to a local maximum for the increase in substrate volume fraction on day 28 of samples under stimulated over controls loading conditions. If the initial conditions are within the locality of this suggested point the predicted increase in substrate volume fraction for samples under stimulated over control loading conditions remains high. As discussed in Section 3.3, a global maximum does exist at the initial conditions of $(\theta_C(0), \theta_J(0)) = (0.003, 0.080)$ (3 d.p.). However, we do not advise using this as the number of cells cannot be measured exactly, errors do occur during pipetting of volumes and there is inherent stochasticity in biology which means the model may not necessarily be applicable for these initial cell numbers. Therefore, this exact point is unlikely to be obtained and there is a sharp drop in the increase in substrate volume fraction either side of this point.

Due to the limitations of the bioreactor equipment currently in use we suggest keeping the frequency of the cyclic loading at 1 Hz and increasing the amplitude to 150 kPa for the initial conditions current used. Optimising on the length of time in the bioreactor would suggest that the construct is kept in the bioreactor under a cyclic loading regime for the whole experimental timeframe. This would maximise the function $K_p(t, p(t))$ and, thus, the substrate deposition. However, this is not biologically realistic. Cartmell and El Haj [2005] comment that "extended

periods of loading are known to have a diminishing effect upon load induction, as the bone formation response becomes saturated". This effect could be included in later work; for example, we could consider a maximum quantity of stimulation to which the cells can respond and above which additional stimulation has no further effect before a certain relaxation or rest time. If the bioreactor equipment were to be altered we could reconsider employing a higher amplitude or higher frequency of loading during the cyclic loading sessions.

Note that, in this mathematical model, there is no upper limit to the amplitude that can be applied and that the model predicts that ever increasing amplitudes will result in ever increasing, although very small, gains in the substrate volume fraction under stimulated loading conditions. However, as discussed in Section 1.1.4, high hydrostatic pressure has a detrimental effect on mammalian cells. We have not included pressure–induced cell death in our model as high pressures are not exerted in the current loading strategy. Including these would show that, above certain amplitudes, cells die and accordingly we expect this would prevent substrate deposition.

It may be noted that the equilibrium value attained by the cell volume fraction is higher than might be expected. Lacking experimental data on cell numbers we are unable to comment on what the exact number is supposed to be. There are several explanations for why the model may predict a higher volume fraction of cells than in the *in vitro* experiments. Firstly, from Section 3.1.5, we have assumed that the pressure threshold value is 210 kPa above atmospheric pressure in Section 3.2 for the model with memory effects. This value may be inaccurate and, when further experimental data are obtained, performing a parameter sweep for the model in Section 3.2 over the parameters P_1, K_3 and α may reveal a different result for the threshold. Secondly, the values for the rates of cell death and substrate deposition at atmospheric pressure, K_d and K_1, have been taken from literature as discussed in Section 3.1.2. It may be that these chosen values are not appropriate for this setup. Equally the rate of cell birth, k_b, chosen could be inaccurate. Further experimental data, in particular averages for days 7 and 14 and data on cell numbers, from our collaborators will enable us to perform further parameter sweeps. In addition, there are limitations of the model presented in this chapter due to the assumptions made in building the model. These are mentioned in Chapter 2 and further discussed below.

A current assumption inherent in our model is that cells instantaneously sense any change

in pressure and instantaneously react to this change. This is not realistic. It actually takes several days for cells to differentiate and synthesise new tissue [Boccaccio *et al.*, 2011], and the research carried out in Nagatomi *et al.* [2001, 2003] showed that several days of consecutive cyclic hydrostatic loading was needed before any significant effect was seen. Furthermore, as the collagen is seeded with human MSCs, which are multipotent, there will be a number of different cell types with different degrees of differentiation. This model considers one cell type. Future work could include multiple cell populations with the delays needed for cells to differentiate and to respond to their loading environment included, and this is discussed in Chapter 8.

3.5 Including spatial effects

In order to understand how bone cells respond to cyclic hydrostatic pressure loading we have built and investigated a non–spatial model to quantitatively describe the experimental system. The nature of this model is that it describes the temporal evolution of spatially averaged quantities and, in the case of a constant substrate deposition rate, is amenable to phase plane analysis. Furthermore, we have used the model to optimise experimentally variable inputs in Section 3.3.

As well as gaining an understanding of how the averaged quantities of interest (the cell, substrate and fluid phase volume fractions) vary over time, we wish to investigate the spatial distribution of the constitutive phases and in particular the factors inducing the heterogeneous spatial distribution in the mineralisation that occurs experimentally (see Figure 2.9). Such an understanding could enable future work to investigate methods for improving the experimental protocol.

Spatial effects are included in Chapters 4 – 7. The model in Chapter 4 investigates the effects of biochemically–induced spatial patterning and tests the hypothesis that nutrient distributions in the construct are responsible for the spatially heterogeneous mineralisation seen. The model considered in Chapters 5 – 7 allows us to examine both the fluid shear stress magnitude (FSSM) and the pressure distribution within the construct. This allows us to investigate the effects of biomechanically–induced spatial patterning and test the hypothesis that the rim of mineralisation that develops experimentally is caused by increased fluid shear stresses.

The *in vitro* experiments performed by our collaborators, described in Chapter 2, encompass

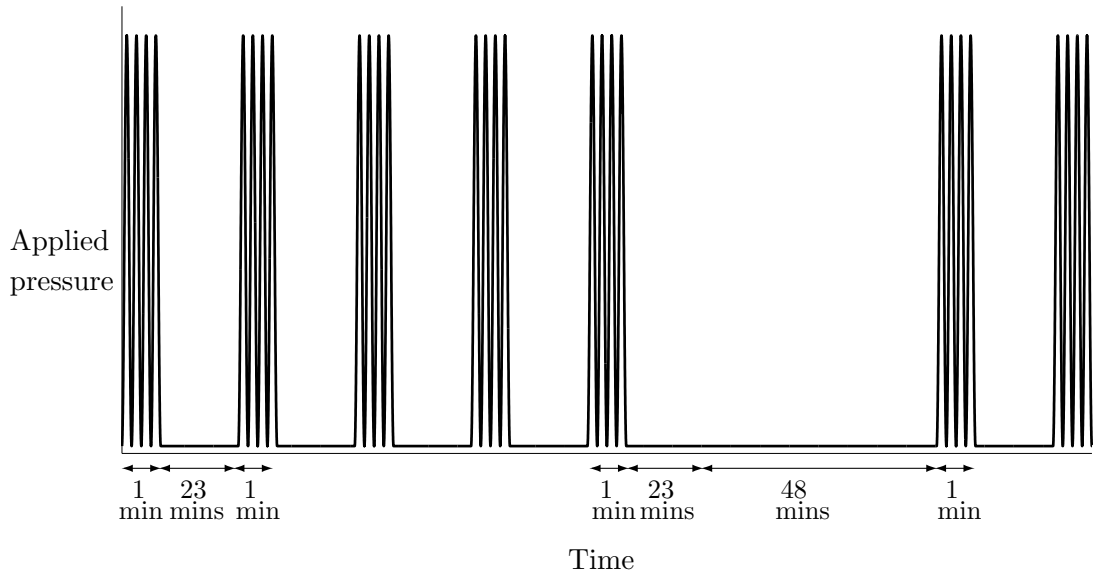

Figure 3.25: A schematic of a portion of the *stimulated* loading strategy considered in Chapters 4 – 7, where a qualitative representation of the experimental methods is made. Samples subjected to stimulated loading conditions experience one minute of cyclic loading followed by 23 minutes of atmospheric pressure. After five repetitions, samples experience a 48 minute rest period. The horizontal axis illustrates time (not to scale) and the vertical axis illustrates applied pressure. Minute(s) is abbreviated to *min(s)*.

a wide variety of timescales, from cell memory on the timescale of deciseconds, cyclic loading with a period on the timescale of seconds, to the total experiment on the timescale of a month. In order to capture the oscillations of the cyclic loading and the exponential decay in the substrate deposition rate for pressures above the threshold, a very small timestep needs to be used in the numerical method. Due to the increased number of degrees of freedom for the spatial models, simulation on the full experimental timescale of 28 days is computationally very demanding. In the remainder of this thesis we seek a qualitative description of the experimental setup. In order to achieve this we now consider a shorter experiment on the timescale of hours, where the constructs subjected to *stimulated* loading conditions experience 1 minute of cyclic loading followed by 23 minutes of rest at atmospheric pressure. This is repeated a total of five times, followed by two 24–minute periods of no loading, as illustrated in Figure 3.25. The extended rest period is added to represent the break in the loading applications in the bioreactor over the weekend in the original experiments. As before, constructs subjected to *control* loading conditions experience constant atmospheric pressure. In addition to rescaling time, we make further modifications to the following models to aid numerical simulation. In

Chapter 4 we set the sizes of the cellular diffusion coefficient and the oxygen uptake artificially high to accelerate the effects of cellular diffusion and a heterogeneous spatial distribution of the nutrient on the constitutive volume fractions. In Chapters 5 – 7 we used an averaged form of the substrate deposition rate, set the size of fluid phase macroscale viscosity artificially high and used spatially smoothed initial conditions to allow numerical simulations to be performed on a reasonable timescale.

Chapter 4

Diffusion driven cell model

In this chapter we extend the model which included memory effects, developed in Chapter 3, to include spatial effects through including diffusion of the cell phase. As the substrate phase is assumed to be solid, there is no diffusion of this phase. With this assumption we are left with solving a reaction–diffusion partial differential equation for the cell phase coupled to an ordinary differential equation for the substrate phase and an algebraic equation for the fluid phase. We consider this system on the domain defined by a cross–section of the hemispherical construct, which is assumed to stay constant in size and shape throughout the experimental timeframe. We first assume that nutrients are freely available in the fluid phase, in Section 4.1, and so are not rate–limiting. It is shown that this is not sufficient to reproduce the spatial effects seen experimentally, where a rim of mineralisation at the edge of the construct develops. In Section 4.2, we introduce the dependence of cell birth and substrate deposition on a representative nutrient in solution, chosen to be oxygen, to investigate the spatial patterning induced by biochemical effects. This is sufficient qualitatively to reproduce the spatial effects in the substrate phase seen experimentally.

In Chapter 3, a non–spatial model was developed in order to examine the change of averaged quantities over time. We now wish to gain an understanding of the spatio–temporal distribution of the constituent phase volume fractions in the construct. We start off by investigating whether

diffusion–driven cell movement alone can qualitatively predict the spatially heterogeneous mineralisation seen in the experiments performed by our collaborators.

4.1 Freely available nutrients

As discussed in Appendix A, we consider the two–dimensional (2D) cross–section of the experimental setup. We consider the construct–only region, assumed to be semicircular in shape, and impose the condition that the construct remains constant in size and shape throughout the simulation. The domain is denoted by

$$\Omega_C = \left\{(x,z) \in \mathbb{R}^2 : x^2 + (z - s_h)^2 \leq r_c^2, z \geq s_h\right\}, \tag{4.1}$$

with boundary

$$\partial\Omega_C = \left\{(x,z) \in \mathbb{R}^2 : x^2 + (z - s_h)^2 = r_c^2, z > s_h\right\} \cup \left\{(x,z) \in \mathbb{R}^2 : z = s_h, -r_c < x < r_c\right\}, \tag{4.2}$$

and the region Ω_C is illustrated in Figure 4.1. As in Chapter 2 $r_c > 0$ is the radius of the construct and $s_h \geq 0$ is the vertical distance between the base of the construct and the base of the well. The region outside Ω_C contains culture medium only.

Notation is chosen to be consistent with the previous chapters, so that $\theta_k(\mathbf{x}, t) \in [0, 1]$, for all $\mathbf{x} = (x, z) \in \Omega_C$, $t \geq 0$, for $k = C, J, W$ represents the volume fraction of cells, substrate and fluid respectively. The no voids condition is

$$\theta_C(\mathbf{x}, t) + \theta_J(\mathbf{x}, t) + \theta_W(\mathbf{x}, t) = 1, \quad \mathbf{x} \in \Omega_C. \tag{4.3}$$

We introduce spatial effects in the form of cellular diffusion [Murray, 2002], which models the random movement of cells, to the three phase model in Chapter 3. The transfer of mass terms, as described in Chapter 3, are retained and we assume that all the phases have the same constant density. This gives the following conservation of mass equations for the cell and substrate

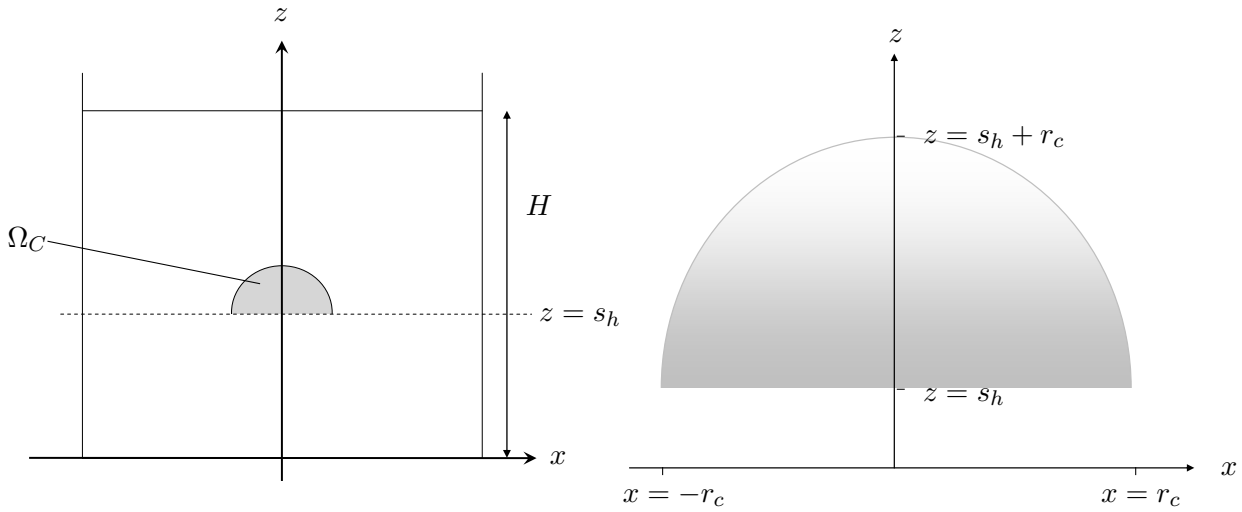

(a) Position of Ω_C within the well

(b) Construct–only domain Ω_C

Figure 4.1: The position and the shape of the construct–only domain, Ω_C. Figure (a) shows the position of Ω_C within the full well domain. Figure (b) illustrates the domain Ω_C, used for numerical simulation, for the Cartesian coordinates x, z.

phases:

$$\frac{\partial \theta_C}{\partial t} = \left(k_b \theta_J \theta_W - k_d\right) \theta_C + D_C \nabla^2 \theta_C, \qquad \mathbf{x} \in \Omega_C, \tag{4.4}$$

$$\frac{\partial \theta_J}{\partial t} = \left(k_p\left(\mathbf{x}, t, p(\mathbf{x}, t)\right) \theta_W - k_{jd} \theta_J\right) \theta_C, \qquad \mathbf{x} \in \Omega_C, \tag{4.5}$$

where $D_C > 0$ is the diffusion coefficient of the cell phase, which we assume to be constant in the absence of further experimental information, and $p(\mathbf{x}, t)$ is the pressure. As in Chapter 3, $k_b > 0$, $k_d > 0$, $k_p > 0$ and $k_{jd} \geq 0$ are the cell birth, cell death, substrate deposition and substrate degradation rates respectively and we assume that k_b, k_d and k_{jd} are constants. We note that there is no diffusion term within Equation (4.5) as we assume that the substrate phase is solid and stationary. Once θ_C and θ_J are determined the fluid volume fraction, θ_W, can be calculated from the cell and substrate volume fractions by Equation (4.3).

In Chapter 3 we demonstrated that the deposition rate needs to include the effects of the cell memory of the loading history in order to reproduce experimental data. Consequently, we extend the model with cell memory for the substrate deposition rate, introduced in Section 3.2,

so that the substrate deposition rate is given by

$$k_p\left(\mathbf{x},t,p(\mathbf{x},t)\right)=\begin{cases}k_1, & \text{if } p(\mathbf{x},t)<p_1,\\ k_1+(k_3-k_1)\exp\left(-\frac{\tau(\mathbf{x},t)}{\alpha}\right), & \text{if } p(\mathbf{x},t)\geq p_1,\end{cases}\qquad \mathbf{x}\in\Omega_C. \tag{4.6}$$

Here $k_3 > k_1 > 0$ are the rates of substrate deposition as described in Section 3.2, $p_1 > p_{\text{atm}}$ is the pressure threshold and $\alpha > 0$ is a measure of the length of time in seconds that it takes for cells to become desensitised to pressures above the threshold value. We assume that k_1, k_3, α and p_1 are constants. As in Section 3.2, τ is the length of time for which the pressure has been above the threshold, given by

$$\tau(\mathbf{x},t)=\begin{cases}t-t_1(\mathbf{x},t), & \text{if } p(\mathbf{x},t)\geq p_1,\\ 0, & \text{otherwise}\end{cases}\qquad \mathbf{x}\in\Omega_C. \tag{4.7}$$

Here $t_1(\mathbf{x},t)$ is the last time at which the pressure was equal to the threshold with an increasing gradient with respect to time at $\mathbf{x}\in\Omega_C$:

$$t_1(\mathbf{x},t)=\max\left\{T : p(\mathbf{x},T)=p_1, \frac{\partial p(\mathbf{x},t)}{\partial t}\Big|_{t=T}>0, \mathbf{x}\in\Omega_C\right\}, \tag{4.8}$$

with $t_1(\mathbf{x},0)=0$. Sketches of the substrate deposition rate and the variables τ and t_1 for the spatially independent case are given in Section 3.2. We note that t_1, and, consequently, τ, are now dependent on the spatial variable $\mathbf{x}\in\Omega_C$ in addition to the temporal variable $t\geq 0$.

It remains to determine the pressure, $p(\mathbf{x},t)$. The effects of gravity enter the system when the construct is subjected to the stimulated loading regime by the fact that the cells at the base of the construct experience pressures above the threshold for marginally longer than the cells at the top of the construct. However, the construct is small (a radius on the scale of mm) and the ratio of gravity effects to loading amplitude is also small (at a value of 1.18×10^{-3} (3 s.f.) when taking the density of water and the magnitude of gravitational acceleration to be 991.27 kg m^{-3} and 9.8 mm/s^2 respectively). Combined with the exponential decay term in the substrate deposition rate, given by Equation (4.19), the effects of gravity are negligible and so

we ignore them. Hence, pressure is given by

$$p(\mathbf{x},t) = p(t) = \begin{cases} p_{\text{atm}} + a\left(1 - \cos\left(2\pi\omega t\right)\right), & \text{if the construct is in the bioreactor,} \\ p_{\text{atm}}, & \text{otherwise,} \end{cases} \quad \mathbf{x} \in \Omega_C, \tag{4.9}$$

and is spatially constant. Here p_{atm} is atmospheric pressure and a and ω are the amplitude and frequency of the cyclic loading respectively. In order to close the model, we now prescribe appropriate boundary and initial conditions.

4.1.1 Boundary and initial conditions

A suitable boundary condition on the cell phase is to impose the no flux of cells across $\partial\Omega_C$, the boundary of the construct, so that

$$\nabla\theta_C \cdot \mathbf{n} = 0, \quad \mathbf{x} \in \partial\Omega_C, \tag{4.10}$$

where $\mathbf{n}$ is the outward pointing normal to the boundary $\partial\Omega_C$.

In order to represent the experimental data we require the initial conditions, $\theta_C(\mathbf{x},0)$ and $\theta_J(\mathbf{x},0)$, to satisfy

$$\int_{\Omega_C} \theta_C(\mathbf{x},0)\,\mathrm{d}V = C_0, \qquad \int_{\Omega_C} \theta_J(\mathbf{x},0)\,\mathrm{d}V = J_0, \tag{4.11}$$

along with $0 \leq \theta_C(\mathbf{x},0) + \theta_J(\mathbf{x},0) \leq 1$, where C_0 and J_0 are, respectively, the volume of cells and collagen in the construct at the initial time as given in Section 2.2.3. By Equation (4.3) we have $\theta_W(\mathbf{x},0) = 1 - \theta_C(\mathbf{x},0) - \theta_J(\mathbf{x},0)$. As discussed in Section 2.2.3, image analysis indicates that the cell and collagen distributions are initially homogeneous within the construct. For the data given in Section 2.2.3, this yields the initial conditions

$$\theta_C(\mathbf{x},0) = \frac{0.3}{1.37}, \quad \text{and} \quad \theta_J(\mathbf{x},0) = \frac{0.11}{1.37}, \quad \mathbf{x} \in \partial\Omega_C. \tag{4.12}$$

As the effects of gravity are negligible, using homogeneous initial conditions would result in spatially homogeneous solutions through time. Consequently, the model would then reduce to the ODE model presented in Chapter 3. To illustrate the potential behaviour of the model we investigate heterogeneous initial conditions. We choose the initial volume fractions of the cell

and substrate phases to be given by

$$\theta_k(\mathbf{x},0) = a_k \tanh\left(b_k\left((x^2+(z-s_h)^2-r_c^2)(z-s_h)\right)\right)+c_k, \quad \text{for } k=C,J, \quad \mathbf{x}\in\partial\Omega_C, \tag{4.13}$$

where $\theta_k(\mathbf{x},0)\in[0,1]$ for $k=C,J$. This gives initial cell and substrate phase conditions that have a higher volume fraction on the periphery of the construct than in the centre. Here the parameter b_k controls the gradient of the initial spatial distribution, and c_k controls the value of the minimum volume fraction for phase k. The multiplication factor, a_k, is chosen such that Equation (4.11) is satisfied for $k=C,J$, which yields

$$a_C = (C_0 - c_C V_0)\left[\int_{\Omega_C} \tanh\left(b_C\left((x^2+(z-s_h)^2-r_c^2)(z-s_h)\right)\right)\,\mathrm{d}V\right]^{-1}, \tag{4.14}$$

$$a_J = (J_0 - c_J V_0)\left[\int_{\Omega_C} \tanh\left(b_J\left((x^2+(z-s_h)^2-r_c^2)(z-s_h)\right)\right)\,\mathrm{d}V\right]^{-1}. \tag{4.15}$$

The initial cell and substrate volume fractions used for numerical simulation are plotted in Figure 4.3 in Section 4.1.4.

Thus, we have three equations, (4.3), (4.4) and (4.5), for three unknowns, θ_C, θ_J and θ_W, with the substrate deposition rate given by Equation (4.6) and the pressure imposed in Equation (4.9). Boundary conditions are given by Equation (4.10). Initial conditions are given by Equation (4.13) with parameters chosen such that Equations (4.14) and (4.15) are satisfied.

4.1.2 Nondimensionalisation

We nondimensionalise the system of equations by setting

$$t = \frac{\hat{t}}{k_b}, \qquad \mathbf{x} = H\hat{\mathbf{x}}, \qquad p(\mathbf{x},t) = p_0\hat{p}(\hat{\mathbf{x}},\hat{t}) + p_{\text{atm}}, \quad \text{and} \quad \tau = \frac{\hat{\tau}}{k_b}, \tag{4.16}$$

where the caret denotes the dimensionless variable, $p_0 = 1$ kPa as in Chapter 3 and H is height of the culture medium in well to maintain consistency with the other chapters in this thesis.

This yields the dimensionless equations (note θ_k for $k = C, J, W$ are dimensionless) given by

$$\frac{\partial \theta_C}{\partial \hat{t}} = \left(\theta_J \theta_W - K_d\right)\theta_C + \hat{D}_C \hat{\nabla}^2 \theta_C, \qquad \hat{\mathbf{x}} \in \hat{\Omega}_C, \tag{4.17}$$

$$\frac{\partial \theta_J}{\partial \hat{t}} = \left(K_p\big(\hat{\mathbf{x}}, \hat{t}, \hat{p}(\hat{\mathbf{x}}, \hat{t})\big)\theta_W - K_{jd}\theta_J\right)\theta_C, \qquad \hat{\mathbf{x}} \in \hat{\Omega}_C, \tag{4.18}$$

where $K_d = \dfrac{k_d}{k_b}$, $\hat{D}_C = \dfrac{D_C}{k_b H^2}$, $K_p\big(\hat{\mathbf{x}}, \hat{t}, \hat{p}(\hat{\mathbf{x}}, \hat{t})\big) = \dfrac{k_p\left(\mathbf{x}, t, p(\mathbf{x}, t)\right)}{k_b}$ and $K_{jd} = \dfrac{k_{jd}}{k_b}$. The substrate deposition rate is given by

$$K_p\left(\hat{\mathbf{x}}, \hat{t}, \hat{p}(\hat{\mathbf{x}}, \hat{t})\right) = \begin{cases} K_1, & \text{if } \hat{p}(\hat{\mathbf{x}}, \hat{t}) < P_1, \\ K_1 + (K_3 - K_1)\exp\left(-\frac{\hat{\tau}(\mathbf{x}, \hat{t})}{\hat{\alpha}}\right), & \text{if } \hat{p}(\hat{\mathbf{x}}, \hat{t}) \geq P_1, \end{cases} \quad \hat{\mathbf{x}} \in \hat{\Omega}_C, \tag{4.19}$$

where $K_1 = \dfrac{k_1}{k_b}$, $K_3 = \dfrac{k_3}{k_b}$, $P_1 = \dfrac{p_1 - p_{\text{atm}}}{p_0}$ and $\hat{\alpha} = \alpha k_b$. For the current experimental strategy, the imposed dimensionless pressure is given by

$$\hat{p}(\hat{\mathbf{x}}, \hat{t}) = \hat{p}(\hat{t}) = \begin{cases} A\left(1 - \cos\left(2\pi \Upsilon \hat{t}\right)\right), & \text{if the construct is in the bioreactor,} \\ 0, & \text{otherwise,} \end{cases} \quad \hat{\mathbf{x}} \in \hat{\Omega}_C \tag{4.20}$$

where $\Upsilon = \dfrac{\omega}{k_b}$ and $A = \dfrac{a}{p_0}$. The dimensionless domain is given by

$$\hat{\Omega}_C = \{(\hat{x}, \hat{z}) \in \mathbb{R}^2 : \hat{x}^2 + (\hat{z} - \hat{s}_h)^2 \leq \hat{r}_c^2, \hat{z} \geq \hat{s}_h\}, \tag{4.21}$$

with the boundary

$$\partial\hat{\Omega}_C = \left\{(\hat{x}, \hat{z}) \in \mathbb{R}^2 : \hat{x}^2 + (\hat{z} - \hat{s}_h)^2 = \hat{r}_c^2, \hat{z} > \hat{s}_h\right\} \cup \left\{(\hat{x}, \hat{z}) \in \mathbb{R}^2 : \hat{z} = \hat{s}_h, -\hat{r}_c < \hat{x} < \hat{r}_c\right\}, \tag{4.22}$$

where $\hat{s}_h = \dfrac{s_h}{H}$ and $\hat{r}_c = \dfrac{r_c}{H}$. The boundary condition is given by

$$\hat{\nabla}\theta_C \cdot \mathbf{n} = 0, \quad \hat{\mathbf{x}} \in \partial\hat{\Omega}_C, \tag{4.23}$$

and the initial cell and substrate conditions, by Equation (4.13), are given by

$$\theta_k(\hat{\mathbf{x}}, 0) = a_k \tanh\left(\hat{b}_k\left((\hat{x}^2 + (\hat{z} - \hat{s}_h)^2 - \hat{r}_c^2)(\hat{z} - \hat{s}_h)\right)\right) + c_k, \quad \text{for } k = C, J, \quad \hat{\mathbf{x}} \in \hat{\Omega}_C, \tag{4.24}$$

where $\hat{b}_k H^3 = b_k$ for $k = C, J$, with

$$a_C = (C_0 - c_C V_0)\, H^{-2} \left[\int_{\hat{\Omega}_C} \tanh\left(\hat{b}_C \left((\hat{x}^2 + (\hat{z} - \hat{s}_h)^2 - \hat{r}_c^2)(\hat{z} - \hat{s}_h) \right) \right) \mathrm{d}\hat{V} \right]^{-1}, \tag{4.25}$$

$$a_J = (J_0 - c_J V_0)\, H^{-2} \left[\int_{\hat{\Omega}_C} \tanh\left(\hat{b}_J \left((\hat{x}^2 + (\hat{z} - \hat{s}_h)^2 - \hat{r}_c^2)(\hat{z} - \hat{s}_h) \right) \right) \mathrm{d}\hat{V} \right]^{-1}. \tag{4.26}$$

Dimensionless parameters

We use dimensionless parameters relating to the transfer of mass terms and describing the stimulated loading strategy as discussed in Chapter 3 and listed in Table 3.5. The origins of these parameters are also given in this table. Existing research indicates that a suitable cell diffusion coefficient is on the order of 10^{-7} mm^2 s^{-1} [Sengers *et al.*, 2007a, 2009]. Due to the fact that we are considering an experiment on the timescale of hours, rather than days, and are seeking a qualitative description of the experimental setup, we increase the cellular diffusion coefficient to be 10^{-5} mm^2 s^{-1}. This is equivalent to a dimensionless value of 3.0×10^{-3} and has the effect of accelerating diffusive cellular flux, so that a visible effect over the experimental timescale of 12 hours can be seen. Dimensional spatial variables describing the experimental setup are taken from Table 2.1, with the construct radius of $r_c = 0.8681$ mm being used by Equation (2.3). Consequently, parameters are given in Table 4.1.

We now have the system of equations given by Equations (4.3), (4.17) and (4.18), with Equation (4.19) and pressure imposed by Equation (4.20), on the domain given by Equation (4.21), along with boundary conditions given by Equation (4.23) for the unknowns θ_C, θ_J and θ_W. Initial conditions are given by Equation (4.24) with parameters chosen such that Equations (4.25) and (4.26) are satisfied. We now discuss the numerical scheme employed before presenting numerical results.

4.1.3 Numerical scheme

We adopt the following numerical methods to find approximate solutions to the system of governing equations. We first eliminate θ_W from Equations (4.17) and (4.18) by Equation (4.3). We then discretise time, using Euler methods, where, as in Section 3.2.1, a variable timestep size is used according to Equation (3.38). We obtain numerical solutions by proceeding through

Table 4.1: Default parameters used in the numerical simulations. All parameters are dimensionless except for the temporal and spatial scaling parameters, k_b and H respectively.

Parameters describing rates					
K_d	=	0.006	K_{jd}	=	0.12
K_1	=	0.57	K_3	=	231.3
$\hat{D}_C$	=	3.0×10^{-3}	$\hat{\alpha}$	=	$0.25/(24 \times 60 \times 60)$
P_1	=	210			
Spatial parameters					
$\hat{s}_h$	=	2.9/17	$\hat{r}_c$	=	0.8681/17
Loading parameters					
Υ	=	$24 \times 60 \times 60$	A	=	140
Parameters describing initial conditions					
a_C	=	94.5240	a_J	=	34.6588
$\hat{b}_C$	=	75	$\hat{b}_J$	=	75
c_C	=	0.3781	c_J	=	0.1386
C_0	=	0.3	J_0	=	0.11
V_0	=	1.37			
Timestep sizes					
$(\hat{\Delta}t)_l$	=	10^{-5}	$(\hat{\Delta}t)_m$	=	10^{-6}
$(\hat{\Delta}t)_h$	=	10^{-8}			
Temporal and spatial scaling					
k_b	=	$(60 \times 60 \times 24)^{-1}$ s^{-1}	H	=	17 mm

time. Continuous Galerkin FEMs with linear basis functions are first used to approximate the spatial solution of the cell phase volume fraction at each timestep. As the pressure, given by Equation (4.20), is known and spatially constant through the domain, the discretised substrate volume fraction equation is an ODE at each spatial point and can then be solved at each mesh point to give the updated substrate volume fraction.

Numerical simulations are performed in two spatial dimensions in Cartesian coordinates on the semicircular domain Ω_C, sketched in Figure 4.1(b). The mesh used for these numerical simulations is shown in Figure 4.2 and the results are visually indistinguishable if a finer mesh is used. The system of equations in nondimensional variables is solved but results are presented

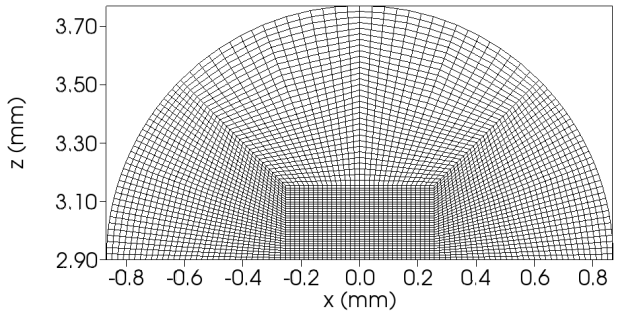

Figure 4.2: The mesh used for numerical results presented in Section 4.1.4, which contains 1024 elements.

in dimensional quantities to allow an easy comparison to the experimental setup and quantities. Further details on the computational methods used may be found in Appendix A.

4.1.4 Numerical results

Numerical results are presented for both control (constant atmospheric pressure) and stimulated (intermittent cyclic loading) strategies for a 12 hour experiment, as described in Section 3.5. The initial conditions for the cell and substrate phases used, given by Equation (4.24) with parameters in Table 4.1, are plotted in Figure 4.3.

Figure 4.4 shows the spatial distribution of the substrate phase volume fraction after 12 hours under both the control and the stimulated loading regimes. The substrate volume fraction is higher under the stimulated than the control loading regime, indicating that there is more substrate deposition under the former loading regime than the latter. This is expected from the higher average substrate deposition rate for the stimulated loading regime, and can clearly be seen in Figure 4.4(c). By comparing the range of substrate volume fraction spatial values, $\max_{\mathbf{x}\in\Omega_C}(\theta_J(\mathbf{x},t)) - \min_{\mathbf{x}\in\Omega_C}(\theta_J(\mathbf{x},t))$, at the initial time point, Figure 4.3(b), in comparison to after 12 hours, Figure 4.4 (by inspecting the colourbar ranges), it can be seen that the spatial variation across the substrate phase decreases with time. This can also be seen in Figure 4.5, which shows the temporal evolution of the standard deviation of the substrate phase volume fraction. As time evolves the standard deviation of the substrate phase volume fraction gradually decreases under both of the loading regimes, with the decrease under the stimulated loading regime being more pronounced.

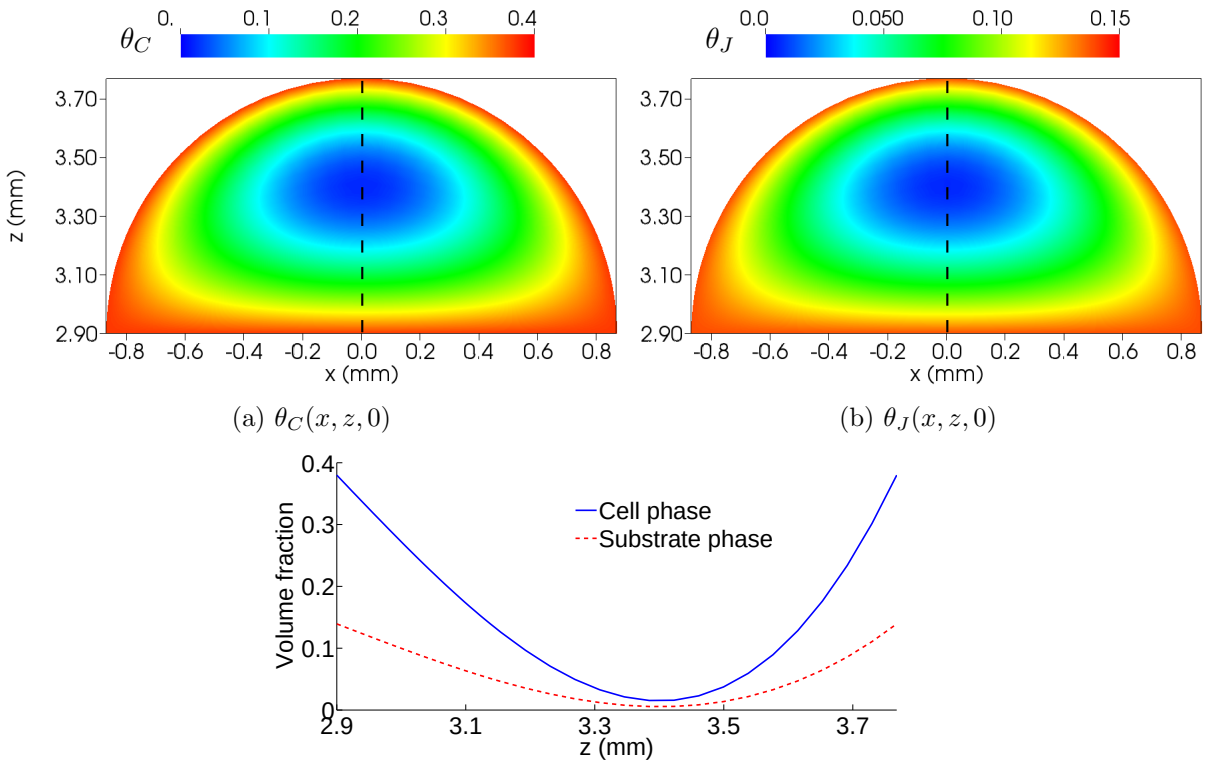

(a) $\theta_C(x, z, 0)$ (b) $\theta_J(x, z, 0)$

(c) Cut along the z–axis

Figure 4.3: The initial conditions for (a) the cell, $\theta_C(\mathbf{x}, 0)$, and (b) the substrate, $\theta_J(\mathbf{x}, 0)$, phases as given by Equation (4.24) with parameters given in Table 4.1. These initial conditions along the z–axis, indicated by dashed black lines in Figures (a) and (b), are shown in (c), where the blue full and red dashed lines indicate the cell and substrate volume fractions respectively.

In comparison to the substrate phase volume fraction, the initial spatial variation in the cell phase quickly decreases and, over the timeframe of the experiment, the cell phase volume fraction effectively becomes spatially homogeneous. This can be seen by inspecting both the standard deviation of the cell phase through time in Figure 4.6 and the spatial distribution in the cell phase along the z–axis for the first few hours under the control loading regime in Figure 4.7. As time evolves, there is a net movement of cells down cell volume fraction gradients, from the edges towards the centre of the construct, due to the cell diffusion term and no flux boundary conditions. By comparison it takes substantially longer for the substrate phase to become homogeneous under both the loading regimes (on the order of days rather than hours), as can be seen in Figure 4.5. This is due to the fact that the substrate phase is assumed to be solid and so there is no diffusion term for the substrate phase in Equation (4.18). From Equation (4.18), along with Equation (4.3), the rate of substrate deposition is $K_p\theta_C\left(1-\theta_C-\theta_J\right)$, and the rate of substrate degradation is $K_{jd}\theta_C\theta_J$. Thus, once θ_C is effectively homogeneous, substrate will

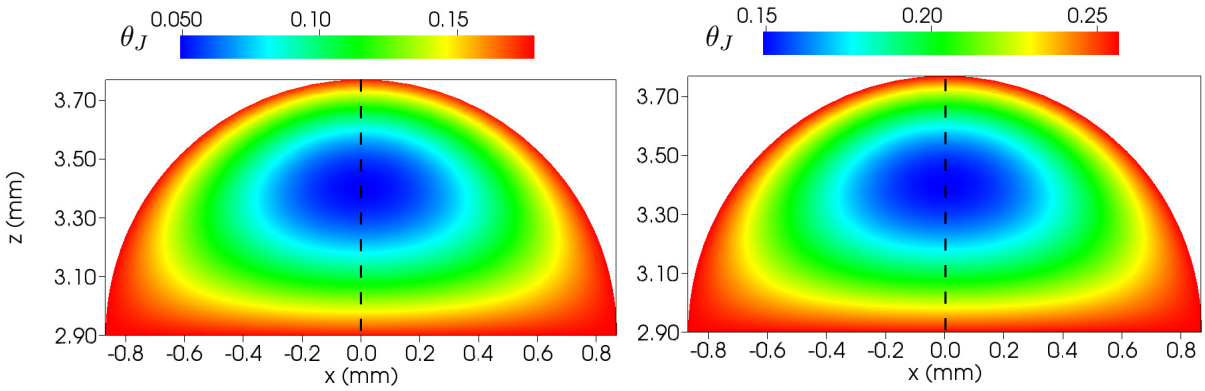

(a) Control

(b) Stimulated

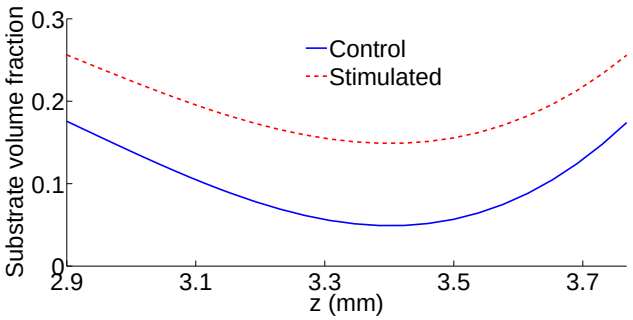

(c) Cut along the z–axis

Figure 4.4: Numerical results for the substrate phase spatial distribution after 12 hours under the (a) control and the (b) stimulated loading regimes. Initial conditions are given by Equation (4.24) and parameters are given in Table 4.1. The substrate phase spatial distribution along the z–axis, indicated as dashed lines in Figures (a) and (b), is shown in Figure (c).

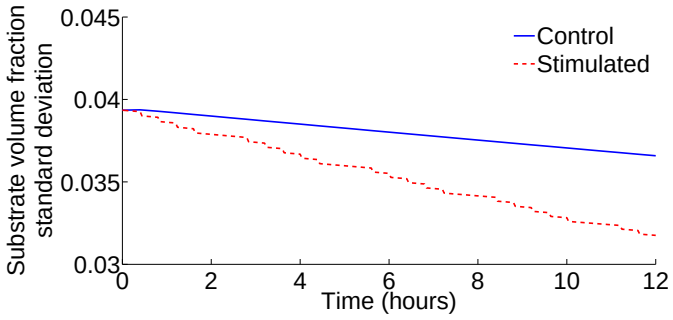

Figure 4.5: The standard deviation in the spatial distribution of the substrate phase volume fraction through time. The initial conditions are given by Equation (4.24) and parameters are given in Table 4.1.

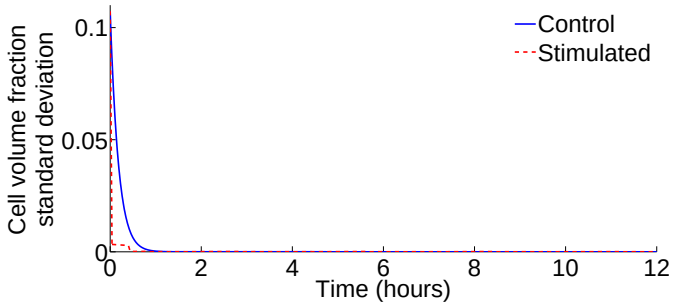

Figure 4.6: The standard deviation in the spatial distribution of the cell phase volume fraction through time. The initial conditions are given by Equation (4.24) and parameters are given in Table 4.1.

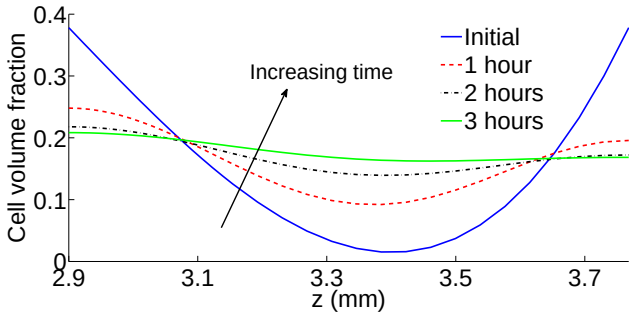

Figure 4.7: The cell phase volume fraction, θ_C, along the z–axis under the control loading regime showing how the cell volume fraction changes over the first few hours. The arrow shows the direction of increasing time. Initial conditions are given by Equation (4.24) and parameters are given in Table 4.1.

be deposited at a higher rate and degraded at a lower rate for lower θ_J which will reduce the spatial variation in the substrate phase over time. Due to the higher rate of substrate deposition during the loading periods, the spatial distribution in the substrate phase decreases faster. This also explains why the patterns of loading may be seen under the stimulated loading regime in Figure 4.5.

In addition to the spatial variation we are also interested in the change in total quantity of the constituent phases over time. To compare results with those from Chapter 3 we define the *average volume fraction* of the cell and substrate phases to be

$$\bar{\theta}_k(t) = \frac{1}{\mathcal{V}_C} \int_{\Omega_C} \theta_k(\mathbf{x}, t)\, \mathrm{d}V, \quad \text{for } k = C, J, \tag{4.27}$$

where $\mathcal{V}_C$ indicates the area of the domain Ω_C. The average volume fractions for the cell and substrate phases over time, under both loading strategies, are shown in Figure 4.8. There is

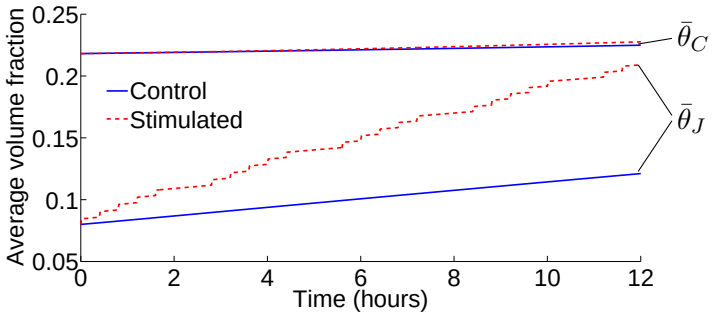

Figure 4.8: The evolution of the average cell and substrate phase volume fractions, $\bar{\theta}_C(t)$ and $\bar{\theta}_J(t)$, through time. The average volume fraction of phase k is defined in Equation (4.27). Initial conditions are given by Equation (4.24) and parameters are given in Table 4.1. The top two lines show the evolution of the average cell phase volume fraction, whereas the two bottom lines show the evolution of the average substrate volume fraction.

little change over time in the average cell volume fraction, due to the low cell birth and death rates (the expected change in cell volume fraction over 12 hours is an increase of approximately 6.2×10^{-3} and decrease of 6.6×10^{-4} due to cell birth and death respectively). However, the change in the average substrate volume fraction over time is clear, with the increase under the stimulated loading regime being substantially greater as expected. A comparison of the average cell and substrate volume fractions over time with the equivalent non–spatial model shows that the results from the two models are visually indistinguishable (not shown). This is because the effect of the cellular diffusion acts to smooth everything out so that the model reduces to the ODE model with memory presented in Section 3.2.

Although this model qualitatively gives similar results to the experiments in terms of the average volume fraction, it does not accurately represent the spatial variation seen experimentally. These results predict a decrease in the spatial variation of both the cell and substrate phases as time evolves. This is contrary to what is seen in the *in vitro* experiments, where the spatial variation in the substrate phase increases with time and a rim of mineralisation develops at the periphery of the construct as illustrated in Figure 2.9.

Nutrient transport is known to be important in determining the spatial structure of the construct. It has been shown in both experimental and theoretical previous work, as discussed in Sections 1.1.2 and 1.2.2, that, without fluid perfusion, the construct develops a rim of proliferating cells with a necrotic core. To test the hypothesis that gradients in nutrient concentrations drive the spatial distribution in the substrate phase seen experimentally, we modify the model

by including the dependence of cell birth and substrate deposition on a diffusible nutrient in solution in the next section.

4.2 Nutrient–dependent growth

We are interested in the qualitative effect the spatial distribution of a nutrient has on the spatial distribution the constituent phase volume fractions. It is a common modelling assumption to use one nutrient as representative of all nutrients and waste products in solution in order to simplify the model, as discussed in Section 1.2.2. We use oxygen as a representative rate–limiting nutrient.

Let us denote the concentration of oxygen at the point $\mathbf{x} \in \Omega_C$ and time $t \geq 0$ by $n(\mathbf{x}, t)$. As the diffusion timescale of oxygen is much shorter than the cell growth timescale we assume that oxygen concentration is quasi–steady [Byrne *et al.*, 2003, Byrne and Chaplain, 1997, Breward *et al.*, 2002]. Assuming that the oxygen is diffusible only in the cell and fluid phases, and that the diffusion between these two phases is so fast that the concentration of oxygen can be considered the same in both phases [Astanin and Preziosi, 2008], we have

$$D_n \nabla \cdot ((1 - \theta_J) \nabla n) = R(\mathbf{x}, t), \quad \mathbf{x} \in \Omega_C, \tag{4.28}$$

where $R(\mathbf{x}, t)$ is the uptake term, and can depend on other variables such as the constitutive phase volume fractions, and D_n is the diffusion coefficient which we assume to be constant. We use a linear uptake term, which is one of the simpler uptake functions that can be used, and is a first order approximation to the Michaelis-Menten uptake term. Lewis *et al.* [2005] showed that a linear uptake term represents tissue engineering experimental data well, and it has been used in several theoretical tissue engineering studies [Breward *et al.*, 2001, Lemon and King, 2007a, Shipley *et al.*, 2009, Osborne and Whiteley, 2010]. Other options include Michaelis–Menten kinetics [Coletti *et al.*, 2006, Shipley *et al.*, 2011, Shipley and Waters, 2012] or a saturation function [Osborne, 2009]. In this chapter we are interested in the qualitative effect the nutrient spatial distribution has on the constituent phase volume fractions and adopting a linear uptake term is sufficient to qualitatively reproduce the heterogeneous distribution in the substrate

phase seen in the *in vitro* experiments. Using a linear uptake term for oxygen we have

$$D_n \nabla \cdot ((1-\theta_J)\nabla n) = \eta n \theta_C, \quad \mathbf{x} \in \Omega_C, \tag{4.29}$$

where the term on the right hand side models oxygen uptake at a rate proportional to both the cell volume fraction and oxygen concentration with $\eta \geq 0$ the rate of oxygen uptake by the cells.

As the medium is refreshed regularly we assume that the fluid surrounding the construct has a constant oxygen concentration. In addition we assume that the pressures applied do not alter this concentration. This yields a Dirichlet boundary condition of the form

$$n = n_0, \quad \text{on} \quad \mathbf{x} \in \partial\Omega_C, \tag{4.30}$$

where n_0 is the constant concentration of oxygen in the surrounding culture medium.

As before we have the no voids condition, Equation (4.3). Both proliferation and substrate deposition involve the creation of new material which requires nutrients [Murray, 2002, Yeatts and Fisher, 2011]. Therefore, we modify the cell and substrate conservation of mass equations, Equations (4.4) and (4.5), to include oxygen–dependent cell birth and substrate deposition as follows:

$$\frac{\partial \theta_C}{\partial t} = \left(\frac{\tilde{k}_b}{n_0} n \theta_J \theta_W - k_d \right) \theta_C + D_C \nabla^2 \theta_C, \qquad \mathbf{x} \in \Omega_C, \tag{4.31}$$

$$\frac{\partial \theta_J}{\partial t} = \left(\frac{\tilde{k}_p(\mathbf{x},t,p)}{n_0} n \theta_W - k_{jd} \theta_J \right) \theta_C, \qquad \mathbf{x} \in \Omega_C, \tag{4.32}$$

where $\tilde{k}_b$, k_d, $\tilde{k}_p$ and k_{jd} are the cell birth, cell death, substrate deposition and substrate degradation rates respectively. The substrate deposition rate is given by a modified version of Equation (4.6):

$$\tilde{k}_p\left(\mathbf{x},t,p(\mathbf{x},t)\right) = \begin{cases} \tilde{k}_1, & \text{if } p(\mathbf{x},t) < p_1, \\ \tilde{k}_1 + (\tilde{k}_3 - \tilde{k}_1)\exp\left(-\frac{\tau(\mathbf{x},t)}{\alpha}\right), & \text{if } p(\mathbf{x},t) \geq p_1, \end{cases} \quad \mathbf{x} \in \Omega_C, \tag{4.33}$$

where α, τ and p_1 are the same as in Section 4.1, and $\tilde{k}_1$ and $\tilde{k}_3$ are rates which are measured in

time^{-1}. We note that the only difference between Equations (4.6) and (4.33) is the difference in the rates, denoted by tildes in the latter equation. The domain, Ω_C, the no voids condition, Equation (4.3), the imposed pressure, Equation (4.9), and the cell phase boundary condition, given by Equation (4.10), remain the same as in Section 4.1.

In the following we consider two sets of initial conditions relating to the forms given by Equations (4.12) and (4.13), which represent homogeneous and heterogeneous initial conditions respectively. This enables us to compare results to those in Section 4.1 and to consider how the initial seeding strategy affects the spatial distribution of the constituent phases in the end product.

4.2.1 Nondimensionalisation

We nondimensionalise in a similar manner to in Section 4.1.2, using carets to denote the dimensionless variables and setting

$$t = \frac{\hat{t}}{\tilde{k}_b}, \qquad \mathbf{x} = H\hat{\mathbf{x}}, \qquad p(\mathbf{x},t) = p_0\hat{p} + p_{\text{atm}}, \qquad \tau = \frac{\hat{\tau}}{\tilde{k}_b}, \quad \text{and} \quad n = n_0\hat{n}. \tag{4.34}$$

The dimensionless version of Equation (4.29) is given by

$$\hat{D}_n\hat{\nabla}\cdot\left((1-\theta_J)\,\hat{\nabla}\hat{n}\right) = \hat{n}\theta_C, \quad \hat{\mathbf{x}} \in \hat{\Omega}_C, \tag{4.35}$$

where $\hat{D}_n = \dfrac{D_n}{(\eta H^2)}$ along with the boundary conditions

$$\hat{n} = 1, \quad \text{on} \quad \hat{\mathbf{x}} \in \partial\hat{\Omega}_c. \tag{4.36}$$

The conservation of mass equations for the cell and substrate phase are given by

$$\frac{\partial\theta_C}{\partial\hat{t}} = \left(\hat{n}\theta_J\theta_W - \tilde{K}_d\right)\theta_C + \hat{\tilde{D}}_C\hat{\nabla}^2\theta_C, \qquad \hat{\mathbf{x}} \in \hat{\Omega}_C, \tag{4.37}$$

$$\frac{\partial\theta_J}{\partial\hat{t}} = \left(\tilde{K}_p(\hat{\mathbf{x}},\hat{t},\hat{p})\hat{n}\theta_W - \tilde{K}_{jd}\theta_J\right)\theta_C, \qquad \hat{\mathbf{x}} \in \hat{\Omega}_C, \tag{4.38}$$

where

$$\tilde{K}_p\left(\hat{\mathbf{x}},\hat{t},\hat{p}(\hat{\mathbf{x}},\hat{t})\right) = \begin{cases} \tilde{K}_1, & \text{if } \hat{p}(\hat{\mathbf{x}},\hat{t}) < P_1, \\ \tilde{K}_1 + (\tilde{K}_3 - \tilde{K}_1)\exp\left(-\frac{\hat{\tau}(\mathbf{x},\hat{t})}{\hat{\alpha}}\right), & \text{if } \hat{p}(\hat{\mathbf{x}},\hat{t}) \geq P_1, \end{cases} \quad \hat{\mathbf{x}} \in \hat{\Omega}_C, \tag{4.39}$$

and dimensionless pressure is given by Equation (4.20). The dimensionless parameters with the tilde notation are equivalent to those given in Section 4.1.2, so that $\tilde{K}_d = \frac{k_d}{\tilde{k}_b}$, $\tilde{K}_{jd} = \frac{k_{jd}}{\tilde{k}_b}$, $\tilde{K}_p = \frac{\tilde{k}_p}{\tilde{k}_b}$, $\tilde{K}_1 = \frac{\tilde{k}_1}{\tilde{k}_b}$ and $\tilde{K}_3 = \frac{\tilde{k}_3}{\tilde{k}_b}$. The spatial, pressure and temporal scalings are not altered from Section 4.1.2, and, consequently, Equations (4.20) – (4.26) remain unaltered.

Dimensionless parameters

We are interested in the qualitative behaviour of the system, and in particular how the inclusion of a diffusible nutrient affects the spatial distribution of the constituent phases within the construct. We use the same values as for the corresponding tilde–less parameters in Section 4.1.2 and given in Table 4.1. We note that, for these parameters, if $\hat{n}(\hat{\mathbf{x}},\hat{\mathbf{t}}) = 1$ for all $\hat{\mathbf{x}} \in \hat{\Omega}_C$, $\hat{t} \geq 0$, the numerical results would be identical to those in Section 4.1.

Due to the extra equation describing the oxygen concentration, we are required to specify further parameters. We set the oxygen concentration within the well external to the construct to be a typical value used in tissue engineering applications, and use $n_0 = 205$ μM ($205\ 10^{-3}$ mol m^{-3}) from Sengers *et al.* [2005]. We use a diffusion coefficient for oxygen of $D_n = 2 \times 10^{-9}$ m^2 s^1 from Jamnongwong *et al.* [2010]. In the absence of appropriate data for the cell uptake term, we set $\eta = 1$ s^{-1}. This rate is likely to be lower, for example the values used in Shipley *et al.* [2009] range from 6×10^{-6} s^{-1} to 7.7×10^{-3} s^{-1} for Bovine articular chondrocytes in three–dimensional culture. Using such a large value of η accelerates the effects of the heterogeneous nutrient distribution on the constituent phase volume fractions and means we can examine these effects over a shorter timescale. This gives $\hat{D}_n = 6.92 \times 10^{-6}$.

In summary we have the system of equations given by Equations (4.3), (4.35), (4.37) and (4.38), with the substrate deposition rate given by Equation (4.39). Boundary conditions are given by Equations (4.23) and (4.36), with pressure imposed by Equation (4.20). Two sets of initial conditions are used, either given by Equation (4.12) (homogeneous) or by Equation (4.24)

(heterogeneous). The domain in dimensionless variables remains as given by Equation (4.21), with the boundary given by Equation (4.22).

4.2.2 Numerical scheme

We proceed to seek numerical solutions in a similar manner to the well perfused case in Section 4.1.3. First, the fluid phase volume fraction, θ_W, is eliminated from the system of equations by Equation (4.3). We then decouple the system of equations and solve the equations for the oxygen concentration and the conservation of mass equations for the cell and substrate phases, Equations (4.35), (4.37) and (4.38), separately. As before we use Euler methods to discretise time and three separate timestep sizes are used according to Equation (3.38) as in previous sections. At each timestep continuous Galerkin FEMs with linear basis functions are used first to solve for the oxygen concentration and then for the cell volume fraction. We note that, although the oxygen equation, Equation (4.35), has no time derivative, it will need to be updated at each timestep due to the dependence of θ_J on time. Finally, the substrate phase conservation of mass equation, Equation (4.38), is solved at each spatial point. As before, numerical simulations are performed in two spatial dimensions, on the semicircular domain sketched in Figure 4.1(b), with the mesh given in Figure 4.2.

4.2.3 Numerical results

The initial oxygen concentration for the two sets of initial conditions, given by Equations (4.12) and (4.24), is shown in Figure 4.9. Due to the Dirichlet boundary condition, given by Equation (4.36), the oxygen concentration is equal to the external oxygen concentration at the boundary of the construct (205 μM). However, as the distance from the edge of the construct increases, the oxygen concentration rapidly decreases so that it is lower in the centre of the construct. The minimum oxygen concentration is initially higher for the heterogeneous than for the homogeneous initial conditions, see Figure 4.9(c). This is because oxygen consumption is proportional to the cell phase volume fraction, which is initially lower in the centre of the construct for the former than for the latter initial conditions, and, as a result, the oxygen concentration is higher.

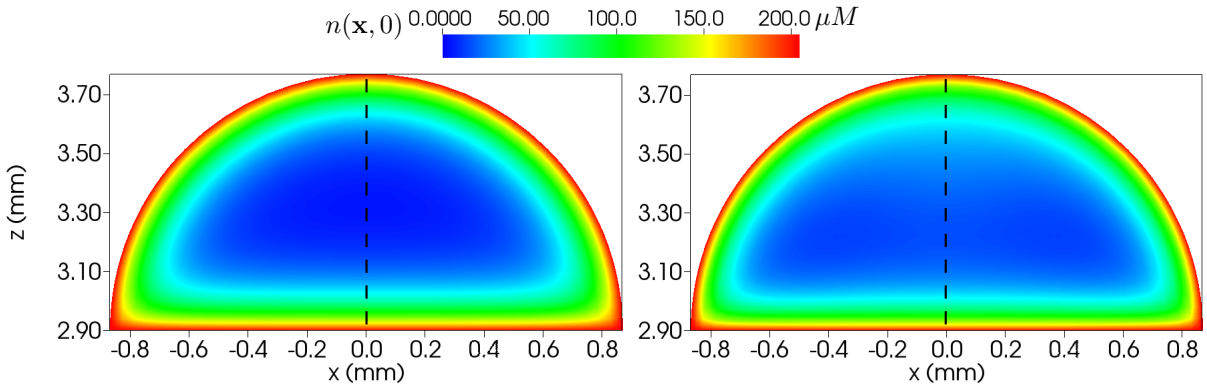

(a) Homogeneous initial conditions

(b) Heterogeneous initial conditions

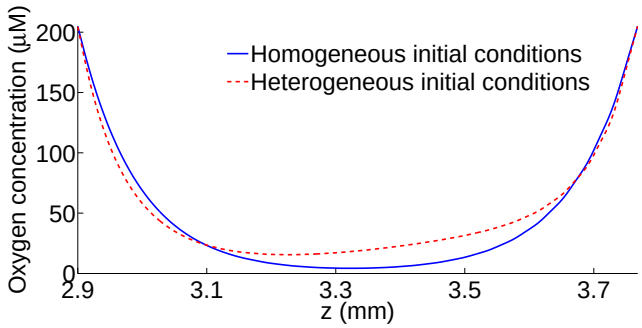

(c) Cut along the z–axis

Figure 4.9: Numerical results for the oxygen concentration at time $t = 0$, $n(\mathbf{x}, 0)$, in μM. Figure (a) show the numerical results for the homogeneous initial conditions given by Equation (4.12) and Figure (b) shows the numerical results for the heterogeneous initial conditions given by Equation (4.24). Figure (c) shows the oxygen concentration along the z–axis, illustrated by the dashed lines in (a) and (b), for both sets of initial conditions. Parameters are given in Table 4.1 with $\hat{D}_n = 6.92 \times 10^{-6}$.

The spatial distribution of the oxygen concentration does not change much as time evolves. Figure 4.10 compares the oxygen concentration initially and after 12 hours along the z–axis under both loading regimes and for both sets of initial conditions. For the homogeneous initial conditions the oxygen concentration remains almost identical throughout the simulation and under both the loading regimes, as the lines in Figure 4.10(a) are difficult to distinguish. In contrast, the oxygen concentration in the centre of the construct decreases quickly as time evolves for the heterogeneous initial conditions, and then does not change significantly over the course of the experiment. As for the homogeneous initial conditions, it can be seen that the oxygen concentration spatial distribution for the heterogeneous initial condition after 12 hours is very similar under both the loading regimes, Figure 4.10(b).

Due to the heterogeneity of the spatial distribution of oxygen concentration, the quantity of cell

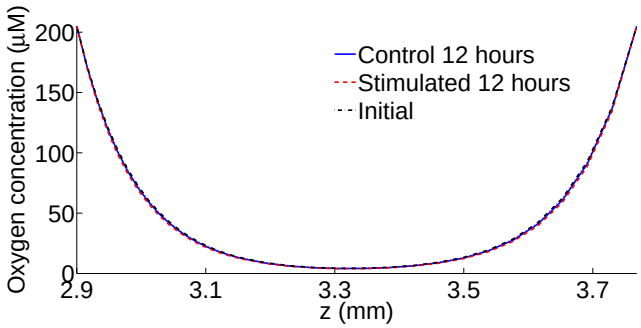

(a) Homogeneous initial conditions

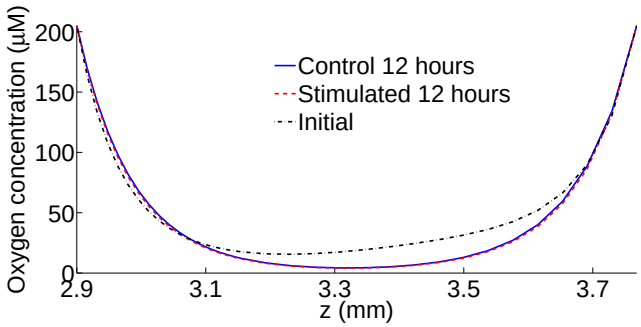

(b) Heterogeneous initial conditions

Figure 4.10: Illustration of the change in the oxygen concentration through time under both loading regimes along the z–axis for (a) the homogeneous initial conditions given by Equation (4.12) and (b) the heterogeneous initial conditions given by Equation (4.24). Parameters are given in Table 4.1 with $\hat{D}_n = 6.92 \times 10^{-6}$. The black dash–dotted lines shows the oxygen distribution at the initial time point and the blue full and red dashed lines show the oxygen concentration at 12 hours under the control and the stimulated loading regimes respectively.

birth and substrate deposition decreases as the distance from the periphery of the construct increases. This results the spatial variation in the substrate phase increasing over time, for both sets of initial conditions and under both loading regimes. This increase can be clearly seen in Figure 4.11, which shows the change in the standard deviation of the substrate phase volume fraction over time. The homogeneous initial conditions start with a zero standard deviation of both the cell and substrate phases, and so have lower standard deviation than the heterogeneous initial conditions throughout the experimental timeframe. This increase over time is in contrast to the well perfused case, where the equivalent measure decreased over time, as shown in Figure 4.5. Figure 4.12 shows the spatial distribution in the substrate phase volume fraction after 12 hours. By this time obvious spatial heterogeneity has developed in the substrate phase for the homogeneous initial conditions, Figures 4.12(a) and (b). Furthermore, a comparison of the range of substrate volume fraction spatial values $(\max_{\mathbf{x}\in\Omega_C}(\theta_J(\mathbf{x},t)) - \min_{\mathbf{x}\in\Omega_C}(\theta_J(\mathbf{x},t)))$ after 12 hours, Figures 4.12(c) and (d), to initially, Figure 4.3(b), for the heterogeneous initial

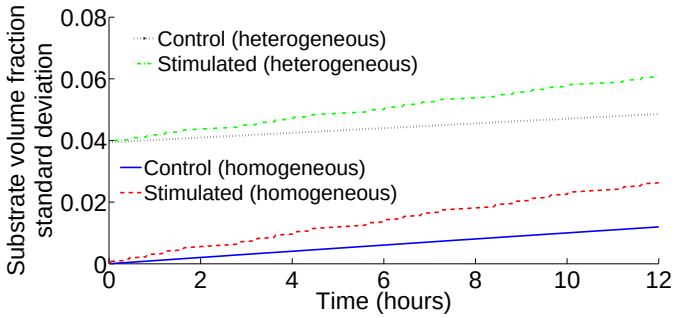

Figure 4.11: The standard deviation in the spatial distribution of the substrate phase volume fraction through time for both sets of initial conditions, as indicated in the brackets in the legend, and both the loading regimes. The homogeneous initial conditions are given by Equation (4.12) and the heterogeneous initial conditions are given by Equation (4.24). Parameters are given in Table 4.1 with $\hat{D}_n = 6.92 \times 10^{-6}$.

conditions illustrates an increase in the spatial heterogeneity at time evolves. It can be seen that the substrate phase has a lower volume fraction at each spatial point under the control in comparison to the stimulated loading regime for both sets of initial conditions, Figures 4.12(e) and (f). In the centre of the construct there is very little difference in the substrate volume fractions under the two different loading regimes. As the distance from the periphery of the construct decreases, however, the difference in volume fraction between control and stimulated loading regimes becomes more pronounced for both sets of initial conditions.

Figure 4.13 shows the temporal evolution of the cell phase volume fraction standard deviation. As in the well perfused case, the spatial heterogeneity in the cell phase for the heterogeneous initial conditions decreases rapidly due to the effect of the cellular diffusion term. In addition, although there is an increase in the spatial variation for the homogeneous initial conditions, the cell phase volume fraction standard deviation remains below 2×10^{-4} throughout the 12 hour experiment as can be seen in Figure 4.13(b). For both sets of initial conditions, the spatial variation in the cell phase is minimal and is not the driving factor behind the increasing heterogeneity in the substrate phase.

A comparison of the average substrate volume fraction over time for the two sets of initial conditions predicts that initially seeding the cell and substrate uniformly results in a slightly higher average substrate volume fraction as time progresses than seeding with more cells and substrate at the edge of the construct for both loading strategies. This can be seen in Figure 4.14. In addition, we compare the average volume fraction of the cell and substrate phases through

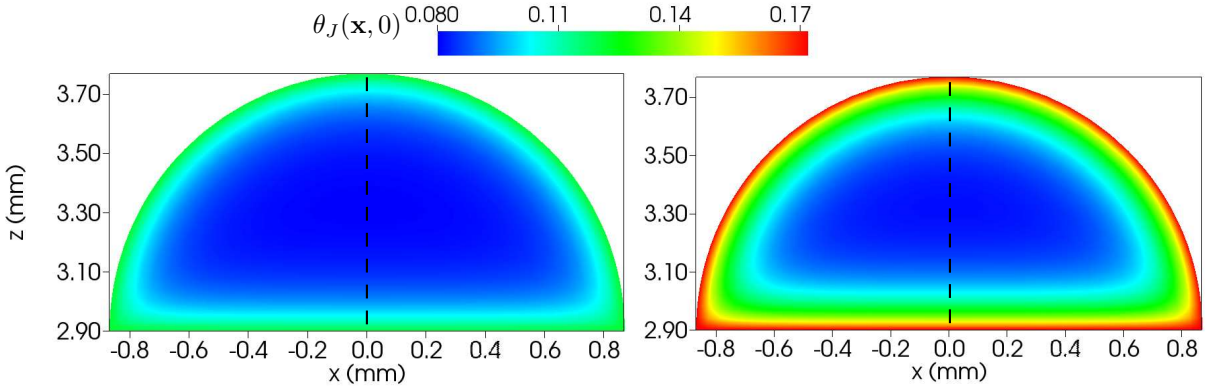

(a) Homogeneous initial conditions, control

(b) Homogeneous initial conditions, stimulated

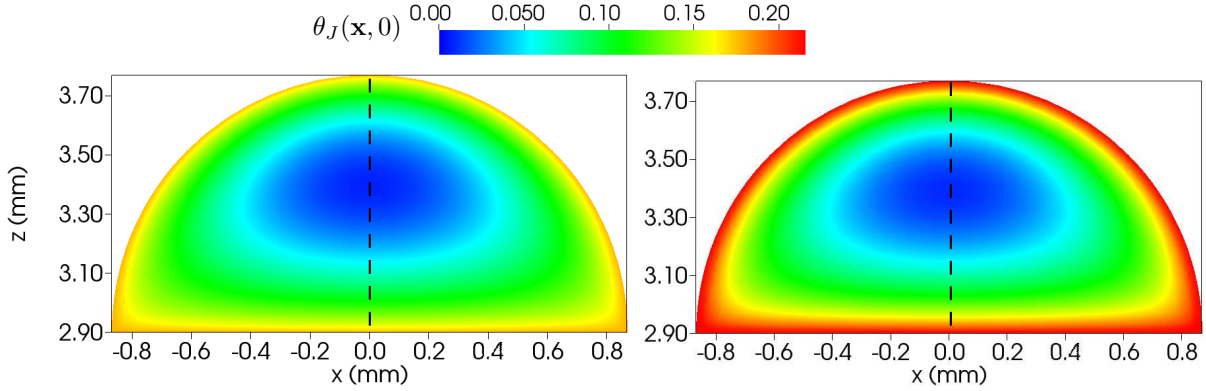

(c) Heterogeneous initial conditions, control

(d) Heterogeneous initial conditions, stimulated

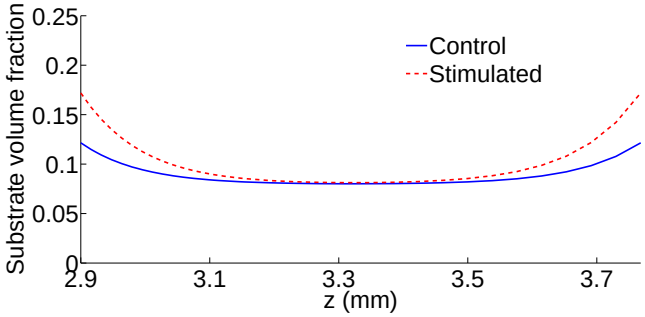

(e) Homogeneous initial conditions, cut along the z–axis

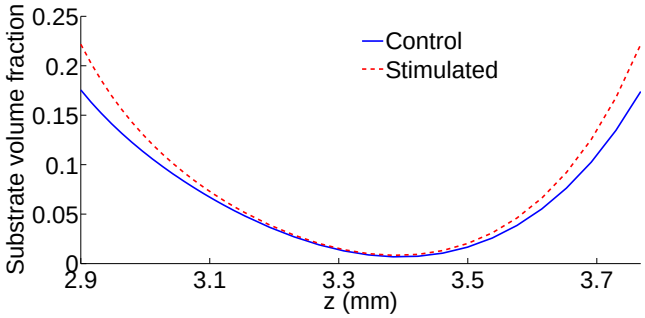

(f) Heterogeneous initial conditions, cut along the z–axis

Figure 4.12: Numerical results for the substrate phase volume fraction, θ_J, after 12 hours under the control (Figures (a) and (c)) and the stimulated (Figures (b) and (d)) loading regimes. Figures (e) and (f) show the substrate volume fraction along the z–axis, illustrated as dashed black lines in (a) – (d). Initial conditions are given by Equations (4.12) (Figures (a), (b) and (e)), and (4.24) (Figures (c), (d) and (f)). Parameters are given in Table 4.1 with $\hat{D}_n = 6.92 \times 10^{-6}$.

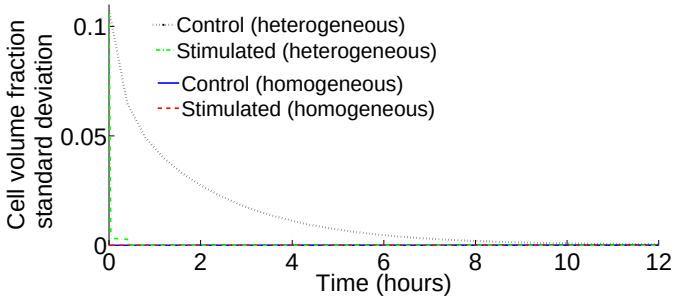

(a)

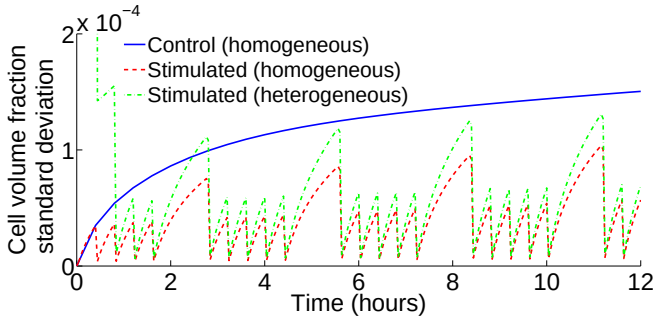

(b)

Figure 4.13: The standard deviation in the spatial distribution of the cell phase volume fraction through time for both sets of initial conditions, as indicated in brackets in the legends, and both the loading regimes. The lines for the results with homogeneous initial conditions for both loading regimes and for the results under the stimulated loading regime for the heterogeneous initial conditions are hard to see in (a), and so (b) shows a magnification of (a) near the horizontal axis, so the change in these over the time period can be visualised. The heterogeneous initial conditions are given by Equation (4.24) and the homogeneous initial conditions are given by Equation (4.12). Parameters are given in Table 4.1 with $\hat{D}_n = 6.92 \times 10^{-6}$.

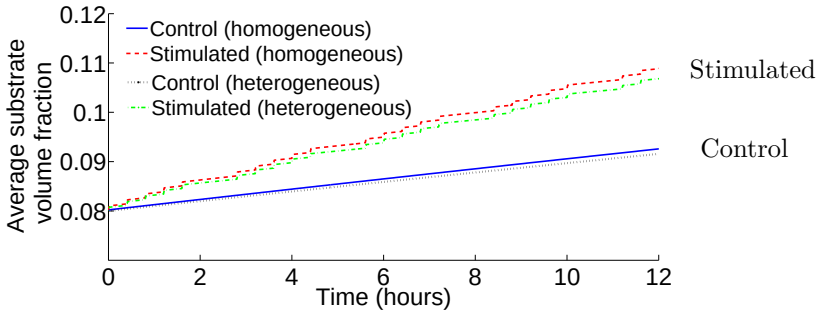

Figure 4.14: Comparison of the average substrate volume fractions, $\bar{\theta}_J(t)$ for the homogeneous and heterogeneous initial conditions. The blue and red lines show the substrate phase average volume fraction under the control and stimulated loading regimes respectively. The homogeneous initial conditions are given by Equation (4.12), and the heterogeneous initial conditions are given by Equation (4.24). Parameters are given in Table 4.1 with $\hat{D}_n = 6.92 \times 10^{-6}$.

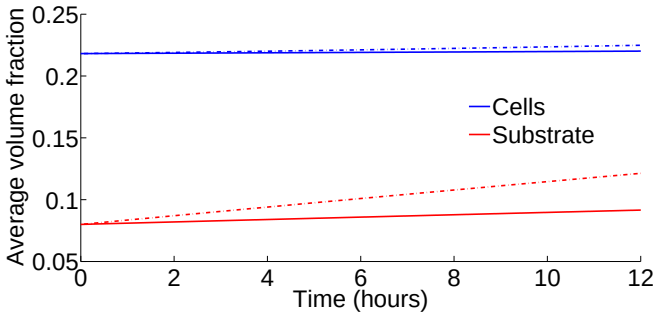

(a) The control loading regime

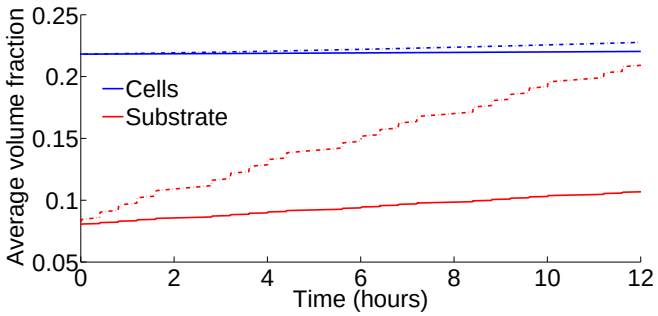

(b) The stimulated loading regime

Figure 4.15: The evolution of the average cell and substrate volume fractions, $\bar{\theta}_C(t)$ and $\bar{\theta}_J(t)$, through time for the model with diffusion of oxygen considered, under the (a) control and the (b) stimulated loading regimes. Initial conditions are given by Equation (4.24) and parameters are given in Table 4.1 with $\hat{D}_n = 6.92 \times 10^{-6}$. The average cell and substrate volume fraction curves are plotted in blue and in red respectively. The dashed lines show the numerical results for the model in Section 4.1 where all nutrients were assumed to be well perfused in the fluid phase.

time with the heterogeneous initial conditions against the results from the well perfused model in Section 4.1 in Figure 4.15. As expected, the model with oxygen–dependent cell birth and substrate deposition has significantly lower average cell and substrate volume fractions as time evolves, when compared to the well perfused model. Recall that, if $n(\mathbf{x}, t) = n_0$ for all $\mathbf{x} \in \Omega_C$ and $t \geq 0$, we would retrieve the same results as the model in Section 4.1. As the average oxygen concentration within the construct is lower than the concentration external to the construct, the average rate of cell birth and substrate deposition is lower than for the well perfused case.

We are interested in predicting which loading strategy and which seeding strategy produces the "best" construct by the end time point. It can be seen from Figure 4.14 that the quantity of substrate produced under the stimulated loading regime is significantly more for both sets of initial conditions than under the control loading regime. However, for a good quality bone construct, we require a uniform distribution of substrate so that it can bear weight. An exami-

nation of Figure 4.11 indicates that, for both sets of initial conditions, the spatial variation of the substrate phase, measured by standard deviation of the substrate volume fraction, increases more slowly under control than under the stimulated loading regime. As a consequence, at the end of the experiment, the spatial distribution in the substrate phase is more uniform under the control loading regime. This may also be seen in Figures 4.12(e) and (f). Furthermore, the model predicts that seeding with an initially homogeneous spatial distribution of cells and substrate results in lower spatial variation in the substrate phase over the 12 hour experiment, and also gives a slightly higher average quantity of substrate, and so may appear to be a better experimental strategy. However, as may be seen in Figure 4.11, the standard deviation of the substrate phase increases more quickly when homogeneous rather than heterogeneous initial conditions are used; for the former set of initial conditions the increase in standard deviation of the substrate phase over the 12 hour experiment is 1.12×10^{-2} (control) and 2.63×10^{-2} (stimulated) whereas for the latter set it is 9.23×10^{-3} (control) and 2.13×10^{-2} (stimulated).

4.3 Conclusion and discussion

In this chapter we have extended the model with cell memory presented in Chapter 3 to include spatial effects through diffusion of the cellular phase. In Section 4.1 nutrients are assumed to be freely available in the fluid phase. Using the parameters found in Chapter 3, and from literature where available, the model predicts that the spatial heterogeneity in the substrate phase decreases through time.

In order to reproduce the increase in spatial heterogeneity in the substrate phase seen experimentally, we include, in Section 4.2, the dependence of cell birth and substrate deposition on a diffusible nutrient in solution. We use oxygen as a representative nutrient and use a linear cell uptake term. Numerical results demonstrate that, as time evolves, this causes the spatial heterogeneity in the substrate phase to increase. This is qualitatively similar to what is seen experimentally.

The model predicts that, although the stimulated loading regime results in greater quantities of substrate, they also result in a less uniform spatial distribution of the substrate phase. Conversely, there is less substrate under control conditions, but it is more uniformly distributed.

To produce a bone implant of good weight–bearing quality, we require a construct with a high but spatially uniform substrate phase volume fraction. In order to improve the quality of the substrate, strategies are needed to increase the quantity of substrate deposition in the centre of the construct. This could be achieved by improving the supply of nutrients to the centre of the construct by using nutrient perfusion techniques, as discussed in Section 1.1.2. Future work could combine perfusion techniques and hydrostatic pressure in order to increase the mass transport to the centre of the construct while also increasing the total quantity of substrate volume fraction.

In addition to the assumptions discussed in Chapter 3, a number of further modelling assumptions are made in this chapter.

In Section 4.2 we only consider one nutrient in solution and use oxygen as a representative nutrient. Substrate deposition and cell birth will actually depend on a multitude of factors, including glucose, build up of lactate, and growth factors. In addition we have not included the effects of hypoxia–induced apoptosis and assumed a linear dependence of cell birth and substrate deposition on oxygen concentration. Future work could involve the validation of the oxygen concentration by the use of probes in the centre of the scaffold. This would allow for the testing of different nutrient uptake terms in order to achieve an accurate oxygen distribution within the construct.

For simplicity, we assume spatially and temporally constant Dirichlet boundary conditions for the oxygen concentration. The culture medium is refreshed every weekday. Consequently, temporal–dependent boundary conditions may be more accurate. Due to the volume of culture medium in comparison to the size of the construct, this is unlikely to have much effect during the week due to the media being refreshed daily, but may have an effect at the weekend where the nutrient is not refreshed for several days. Further we have assumed that the oxygen concentration in the culture medium is not affected by changes in pressure and that it remains constant in time. However, recent work by our experimental collaborators has shown that there is a reversible change in the concentration of oxygen dissolved in the culture medium when pressure is increased [Reinwald *et al.*, 2014]. Future work could include a study of these changes.

In this chapter we assume that cell movement can be represented by diffusion and we have

investigated the spatial patterning induced by biochemical effects. It is known that cells move by a number of different mechanisms. In Chapter 5 we investigate the effects of cell and fluid advection which enables us to examine the magnitude of the fluid shear stresses exerted on the construct. In this chapter we considered the construct–only domain, and assumed that the construct shape and size remains fixed throughout the experimental timeframe. The multiphase model examined in the next chapters considers the whole well domain and allows for the construct to evolve in size and shape with time. This enables us to examine the effect of the surrounding fluid and bioreactor geometry on the evolution of the constituent phases over time.

Chapter 5

A multiphase model: model setup

In this chapter we present a multiphase model describing the experimental setup detailed in Chapter 2 to examine biomechanically–induced spatial patterning. We consider the whole well domain, as opposed to the construct only as in previous chapters, to investigate the effects of the surrounding fluid and bioreactor geometry on the growing tissue construct. Furthermore, our chosen multiphase formulation allows us to model a construct that can evolve in shape and size over time. Three separate constituent phases, cells, substrate and fluid, are considered, where the cell and fluid phases are modelled as viscous fluids and the substrate phase as a solid. In this chapter we first introduce the conservation of mass and momentum equations, along with the constitutive laws required to close the model. We then outline a method for approximating the solution of the system of equations numerically. Numerical solutions are presented in Chapters 6 and 7, where we investigate the spatial distribution at the initial timestep, and the spatio–temporal evolution though time respectively, of the quantities of interest.

In this chapter we wish to test the hypothesis that biomechanical effects alone can cause spatial patterning in the substrate phase qualitatively similar to that seen experimentally. This is achieved by the inclusion of an advective transport mechanism, which allows us to evaluate the magnitude of the fluid shear stresses imparted to the cell phase.

We proceed as in previous chapters, and model the tissue construct as a mixture of three phases,

representing cells, substrate and fluid. In the following we use the subscripts C, J and W for the cell, substrate and fluid phases respectively to identify which phase the given variable represents. We denote the volume fraction of phase k at the spatial point $\mathbf{x} \in \Omega$ (where Ω is the spatial domain) and time $t \geq 0$ by $\theta_k(\mathbf{x}, t) \in (0, 1)$ for $k = C, J, W$. The no voids condition implies that

$$\theta_C(\mathbf{x}, t) + \theta_J(\mathbf{x}, t) + \theta_W(\mathbf{x}, t) = 1. \tag{5.1}$$

In order to investigate the effects of biomechanically–induced spatial patterning in isolation, nutrients are assumed to be well perfused in the fluid phase. Using the previously introduced mass transfer functions (fully described in Chapter 3), conservation of mass for each phase yields

$$\frac{\partial \theta_C}{\partial t} + \nabla \cdot (\theta_C \mathbf{v}_C) = (k_b \theta_W \theta_J - k_d)\, \theta_C, \tag{5.2}$$

$$\frac{\partial \theta_J}{\partial t} = (k_p\,(\mathbf{x}, t, p_C(\mathbf{x}, t))\, \theta_W - k_{jd} \theta_J)\, \theta_C, \tag{5.3}$$

$$\frac{\partial \theta_W}{\partial t} + \nabla \cdot (\theta_W \mathbf{v}_W) = (-k_b \theta_W \theta_J - k_p\,(\mathbf{x}, t, p_C(\mathbf{x}, t))\, \theta_W + k_d + k_{jd} \theta_J)\, \theta_C, \tag{5.4}$$

where $\mathbf{v}_k = (u_k, v_k)^{\mathrm{T}}$ is the velocity of phase k for $k = C, J, W$, and p_C is the pressure in the cell phase. The term $\nabla \cdot (\theta_k \mathbf{v}_k)$ for $k = C, W$ represents the advection of phase k. We assume that the substrate phase is stationary and impose $\mathbf{v}_J = \mathbf{0}$ and so no advection effects appear in Equation (5.3). As described previously, $k_b > 0$, $k_d > 0$, $k_p > 0$ and $k_{jd} \geq 0$ are the rates of cell birth, cell death, substrate deposition and substrate degradation respectively. We assume that k_b, k_d and k_{jd} are spatially and temporally constant.

In Chapter 3 we demonstrated that the inclusion of the effects of the loading history is important to ensure the quantity of substrate deposition is not overestimated when the construct experiences extended periods of elevated pressure. The form of the substrate deposition rate developed in Section 3.2 was extended for use in the spatial model in Chapter 4. In these chapters we are interested in the qualitative effect the stimulated loading regime has on the constituent phase volume fractions in comparison to the control loading regime and, as time evolves, the consequent impact on the fluid shear stress magnitude (FSSM). To do this we use

an averaged version of the substrate deposition rate developed in previous chapters given by

$$k_p(t) = \begin{cases} k_1 & \text{if the construct is out of the bioreactor,} \\ k_4 & \text{if the construct is in the bioreactor,} \end{cases} \tag{5.5}$$

where $k_4 > k_1 > 0$ are constants measured in day^{-1}. Here k_1 is the rate of substrate deposition when the cells are at atmospheric pressure, as in previous chapters, and k_4 is an averaged rate of substrate deposition when the cells are in the bioreactor under cyclic loading. The advantages of using the substrate deposition rate given by Equation (5.5), as opposed to a form where cell memory effects are included as in Equation (4.6), are twofold. Firstly, the spatial distribution of the pressure at a previous time does not need to be stored as cell memory effects are not included, which decreases the number of degrees of freedom for the numerical scheme. Secondly, each oscillation of the applied cyclic loading does not need to be captured, and so a larger timestep can be used throughout the simulation, which increases the speed of numerical simulation. However, we note that the use of Equation (5.5) ignores the effects of cell pressure gradients within the construct, and that each k_4 is only valid for one particular loading strategy.

Summation of the conservation of mass equations over all phases, Equations (5.2) – (5.4), combined with the no voids condition, Equation (5.1), yields the conservation of total mass equation

$$\nabla \cdot (\theta_C \mathbf{v}_C + \theta_W \mathbf{v}_W) = 0. \tag{5.6}$$

Consequently, the total mixture is incompressible.

We are required to determine $\mathbf{v}_C$ and $\mathbf{v}_W$, which we do by considering the conservation of momentum for the cell and fluid phases. Ignoring inertial terms, as is usual in modelling biological tissue growth due to the small Reynolds number (slow flow) [Truskey, 2009], and gravitational forces, the conservation of momentum for the cell and fluid phases [Astanin and Preziosi, 2008, Lemon *et al.*, 2006] gives

$$\nabla \cdot (\theta_k \boldsymbol{\sigma}_k) + \sum_{l \neq k} \mathbf{f}_{kl} = \mathbf{0}, \quad \text{for } k = C, W. \tag{5.7}$$

Here $\boldsymbol{\sigma}_k$ is the stress tensor for phase k, and $\mathbf{f}_{kl}$ is the interphase force exerted on phase k by

phase l. As $\mathbf{v}_J = \mathbf{0}$ is imposed, we do not need to consider conservation of momentum for the substrate phase. The chosen form of the stress tensor of phase k, $\boldsymbol{\sigma}_k$, reflects the choice of material assumptions for phase k.

We assume that the cell and fluid phases are Newtonian viscous fluids [Lemon *et al.*, 2006, O'Dea *et al.*, 2008, Osborne *et al.*, 2010, O'Dea *et al.*, 2010], with the stress tensor given by [Acheson, 1990, Batchelor, 1973]

$$\boldsymbol{\sigma}_k = -p_k\boldsymbol{\mathcal{I}} + \mu_k\Big(\nabla\mathbf{v}_k + \big(\nabla\mathbf{v}_k\big)^{\mathrm{T}} - \frac{2}{3}(\nabla\cdot\mathbf{v}_k)\boldsymbol{\mathcal{I}}\Big), \quad \text{for } k = C, W. \tag{5.8}$$

Here $\mu_k > 0$, which we assume to be a constant, and p_k are the macroscale viscosity and intraphase pressure respectively of phase k and $\boldsymbol{\mathcal{I}}$ is the rank–2 identity tensor.

The interphase forces, $\mathbf{f}_{kl}$, are given as [Lemon *et al.*, 2006, Osborne, 2009, O'Dea *et al.*, 2010, Osborne *et al.*, 2010]:

$$\mathbf{f}_{kl} = p_{kl}\theta_l\nabla\theta_k - p_{lk}\theta_k\nabla\theta_l + \beta_{kl}\theta_k\theta_l\big(\mathbf{v}_l - \mathbf{v}_k\big), \quad \text{for } k \neq l, \quad k = C, W, \quad l = C, J, W, \tag{5.9}$$

where p_{kl} is an interphase pressure and describes the pressure exerted on phase k by phase l. The first two terms on the right hand side represent the interfacial force exerted by phase l on phase k and the reactive force respectively. The final term on the right hand side represents Darcy–type viscous drag, where $\beta_{kl} \geq 0$ is the coefficient describing the drag exerted on phase k by phase l for $k \neq l$.

5.1 Intraphase and interphase forces

So far we have 13 equations but 20 unknown variables (θ_k for $k = C, J, W$; k_p, $\mathbf{v}_k$, p_k and $\boldsymbol{\sigma}_k$ for $k = C, W$; p_{kl} and $\mathbf{f}_{kl}$ for $k \neq l$, $k = C, W$, $l = C, J, W$). In order to close the model we need to specify further constitutive assumptions, which we do as follows. We choose the forms for the intraphase and interphase pressures in accordance with Lemon *et al.* [2006], Osborne [2009],

O'Dea *et al.* [2010] and Osborne *et al.* [2010], and these are given by

$$p_W = p, \qquad p_C = p + \Sigma_C(\theta_C, \theta_W) + \theta_J \psi_{CJ}(\theta_C, \theta_W), \tag{5.10}$$

$$p_{WC} = p_{WJ} = p, \qquad p_{CJ} = p + \psi_{CJ}(\theta_C, \theta_W), \tag{5.11}$$

where $p = p(\mathbf{x}, t)$ is a "common" pressure, and $p_{kl} = p_{lk}$ for $k \neq l$. Here the term $\Sigma_C(\theta_C, \theta_W)$ is an additional pressure to model cell–cell interactions and the term $\psi_{CJ}(\theta_C, \theta_W)$ models the additional pressures produced by the interaction between the cell and substrate phases. It is assumed that no additional pressures are generated in the fluid phase, between the fluid and the cell phases, or between the fluid and the substrate phases.

Following Lemon *et al.* [2006], Byrne *et al.* [2003] and Breward *et al.* [2002] we set

$$\Sigma_C(\theta_C, \theta_W) = \theta_C \left(-\nu + \delta_a \left(\frac{\theta_C}{\theta_W} \right)^m \right), \tag{5.12}$$

with $\nu, \delta_a, m \geq 0$, where ν is the cell aggregation parameter, δ_a is the intraphase repulsion parameter and m is a repulsion scaling parameter. In a similar manner, we set

$$\psi_{CJ}(\theta_C, \theta_W) = -\chi + \delta_b \left(\frac{\theta_C}{\theta_W} \right)^m, \tag{5.13}$$

with $\chi, \delta_b \geq 0$, where χ is the substrate affinity parameter, and δ_b is the interphase repulsion parameter. The same scaling factor, m, is used as in Equation (5.12) [Lemon *et al.*, 2006, Osborne *et al.*, 2010]. The functions Σ_C and ψ_{CJ} are plotted in Figure 5.1 for varying ν and χ in order to illustrate their form for fixed $\delta_a = \delta_b = 50$ Pa with $\theta_J = 0.11\theta_C/0.3$[a]. As ν increases for fixed δ_a the graph of Σ_C, Figure 5.1(a), crosses the θ_C–axis at a higher cell volume fraction. Similarly, as χ increases for fixed δ_b the graph of ψ_{CJ}, Figure 5.1(b), intersects the θ_C–axis at a higher cell volume fraction and crosses the ψ_{CJ}–axis at a lower value.

We investigate the effect of the terms Σ_C and ψ_{CJ} on the initial cell and fluid phase velocity and pressure solutions in Section 6.1. We demonstrate that these two terms, representing additional pressures due to cell–cell and cell–substrate interactions respectively, drive cell and fluid phase flows along gradients of the constituent phase volume fractions.

[a]This ratio of the volume fractions of the substrate phase to the cell phase is motivated by the experimental data for the initial volumes of the collagen and cells, as given in Table 2.2.

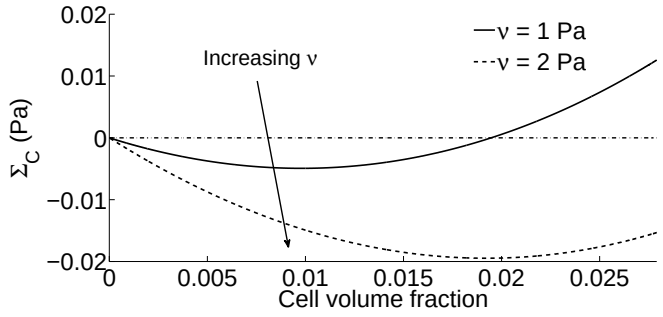

(a)

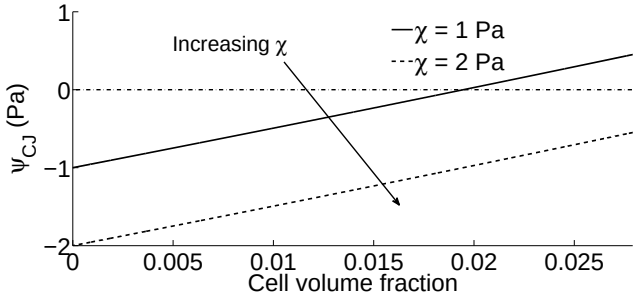

(b)

Figure 5.1: The additional pressures produced by (a) cell–cell interactions, Σ_C, given by Equation (5.12), and (b) cell–substrate interactions, ψ_{CJ}, given by Equation (5.13). Here $\delta_a = \delta_b = 50$ Pa and $\theta_J = 0.11\theta_C/0.3$, while ν in (a) and χ in (b) vary as shown in the legends. The horizontal dash–dotted lines show where the additional pressures are zero.

With the above constitutive laws prescribed, the model now consists of an equal number of equations and unknowns. Substitution of the constitutive assumptions into the conservation of mass and conservation of momentum equations reveals that there are six variables which need solving for; $\mathbf{v}_C, \mathbf{v}_W, p, \theta_C, \theta_J$ and θ_W. Once the solutions to these variables are known, the other quantities of interest, for example the pressure in the cell phase, may be evaluated. We now proceed to defining the domain and appropriate boundary and initial conditions.

5.2 Domain

To gain an understanding of the physical processes involved in the system we examine a simplified two–dimensional problem, as in Chapter 4. Here we consider a 2D cross section of the full cylindrically–shaped well, given by

$$\Omega = \{(x, z) \in \mathbb{R}^2 : -R \leq x \leq R, 0 \leq z \leq H\}, \tag{5.14}$$

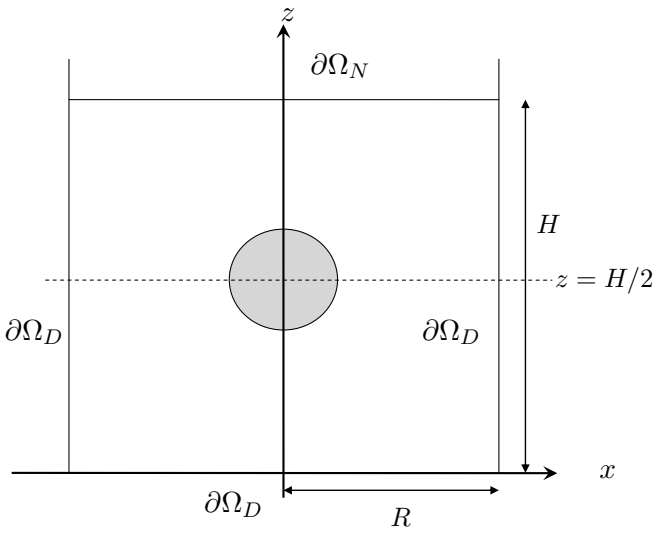

Figure 5.2: Illustration of the domain, Ω. The shaded area indicates the position of the construct for the circular–shaped initial conditions, as given by Equation (5.20). Although a circular–shaped construct is illustrated in this figure, the initial conditions can be chosen to describe any shaped construct in any position in the well as required. The boundary of the domain, Ω, is denoted by $\partial\Omega = \partial\Omega_N \cup \partial\Omega_D$, where $\partial\Omega_N$ and $\partial\Omega_D$ are given by Equations (5.15) and (5.16) respectively. The subscripts D and N are used to denote the boundaries where Dirichlet and Neumann boundary conditions respectively are applied.

where H is the height of the culture medium and R is the radius of the well as indicated in Figure 5.2. We denote the boundary of the domain by $\partial\Omega = \partial\Omega_N \cup \partial\Omega_D$, where

$$\partial\Omega_N = \{(x, z) \in \mathbb{R}^2 : -R \leq x \leq R, z = H\}, \tag{5.15}$$

and

$$\partial\Omega_D = \{(x, z) \in \mathbb{R}^2 : -R \leq x \leq R, z = 0\} \cup \{(x, z) \in \mathbb{R}^2 : x = \pm R, 0 < z < H\}, \tag{5.16}$$

as indicated in Figure 5.2. The subscripts D and N are used to denote the boundaries where Dirichlet and Neumann boundary conditions respectively are applied, the latter boundary describing the surface of the liquid to which the pressure exerted by the bioreactor is applied, as detailed in Chapter 2.

5.3 Boundary conditions

On the walls and the base of the well we assume no–penetration and no–slip conditions, so that

$$\mathbf{v}_k = \mathbf{0}, \qquad \text{on } \mathbf{x} \in \partial\Omega_D, \quad \text{for } k = C, W. \tag{5.17}$$

Stress is applied in the normal direction to the surface of the culture medium at $z = H$. Assuming that the applied force can be partitioned between the phases in proportion to volume fraction, we have

$$\theta_k \boldsymbol{\sigma}_k \mathbf{n} = -\theta_k p_{\text{app}}(t)\mathbf{n}, \qquad \text{on } \mathbf{x} \in \partial\Omega_N, \quad \text{for } k = C, W, \tag{5.18}$$

where $\mathbf{n}$ is the outward pointing unit normal to the boundary $\partial\Omega$ and $p_{\text{app}}(t)$ is the magnitude of the applied force in the direction of the normal to the surface of the culture medium and is determined by the applied loading strategy.

5.4 Initial conditions

Physically we expect a sharp jump in the initial cell and substrate volume fractions at the edge of the construct where we move from $\theta_C = \theta_J = 0$ outside the construct to $\theta_C, \theta_J \neq 0$ inside the construct. Rather than having a step change in the initial conditions for these variables, we use spatially continuous initial conditions which allow rapid changes in these variables to be applied, without the mathematical and numerical issues arising from discontinuities in the solutions. This is achieved by using functions of the hyperbolic tangent to describe initial cell and substrate volume fractions.

As in Section 4.1.1, we require the initial conditions to satisfy

$$\int_\Omega \theta_C(\mathbf{x}, 0)\, \mathrm{d}V = C_0, \qquad \int_\Omega \theta_J(\mathbf{x}, 0)\, \mathrm{d}V = J_0, \tag{5.19}$$

where C_0 and J_0 are the volume of cells and collagen respectively in the construct at the initial time with $\theta_W(\mathbf{x}, 0) = 1 - \theta_C(\mathbf{x}, 0) - \theta_J(\mathbf{x}, 0)$ by Equation (5.1).

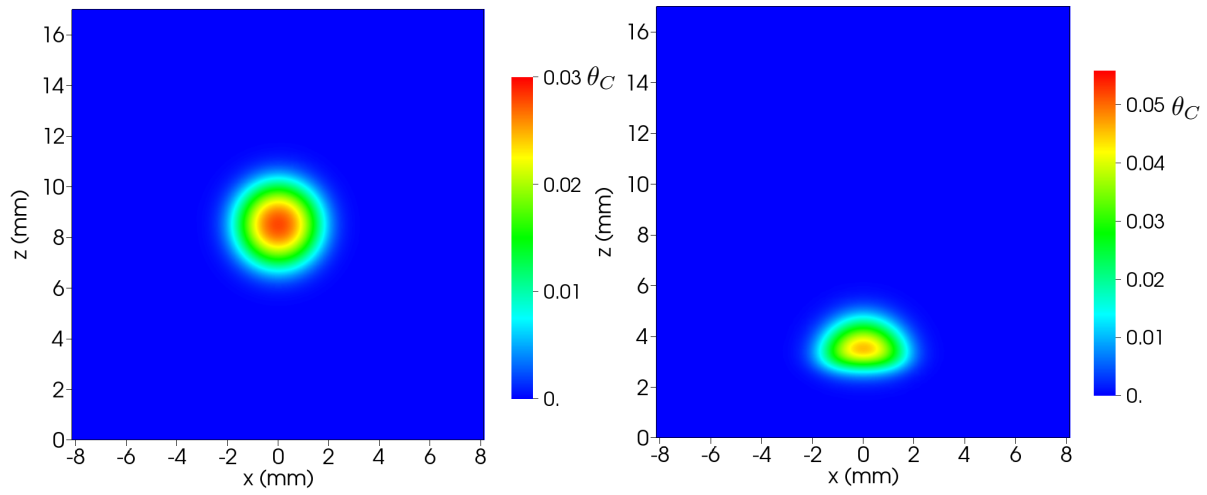

(a) Circular–shaped construct (b) Semicircular–shaped construct

Figure 5.3: Illustration of the initial cell phase volume fraction conditions describing (a) the circular–shaped construct given by Equation (5.20) and (b) the semicircular–shaped construct given by Equation (5.21).

In Chapter 6 two sets of initial conditions are considered, which we now detail. These describe a circular–shaped (Section 5.4.1) and a semicircular–shaped (Section 5.4.2) construct, as illustrated Figure 5.3. Further sets of initial conditions used in Section 7.2 are detailed in Appendix B.

5.4.1 Circular–shaped construct

We begin by considering a circular–shaped construct positioned centrally within the bioreactor at the point $(x, z) = (0, H/2)$ with radius $r_c > 0$. This setup is not practised experimentally. However, for r_c much smaller than H and R, the construct is small in comparison to the size of the well and far away from the walls, and the effect of the geometry of the well is weak. As the initial conditions are radially symmetric in the region surrounding the construct, it enables us, in Section 6.1, to characterise the effect of parameter variations on the initial velocity–pressure distribution by examining the dependent variables from the 2D numerical simulations along one radial line. For a circular–shaped construct we use initial conditions for the cell and substrate phases given by

$$\theta_k(x, z, t = 0) = A_k^s \left(1 - \tanh\left(B_k \left(x^2 + \left(z - \frac{H}{2}\right)^2 - r_c^2\right)\right)\right), \quad \text{for } k = C, J. \tag{5.20}$$

This choice gives a circular–shaped construct, as illustrated in Figure 5.3(a), with the cell and substrate volume fractions approaching zero as the distance from the construct increases. The size of the parameter B_k determines the gradient of the volume fraction for phase k at the periphery of the construct region. The higher this is, the sharper the edge of the construct.

5.4.2 Semicircular–shaped construct

In addition to a circular–shaped construct, we also consider initial conditions describing a semicircular–shaped construct, with base at $z = s_h$, where $s_h \geq 0$ is the height of the base of the transwell insert above the base of the well, and radius r_c. For this construct the initial conditions for the cell and substrate phases are given by

$$\theta_k(x, z, 0) = A_k^h \left(1 - \tanh(B_k(x^2 + (z - s_h)^2 - r_c^2))\right) (\tanh(C_k(z - s_h)) + 1), \quad \text{for } k = C, J, \tag{5.21}$$

and this describes a construct similar in shape to that used experimentally, as illustrated in Figure 5.3(b). As for the circular–shaped construct, the size of the parameter B_k and C_k determine the gradient of the k^{th} volume fraction at the periphery of the construct, and we use the same value of B_k as in Equation (5.20) for simplicity.

5.5 A measure of shear stress

Osteocytes respond to fluid shear stresses by increasing the quantity of mineralisation through communication with osteoblasts (see Section 1.1.3 on the bone cell response to fluid shear stresses for further details). We are interested in calculating the size of the shear stresses exerted by the fluid phase on the cells in the developing construct so as to understand if this can explain the experimental results. Previous work [Osborne *et al.*, 2010, Osborne and Whiteley, 2010, Acheson, 1990, McCoy and O'Brien, 2010] has evaluated the fluid shear stress magnitude (FSSM) in two spatial dimensions (x, z) by using

$$\mu_W \left(\left(\frac{\partial u_W}{\partial z} \right)^2 + \left(\frac{\partial v_W}{\partial x} \right)^2 \right)^{\frac{1}{2}}, \tag{5.22}$$

where u_W and v_W are the fluid phase velocities in the x and z–coordinate directions respectively. This gives the magnitude of the off-diagonal entries of the fluid stress tensor (given by Equation (5.8) for $k = W$). However, Equation (5.22) is not invariant under coordinate rotation and so is unsuitable for our purposes; the majority of studies using the measure given by Equation (5.22) to date have investigated the effects of fluid flow aligned with the coordinate axes. In Chapter 6 we see that flow in our setup occurs in all directions.

In order to gain an understanding of the fluid shear stress magnitude (FSSM), we evaluate the eigenvalues, λ, of the deviatoric part of the stress tensor for the fluid phase. This is defined as

$$\|\tilde{\boldsymbol{\sigma}}_W - \lambda \boldsymbol{\mathcal{I}}\| = 0, \tag{5.23}$$

where $\|\cdot\|$ denotes the determinant and $\boldsymbol{\sigma}_W = -p\boldsymbol{\mathcal{I}} + \tilde{\boldsymbol{\sigma}}_W$. Equation (5.23) is invariant under coordinate rotation and the size of the maximum absolute eigenvalue, $\max(|\lambda|)$, gives a measure of the magnitude of the shear stress generated by the fluid phase acting in the direction of the eigenvectors of the fluid phase stress tensor.

5.6 Nondimensionalisation

Denoting dimensionless variables by a caret, we nondimensionalise as follows:

$$\begin{aligned}
t &= \frac{\hat{t}}{k_b}, & \mathbf{x} &= H\hat{\mathbf{x}}, & p(\mathbf{x},t) &= p_0\hat{p}(\hat{\mathbf{x}},\hat{t}) + p_{\text{atm}},\\
\mathbf{v}_k &= k_b H\hat{\mathbf{v}}_k, & \mathbf{f}_{kl} &= \frac{p_0}{H}\hat{\mathbf{f}}_{kl}, & \boldsymbol{\sigma}_k &= p_0\hat{\boldsymbol{\sigma}}_k,\\
p_k &= p_0\hat{p}_k + p_{\text{atm}}, & p_{kl} &= p_0\hat{p}_{kl} + p_{\text{atm}}, & \psi_{CJ} &= p_0\hat{\psi}_{CJ},\\
\Sigma_C &= p_0\hat{\Sigma}_C, & \lambda &= p_0\hat{\lambda}, &&
\end{aligned}$$

where $p_0 = 1$ kPa for consistency with previous chapters. This yields the dimensionless versions of Equations (5.2) and (5.3) given by

$$\frac{\partial \theta_C}{\partial \hat{t}} + \hat{\nabla} \cdot \left(\theta_C \hat{\mathbf{v}}_C\right) = \left(\theta_W \theta_J - K_d\right) \theta_C, \tag{5.24}$$

$$\frac{\partial \theta_J}{\partial \hat{t}} = \left(K_p\left(\hat{\mathbf{x}}, \hat{t}, \hat{p}_C(\hat{\mathbf{x}}, \hat{t})\right) \theta_W - K_{jd} \theta_J\right) \theta_C, \tag{5.25}$$

where $K_d = \dfrac{k_d}{k_b}$, $K_p\left(\hat{t}\right) = \dfrac{k_p(t)}{k_b}$ and $K_{jd} = \dfrac{k_{jd}}{k_b}$. Nondimensionalisation of the substrate deposition rate given by Equation (5.5) yields

$$K_p\left(\hat{t}\right) = \begin{cases} K_1 & \text{if the construct is out of the bioreactor,} \\ K_4 & \text{if the construct is in the bioreactor,} \end{cases} \tag{5.26}$$

where $K_1 = \dfrac{k_1}{k_b}$ and $K_4 = \dfrac{k_4}{k_b}$. By Equation (5.6), we have

$$\hat{\nabla} \cdot \left(\theta_C \hat{\mathbf{v}}_C + \theta_W \hat{\mathbf{v}}_W\right) = 0. \tag{5.27}$$

In addition, the dimensionless versions of Equations (5.7) and (5.8), are given by

$$\hat{\nabla} \cdot \left(\theta_k \hat{\boldsymbol{\sigma}}_k\right) + \sum_{l \neq k} \hat{\mathbf{f}}_{kl} = \mathbf{0}, \quad \text{for } k = C, W, \tag{5.28}$$

with $\hat{\mathbf{v}}_J = \mathbf{0}$ and

$$\hat{\boldsymbol{\sigma}}_k = -\left(\hat{p}_k + \hat{p}_{\text{atm}}\right) \boldsymbol{\mathcal{I}} + \hat{\mu}_k \Big(\hat{\nabla} \hat{\mathbf{v}}_k + \left(\hat{\nabla} \hat{\mathbf{v}}_k\right)^{\mathrm{T}} - \frac{2}{3} (\hat{\nabla} \cdot \hat{\mathbf{v}}_k) \boldsymbol{\mathcal{I}} \Big), \quad \text{for } k = C, W, \tag{5.29}$$

where $\hat{\mu}_k = \dfrac{k_b \mu_k}{p_0}$ and $\hat{p}_{\text{atm}} = \dfrac{p_{\text{atm}}}{p_0}$. The dimensionless versions of Equations (5.9), (5.10) and (5.11) are given by

$$\hat{\mathbf{f}}_{kl} = \hat{p}_{\text{atm}} \Big(\theta_l \hat{\nabla} \theta_k - \theta_k \hat{\nabla} \theta_l \Big) + \hat{p}_{kl} \theta_l \hat{\nabla} \theta_k - \hat{p}_{lk} \theta_k \hat{\nabla} \theta_l + \hat{\beta}_{kl} \theta_k \theta_l \big(\hat{\mathbf{v}}_l - \hat{\mathbf{v}}_k \big), \quad \text{for } k \neq l, \quad k = C, W, \quad l = C, J, W, \tag{5.30}$$

where $\hat{\beta}_{kl} = \dfrac{k_b H^2 \beta_{kl}}{p_0}$ along with

$$\hat{p}_W = \hat{p}(\hat{\mathbf{x}}, \hat{t}), \qquad \hat{p}_C = \hat{p}(\hat{\mathbf{x}}, \hat{t}) + \hat{\Sigma}_C(\theta_C, \theta_W) + \theta_J \hat{\psi}_{CJ}(\theta_C, \theta_W), \tag{5.31}$$

$$\hat{p}_{WJ} = \hat{p}_{WC} = \hat{p}(\hat{\mathbf{x}}, \hat{t}), \quad \text{and} \qquad \hat{p}_{CJ} = \hat{p}(\hat{\mathbf{x}}, \hat{t}) + \hat{\psi}_{CJ}(\theta_C, \theta_W). \tag{5.32}$$

In addition, by Equations (5.12) and (5.13), we have

$$\hat{\Sigma}_C(\theta_C, \theta_W) = \theta_C \left(-\hat{\nu} + \hat{\delta}_a \left(\frac{\theta_C}{\theta_W} \right)^m \right), \tag{5.33}$$

$$\hat{\psi}_{CJ}(\theta_C, \theta_W) = -\hat{\chi} + \hat{\delta}_b \left(\frac{\theta_C}{\theta_W} \right)^m, \tag{5.34}$$

where the parameters $\hat{\nu} = \dfrac{\nu}{p_0}$, $\hat{\chi} = \dfrac{\chi}{p_0}$, $\hat{\delta}_a = \dfrac{\delta_a}{p_0}$ and $\hat{\delta}_b = \dfrac{\delta_b}{p_0}$ are dimensionless. The domain, in dimensionless variables, is given by

$$\hat{\Omega} = \{(\hat{x}, \hat{z}) \in \mathbb{R}^2 : -\hat{R} \leq \hat{x} \leq \hat{R}, 0 \leq \hat{z} \leq 1\}, \tag{5.35}$$

where $\hat{R} = \dfrac{R}{H}$, with the boundary $\partial\hat{\Omega} = \partial\hat{\Omega}_N \cup \hat{\Omega}_D$, where

$$\partial\hat{\Omega}_N = \{(\hat{x}, \hat{z}) \in \mathbb{R}^2 : -\hat{R} \leq \hat{x} \leq \hat{R}, \hat{z} = 1\}, \tag{5.36}$$

$$\partial\hat{\Omega}_D = \{(\hat{x}, \hat{z}) \in \mathbb{R}^2 : -\hat{R} \leq \hat{x} \leq \hat{R}, \hat{z} = 0\} \cup \{(\hat{x}, \hat{z}) \in \mathbb{R}^2 : \hat{x} = \pm\hat{R}, 0 < \hat{z} < 1\}. \tag{5.37}$$

The dimensionless versions of the boundary conditions given by Equations (5.17) and (5.18) become

$$\hat{\mathbf{v}}_k = \mathbf{0}, \qquad \text{on } \hat{\mathbf{x}} \in \partial\hat{\Omega}_D, \quad \text{for } k = C, W, \tag{5.38}$$

$$\theta_k \hat{\boldsymbol{\sigma}}_k \cdot \mathbf{n} = -\theta_k \left(\hat{p}_{\text{app}} + \hat{p}_{\text{atm}} \right) \mathbf{n}, \qquad \text{on } \hat{\mathbf{x}} \in \partial\hat{\Omega}_N, \quad \text{for } k = C, W, \tag{5.39}$$

where $\hat{p}_{\text{app}} = \dfrac{p_{\text{app}} - p_{\text{atm}}}{p_0}$. Nondimensionalisation of the initial conditions describing the circular–shaped and semicircular–shaped constructs, given by Equations (5.20) and (5.21) respectively, gives

$$\theta_k(\hat{x}, \hat{z}, 0) = A_k^s \left(1 - \tanh\left(\hat{B}_k \left(\hat{x}^2 + (\hat{z} - \hat{s}_h)^2 - \hat{r}_c^2 \right) \right) \right), \tag{5.40}$$

and

$$\theta_k(\hat{x},\hat{z},0) = A_k^h\left(1-\tanh\left(\hat{B}_k\left(\hat{x}^2+(\hat{z}-\hat{s}_h)^2-\hat{r}_c^2\right)\right)\right)\left(\tanh(\hat{C}_k(\hat{z}-\hat{s}_h))+1\right), \tag{5.41}$$

where $\hat{B}_k = B_k H^2$ and $\hat{C}_k = C_k H$ for $k = C, J$, $\hat{r}_c = \dfrac{r_c}{H}$ and $\hat{s}_h = \dfrac{s_h}{H}$. By Equation (5.19), Equations (5.40) and (5.41) must satisfy

$$H^2\int_{\hat{\Omega}}\theta_C(\hat{\mathbf{x}},0)\,\mathrm{d}\hat{V} = C_0, \qquad H^2\int_{\hat{\Omega}}\theta_J(\hat{\mathbf{x}},0)\,\mathrm{d}\hat{V} = J_0. \tag{5.42}$$

In summary, the dimensionless system of equations is given by Equations (5.1), (5.24), (5.25), (5.27) and (5.28), along with Equations (5.26), (5.29) – (5.34), on the domain given by Equation (5.35) with boundary given by Equations (5.36) and (5.37) for the unknowns $\hat{\mathbf{v}}_C$, $\hat{\mathbf{v}}_W$, $\hat{p}$, θ_C, θ_J and θ_W with $\hat{\mathbf{v}}_J = \mathbf{0}$ imposed. Boundary conditions are given by Equations (5.38) and (5.39), and initial conditions are given by either Equation (5.40) or Equation (5.41) with parameters chosen such that Equation (5.42) is satisfied.

We now discuss the choice of parameters for the system of equations before describing the method used to obtain a numerical solution.

5.6.1 Parameters

Dimensional spatial parameters are taken from the experimental setup, as described in Chapter 2, and given by Tables 2.1 and Equation (2.3). We are interested in a qualitative description of the experimental setup. In the following chapters, we use smoothed initial conditions and set $\hat{B}_k = 90$ and $\hat{C}_k = 30$ for $k = C, J$, with the parameters V_0, C_0 and J_0 taken from Table 2.2 so as to represent the experimental data presented in Chapter 2. This yields $\theta_J(x,z,0) = \dfrac{A_J^s}{A_C^s}\theta_C(x,z,0)$.

For the volume fraction system, we use the parameters K_1, K_{jd} and K_d as detailed in Chapter 3. The values of these and their origins are given in Table 3.5. In order to calculate the value of K_4 we perform a least–squares fit between the numerical and experimental results in the spatially independent case for the stimulated loading regime, in a similar manner to the parameter

fitting performed in Chapter 3. This gives a dimensionless value of $K_4 = 43.8$. We note that this parameter is only valid for the stimulated loading regime currently used: intermittent cyclic loading of one hour per weekday with a frequency of 1 Hz and amplitude of 140 kPa.

We assume that the viscous drag coefficients are the same between all the different phases, *i.e.* that $\beta_{kl} = \beta$ for all $k \neq l$, $k = C, W$, $l = C, J, W$. We set $\beta = 4.5 \times 10^7$ kg s^{-1} m^{-3} [Lubkin and Jackson, 2002, O'Dea *et al.*, 2008] and this yields a dimensionless value of $\hat{\beta} = 1.505 \times 10^{-4}$. We set the dimensional viscosity of the cell phase to be equivalent to the viscosity of human MSCs at 37 °C (temperature of experiments), so that $\mu_C = 5290$ Pa s [Tan *et al.*, 2008]. Assuming that the viscosity of the culture medium is the same as that of water would yield a dimensional value of $\mu_W = 6.914 \times 10^{-4}$ Pa s [Kestin *et al.*, 1978]. However, using this value results in a very large disparity in scales between cell and fluid macroscale viscosities. In the following we examine the qualitative behaviour exhibited by the model. In order to aid numerical simulation while considering a higher viscosity in the cell phase in comparison to the fluid phase, we increase the viscosity of the fluid phase and use the dimensionless parameters given by

$$\hat{\mu}_C = 6.123 \times 10^{-5}, \qquad \hat{\mu}_W = 8.002 \times 10^{-8}.$$

Obtaining measurements for the parameters ν, χ, δ_a and δ_b experimentally is difficult. Furthermore, we are interested in a qualitative description of the behaviour of the mathematical model. Following Osborne *et al.* [2010] we set the intraphase and interphase repulsion parameters to be equal, at a value of $\hat{\delta}_a = \hat{\delta}_b = 0.05$, which is equivalent to a dimensional value of 50 Pa. In Section 6.1 we investigate the effect of varying ν and χ, the cell aggregation and the substrate affinity parameters, and demonstrate qualitative changes in behaviour.

We now proceed with the details of the numerical implementation. As in previous chapters, we solve the dimensionless system using numerical methods but present solutions in dimensional variables to allow us to understand the size of the quantities of interest in comparison to experimentally relevant values. We now discuss the numerical methods employed in Chapters 6 and 7 to achieve a numerical solution of the system of equations presented above.

5.7 Numerical scheme

We decouple the system into two in a similar manner to that described by Osborne and Whiteley [2010] and Hubbard and Byrne [2013]: a velocity–pressure system and a volume fraction system. The former system is given by Equations (5.1), (5.27) and (5.28) along with Equations (5.29) – (5.34) for known $\theta_C, \theta_J, \theta_W$, and boundary conditions given by Equations (5.38) and (5.39). The latter system is given by Equations (5.1), (5.24) and (5.25) along with Equation (5.26) and initial conditions, for known $\hat{\mathbf{v}}_C, \hat{\mathbf{v}}_W$ and $\hat{p}$.

In order to achieve a numerical solution, the time derivative in Equations (5.24) and (5.25) is discretised by Euler methods. We proceed through time and solve the discretised system using FEMs at each timestep in the following manner. Initially, and then at each timestep, the velocity–pressure system is solved (as described in Section 5.7.1) using θ_k for $k = C, J, W$ from the previous timestep, to give updated values for $\hat{\mathbf{v}}_C, \hat{\mathbf{v}}_W$ and $\hat{p}$. The volume fraction system is then solved (as described in Section 5.7.2) in order to give the updated values for the constituent phase volume fractions. Figure 5.4 shows a flowchart to illustrate how this is performed.

5.7.1 Velocity–pressure system

The velocity–pressure system is a generalised Stokes flow problem, and is solved in a similar manner to that outlined in Osborne and Whiteley [2010]. The Taylor–Hood approximation on each element is used, where a quadratic approximation is made to the velocity and a linear approximation to the pressure on each element of the mesh [Elman *et al.*, 2005].

5.7.2 Volume fraction system

In contrast to Osborne and Whiteley [2010] and Hubbard and Byrne [2013], discontinuous Galerkin finite elements with quadratic basis functions are used to solve the discretised volume fraction system to give updated values for the volume fractions of the constituent phases. At each timestep the discretised conservation of mass equation for the cell phase was first solved to give the numerical solution to the cell phase volume fraction at the new time point. The discretised conservation of mass equation for the substrate phase is an ODE at each spatial

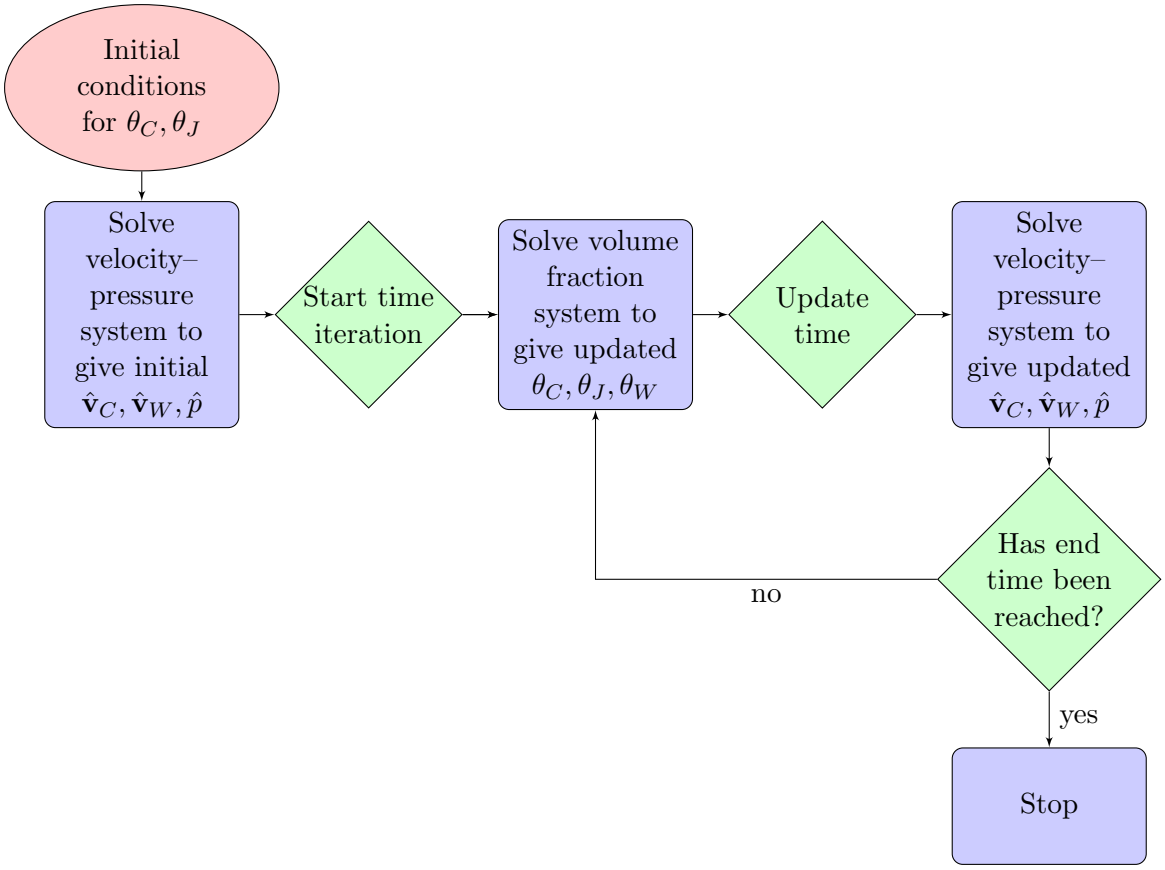

Figure 5.4: Flowchart to illustrate the algorithm used for numerically solving the system of equations. The system of equations is decoupled into two. The velocity–pressure system, given by Equations (5.1), (5.27) and (5.28) along with Equations (5.29) – (5.34) and boundary conditions given by Equations (5.38) and (5.39), is solved using continuous Galerkin FEMs as described in Section 5.7.1. The volume fraction system, given by Equations (5.1), (5.24) and (5.25) along with Equation (5.26) and initial conditions, is solved using discontinuous Galerkin FEMs as described in Section 5.7.2.

point, and so this was then solved at each mesh point to give the new substrate phase volume fraction. The computational code for the volume fraction system was extended from the 30$^{\text{th}}$ deal.II tutorial [Step-30, Bangerth *et al.*, 2013], which uses the discontinuous Galerkin finite element method to solve a linear transport equation. This method was chosen as it stabilises the hyperbolic conservation of mass equations without the need to interpolate the solution at each timestep.

5.7.3 Numerical implementation

Code was written in deal.II [Bangerth *et al.*, 2013, 2007] and Appendix A gives further details of the computational methods used and includes a discussion on the reasons for using deal.II.

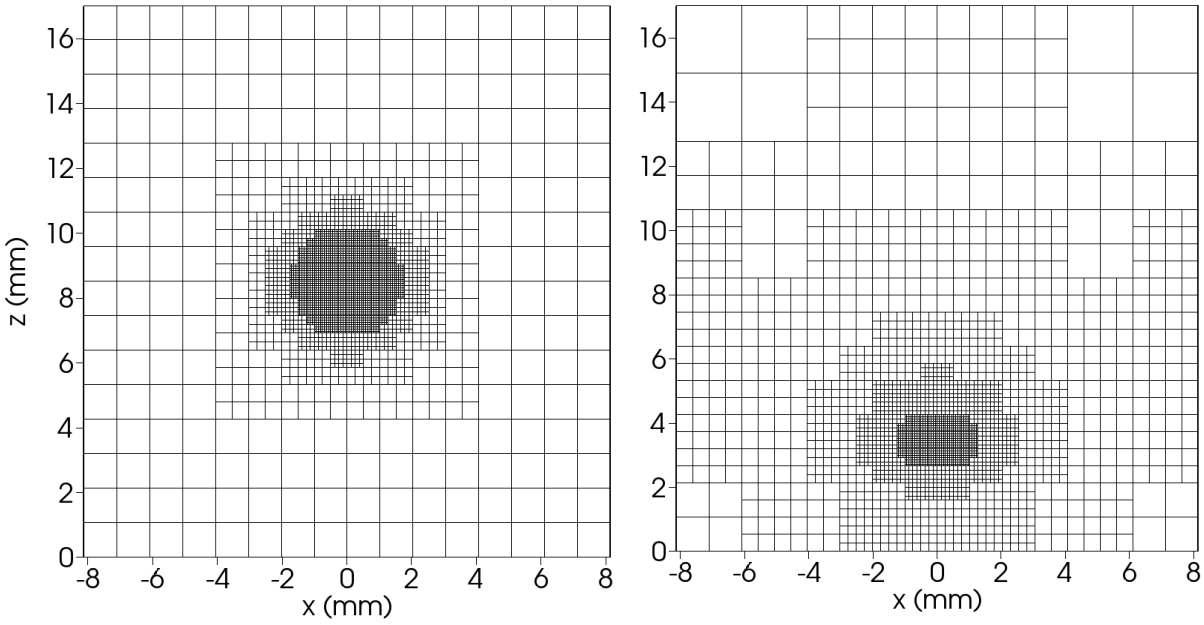

(a) Circular–shaped initial conditions

(b) Semicircular–shaped initial conditions

Figure 5.5: The computational meshes used at the initial time point for the initial conditions describing the (a) circular–shaped and (b) semicircular–shaped constructs, given in Equation (5.40) and (5.41) respectively. The mesh is first refined uniformly, then refined in the region of the construct, and finally refined according to the magnitude of the gradient of the cell flux. The mesh is further refined and coarsened through time every one dimensional minute.

The computational implementation of the algorithm used to solve the system of equations was verified by altering the domain and the boundary conditions to describe the problem presented in Osborne *et al.* [2010], and comparing numerical results.

Examination of the velocity–pressure system equations shows that pressure is defined up to a constant, determined by the applied traction boundary conditions given by Equation (5.39). Consequently, we are able to find the solution for any given applied pressure by solving the governing equations and boundary conditions for zero applied pressure, and adding the constant to the pressure solution.

The values of $\hat{\mathbf{v}}_C$ and $\hat{\mathbf{v}}_W$ in the FEM solution are undefined when $\theta_C = 0$ or $\theta_W = 0$ and the linear system describing the discretised problem is singular [Osborne, 2009]. For the initial conditions given by Equation (5.40) we have $\theta_W(\hat{\mathbf{x}}, 0) > 0$ for $\hat{\mathbf{x}} \in \hat{\Omega}$. However, the cell volume fraction is very small far from the construct and this can cause numerical issues. To avoid the linear system becoming singular or poorly conditioned we increase the given cell volume fraction by 10^{-6}, which is small enough not to considerably affect the solutions.

In order to achieve an accurate solution in the region of the construct where solutions vary rapidly, with only a modest increase in the total number of degrees of freedom, adaptive refinement of the computational mesh is used. One of the advantages of writing code in deal.II is the ability to use adaptive meshing and hanging nodes for continuous, as well as discontinuous, Galerkin test functions [Bangerth *et al.*, 2007]. The mesh is first refined uniformly, then in the region of the construct and finally according to the magnitude of the gradient of the cell flux. The numerical solution is sought at each successive refinement and interpolated onto the new mesh to give an initial guess for the iterative method. This decreases the time it takes to find a solution on the most refined mesh for the initial timestep. Examples of refined meshes are shown in Figure 5.5. The location of the constructs can be seen to be due to the increased number of elements in their vicinity. Through time the mesh is refined and coarsened every dimensional minute, alternating between refinement according to the magnitude of the cell flux gradient and refinement according to the magnitude of the cell and substrate phase volume fraction gradients.

5.8 A discussion of some of the assumptions made

In order to build the system of equations presented in this chapter, several assumptions and simplifications have been made in addition to those discussed in previous chapters.

We have chosen the sizes of the parameters ν, χ, δ_a and δ_b in order to illustrate behaviour, rather than basing their values on experimental measurements. As a consequence, the numerical results presented in Chapters 6 and 7 are illustrative of behaviour rather than quantitative descriptions of the dynamics within the experimental setup and the shapes of the solutions presented are representative of the flows, pressure distribution and FSSMs involved.

We will demonstrate in Chapter 6 that gradients in the constituent phase volume fractions drive flow in the model, and, hence, the fluid shear stresses. We note that Figures 2.7 and 2.8 justified assuming a homogeneous initial spatial distribution of the cell and substrate phases in Chapter 4. In Chapters 6 and 7 we used smoothed initial conditions of functions of hyperbolic tangent in order to aid numerical simulation. If sharper initial conditions were used, such that the spatial distribution of the cells and substrate were spatially homogeneous inside the

construct area, there would still be spatial gradients in the constituent phase volume fractions at the edge of the construct that would drive the flows and fluid shear stresses.

We have made the assumption that the cell and the fluid phases behave as viscous fluids, and that the substrate phase is immobile and solid. For the fluid phase, a material assumption of a viscous fluid is a sensible assumption. In addition, although cells behave in a viscoelastic manner on short timescales, on the timescale of growth, they behave as a viscous fluid and so this assumption is often used [Franks and King, 2003, Preziosi and Tosin, 2009, Lemon *et al.*, 2006]. The substrate phase will undergo compression and deformation during the experiment, which will impart additional strains and compressive forces to the cells. These are known to be sensed by bone–producing cells, and are thought to have the effect of increasing osteoprogenitor differentiation and bone mineralisation [Chen *et al.*, 2010, Mullender *et al.*, 2004]. Although the compression and deformation will be small in magnitude, extending the model to allow for an elastic phase in future work could additionally explain the mineralisation seen experimentally.

Due to the lack of experimental data and in order to simplify the system of equations, we have assumed that the viscous drag between all the phases, β_{kl}, is equal. Assuming the viscosity of the cell and fluid phases to be the same as that of MSCs and water at 37 °C respectively, parameters from literature suggest a difference of 7.7×10^7 Pa s in the macroscale viscosity between the two phases. We increase the viscosity of the fluid phase, so that the difference in magnitudes between the two phases is 7.7×10^2 Pa s to aid numerical simulation.

The assumption is made that there is no additional pressure generated in the fluid phase, and between the fluid and cell, and fluid and substrate phases, so that $p_W = p_{CW} = p_{JW} = p$, where p is a common pressure. Following Lemon *et al.* [2006], Osborne [2009], O'Dea *et al.* [2010], Osborne *et al.* [2010], we assume the pressure produced in the cell phase may be modelled as the sum of the common pressure and additional pressures produced by interactions within the cell phase and between the cell and substrate phases, so that $p_C = p + \Sigma_C + \theta_J \psi_{CJ}$. Similarly, we assume that the interphase pressure produced between the cell and substrate phases may be modelled as the sum of the common pressure and additional pressure produced by interactions between the cell and substrate phases, so that $p_{CJ} = p + \psi_{CJ}$. In addition, we assume that the Σ_C and ψ_{CJ} terms, representing these additional pressures, take the forms as given in Equations (5.12) and (5.13) with $m = 1$.

We use an averaged form of the substrate deposition rate, given by Equation (5.5), because this allows us to achieve numerical results in a reasonable timeframe. This substrate deposition rate is independent of the current applied pressure, and each parameter set is only valid for one particular loading regime. Using a substrate deposition rate with the effects of cell memory included, as an extension to the form hypothesised in Section 3.2, with dependence on space and cell pressure could be investigated in future work.

We note that we have not included the effects of the impermeable walls of the transwell insert in the domain, Ω. Their inclusion could alter the quantities of interest, although this is likely to be very minor as the construct is small in comparison to the radius of the transwell membrane. Including the transwell insert would be especially important if the construct were larger, and in particular touching the transwell insert walls.

5.9 Close of chapter

In this chapter we have presented a three phase model to describe the evolution of a tissue engineered bone construct under the application of dynamic hydrostatic pressure loading. The inclusion of advective transport allows us to evaluate and examine the spatial distribution of the FSSMs. Furthermore, we have performed nondimensionalisation and detailed a method of finding a numerical solution.

The solution of the velocities and pressure at a particular point in time is dependent on the constitutive phase volume fractions and the parameter choices. By examining the initial velocity–pressure solution we are able to understand further how the spatial distribution of these variables depends on the parameters chosen and the initial cell and substrate conditions imposed. This is performed in Chapter 6. In Section 6.1 we demonstrate that flows are driven by the additional pressures caused by cell–cell and cell–substrate interactions, through spatial variation in the constituent phase volume fractions. Therefore, in Section 6.2 we prescribe different initial conditions in order to illustrate how variations in these can cause qualitative changes in the velocity–pressure solution.

In Chapter 7 we present numerical simulations through time in order to investigate whether there is a difference in the FSSMs predicted by the mathematical model between stimulated

and control loading conditions. Furthermore, we test a number of experimental setups, altering the shape and position of the construct within the well, in order to investigate how this affects the spatial evolution of the quantities of interest through time.

Chapter 6

A multiphase model: spatial variation in the initial velocity and pressure solutions

In Chapter 5 we presented a three phase model to examine the role of advective transport in the experimental setup and measure the magnitude of the fluid shear stresses generated. Three phases are represented in the model, cells, substrate and fluid, where the substrate phase is assumed to be solid and stationary. In this chapter we investigate the spatial distribution of the cell and fluid phase velocities and pressures as well as the magnitude of the fluid shear stress at the initial time point. In Section 6.1 we show that flows are driven by cell–cell and cell–substrate interactions, and demonstrate a qualitative change in the cell and fluid phase velocities as the parameters describing these interactions are altered. In Section 6.2, we illustrate the effect of altering the initial conditions describing the shape and position of the construct on the constitutive phase velocities, pressures and shear stresses predicted by the model. Numerical simulations of the system through time are presented in Chapter 7.

The multiphase model given in Chapter 5 describes the spatio–temporal evolution of three phases representing cells, substrate and fluid. Each phase has an associated volume fraction

and velocity field, denoted by $\theta_k \in (0,1)$ and $\mathbf{v}_k$ respectively for $k = C$ (cells) $k = J$ (substrate) and $k = W$ (fluid). Furthermore, the mathematical model describes the pressure in the cell and fluid phases, and between each of the constituent phases, denoted by p_k for $k = C, W$ and p_{kl} for $k \neq l$, $k, l = C, J, W$ respectively.

The system of equations describing the model may be split into two coupled systems. The velocity–pressure system, given by Equations (5.1), (5.27) and (5.28) with $\mathbf{v}_J = \mathbf{0}$ imposed along with constitutive assumptions given by Equations (5.29) – (5.34) and boundary conditions given by Equations (5.38) and (5.39), has no temporal derivatives. Thus, its solution at any time point depends on the constitutive volume fractions, along with parameter choices. In this chapter we want to understand how the spatial variation in the cell, substrate (and by the no voids condition, the fluid) phase volume fractions influences the spatial distribution of the velocity and pressure solutions. We, therefore, investigate the solutions at the initial time point, where the constitutive volume fractions are given by the initial conditions, and hence known. As such, this study in an extension of the work performed in O'Dea [2007] and O'Dea *et al.* [2013], where the effect of the size of the aggregation and attachment parameters, in comparison to the repulsion parameters, on the velocity solution, for the reduced system of equations in 1D describing tissue growth in a perfusion bioreactor with a small aspect ratio, was investigated.

6.1 The forcing terms

When the constitutive assumptions are applied, assuming $\beta = \beta_{kl}$ for $k \neq l$, the conservation of momentum equations for the cell and fluid phases are given by

$$\beta\theta_C\left(\left(1-\theta_C\right)\mathbf{v}_C - \theta_W\mathbf{v}_W\right) - \mu_C\left(\nabla\cdot\left(\theta_C\left(\nabla\mathbf{v}_C + \left(\nabla\mathbf{v}_C\right)^{\mathrm{T}}\right)\right) - \frac{2}{3}\nabla\left(\theta_C\left(\nabla\cdot\mathbf{v}_C\right)\right)\right) + \theta_C\nabla p$$
$$= \overbrace{-\nabla\left(\theta_C\Sigma_C\right)}^{\text{cellular forcing}}\underbrace{-\theta_C\theta_J\nabla\psi_{CJ} - 2\theta_C\psi_{CJ}\nabla\theta_J}_{\text{cell–substrate traction forcing}}, \quad (6.1)$$

where Σ_C and ψ_{CJ} describe additional pressures due to cell–cell and cell–substrate interactions respectively and are given by Equations (5.33) and (5.34), and

$$\beta\theta_W\left(\left(1-\theta_W\right)\mathbf{v}_W-\theta_C\mathbf{v}_C\right)-\mu_W\left(\nabla\cdot\left(\theta_W\left(\nabla\mathbf{v}_W+\left(\nabla\mathbf{v}_W\right)^{\mathrm{T}}\right)\right)-\frac{2}{3}\nabla\left(\theta_W\nabla\cdot\mathbf{v}_W\right)\right)+\theta_W\nabla p=\mathbf{0}. \quad (6.2)$$

These must be solved together with the total conservation of mass equation (Equation (5.27)):

$$\nabla\cdot\left(\theta_C\mathbf{v}_C+\theta_W\mathbf{v}_W\right)=0, \quad (6.3)$$

and the boundary conditions given by Equations (5.39) and (5.38).

The terms describing additional pressures due to cell–cell and cell–substrate interactions, Σ_C and ψ_{CJ} respectively, appear in the conservation of momentum equation for the cell phase only, Equation (6.1). Setting $\Sigma_C=\psi_{CJ}=0$ an examination of Equations (6.1), (6.2) and (6.3) reveals that the cell and fluid phase velocity fields are zero and that the common pressure and all interphase and intraphase pressures are spatially constant and equal to the applied pressure. The terms $-\nabla\left(\theta_C\Sigma_C\right)$ and $-\left(\theta_C\left(\theta_J\nabla\psi_{CJ}+2\psi_{CJ}\nabla\theta_J\right)\right)$, which we refer to as the *cellular forcing term* and *cell–substrate traction forcing term* respectively, drive the flow. As $\beta(1-\theta_C)>0$ for $\beta>0$, reorganisation of Equation (6.1) shows that the direction of the cell flux field, $\theta_C\mathbf{v}_C$, is determined by the direction of these forcing terms, $-\nabla\left(\theta_C\Sigma_C\right)-\theta_C\theta_J\nabla\psi_{CJ}-2\theta_C\psi_{CJ}\nabla\theta_J$, plus additional terms such as pressure gradients, macroscale viscosity and viscous drag between the phases.

The influence of the bioreactor geometry on the velocity–pressure solution is weak for the circular–shaped initial conditions given by Equation (5.40) and $r_c\ll R$, $r_c\ll H$. Thus, for these initial conditions we can investigate effects along one radial line ($z=H/2$, $x\geq 0$) of the 2D problem in order to understand the spatial variation in the region around the construct and the effect of the forcing terms. A sketch of the initial cell phase volume fraction is shown in Figure 6.1(a). As the region occupied by the construct is very small in comparison to the size of the whole well, in the next sections we plot the quantities of interest in the region surrounding the construct only. This region is indicated by the black box in Figure 6.1(a) and shown for

Table 6.1: Default dimensionless parameters for velocity–pressure simulations. All parameters are dimensionless except for the temporal and spatial scaling parameters, k_b and H respectively.

Parameters describing the velocity–pressure system					
$\hat{\mu}_C$	=	6.123×10^{-5}	$\hat{\mu}_W$	=	8.002×10^{-8}
$\hat{\beta}$	=	1.505×10^{-5}	$\hat{\delta}_a$	=	0.05
$\hat{\delta}_b$	=	0.05	$\hat{p}_{\text{app}}$	=	0
m	=	1			
Spatial parameters					
$\hat{R}$	=	8.13/17	$\hat{r}_c$	=	0.8681/17
Parameters describing initial conditions					
A_C^s	=	0.02268	A_J^s	=	$0.11A_C^s/0.3$
$\hat{B}_J = \hat{B}_C$	=	90			
Temporal and spatial scaling					
k_b	=	$(60 \times 60 \times 24)^{-1}$ s^{-1}	H	=	17 mm

the initial cell phase conditions in Figure 6.1(b). The cell and substrate phase initial volume fractions are continuous so we employ a threshold of $\theta_C = 0.005$ in order to define where the "edge" of the construct is, as shown by the black contour line in Figure 6.1(b). The choice of this threshold is for illustrative purposes only, and could equally be chosen to take a higher or lower value. The cell phase volume fraction along the radial line $z = H/2$ with $x \geq 0$, indicated by the solid black line in Figure 6.1(b), is plotted in Figure 6.2(a) and its gradient with respect to x is plotted in Figure 6.2(b). It can be seen that the cell phase volume fraction is highest in the centre of the construct, Figure 6.2(a), and decreases monotonically to be close to zero outside the construct region. The gradient of the cell phase, shown in Figure 6.2(b), is maximal in magnitude near the edge of the construct, as indicated by a vertical dash–dotted line. For these initial conditions the shapes of Σ_C and ψ_{CJ} along the radial line $z = H/2$, for $x \geq 0$, are sketched in Figure 6.3 for the parameters given in Table 6.1.

We now, in Sections 6.1.1 and 6.1.2, investigate the effect of the two forcing terms separately in order further to understand how the forcing produced by the additional pressures Σ_C and ψ_{CJ} influences the velocity and pressure solutions.

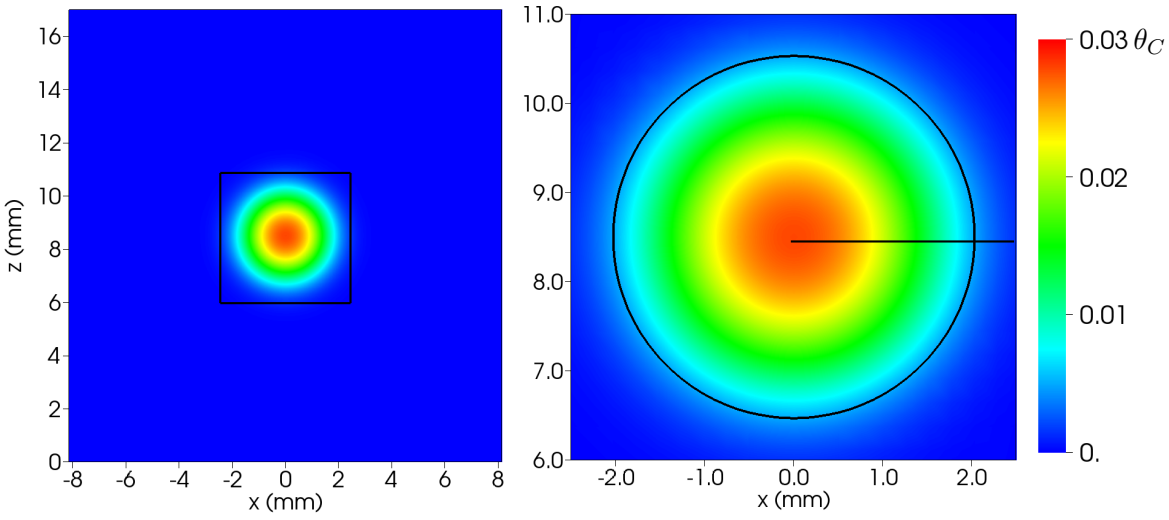

(a) Whole well (b) Region around the construct

Figure 6.1: Initial cell volume fraction conditions for the circular–shaped construct, given by Equation (5.40), with parameters in Table 6.1. Figure (a) indicates the whole domain. The box shows the region expanded in Figure (b), where the construct and surrounding region only is plotted, so that the region of interest can be easily seen. The black contour line in Figure (b) indicates the "edge" of the construct, where $\theta_C = 0.005$, and the horizontal solid black line indicates the line $z = H/2$ for $x \geq 0$, along which slices are taken for plotting purposes. The cell volume fraction along this line ($z = H/2$, $x \geq 0$) is plotted in Figure 6.2(a).

6.1.1 The cellular forcing term

We first consider the effect of the cellular forcing term, $-\nabla(\theta_C \Sigma_C)$, on the velocity–pressure system by setting $\chi = \delta_b = 0$ by Equation (5.12) so that $\psi_{CJ} = 0$. By Equation (5.12), assuming that $m = 1$, we have

$$-\nabla\left(\theta_C \Sigma_C\right) = -\theta_C \left(\left(-2\nu + 3\delta_a \frac{\theta_C}{\theta_W} \right) \nabla\theta_C - \delta_a \frac{\theta_C^2}{\theta_W^2} \nabla\theta_W \right). \tag{6.4}$$

Hence when either $\theta_C = 0$, or both $\nabla\theta_C$ and $\nabla\theta_W$ are the zero vector so that θ_C, θ_J and θ_W are constant, the cellular forcing term given by Equation (6.4) is zero and solutions are trivial (cell and fluid velocity fields are zero, and common pressure is constant and equal to the applied pressure). This is verified by numerical simulation. We can conclude that all flows are generated by spatial variations in the volume fractions of the constituent phases.

Due to the symmetry of the initial conditions describing the circular–shaped construct and the weak effect of the domain for these initial conditions, we may consider the effect of $-\dfrac{\partial}{\partial x}\left(\theta_C \Sigma_C\right)$ along the radial line $z = H/2$, $x \geq 0$ as being representative of the solution along any radial

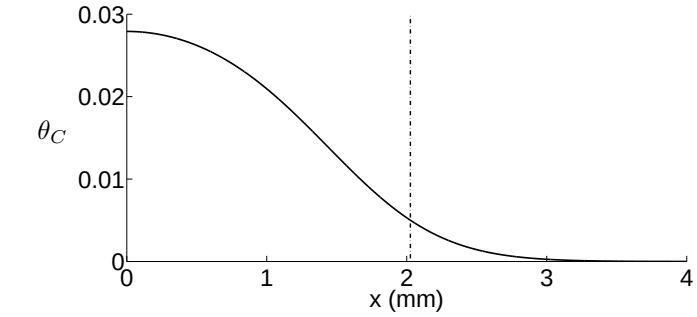

(a)

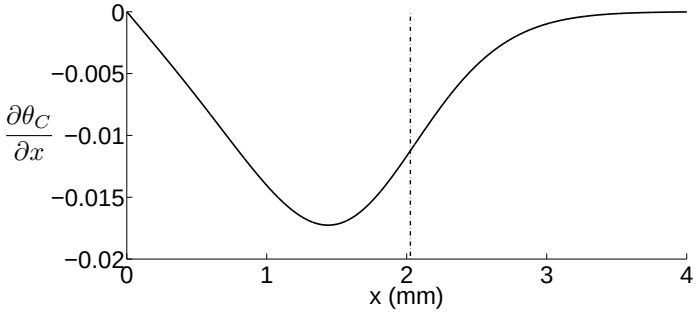

(b)

Figure 6.2: The initial (a) cell volume fraction and (b) its gradient with respect to x along the line $z = H/2$ (as indicated by the solid horizontal line in Figure 6.1(b)). Initial conditions are given by Equation (5.40) with parameters in Table 6.1. The vertical dash–dotted lines indicate the "edge" of the construct, where $\theta_C = 0.005$.

line. For the initial conditions given by Equation (5.40), the component in the x–direction of Equation (6.4) along this line becomes

$$-\frac{\partial}{\partial x}\left(\theta_C \Sigma_C\right) = -2B_C x \theta_C^2 \left(\frac{\theta_C}{A_C^s} - 2\right)\left(-2\nu + \frac{\theta_C \delta_a \left(3 - 2\theta_C\left(1 + \frac{A_J^s}{A_C^s}\right)\right)}{\left(1 - \theta_C\left(1 + \frac{A_J^s}{A_C^s}\right)\right)^2}\right). \tag{6.5}$$

A sketch of $-\dfrac{\partial}{\partial x}\left(\theta_C \Sigma_C\right)$ along the radial line $z = H/2$ against $x \geq 0$ is given in Figure 6.4 for δ_a fixed at 50 Pa and $\nu = 1$ Pa and 2 Pa. When the cellular forcing term is negative its effect is to cause negative cell fluxes. The imposed cell volume fraction, as sketched in Figure 6.2(a), is monotonically decreasing so this responds to cell aggregation behaviour, with cells moving up the cell volume fraction gradient. In contrast, when the cellular forcing term is positive its effect is to cause positive cell fluxes, which here responds to cell repulsion behaviour. By Equation (6.5), $\dfrac{\partial}{\partial x}\left(\theta_C \Sigma_C\right) = 0$ when one of:

1. $x = 0$ (for which the cell volume fraction is maximal) as expected by the symmetry of the

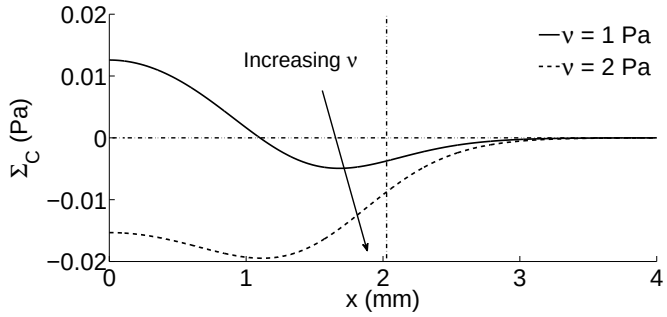

(a)

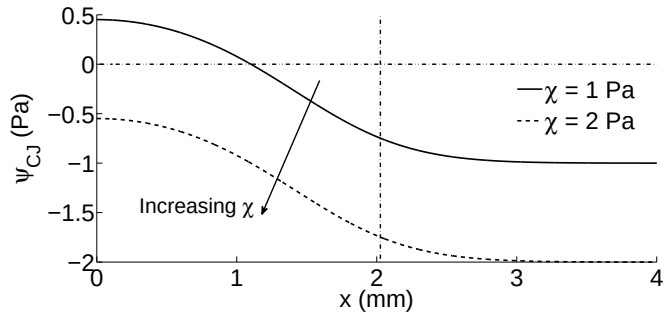

(b)

Figure 6.3: The pressures produced (a) in the cell phase, Σ_C, and (b) by interactions between the cell and substrate phases, ψ_{CJ}, given by Equations (5.12) and (5.34) respectively, along the line $z = H/2$ for $x \geq 0$, as illustrated by the solid horizontal line in Figure 6.1(b). The cell and substrate volume fractions are given by Equation (5.40) with parameters in Table 6.1. The vertical dash–dotted lines indicate the "edge" of the construct, where $\theta_C = 0.005$, and the horizontal dash–dotted lines indicate where the pressures are zero.

initial conditions,

2. $\theta_C = 0$ (the minimal value of the cell volume fraction),

3. $\theta_C = 2A_C^s$ (which is not a valid root as $2A_C^s > \max(\theta_C)$), or

4. (for $\theta_W > 0$) the roots of the equation given by

$$2\nu\left(1-\theta_C\left(1+\frac{A_J^s}{A_C^s}\right)\right)^2 = \delta_a\theta_C\left(3-2\theta_C\left(1+\frac{A_J^s}{A_C^s}\right)\right). \tag{6.6}$$

We denote the solutions to this quadratic equation in θ_C by $\theta_{C_\pm}$ and these determine where, for varying ν, δ_a, the graph of $-\dfrac{\partial}{\partial x}(\theta_C\Sigma_C)$ crosses the θ_C–axis, moving from negative to positive

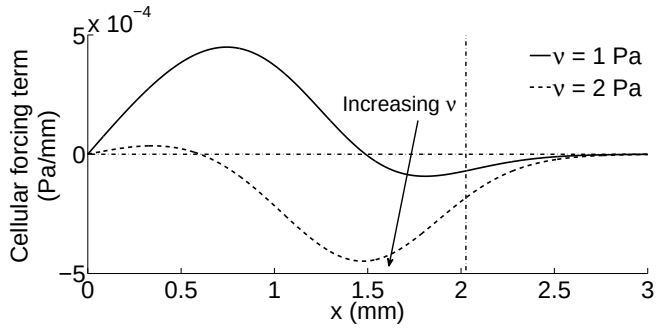

Figure 6.4: The cellular forcing term in the x–coordinate direction, $-\frac{\partial}{\partial x}(\theta_C \Sigma_C)$, given by Equation (6.5) along the radial line $z = H/2$ (as indicated by the solid horizontal line in Figure 6.1(b)) against x for varying ν as shown in the legend. The initial conditions are given in Equation (5.40) and the parameters are given in Table 6.1. The dash–dotted black horizontal lines indicate where cellular forcing is zero. The vertical dash–dotted line indicates the "edge" of the construct, where $\theta_C = 0.005$.

values of cellular forcing. Solutions to Equation (6.6) are given by

$$\theta_{C_\pm} = \frac{4\nu\left(1+\frac{A_J^s}{A_C^s}\right) + 3\delta_a \pm \sqrt{8\delta_a\nu\left(1+\frac{A_J^s}{A_C^s}\right) + 9\delta_a^2}}{4\left(1+\frac{A_J^s}{A_C^s}\right)\left(\nu\left(1+\frac{A_J^s}{A_C^s}\right)+\delta_a\right)}, \tag{6.7}$$

where the plus and minus sign subscript refers to the positive and negative square root respectively. These two roots are plotted in Figure 6.5(a) for fixed $\delta_a = 50$ Pa and varying ν. For a valid root we must have $\min(\theta_C) \leq \theta_{C_\pm} \leq \max(\theta_C)$, the upper value being illustrated by a horizontal dashed line. From Figure 6.5(a) it can be seen that, for these initial conditions, θ_{C_+} is never a valid solution. Figure 6.5(b) shows the area around the origin in Figure 6.5(a) magnified, so that the region where the line $\theta_C = \theta_{C_-}$ crosses the line $\theta_C = \max(\theta_C)$ can be seen. For each pair ν, δ_a, when $\theta_C > \theta_{C_-}$, if θ_{C_-} is a valid solution, the cellular forcing term is positive and so has the effect of causing positive cell flux. This is illustrated in Figure 6.6 for $\nu = 1$ Pa and $\nu = 2$ Pa; when the cell volume fraction is larger than the vertical dash–dotted line, illustrating the position of θ_{C_-}, cellular forcing is positive. When $\theta_C < \theta_{C_-}$, if θ_{C_-} is a valid solution, the cellular forcing term is negative and has the effect of causing negative cell flux. If $\theta_{C_-} > \max(\theta_C)$ then the cellular forcing term is always negative for $\min(\theta_C) \leq \theta_C \leq \max(\theta_C)$, and so has the effect of causing negative cell fluxes only. This occurs, for these initial conditions and parameters, when $\nu > 2.20$ (2 d.p.) as can be seen in Figure 6.5(b). Consequently, when $\nu = 3$ Pa, θ_{C_-} is greater than the maximum cell volume fraction and so cellular forcing is always negative for valid θ_C as illustrated in Figure 6.6.

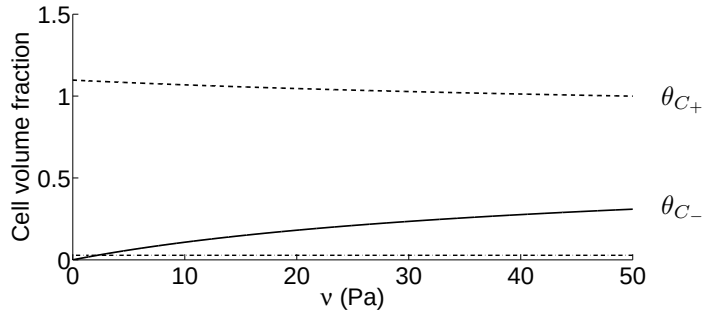

(a) θ_{C_+} and θ_{C_-} for 0 Pa $\leq \nu \leq$ 50 Pa

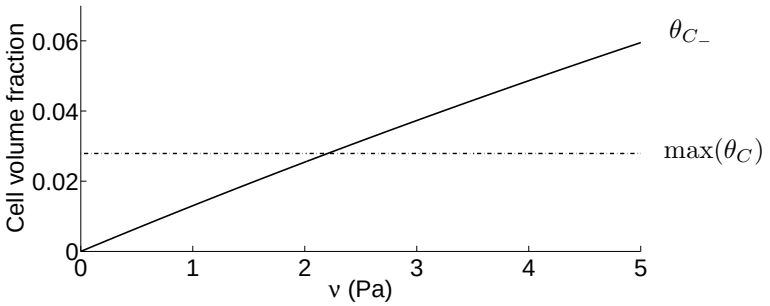

(b) θ_{C_-} for 0 Pa $\leq \nu \leq$ 5 Pa

Figure 6.5: Plots of the roots of the quadratic Equation (6.6), θ_{C_+} and θ_{C_-}, given by Equation (6.7), illustrating the value of the cell volume fraction where the cellular forcing term changes sign for (a) 0 Pa $\leq \nu \leq$ 50 Pa and (b) 0 Pa $\leq \nu \leq$ 5 Pa with $\delta_a = 50$ Pa. The dashed line shows θ_{C_+} and the solid lines shows θ_{C_-}. Initial conditions are given by Equation (5.40) and other parameters are given in Table 6.1. The dot–dashed black horizontal lines show the position of the maximal value for the cell volume fraction. Figure 6.5(b) only shows θ_{C_-}, so that the region around the point where $\theta_{C_-} = \max(\theta_C)$ can be seen.

Simulation results for the cell flux, $\theta_C \mathbf{v}_C$, and fluid flux, $\theta_W \mathbf{v}_W$, at the initial time, with $\nu = 1, 2$ Pa and $\delta_a = 50$ Pa fixed, in the region of the construct, are plotted in Figure 6.7. As in Figure 6.1(b), the black contour line denotes the "edge" of the construct (where $\theta_C = 0.005$). It can be seen that there is a change in cell flux behaviour as ν increases. When $\nu = 1$ Pa we see predominantly cell repulsion behaviour, with cells moving away from the centre to the periphery of the construct, Figure 6.7(a). However, when $\nu = 2$ Pa we see predominantly cell aggregation behaviour, with cells moving towards the centre of the construct, Figure 6.7(c). Outside the construct region cell flux is negligible in both cases. As expected, due to the total conservation of mass, Equation (6.3), which means that $\theta_C \mathbf{v}_C = -\theta_W \mathbf{v}_W$ in the case of radial symmetry, the fluid moves in the opposite direction to the cells, as can be seen from Figures 6.7(b) and (d).

In order to see this change in behaviour more clearly, the initial cell and fluid fluxes in the x–coordinate direction along the line $z = H/2$ are plotted in Figure 6.8 for $x \geq 0$. When $\nu = 1$ Pa,

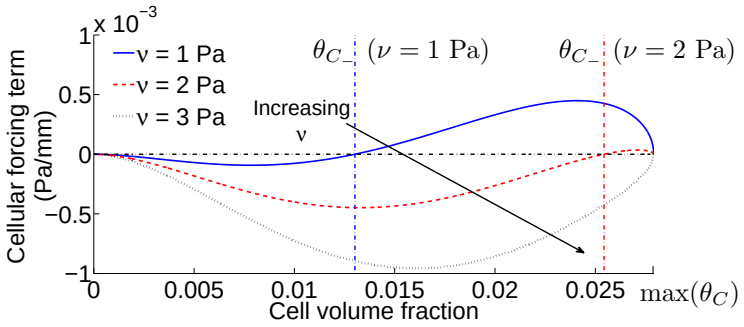

Figure 6.6: The cellular forcing term in the x–coordinate direction, $-\frac{\partial}{\partial x}(\theta_C \Sigma_C)$, along the line $z = H/2$ against θ_C, for $\nu = 1, 2, 3$ Pa with the arrow indicating the direction of increasing ν. Initial conditions are given by Equation (5.40) and other parameter are given in Table 6.1. The vertical dash–dotted lines indicate the position of $\theta_{C\_}$ for $\nu = 1$ Pa and $\nu = 2$ Pa in blue and red respectively. When $\nu = 3$ Pa $\theta_{C\_} > \max(\theta_C)$ and so the position of $\theta_{C\_}$ for this parameter set is not shown.

the cell flux is mostly positive (negative cell flux is predicted for 2.1 mm $\leq x \leq$ 3.6 mm but this is very small in magnitude in comparison to the magnitude of the positive cell flux), Figure 6.8(a), and when $\nu = 2$ Pa, the cell flux is negative, Figure 6.8(b). By the conservation of total flux, Equation (6.3), the fluid fluxes are mostly negative for $\nu = 1$ Pa and positive for $\nu = 2$ Pa, as illustrated in Figures 6.8(a) and (b) respectively. From the initial cell phase conditions, Figure 6.2(a), we see that in the centre of the construct the cell volume fraction is about 0.028 before decreasing at the edge of the construct to be close to zero. In addition, examining Figure 6.6, it can be seen that, as ν increases from 1 Pa to 2 Pa the cellular forcing term moves from positive to negative for cell volume fractions in the region of $0.0013 \leq \theta_C \leq 0.0254$. Thus, the effect of the cellular forcing term on cell movement changes from causing positive cell flux to negative cell flux. This here corresponds to changing from cell repulsion to cell aggregation behaviour. This explains why, for the cell seeding density given by Equation (5.40) with parameters in Table 6.1, we see a qualitative change in the cell flux behaviour as the cell aggregation parameter ν is increased from 1 Pa to 2 Pa. If we seed at a higher cell density, for example at double the initial cell volume fraction, then we see only positive cell flux corresponding to cellular repulsion behaviour for these values of ν. Similarly if we seed at a lower cell density, for example at half the initial cell volume fraction, then we see only negative cell flux corresponding to aggregation cell behaviour as we move from $\nu = 1$ Pa to $\nu = 2$ Pa.

The spatial variation of the common pressure distribution, $p(x, z, 0)$, in the region around the construct is plotted in Figure 6.9. The simulations we present are for an applied pressure equal

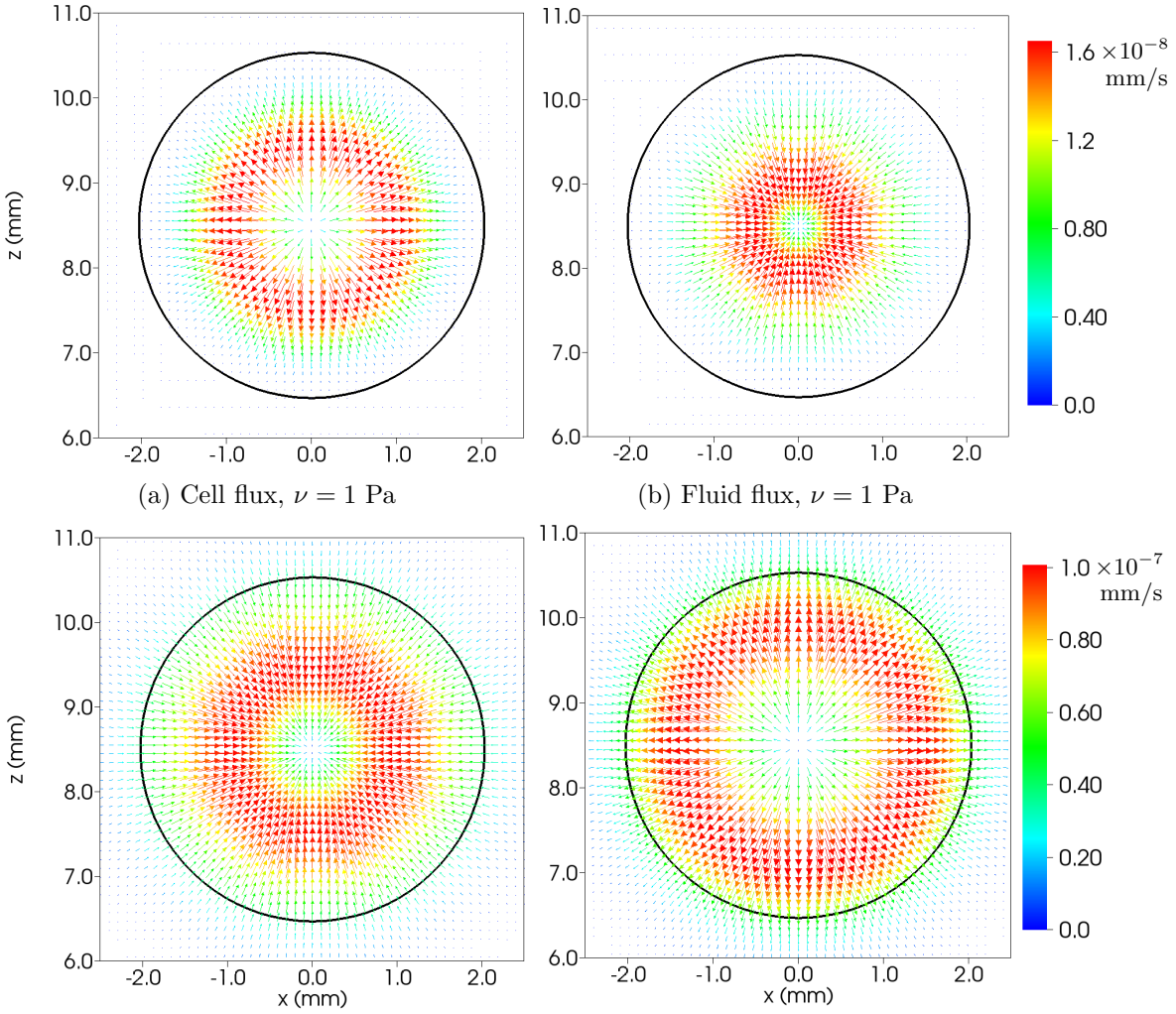

(a) Cell flux, $\nu = 1$ Pa

(b) Fluid flux, $\nu = 1$ Pa

(c) Cell flux, $\nu = 2$ Pa

(d) Fluid flux, $\nu = 2$ Pa

Figure 6.7: The initial cell and fluid flux, $\theta_C(x, z, 0)\mathbf{v}_C(x, z, 0)$ and $\theta_W(x, z, 0)\mathbf{v}_W(x, z, 0)$ respectively, in the region of the construct. The initial conditions are given by Equation (5.40), with parameters in Table 6.1 where $\chi = \delta_b = 0$, with $\nu = 1$ Pa in (a) and (b), and $\nu = 2$ Pa in (c) and (d). Figures (a) and (c) illustrate the cell flux field and Figures (b) and (d) illustrate the fluid flux field. The size and the colour of the arrows indicate the magnitude of the flux, with arrows pointing in the direction of the vector. The black lines indicate the "edge" of the construct, where $\theta_C = 0.005$.

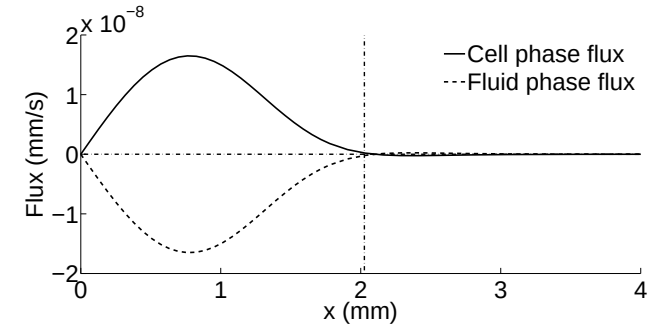

(a) $\nu = 1$ Pa

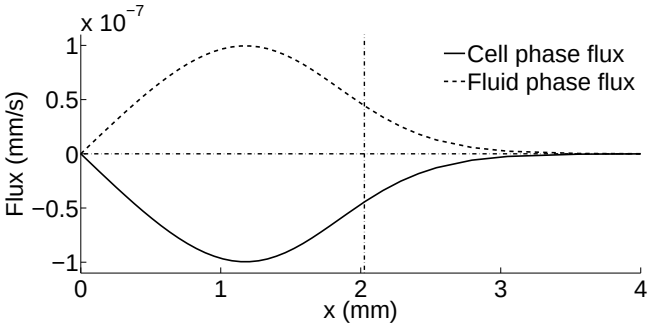

(b) $\nu = 2$ Pa

Figure 6.8: Initial cell and fluid fluxes in the x–coordinate direction along the line $z = H/2$, as indicated by the solid horizontal line in Figure 6.1(b), given by $\theta_C u_C(x, H/2, 0)$ and $\theta_W u_W(x, H/2, 0)$ respectively, against x for $\psi_{CJ} = 0$. Cell and substrate phase conditions are given by Equation (5.40) with parameters given in Table 6.1, where $\chi = \delta_b = 0$, with $\nu = 1$ Pa in (a) and $\nu = 2$ Pa in (b). The dash–dotted vertical line shows the position of the "edge" of the construct, where $\theta_C = 0.005$, and the horizontal dash–dotted line indicates where the flux is zero.

to atmospheric pressure. This is because increasing the applied pressure only alters the pressure solutions by a constant. Moving away from the construct, the pressure returns to the applied pressure. As for the cell and fluid fluxes, the common pressure spatial gradient changes sign as ν increases from 1 Pa to 2 Pa, with the common pressure increasing for $\nu = 1$ Pa, Figure 6.9(a), and the common pressure decreasing for $\nu = 2$ Pa, Figure 6.9(b), as the distance from the centre of the construct.

Figure 6.10 shows the common pressure, p, and the pressure in the cell phase, p_C, against $x \geq 0$ along the line $z = H/2$ for $\nu = 1, 2$ Pa. As the common pressure is small in magnitude in comparison to the additional pressures caused by cell–cell interactions, it can be seen that the shape of the cell pressure, $p_C = p + \Sigma_C$ by Equation (5.31), is determined by the shape of Σ_C, as can be seen by comparing Figure 6.10(b) with Figure 6.3(a). The pressure in the fluid phase, and the interphase pressures, are equal to the common pressure, as $p_W = p$ and $p_{kl} = p$,

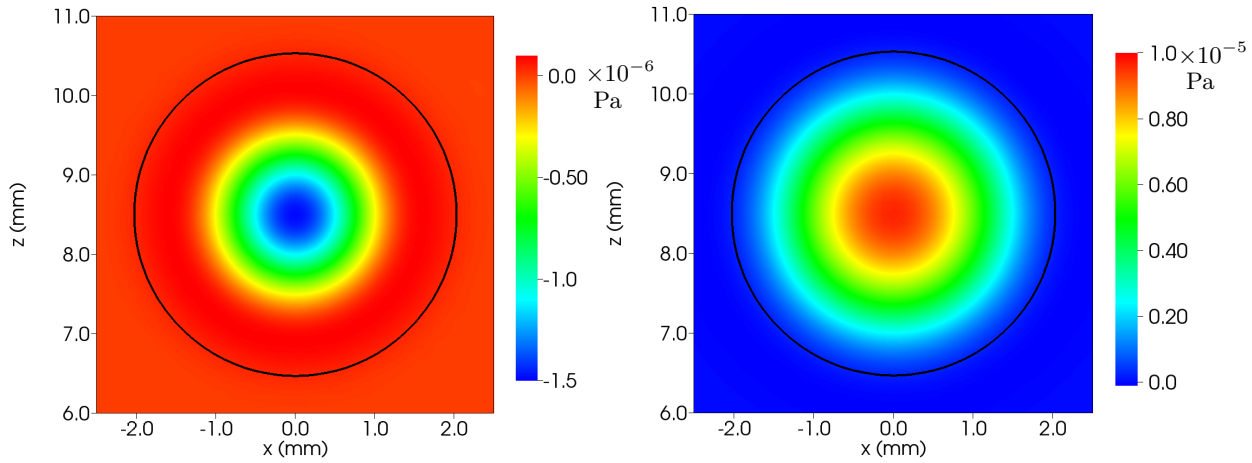

(a) $\nu = 1$ Pa (b) $\nu = 2$ Pa

Figure 6.9: Initial common pressure, $p(x, z, 0)$, in the region of the construct, for (a) $\nu = 1$ Pa and (b) $\nu = 2$ Pa, with $\psi_{CJ} = 0$. The cell and substrate phase initial conditions are given by Equation (5.40) with parameters in Table 6.1 where $\chi = \delta_b = 0$. The black line indicates the "edge" of the construct, where $\theta_C = 0.005$.

when $\psi_{CJ} = 0$, for all $k, l = C, J, W$, $k \neq l$ by Equations (5.31) and (5.32). Consequently, these pressures are small in comparison to the cell pressure and less than 10^{-5} Pa in magnitude.

The spatial variation in the maximum absolute eigenvalue of the deviatoric stress tensor for the fluid phase, which we use as a measure of FSSM, is plotted in Figure 6.11. When $\nu = 1$ Pa, the FSSMs are maximal in a band between the centre and the periphery of the construct. In contrast, when $\nu = 2$ Pa, the FSSM is maximal at the periphery of the construct. For both parameter sets, the FSSM predicted in the centre of the construct is lower than the maximal value. In addition, the maximum value for the FSSM is an order of magnitude higher when $\nu = 2$ Pa, at a value of 1.041×10^{-6} Pa, than when $\nu = 1$ Pa for which the maximal value is 2.337×10^{-7} Pa. It can be shown that when initial conditions for the cell and substrate phases are chosen such that θ_C and θ_J vary more rapidly at the edge of the construct, by increasing B_k for $k = C, J$, the FSSM predicted by the model is much larger, as shown in Figure 6.12(a). This can also be achieved by increasing the magnitude of the cell aggregation parameter, as illustrated by the distribution of the FSSM in Figure 6.12(b).

Due to the form of the cellular forcing term, given by Equation (6.5) and plotted in Figure 6.4, we might expect the cell flux to be small in magnitude and positive close to the centre of the construct when $\nu = 2$ Pa. However, examining Figure 6.8(b) we see that this is not the case and there is non–negligible cell flux of negative sign close to the centre of the construct

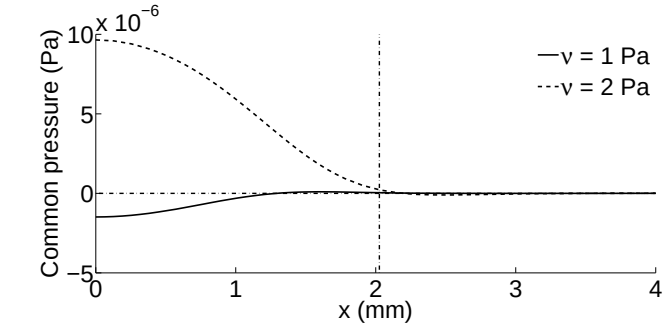

(a) Pressure

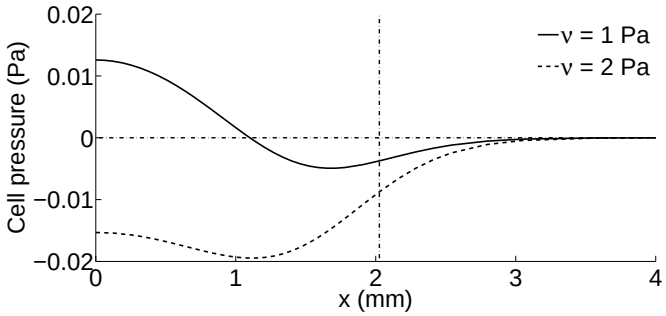

(b) Cell pressure

Figure 6.10: Initial (a) common pressure, $p(x, H/2, 0)$, and (b) pressure in the cell phase, $p_C(x, H/2, 0)$, along the line $z = H/2$, as indicated by the solid horizontal line in Figure 6.1(b), against x, for $\nu = 1$ Pa and $\nu = 2$ Pa, where $\psi_{CJ} = 0$. The cell and substrate phase conditions are given by Equation (5.40), with parameters given in Table 6.1 where $\chi = \delta_b = 0$. The dash–dotted vertical line shows the position of the "edge" of the construct, where $\theta_C = 0.005$.

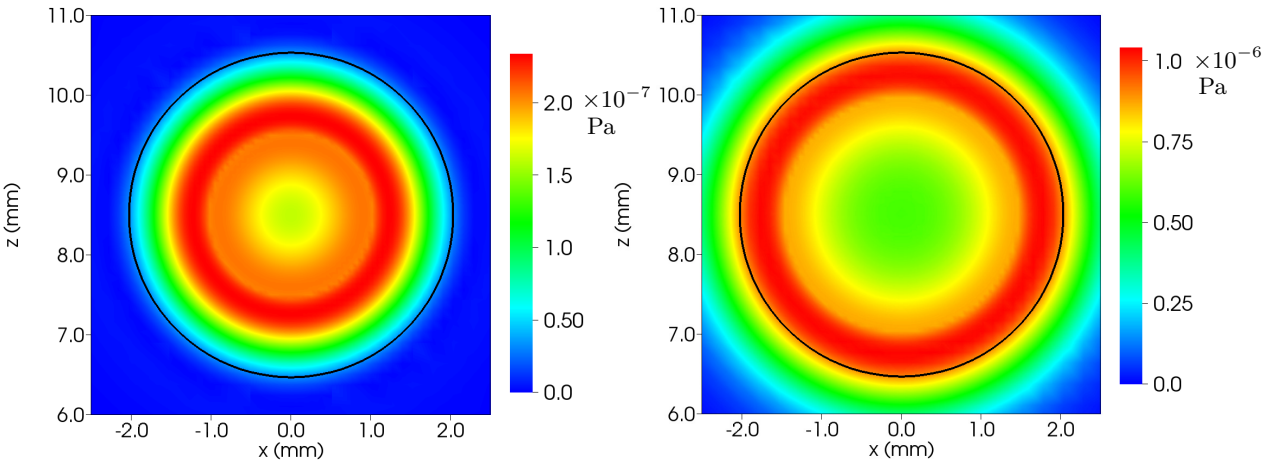

(a) $\nu = 1$ Pa

(b) $\nu = 2$ Pa

Figure 6.11: FSSM, measured as the maximum absolute eigenvalue of the deviatoric part of the fluid phase stress tensor, for (a) $\nu = 1$ Pa and (b) $\nu = 2$ Pa, where $\psi_{CJ} = 0$, with cell and substrate phase conditions given by Equation (5.40). Parameters are given in Table 6.1 with $\chi = \delta_b = 0$. The black line indicates the "edge" of the construct, where $\theta_C = 0.005$.

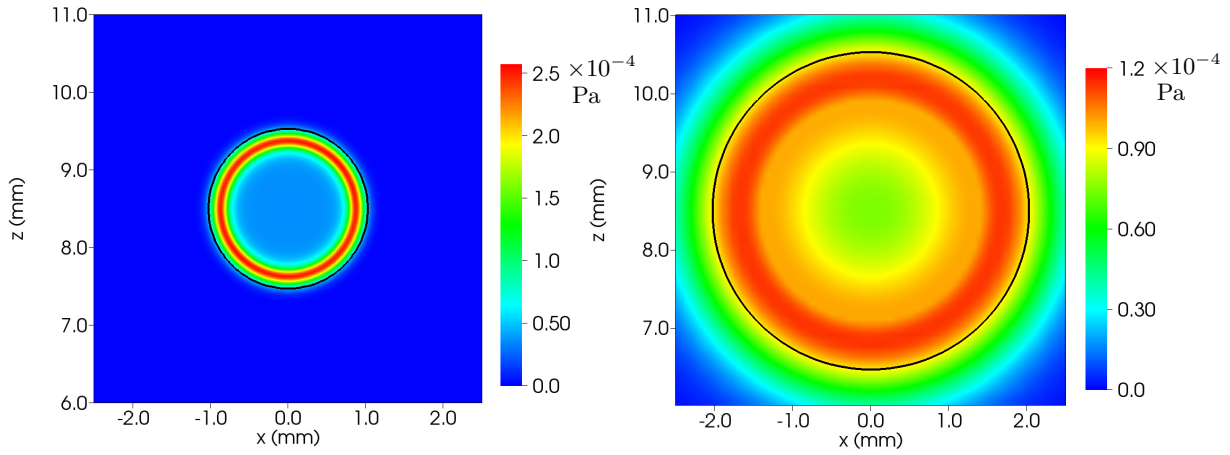

(a) Sharper initial conditions

(b) Increased cell aggregation parameter

Figure 6.12: FSSM, measured as the maximum absolute eigenvalue of the deviatoric part of the fluid phase stress tensor, to illustrate the fact that, (a) when the gradient at the edge of the construct is larger, or (b) when the size of the cell aggregation parameter, ν, is higher, fluid shear stresses of higher magnitude are predicted. Figure (a) illustrates results for $\nu = 2$ Pa and $\hat{B}^s_J = \hat{B}^s_C = 1445$ in with $A^s_C = 0.04642$, $A^s_J = 0.11A^s_C/0.3$ so that Equation (5.42) is satisfied. Figure (b) illustrates results when $\nu = 100$ Pa. All other parameters are given in Table 6.1. The black contour lines indicates the "edge" of the construct where $\theta_C = 0.005$.

where the cellular forcing term is very small and positive. We now show that this effect is due to the size of the macroscale viscosity of the cell phase, μ_C. Figure 6.13(a) illustrates the initial cell flux in the x–coordinate direction along the line $z = H/2$ for $\nu = 2$ Pa to demonstrate how the shape of the cell flux changes as μ_C is increased. Using dimensionless values for the cell macroscale viscosity of $10^{-9}, 10^{-8}, 10^{-7}$ and 10^{-6}, equivalent to dimensional values of $7.7205\times10^{-2}, 7.7205\times10^{-1}, 7.7205$ Pa s and 7.7205×10^{1} Pa s respectively, it can be seen that, as the cell macroscale viscosity is increased, the graph of the cell flux in Figure 6.13(a) moves from the shape of the forcing graph, Figure 6.4, with very small cell fluxes close to the centre of the construct, to the shape of the cell flux graph seen in Figure 6.8(b), where there is non–negligible cell flux near the centre of the construct. In addition, when μ_C is small, we see a change in the sign of the cell flux in some regions in Figure 6.13(a), as seen in the cellular forcing (Figure 6.4), whereas as μ_C is increased, cell fluxes are only negative and the change of sign is not seen. This effect is because, when cell phase macroscale viscosity is low, the Darcy–type drag term, $\beta\theta_C\left(\left(1-\theta_C\right)\mathbf{v}_C - \theta_W\mathbf{v}_W\right)$, in Equation (6.1) is a similar size to the forcing term, $-\nabla\left(\theta_C\Sigma_C\right)$, with the macroscale viscosity term , $-\mu_C\left(\nabla\cdot\left(\theta_C\left(\nabla\mathbf{v}_C + \left(\nabla\mathbf{v}_C\right)^{\mathrm{T}}\right)\right) - \frac{2}{3}\nabla\left(\theta_C\left(\nabla\cdot\mathbf{v}_C\right)\right)\right)$, being smaller in magnitude. However, as cell phase macroscale viscosity, μ_C, is increased, the size

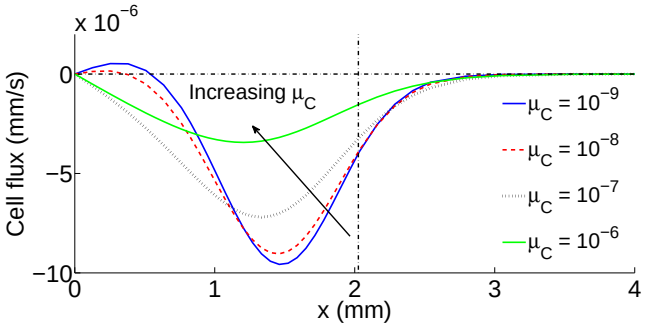

(a) Cell flux

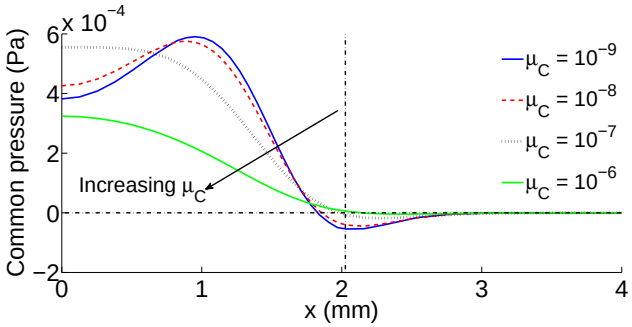

(b) Common pressure

Figure 6.13: An illustration of how the (a) cell flux and (b) common pressure in the x–coordinate direction along the line $z = H/2$, $\theta_C(x, H/2, 0)u_C(x, H/2, 0)$ and $p(x, H/2, 0)$ respectively, change in shape as the size of the macroscale viscosity is increased. Initial conditions are given by Equation (5.40) with $\chi = \delta_b = 0$, $\nu = 2$ Pa and dimensionless values for the cell macroscale viscosity of $10^{-9}, 10^{-8}, 10^{-7}$ and 10^{-6} as illustrated in the legends. Other parameters are given in Table 6.1. The arrows show the direction of increasing cell phase macroscale viscosity and the vertical dash–dotted lines indicate the "edge" of the construct, where $\theta_C = 0.005$.

of the macroscale viscosity term increases in magnitude, and the forcing term and the macroscale viscosity term become similar in size, with the Darcy–type viscous drag term being smaller in magnitude. We additionally note that, as μ_C is increased, the maximal magnitude of the cell flux decreases due to the dissipative nature of macroscale viscosity effects. The same effect is seen in the fluid flux, which takes the opposite sign to the cell flux field by the conservation of total mass equation due to the approximate radial symmetry of the initial conditions (not plotted). Similarly, as the cell phase macroscale viscosity is increased, there is a change in sign of the common pressure spatial gradient towards the centre of the construct, so that the maximal pressures obtained are in the centre rather than towards the edge of the construct, as can be seen in Figure 6.13(b).

6.1.2 The cell–substrate traction forcing term

We now investigate the effect of the term ψ_{CJ}, the additional pressures modelling the interaction between the cell and substrate phases, on the initial velocity–pressure solution by setting $\Sigma_C = 0$. We are interested in the behaviour of the cell–substrate traction forcing term, given by

$$-\left(\theta_C\theta_J\nabla\psi_{CJ} + 2\theta_C\psi_{CJ}\nabla\theta_J\right) = -\theta_C\left[\left(\frac{\delta_b\theta_J}{\theta_W} - 2\psi_{CJ}\right)\nabla\theta_C - \left(\frac{\delta_b\theta_J\theta_C}{\theta_W^2} + 2\psi_{CJ}\right)\nabla\theta_W\right]. \tag{6.8}$$

Thus, as for the cellular forcing term, flows are driven by variations in the constituent volume fractions.

Contributions to the cell–substrate traction forcing term from the interphase forces in the cell phase conservation of momentum equation, given by Equation (5.28), come in the form of $-\nabla\left(\theta_C\theta_J\psi_{CJ}\right)$ from the term $\nabla\cdot\left(\theta_C\boldsymbol{\sigma}_C\right)$ and in the form $\psi_{CJ}\left(\theta_J\nabla\theta_C - \theta_C\nabla\theta_J\right)$. In the case of the initial conditions given by Equation (5.40) with parameters in Table 6.1 so that $\theta_J(x,z,0)$ is proportional to $\theta_C(x,z,0)$, the term $\psi_{CJ}\left(\theta_J\nabla\theta_C - \theta_C\nabla\theta_J\right)$ is zero[a]. Hence in this case flow is driven by the term $-\nabla\left(\theta_C\theta_J\psi_{CJ}\right)$. Using Equation (5.13) with $m = 1$, this can be simplified

[a]However, for experimentally relevant cell and substrate phase conditions, this term is small and does not have a significant effect on behaviour.

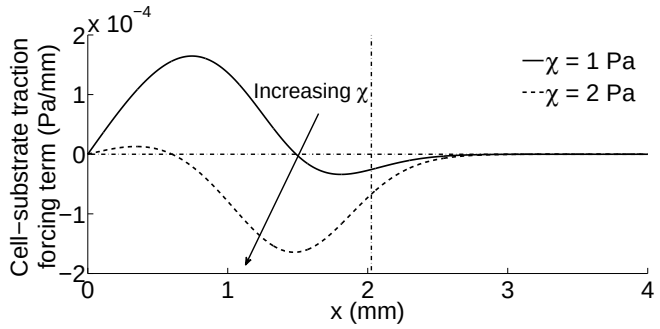

(a) Cell–substrate traction forcing term as a function of x

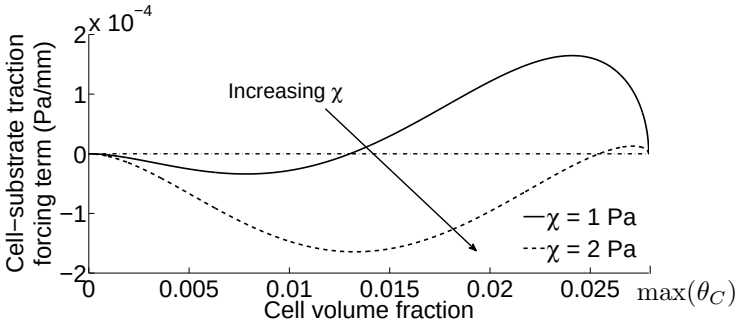

(b) Cell–substrate traction forcing term as a function of θ_C

Figure 6.14: The cell–substrate traction forcing term in the x–coordinate direction, given by Equation (6.10), along the line $z = H/2$ as indicated by the solid horizontal line in Figure 6.1(b), against (a) x and (b) θ_C for varying χ. The initial conditions are given by Equation (5.40) and parameters are given in Table 6.1. The dash–dotted horizontal black lines indicate the line where forcing equals zero. The vertical dash–dotted line in (a) indicates the "edge" of the construct, where $\theta_C = 0.005$.

to give

$$-\nabla\left(\theta_C\theta_J\psi_{CJ}\right) = -\frac{A_J^s}{A_C^s}\theta_C\left(\theta_C\frac{\delta_b}{\theta_W^2}\left(3-2\left(1+\frac{A_J^s}{A_C^s}\right)\theta_C\right)-2\chi\right)\nabla\theta_C. \tag{6.9}$$

Because of the symmetry of the initial conditions given by Equation (5.40) in the region around the construct and the weak effect of the bioreactor geometry, we may again consider the forcing terms in the x–coordinate direction along the line $z = H/2$, which is given by

$$-\frac{\partial}{\partial x}\left(\theta_C\theta_J\psi_{CJ}\right) = -2B_C\frac{A_J^s}{A_C^s}x\theta_C^2\left(\frac{\theta_C}{A_C^s}-2\right)\left[\delta_b\frac{\theta_C}{\theta_W^2}\left(3-2\left(\frac{A_J^s}{A_C^s}+1\right)\theta_C\right)-2\chi\right]. \tag{6.10}$$

This is plotted in Figure 6.14 for fixed $\delta_b = 50$ Pa and varying χ.

For the initial conditions given by Equation (5.40) the cellular forcing and the cell–substrate traction forcing terms have similar shapes, as can be seen by comparing Figures 6.4 and 6.14(a). Consequently, for these initial conditions, the two terms have a similar effect on the velocity–

pressure solution, which can be seen by examining the numerical results of the cell flux, fluid flux, common pressure and cell pressure given in Figure 6.15. There is a change in sign of the cell flux when χ, the substrate affinity parameter, is increased from $\chi = 1$ Pa to $\chi = 2$ Pa for fixed $\delta_b = 50$ Pa, as can be seen in Figure 6.15(a), with cell behaviour changing from predominantly repulsive to predominantly aggregative. The same effect as discussed for the cellular forcing term is also seen in the results of the fluid flux, Figure 6.15(b), and common pressure, Figure 6.15(c). Furthermore, as the common pressure is much smaller in magnitude than the additional pressures caused by cell–substrate interactions, the shape of the spatial distribution in the cell pressure, Figure 6.15(d), is determined by the quantity $\theta_J \psi_{CJ}$.

Setting $\nu = \chi$ and $\delta_a = \delta_b$, the sum of the cellular and the cell–substrate traction forcing terms, Equations (6.4) and (6.8), is given by

$$\begin{aligned} &-\left(\nabla\left(\theta_C \Sigma_C\right) + \theta_C \theta_J \nabla \psi_{CJ} + 2\theta_C \psi_{CJ} \nabla \theta_J\right) \\ &\qquad = -\theta_C \left[\frac{\delta_a}{\theta_W}\left(1-\theta_W\right)\nabla\theta_C - \left(-2\chi + \frac{\delta_a \theta_C}{\theta_W^2}\left(1+\theta_W\right)\right)\nabla\theta_W\right]. \end{aligned} \tag{6.11}$$

For the initial conditions given by Equation (5.40), this reduces to

$$\begin{aligned} &-\left(\nabla\left(\theta_C \Sigma_C\right) + \theta_C \theta_J \nabla \psi_{CJ} + 2\theta_C \psi_{CJ} \nabla \theta_J\right) \\ &= -2B_C \theta_C \left(\frac{\theta_C}{A_C^s} - 2\right)\theta_C \left(\frac{A_J^s}{A_C^s} + 1\right)\left[-2\chi + \frac{\delta_a \theta_C}{\theta_W^2}\left(3 - 2\left(\frac{A_J^s}{A_C^s}+1\right)\theta_C\right)\right]\begin{pmatrix} x \\ z - H/2 \end{pmatrix}. \end{aligned} \tag{6.12}$$

As μ_C is reduced in magnitude, we expect the change in sign of cell flux to occur near the solution of $-2\nu + \delta_a \dfrac{\theta_C}{\theta_W^2}\left(3 - 2\theta_C\left(1 + \dfrac{A_J^s}{A_C^s}\right)\right) = 0$. Writing $\theta_W = 1 - \theta_C\left(1 + \dfrac{A_J^s}{A_C^s}\right)$, this is a quadratic equation in the cell phase volume fraction which has one valid solution ($0 \leq \theta_C \leq 1$) when $\delta_a > 0$ and $\nu \leq \delta_a\left(\dfrac{A_C^s}{4A_J^s} + 1\right)$. As a consequence, if $\delta_a = 0$ or $\nu > \delta_a\left(\dfrac{A_C^s}{4A_J^s} + 1\right)$, as μ_C gets small, we will only see negative cell fluxes corresponding to cell aggregation behaviour. For simplicity and due to lack of experimental information we set $\nu = \chi$ and $\delta_a = \delta_b$ in the next section.

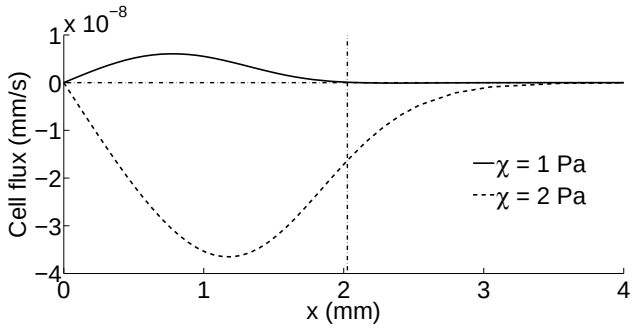

(a) Cell flux

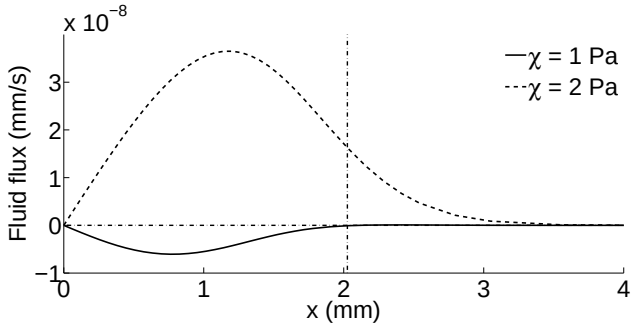

(b) Fluid flux

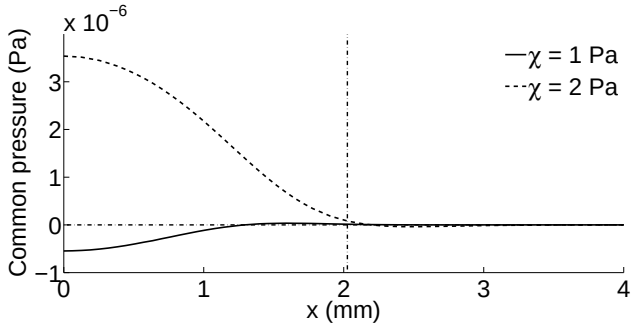

(c) Common pressure

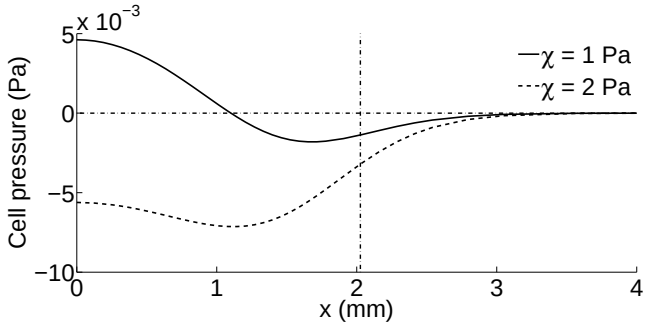

(d) Cell pressure

Figure 6.15: Numerical results along the line $z = H/2$, as illustrated by the solid horizontal line in Figure 6.1(b), against x in the case $\Sigma_C = 0$. Initial conditions are given by Equation (5.40) with parameters in Table 6.1, where $\nu = \delta_a = 0$ and χ is as given in the legends. Figure (a) shows the cell flux in the x–coordinate direction, $\theta_C(x, H/2, 0)u_C(x, H/2, 0)$, (b) shows the fluid flux in the x–coordinate direction, $\theta_W(x, H/2, 0)u_W(x, H/2, 0)$, (c) shows the common pressure, $p(x, H/2, 0)$, and (d) shows the pressure in the cell phase, $p_C(x, H/2, 0)$. The horizontal dash–dotted lines indicate where the quantities are zero, and the vertical dash–dotted lines indicate the "edge" of the construct, where $\theta_C = 0.005$.

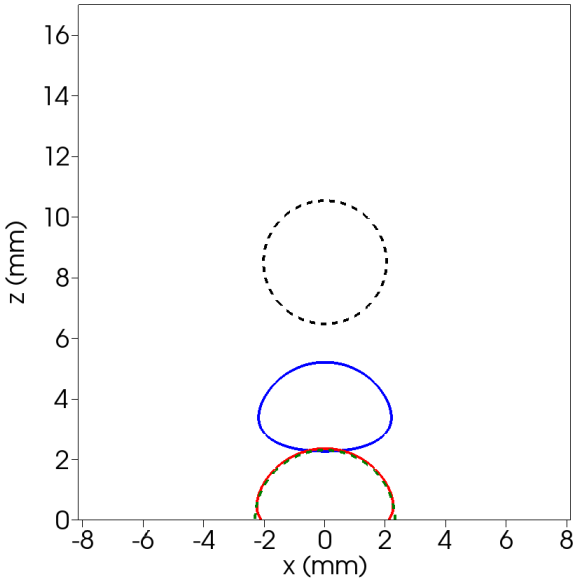

Figure 6.16: Full well domain with contours illustrating the edges of the constructs for the four different setups considered. In each the threshold $\theta_C = 0.005$ is plotted. The black dashed line indicates Setup 1, with initial conditions given by Equation (5.40), and the blue full line indicates Setup 2, with initial conditions given by Equation (5.41). The red solid and green dashed lines indicate Setups 3 and 4, with initial conditions given by Equations (6.13) and (6.14), respectively. Parameters are given in Tables 6.1 and 6.2.

6.2 Construct shape and position

In this section we consider the effect of altering the initial conditions on the velocity–pressure solution. Due to the forms of the cellular forcing and cell–substrate traction forcing terms, variation in the cell and substrate volume fractions (and hence, by Equation (5.1), the fluid phase) drive the cell and fluid fluxes and pressure variations. To demonstrate this effect we consider four different sets of initial conditions: one circular–shaped construct and three semicircular–shaped constructs. The positions of the four separate setups can be seen in Figure 6.16.

Setup 1 uses the initial conditions of a circular–shaped construct as used in Section 6.1 and given by Equation (5.40).

Setup 2 uses the initial conditions of a semicircular–shaped construct, given by Equation (5.41). We note that, from Figure 6.16, this construct does not look totally semicircular in shape. This is due to the use of functions of hyperbolic tangent to describe the initial conditions for the cell and substrate volume fractions, and the choice of the parameters B_k and C_k. If B_k and C_k were chosen to be larger, the edges of the construct would be sharper, and so it would appear

more semicircular.

Setup 3 is a construct on the base of the well, where we use similar initial conditions to those given by Equation (5.41) with $s_h = 0$, so that (in dimensionless variables) we have

$$\theta_k(x, z, 0) = A_k^{b_1} \left(1 - \tanh\left(\hat{B}_k \left(\hat{x}^2 + \hat{z}^2 - \hat{r}_c^2\right)\right)\right) \left(\tanh(\hat{C}_k \hat{z}) + 1\right), \quad \text{for } k = C, J. \tag{6.13}$$

Setup 4 is also a semicircular–shaped construct on the base of the well but using similar initial conditions to those given by Equation (5.40), so that (in dimensionless variables) the initial cell and substrate phases are given by

$$\theta_k(x, z, 0) = A_k^{b_2} \left(1 - \tanh\left(\hat{B}_k \left(\hat{x}^2 + \hat{z}^2 - \hat{r}_c^2\right)\right)\right), \quad \text{for } k = C, J. \tag{6.14}$$

As for the circular–shaped and semicircular–shaped constructs, we require the initial conditions given by Equations (6.13) and (6.14) to satisfy Equation (5.42).

We note that an examination of Figure 6.16 indicates that Setups 3 and 4 are very similar; both having semicircular–shaped constructs placed on the base of the well plate. However, the distribution of the constitutive volume fractions is different and so the forcing terms will not be the same. Thus, we expect the spatial distribution of the quantities of interest predicted by the model to be slightly different.

The initial cell phase conditions for the four different setups are plotted in Figure 6.17, where both the full well domain, so that the position of the construct can be seen, and close ups of the construct and the surrounding region are shown. In the following figures we plot the spatial variation of the dependent variables in the construct and surrounding the region only, so that any spatial variation can be clearly seen. The area of the circular–shaped construct is about twice the size of the areas of the three semicircular–shaped constructs. Consequently, the cell and substrate phase volume fractions are about half the size and so the cell and fluid fluxes, pressure and fluid shear stress distributions are of a different magnitude. In the following Setup 1 has a separate colourbar to Setups 2, 3 and 4 so that the spatial variation can be seen.

Figure 6.18 shows the initial common pressure and FSSM distributions in the region around the constructs for the four different setups considered. It can be seen that the pressure variation in

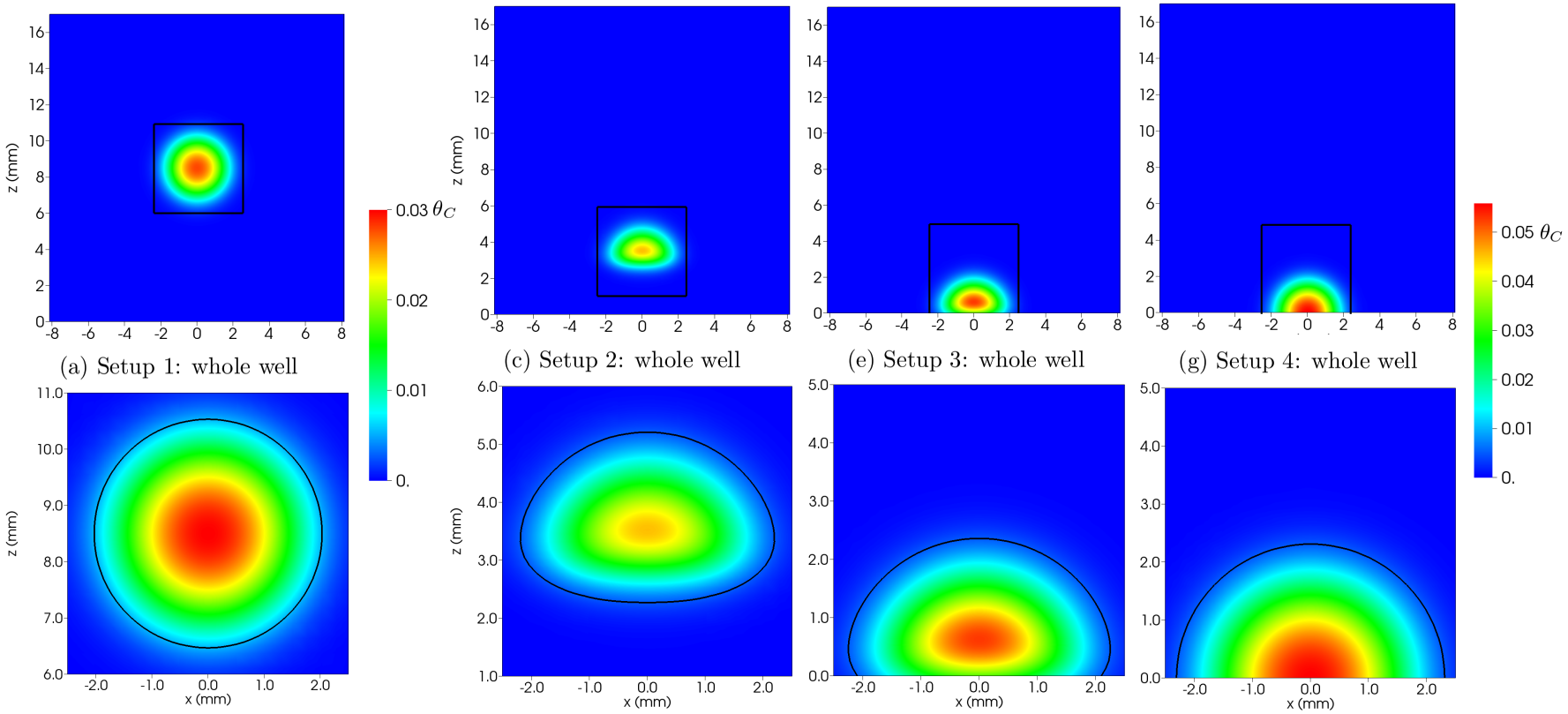

(a) Setup 1: whole well

(b) Setup 1: construct region

(c) Setup 2: whole well

(d) Setup 2: construct region

(e) Setup 3: whole well

(f) Setup 3: construct region

(g) Setup 4: whole well

(h) Setup 4: construct region

Figure 6.17: Cell phase volume fractions for the four setups considered, given by Equations (5.40), (5.41), (6.13) and (6.14), with parameters given in Tables 6.1 and 6.2. The figures in the top row, (a), (c), (e) and (g), indicate the position of the construct within the whole domain. The boxes show the regions plotted in (b), (d), (f) and (h) respectively, where the construct and surrounding region only are plotted so that the region of interest can be easily seen. The black lines in the bottom row of figures show the "edge" of the constructs, where $\theta_C = 0.005$. We note the figures showing Setup 1, (a) and (b), are reproduced from Figure 6.1, and have a different colourbar than Setups 2 – 4, (c) – (h), due the difference in scales so that the spatial variation can be seen. The colourbar on the far right refers to the Figures (c) – (h), describing the cell phase volume fraction for the three semicircular–shaped constructs, Setups 2 – 4.

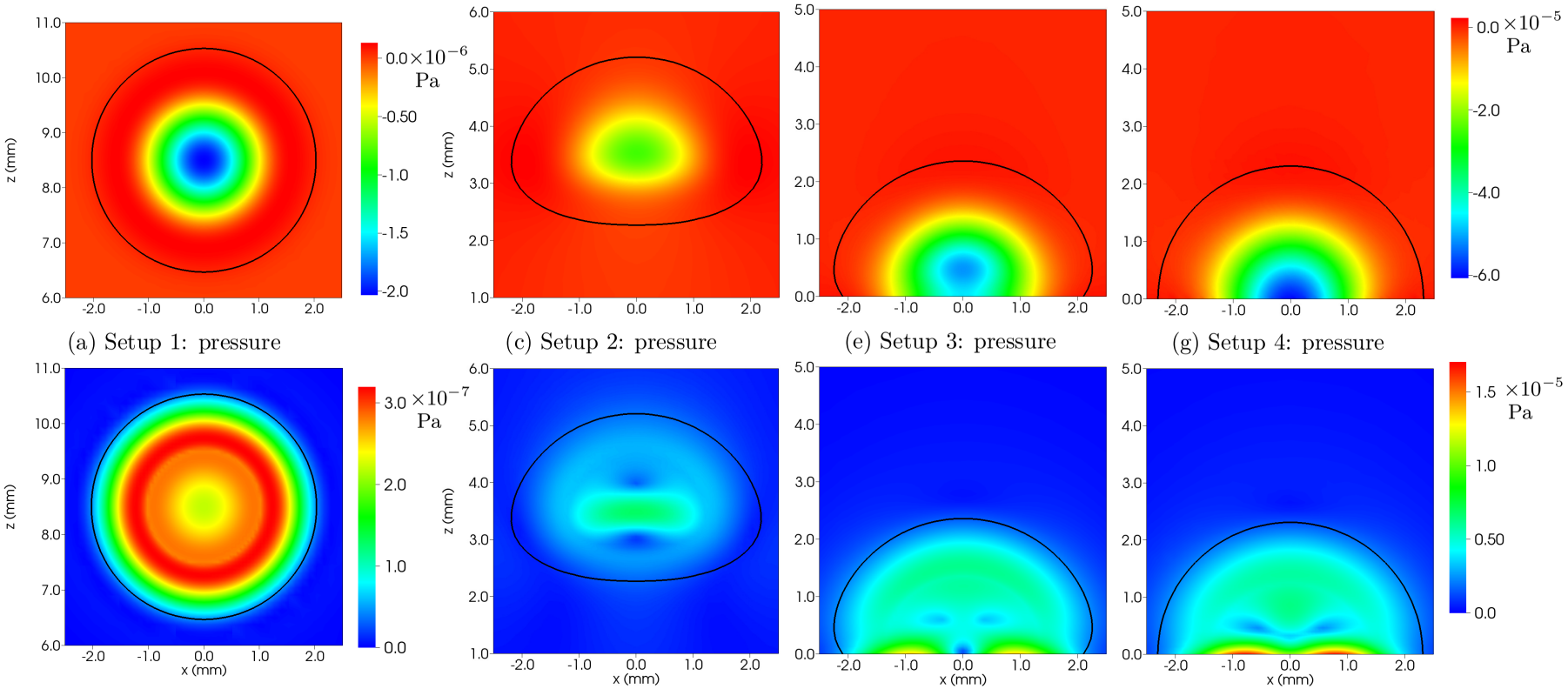

(a) Setup 1: pressure (c) Setup 2: pressure (e) Setup 3: pressure (g) Setup 4: pressure

(b) Setup 1: FSSM (d) Setup 2: FSSM (f) Setup 3: FSSM (h) Setup 4: FSSM

Figure 6.18: Initial common pressure and FSSM distributions in the region of the construct for the four different setups considered. The figures in the top row, (a) (c), (e) and (g), show the common pressure distribution, $p(x, z, 0)$. The figures in the bottom row, (b), (d), (f) and (h), show the distribution of the FSSM, which is measured by the maximum eigenvalue of the fluid stress tensor. The initial conditions are given by Equations (5.40), (5.41), (6.13) and (6.14) for Setups 1 – 4 respectively. Parameters are given in Tables 6.1 and 6.2 with $\nu = \chi = 1$ Pa. The black lines show the "edge" of the constructs, where $\theta_C = 0.005$. We note that, due to the difference in magnitude, Setup 1 has its own colourbars, while the colourbars on the right hand side refers to Setups 2 – 4.

Table 6.2: Dimensionless parameters describing the initial conditions for the semicircle–shaped constructs.

A_C^h	=	0.04531	A_J^h	=	$0.11A_C^h/0.3$
$A_C^{b_1}$	=	0.05258	$A_J^{b_1}$	=	$0.11A_C^{b_1}/0.3$
$A_C^{b_2}$	=	0.04536	$A_J^{b_2}$	=	$0.11A_C^{b_2}/0.3$
$\hat{B}_C = \hat{B}_J$	=	90	$\hat{C}_C = \hat{C}_J$	=	30
$\hat{s}_h$	=	2.9/17			

Setup 4, Figure 6.18(g), is the highest of those considered, with a pressure below the applied pressure at the base of the construct. A similar common pressure distribution is seen for the third setup, Figure 6.18(e). The pressure distribution in the second setup is slightly different, Figure 6.18(c), with pressures below the applied pressure only in the very centre of the construct and almost no deviation from the applied pressure seen on the base of the construct. Setup 1, Figure 6.18(a), similarly has a common pressure lower than the applied pressure in the centre of the construct, with the magnitude of the pressure distribution being an order of magnitude lower than that for the semicircular–shaped constructs. The fourth setup, Figure 6.18(h), also has the highest FSSM of the setups considered, with the highest shear stresses felt at the very base of the construct. Likewise, the highest FSSMs are experienced at the base of the construct for the other gel placed on the base of the well, Setup 3, as can be seen in Figure 6.18(f). The FSSM is maximal in the centre of Setup 2, Figure 6.18(d), while the FSSM predicted by the model is maximal in a band between the centre and the edge of the circular–shaped construct, Setup 1, as can be seen in Figure 6.18(b).

The cell and fluid flux fields in the region of the constructs are plotted in Figure 6.19. It can be seen that for $\nu = \chi = 1$ Pa, the cell flux for all the setups causes the cells to move outwards and fluid to flow into the construct. As $\nu = \chi$ is increased, cell fluxes causing the cell phase to move inwards is predicted by the model as expected from Section 6.1. As in the case for the pressure and FSSM distributions, the magnitude of the cell and fluid fluxes are highest in Setups 3 and 4, where the gel is placed on the base of the well, with the former experiencing marginally higher magnitudes. Again, the circular–shaped construct, Setup 1, Figure 6.19(a), experiences cell fluxes an order of magnitude lower than in the semicircular–shaped setups considered. There is a non–negligible fluid flow outside the construct region in Setup 2, Figure 6.19(d). In

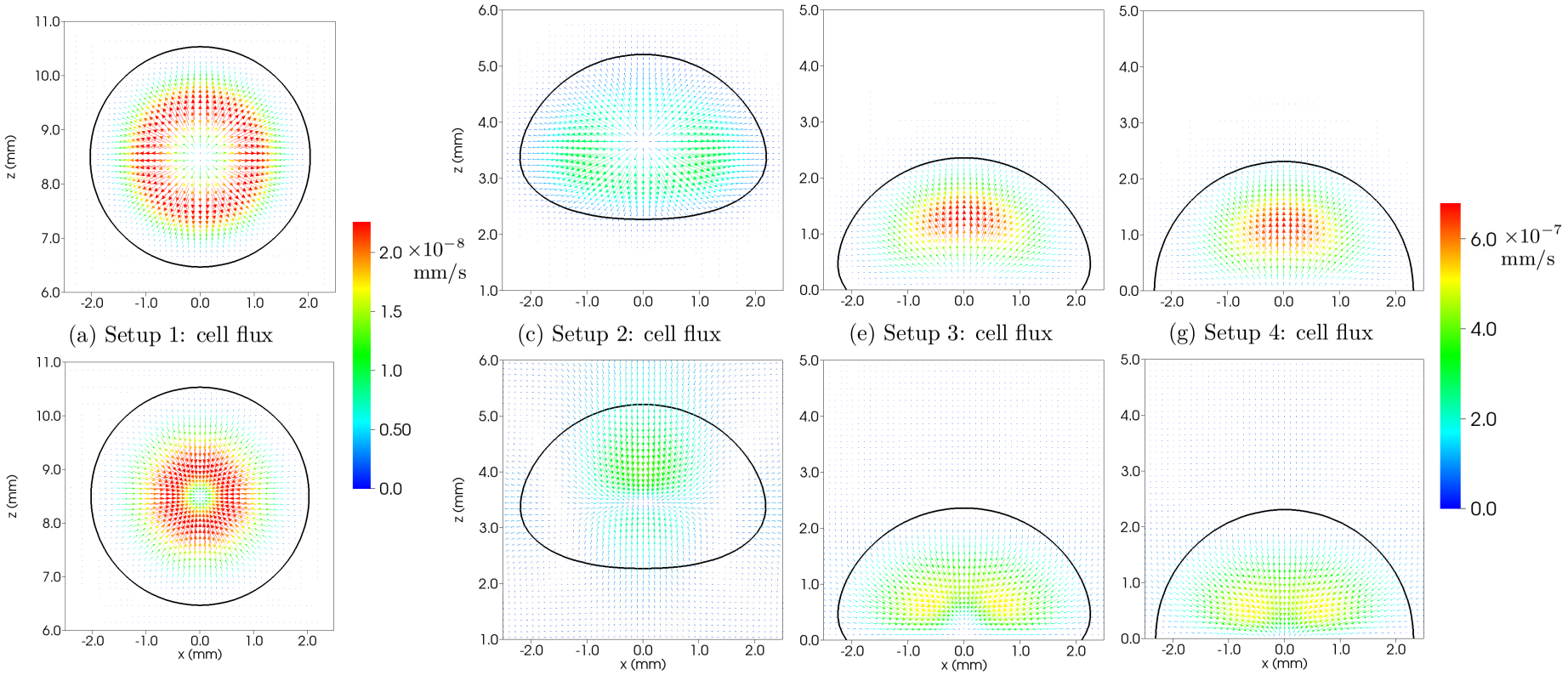

(a) Setup 1: cell flux

(b) Setup 1: fluid flux

(c) Setup 2: cell flux

(d) Setup 2: fluid flux

(e) Setup 3: cell flux

(f) Setup 3: fluid flux

(g) Setup 4: cell flux

(h) Setup 4: fluid flux

Figure 6.19: Initial cell and fluid flux fields in the region of the construct for the four different setups considered. The figures in the top row, (a), (c), (e) and (g), show the cell flux, $\theta_C \mathbf{v}_C$. The figures in the bottom row, (b), (d), (f) and (h), show the fluid flux, $\theta_W \mathbf{v}_W$. The initial conditions are given by Equations (5.40), (5.41), (6.13) and (6.14) for Setups 1 – 4 respectively. Parameters are given in Tables 6.1 and 6.2, with $\nu = \chi = 1$ Pa. The black lines show the "edge" of the constructs, where $\theta_C = 0.005$. We note that, due to the difference in magnitude, Setup 1 has its own colourbar, while the colourbar on the right hand side refers to Setups 2 – 4.

particular, flow occurs at the base of the construct which does not occur in any of the other semicircular–shaped other setups considered, due to them being placed on the base of the well.

6.3 Conclusion

In this chapter we have demonstrated that flow is driven by two terms which model the pressures produced by cell–cell and by cell–substrate interactions. When either of the forcing terms is non–zero, non–zero velocity and pressures distributions are predicted. Due to the form of the forcing terms, flow is generated by spatial variation in the constituent phase volume fractions. We have used FEMs to solve the velocity–pressure system at the initial time step, and presented numerical results in two spatial dimensions for a circular–shaped construct. We have shown how altering the parameters ν and χ, the cell aggregation and substrate affinity parameters, with all other parameters fixed, results in a qualitative change in the cell and fluid flux behaviours in the construct region, changing the direction of cell (and, as a consequence, fluid) movement. In addition, we demonstrated how the cell macroscale viscosity affects the shape of the cell flux solutions.

In order to investigate the effect of the initial conditions, the geometry and placement of the construct and the initial seeding of cells on the velocity and pressure solutions, we considered four different experimental setups. Using the same domain and parameters, except for those parameters describing the initial conditions, we saw how the initial setup significantly alters the velocity–pressure solution, and the shear stress magnitudes. Because of the forms of the cell and the cell–substrate traction forcing terms, the size and shape of the forcing terms are highly dependent on the cell and the substrate initial conditions and in particular their gradient.

Of the four setups considered in Section 6.2, Setups 3 or 4 may seem preferable because of the higher FSSMs. However, the concentration of nutrients and waste products are not included in the current model. When the construct is placed directly onto the base of the well there may be a decrease in nutrient transport to the bottom of the construct because no fluid flow can occur through the base of the well. This could results in a decrease in cell birth and substrate deposition, which would, in turn, alter the fluid velocities through the forcing terms and, consequently, change the shear stress profiles. Inclusion of a nutrient in concentration

could be investigated in future work and is discussed in Chapter 8.

In this chapter we have considered the behaviour of the system at the initial time point, where the cell and substrate volume fractions are known and given by the initial conditions. As time evolves, the cell and substrate volume fractions will change, which will in turn alter the forcing terms. As a consequence, the distribution of the cell and fluid phase fluxes and fluid shear stresses will also evolve. In Chapter 7 we, therefore, extend the work presented in this chapter to consider simulations through time. This allows us to investigate firstly whether there is any difference between the quantities of interest under control and stimulated loading conditions, and secondly whether the construct placement and position has a significant effect on the quantities of interest through time.

Chapter 7

A multiphase model: temporal evolution

In this chapter we present numerical simulations for the multiphase model (introduced in Chapter 5) over time. We illustrate how the constituent phase volume fractions, and the associated fluid shear stress magnitudes, evolve as the experiment progresses. We first consider a semicircular–shaped construct sitting in the transwell insert, which is similar to the setup examined experimentally. We show that the mean and maximal fluid shear stress magnitude are higher under stimulated than under control loading conditions after a six hour time period, which illustrates a mechanism by which there are increased patches of mineralisation under stimulated loading conditions. We then investigate eight different experimental setups under stimulated loading conditions, in order to demonstrate the versatility of our model in making predictions and guiding experimentalists in their choice of experimental setup. Our model predicts that the shape and position of the construct have little effect on the total quantity of cells and substrate through time, but do have a significant effect on the spatial distribution and magnitude of the fluid shear stresses within the bioreactor which are predicted by the model.

In Chapter 6 we demonstrated that two forcing terms, describing cell–cell and cell–substrate

interactions, drive flows and pressure spatial variation in our multiphase model (described in Chapter 5). The forcing terms are functions of the constituent phase volume fractions and their spatial gradients, and an investigation of their effect at the initial time point, where these quantities were known explicitly through the initial conditions, was made. We now investigate the spatial patterning induced by biomechanical effects as time progresses, and examine how the quantities of interest evolve through time and space.

Table 7.1: Default dimensionless parameters used for numerical simulations. All parameters are dimensionless except for the temporal and spatial scaling parameters, k_b and H respectively.

Parameters describing rates					
K_d	=	0.006	K_{jd}	=	0.12
K_1	=	0.57	K_4	=	43.8
Parameters describing the velocity–pressure system					
$\hat{\mu}_C$	=	6.123×10^{-5}	$\hat{\mu}_W$	=	8.002×10^{-8}
$\hat{\beta}$	=	1.505×10^{-5}	$\hat{p}_{\text{app}}$	=	0
$\hat{\delta}_a = \hat{\delta}_b$	=	0.05	$\hat{\nu} = \hat{\chi}$	=	0.002
m	=	1			
Spatial parameters					
$\hat{s}_h$	=	2.9/17	$\hat{r}_c$	=	0.8681/17
$\hat{R}$	=	8.13/17			
Timestep size					
Δt	=	10^{-4}			
Temporal and spatial scaling					
k_b	=	$(60 \times 60 \times 24)^{-1}$ s^{-1}	H	=	17 mm

In this chapter we present numerical solutions for a six hour experiment. Throughout we use the parameter set $\nu = \chi = 2$ Pa and $\delta_a = \delta_b = 50$ Pa, so that the effect of both forcing terms is examined. All parameters are given in Table 7.1. The results presented in this chapter are split into two. In Section 7.1 we present solutions for a semicircular–shaped construct held in the transwell insert. This setup is similar to that used experimentally. We compare the effect of the stimulated to the control loading conditions on the quantities of interest. In Section 7.2 we investigate eight different forms of initial conditions under the stimulated loading conditions in order to predict the effect of the position and shape of the construct on the spatial distributions

of the constituent phases and the FSSM distribution through time.

7.1 The loading conditions

In the following we use the initial conditions for the second setup investigated in Section 6.2 and given by Equation (5.41) with parameters given in Table 6.2. These describe a semicircular–shaped construct in the transwell insert, similar to that used in the experiments described in Chapter 2. The initial cell phase volume fraction is shown in Figures 6.17(c) and (d). As in Chapter 6, we plot the numerical solutions in the region of the construct, illustrated by the box in Figure 6.17(c), so that the spatial distribution of the quantities of interest can be seen.

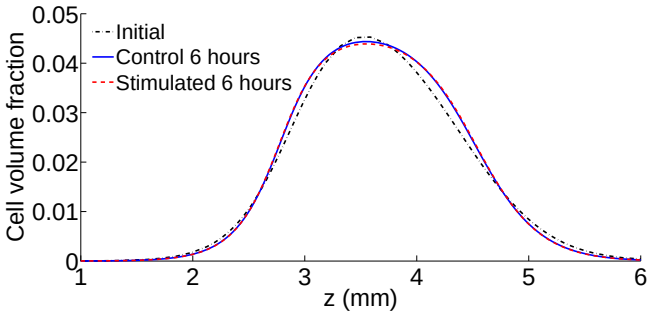

(a) Cell phase

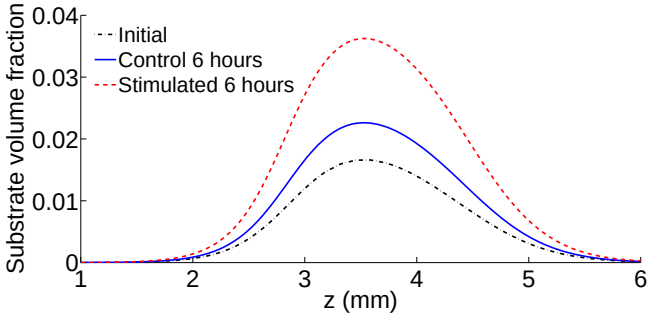

(b) Substrate phase

Figure 7.1: The (a) cell phase, θ_C, and (b) substrate phase, θ_J, volume fractions initially and after 6 hours for both loading conditions along the z–axis. The blue solid and red dashed lines indicate the spatial distribution after 6 hours under control and stimulated loading conditions respectively, and the black dash–dotted lines indicates the spatial distribution at the initial time. Parameters are given in Table 7.1.

Figure 7.1 shows the initial cell and substrate phase volume fractions along the z–axis at the initial time and after six hours under both loading conditions. As time progresses, there is a very slight decrease in the cell volume fraction in the centre of the construct under both

loading conditions, Figure 7.1(a), with cells moving outwards near the centre and inwards at the periphery of the construct due to the form of the cell flux field. As the cell birth and death rates are small in comparison to the length of the experiment, and the magnitude of the cell flux field is also small, the change in the spatial distribution of the cell phase volume fraction over the six hour experiment is minor. In contrast, there is a large change in the substrate phase volume fraction over the first six hours, Figure 7.1(b). As expected, due to the higher substrate deposition rate during the loading periods, the volume fraction of the substrate phase increases faster under stimulated than under control loading conditions, and particularly in the centre of the construct. Recall that, by Equation (5.3), the quantity of substrate deposited is proportional to both the volume fraction of cells and of fluid, and so this faster increase in the centre of the construct is due to the higher volume fraction of cells here than at the edge. The difference in the spatial distribution of the cell phase volume fraction between the two loading conditions after 6 hours is very similar, with the cell volume fraction being slightly lower in the centre of the construct under stimulated than under control loading conditions. This is because, by Equation (5.2), the loading conditions have no direct effect on the cell volume fraction but act through changes in the substrate spatial distribution, which then affects the cell phase volume fraction through altering the quantity of cell birth and the cell flux field.

In order to understand how the total quantity of the constituent phases evolve with time, the average cell and substrate volume fractions are plotted in Figure 7.2. Here we use an equivalent definition to that given by Equation (4.27) for the whole well domain so that the average volume fraction is given by

$$\bar{\theta}_k(t) = \frac{1}{\mathcal{V}} \int_\Omega \theta_k(\mathbf{x}, t)\, \mathrm{d}V, \quad \text{for } k = C, J, \tag{7.1}$$

where $\mathcal{V}$ indicates the area of the domain Ω, $\mathcal{V} = \displaystyle\int_\Omega \mathrm{d}V$. As expected, there is a minimal increase in the average cell volume fraction over the six dimensional hours under both control and stimulated loading regimes, Figure 7.2(a), with a slightly greater increase under the latter loading conditions. Conversely, there is a clear increase in the average substrate volume fraction over time, Figure 7.2(b), with the increase under stimulated loading conditions being significantly greater. This results in there being 58.0% (1 d.p.) more substrate under the stimulated than under the control loading conditions after six hours. For the stimulated case, the periods of loading can be identified with the sharp increase in the average substrate volume fraction in

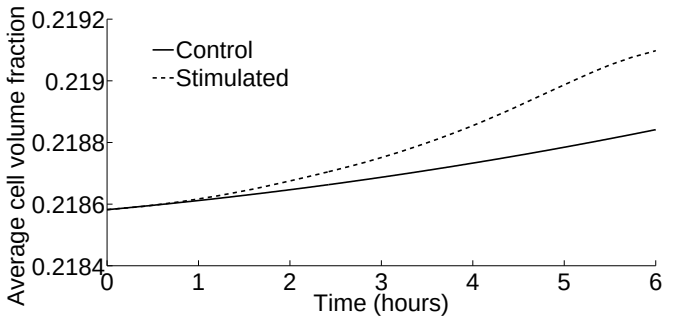

(a) $\bar{\theta}_C(t)$

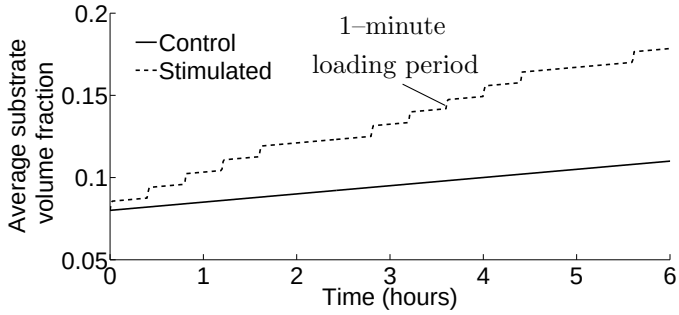

(b) $\bar{\theta}_J(t)$

Figure 7.2: Average (a) cell, $\bar{\theta}_C(t)$, and (b) substrate, $\bar{\theta}_J(t)$, volume fractions through time under both control and stimulated loading conditions, where the average volume fraction of phase k is defined in Equation (7.1). Parameters are given in Table 7.1.

Figure 7.2(b).

In the following we want to measure the heterogeneity of the quantities of interest in the construct. Evaluating the standard deviation over the whole domain is not a representative measure. This can be illustrated as follows. Let us consider two sets of cell phase volume fractions in one spatial dimension for $z \in [0, 17]$ mm, given by

$$\theta_{C_1}(z) = 0.01\left(\tanh(2(z-7)) - \tanh(2(z-10))\right), \tag{7.2}$$

$$\theta_{C_2}(z) = 0.01\left(\tanh(100(z-7)) - \tanh(100(z-10))\right). \tag{7.3}$$

If we evaluate the standard deviation of these over the whole domain, then this measure is lower for θ_{C_1}, at a value of 2.1×10^{-5}, than for θ_{C_2}, at a value of 4.6×10^{-5}. This suggests that θ_{C_2} is more spatially heterogeneous than θ_{C_1}. However, inspecting Figure 7.3 we see that, in the region of the construct, θ_{C_2} is significantly less heterogeneous than θ_{C_1} and, consequently, this measure does not accurately represent what we wish to evaluate. If we consider the standard deviation of the quantities in the construct area only, where $\theta_C \geq 0.005$, then we get a value

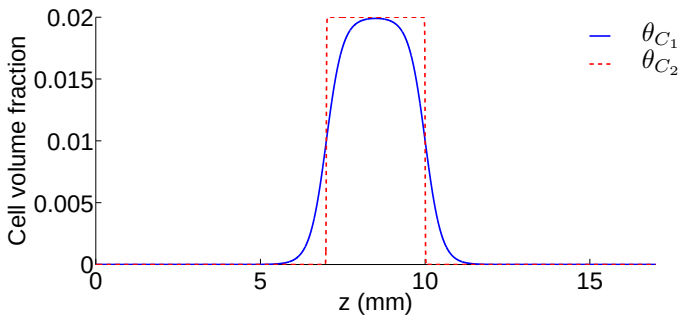

Figure 7.3: An illustration of why evaluating the standard deviation over the whole domain does not accurately represent the spatial distribution of the quantities inside the construct area. The blue solid and red dashed lines illustrate the cell volume fraction given by Equations (7.2) and (7.3) respectively.

of 5.8×10^{-5} for θ_{C_1} and a value of 5.0×10^{-7} for θ_{C_2}. This measure indicates that θ_{C_2} is significantly less heterogeneous in the construct area than θ_{C_1}, as seen in Figure 7.3. Thus, in the following, in order to measure the spatial heterogeneity we evaluate the standard deviation of the quantities of interest in the construct region, where $\theta_C \geq 0.005$.

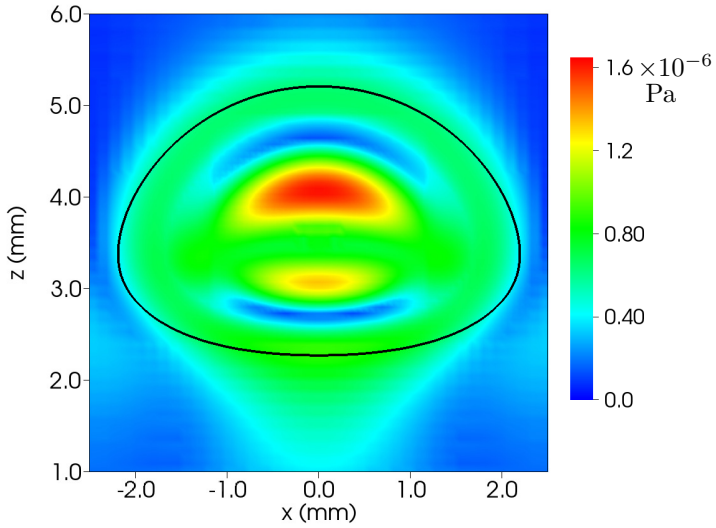

Figure 7.4: The initial distribution of the FSSM, measured by the maximum absolute eigenvalue of the deviatoric part of the fluid phase stress tensor (see Section 5.5), in the region of the construct. Parameters are given in Table 7.1. The black line indicates the "edge" of the cell phase, where we employ the threshold $\theta_C = 0.005$.

We are interested in the spatial distribution of the FSSM and whether this can explain the heterogeneous spatial distribution of the mineralisation seen experimentally, as shown in Figure 2.9. Recall that fluid shear stresses of a large enough magnitude have been recorded as causing increased mineralisation and inducing osteogenesis, as discussed in Section 1.1.3. Thus,

we may wish to see how the mean and maximal FSSM changes in time.

The initial FSSM distribution is shown in Figure 7.4. There are two regions of fluid shear stresses of higher magnitude, below and above the centre of the construct, with the centre of the construct experiencing a lower FSSM. Figure 7.5 shows the FSSM distributions after 6 hours of dimensional time. The mean and the maximal FSSM in construct region are 13.1 % and 17.1 % higher respectively under the stimulated, Figure 7.5(b), than the control, Figure 7.5(a), loading conditions after 6 hours. The increase in the maximal FSSM under stimulated loading conditions can be seen from Figure 7.6, which shows the FSSM in the region of the construct along the z–axis. In particular, the two peaks in FSSM are higher under the stimulated loading conditions than under the control loading conditions. This increase in peak FSSM under the stimulated loading conditions results in the standard deviation of the FSSM being 22.0 % higher under stimulated than under control loading conditions at the end time point.

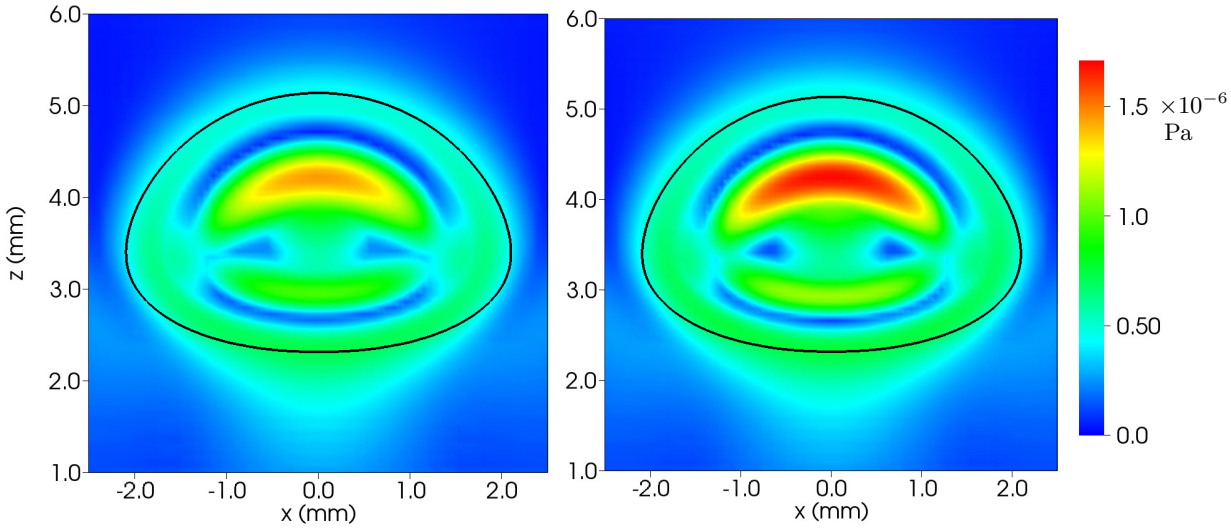

(a) Control (b) Stimulated

Figure 7.5: The FSSM spatial distribution, measured by the maximum absolute eigenvalue of the deviatoric part of the fluid phase stress tensor, in the region of the construct after 6 hours of dimensional time under (a) control and (b) stimulated loading conditions. Parameters are given in Table 7.1. The black line indicates the "edge" of the cell phase, where we employ the threshold $\theta_C = 0.005$.

These larger average and maximal FSSMs under stimulated loading conditions could provide a mechanism to explain the increased mineralisation found experimentally. Furthermore, the higher standard deviation of the FSSMs could explain the heterogeneous distribution of the mineralisation seen experimentally.

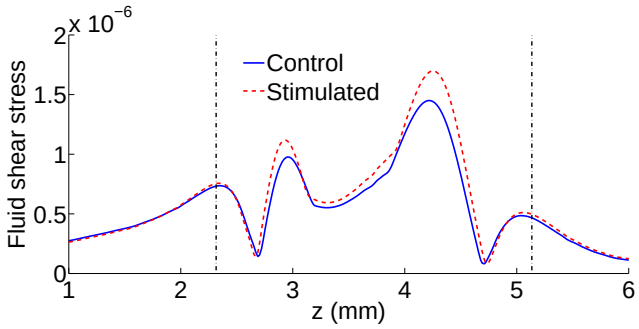

Figure 7.6: A comparison of the FSSM distribution, measured by the maximum absolute eigenvalue of the deviatoric part of the fluid phase stress tensor, after 6 hours of dimensional time along the z–axis, under the two loading regimes. Parameters are given in Table 7.1. The vertical dash–dotted lines indicate the "edge" of the construct, where we employ the threshold $\theta_C = 0.005$.

We know that the magnitude of the forcing term, Equation (6.11), is dependent on the constituent phase volume fractions and their gradients. A comparison of the cell volume fraction distribution between the stimulated and control samples shows little difference after 6 hours, Figure 7.1(a). In contrast, there is an obvious difference in the spatial distribution of the substrate phase volume fraction between the two loading regimes, as can be seen by examining Figure 7.1(b). The mean and standard deviation of the absolute difference in the substrate phase volume fraction between control and stimulated loading conditions after six hours ($|\theta_J^{\text{stimulated}}(\mathbf{x}, t) - \theta_J^{\text{control}}(\mathbf{x}, t)|$ for $t = 6$ hours) in the region of the construct is 41.1 times and 29.1 times larger respectively than the equivalent measures of the cell phase volume fraction. Thus, the difference in the forcing terms, the cell and fluid flux fields, and, as a consequence, the FSSM, between the two loading regimes after 6 hours is predominately due to the difference in the spatial distribution of the substrate phase.

One of the advantages of mathematical modelling and numerical simulations is the ability to test different experimental setups and predict which gives the best results. In the next section we examine eight sets of initial conditions. These describe different shaped constructs in different positions in the well, to investigate how the initial construct configuration affects the spatial distribution of the constituent phases and the FSSM as time evolves. This enables us to examine which setup predicts the best results in terms of the spatial distribution and magnitude of the quantities of interest from those considered. This type of investigation could help direct future experimental procedures.

7.2 Construct shape and position

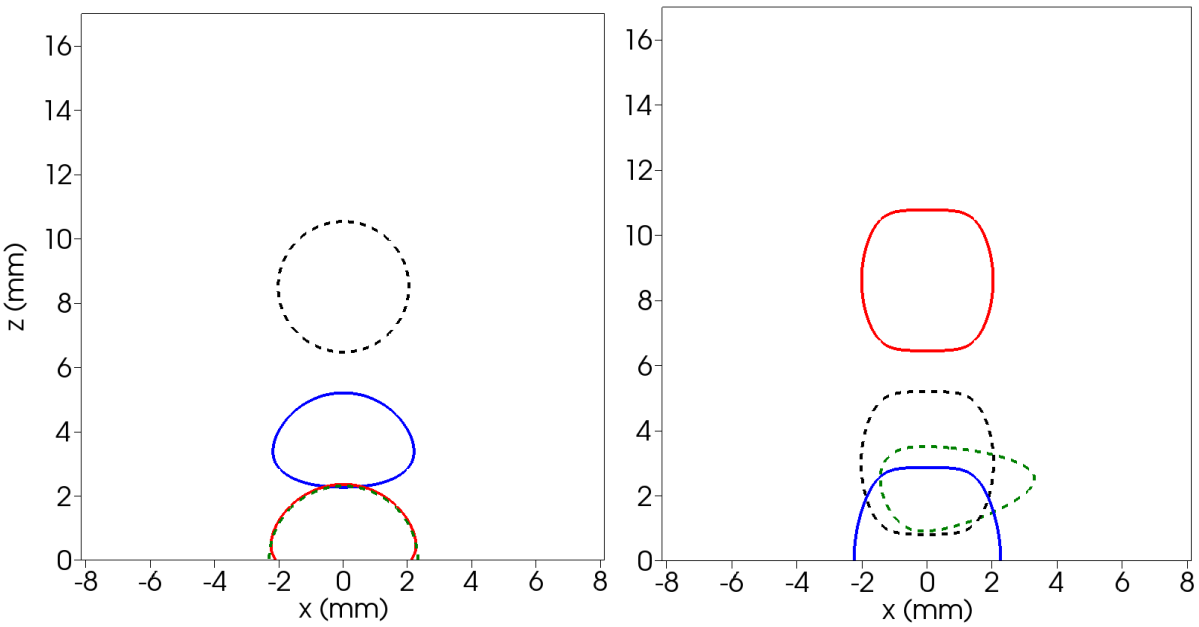

(a) Setups 1, 2, 3 and 4

(b) Setups 5, 6, 7 and 8

Figure 7.7: The full well domain with contours illustrating the position of the constructs for the eight different setups considered. In each the threshold $\theta_C = 0.005$ is plotted in order to indicate the "edge" of the cell phase. Figure (a) is reproduced from Figure 6.16 and shows Setups 1 – 4, as investigated in Section 6.2, where the black dashed, the blue solid, the red solid and the green dashed lines in indicate Setups 1, 2, 3 and 4 respectively. Figure (b) shows the additional setups investigated in Section 7.2, Setups 5 – 8, where the black dashed, the blue solid, red solid and green dashed lines indicate Setups 5, 6, 7 and 8 respectively.

In this section eight different setups are examined under the stimulated loading conditions. We consider the four different setups, one circular and three semicircular, investigated in Section 6.2. Another construct form sometimes used by our experimentalists is a cylindrically–shaped construct. This shape can be achieved by choosing cells and scaffold material that do not contract (or only marginally) once the suspension of cells and scaffold material has been pipetted onto the transwell insert (see Chapter 2 for further details of the experimental methods used to make the gel). In order to represent this type of experimental setup, we additionally consider several "rectangular"–shaped constructs, placed in the transwell insert, on the base and in the centre of the well in Setups 5, 6 and 7 respectively[a]. This enables us to examine the difference in the spatial distribution of the quantities of interest due to the position of the construct within the

[a]We note that these do not look particularly rectangular in shape due to functions of hyperbolic tangent and parameters used in the initial conditions. However, we use the term "rectangular" for ease of reference. If the parameters were changed to give sharper edges to the construct, they would appear more rectangular in shape.

Table 7.2: Percentage change in the standard deviation of the cell and substrate phase volume fractions for the eight different experimental setups considered, in the region where $\theta_C \geq 0.005$, over the six hours of the experiment (2 d.p.). Stimulated loading conditions are considered and parameters are given in Table 7.1.

Setup number	**Percentage change in standard deviation**	
	cell phase volume fraction	**substrate phase volume fraction**
Setup 1	38.73 %	125.21 %
Setup 2	7.55 %	118.51 %
Setup 3	-6.08 %	111.81 %
Setup 4	-8.87 %	110.84 %
Setup 5	47.77 %	135.52 %
Setup 6	13.83 %	120.83 %
Setup 7	50.12 %	134.41 %
Setup 8	-14.22 %	106.29 %

well alone. Finally we consider an asymmetric shape, Setup 8, which allows us to demonstrate how non–symmetric initial conditions affect the evolution of the quantities of interest through time. The total initial quantity of cells and substrate is equivalent for all the setups considered so that Equation (5.19) is satisfied, and, as before, we set the initial substrate phase volume fraction to be proportional to the initial cell phase volume fraction. The initial conditions and parameters used for Setups 5 – 8 are given in Appendix B, and the shapes and positions of the eight constructs within the well may be seen in Figure 7.7. In the following we plot the quantities of interest in the region around the construct so that the spatial distribution may be seen.

The initial and final cell phase volume fractions for the eight setups are shown in Figures 7.8 and 7.9. As in Section 7.1, there is only a small change in the spatial distribution of the cell volume fraction over the six hour time period for all eight setups. As time progresses, the area occupied by the cell phase increases slightly in Setups 3, 4 and 8, Figures 7.8(e) and (f), 7.8(g) and (h), 7.9(g) and (h), and the cell volume fraction in the centre of the construct decreases. These setups describe the semicircular–shaped constructs on the base of the well (Setups 3 and 4) and the asymmetric–shaped construct (Setup 8). This results in the standard deviation of the cell phase volume fraction decreasing over the six hours for these three setups, as can be seen in Table 7.2. In contrast, in the remaining setups (Setups 1, 2, 5, 6 and 7), the area occupied by the cell phase decreases slightly and, consequently, the cell volume fraction in the centre of the construct increases, Figures 7.8(a) and (b), 7.8(c) and (d), 7.9(a) and (b), 7.9(c) and (d),

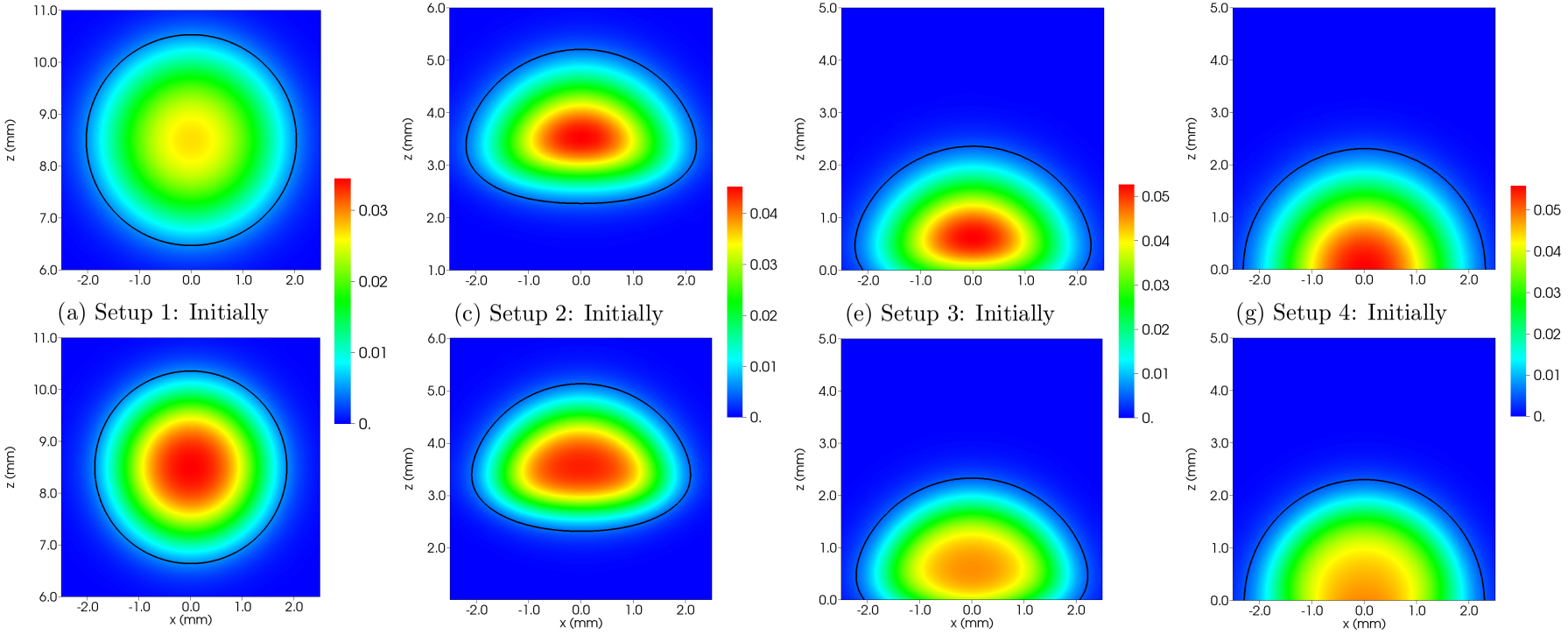

(a) Setup 1: Initially (c) Setup 2: Initially (e) Setup 3: Initially (g) Setup 4: Initially

(b) Setup 1: 6 hours (d) Setup 2: 6 hours (f) Setup 3: 6 hours (h) Setup 4: 6 hours

Figure 7.8: Cell volume fraction, θ_C, in the regions around the constructs for Setups 1 – 4, initially and after six hours. The figures on the top row, (a), (c), (e) and (g), show the spatial distribution at the initial time point. The figures on the bottom row, (b), (d), (f) and (h), show the spatial distribution after six hours of dimensional time. Stimulated loading conditions are considered and parameters are given in Table 7.1. The black contour lines indicate the "edge" of the constructs, where the threshold $\theta_C = 0.005$ is employed.

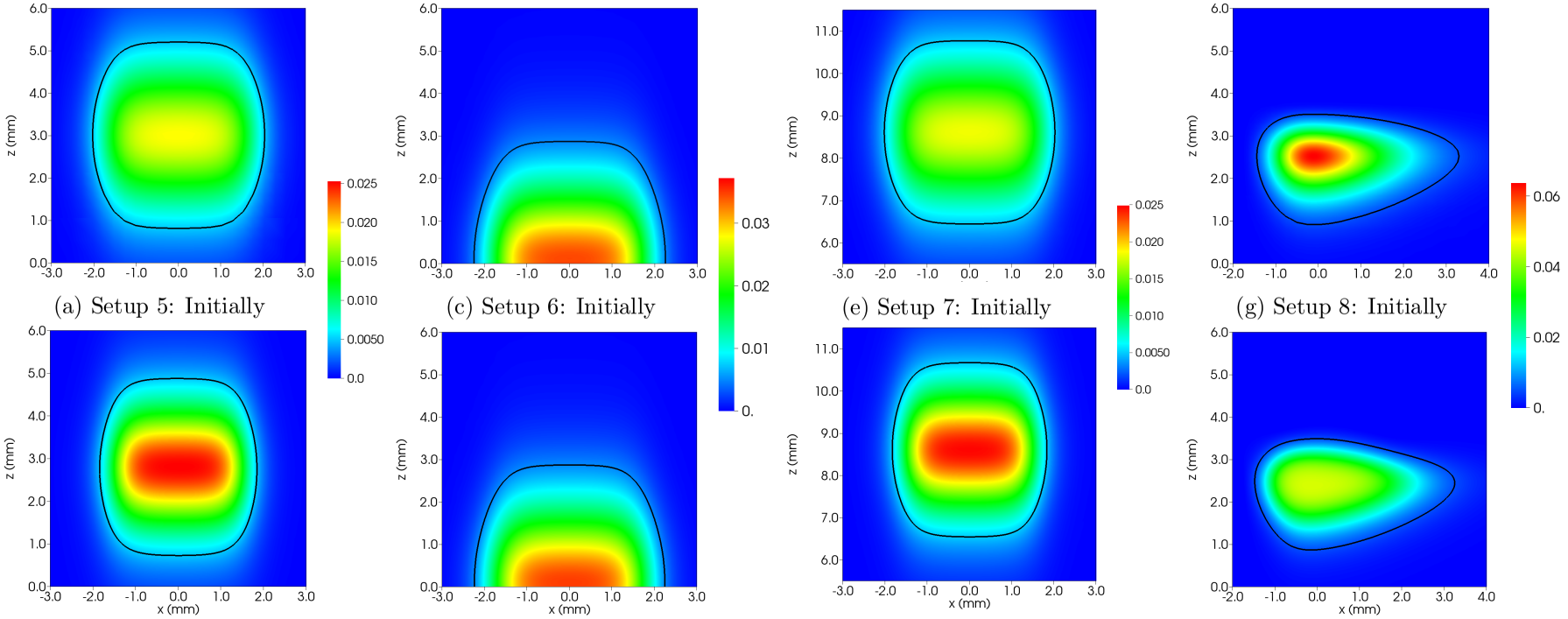

(a) Setup 5: Initially (c) Setup 6: Initially (e) Setup 7: Initially (g) Setup 8: Initially

(b) Setup 5: 6 hours (d) Setup 6: 6 hours (f) Setup 7: 6 hours (h) Setup 8: 6 hours

Figure 7.9: Cell volume fraction, θ_C, in the regions around the constructs for Setups 5 – 8, initially and after six hours. The figures on the top row, (a), (c), (e) and (g), show the spatial distribution at the initial time point. The figures on the bottom row, (b), (d), (f) and (h), show the spatial distribution after six hours of dimensional time. Stimulated loading conditions are considered and parameters are given in Table 7.1. The black contour lines indicate the "edge" of the constructs, where the threshold $\theta_C = 0.005$ is employed.

7.9(e) and (f). This causes the standard deviation of the cell phase volume fraction for these setups to increase with time, as shown in Table 7.2.

Figure 7.10 also illustrates these changes in the size and shape of the cell phase for the different setups, which shows the position of the "edge" of the cell phase initially and after six hours of dimensional time. We note that the change over the first six hours is very minor and hardly visible in the two setups where a semicircular–shaped gel is placed on the base of the well, Setups 3 and 4. Although there is little difference in the position of the edge of the cell phase for these two setups in Figures 7.10(c) and (d), there is a non-negligible decrease in the standard deviation of the cell phase for both, Table 7.2. This is because the cell flux field is large in magnitude at the base of the well, but very small in magnitude at the edge for these setups. Therefore, even though the edge of the construct does not move much, there is evolution of the cell phase spatial distribution inside the construct which can be seen in Figures 7.8(e) and (f), 7.8(g) and (h). Figure 7.10(e) indicates that there is a slight downwards movement of the cell phase as time progresses in Setup 5, the setup of a rectangular–shaped construct placed in the transwell insert. This effect is due to the proximity of the construct to the base of the well. When the rectangular–shaped construct is placed in the centre of the well, Setup 7, the cell flux field below and above the construct is similar (not shown). As a consequence, the cell phase remains centred in the same position as time progresses, as can be seen in Figure 7.10(g).

As in Section 7.1, there is little change in the average cell volume fraction, but a large change in the average substrate volume fraction through time. This can be seen by examining Figures 7.11 and 7.12, which show the spatial distribution in the substrate phase volume fraction at the initial and end time points, for Setups 1 – 4 and Setups 5 – 8 respectively. This is also visible in Figure 7.13, which shows the average volume fraction of the cell and substrate phases through time during the six hour experiment. Due to the large increase in the substrate volume fraction, there is an increase in the standard deviation of the substrate phase through time for all setups, Table 7.2. Those setups that have a cell phase area getting larger show a slightly smaller increase in standard deviation, due to the spreading out of the cell phase. Furthermore, there is very little difference in the curves for the different setups in Figure 7.13, indicating that the initial conditions do not significantly alter the total quantity of substrate and cells over time. Again, the periods of loading can be seen in Figure 7.13 due to the sharp increase in the average

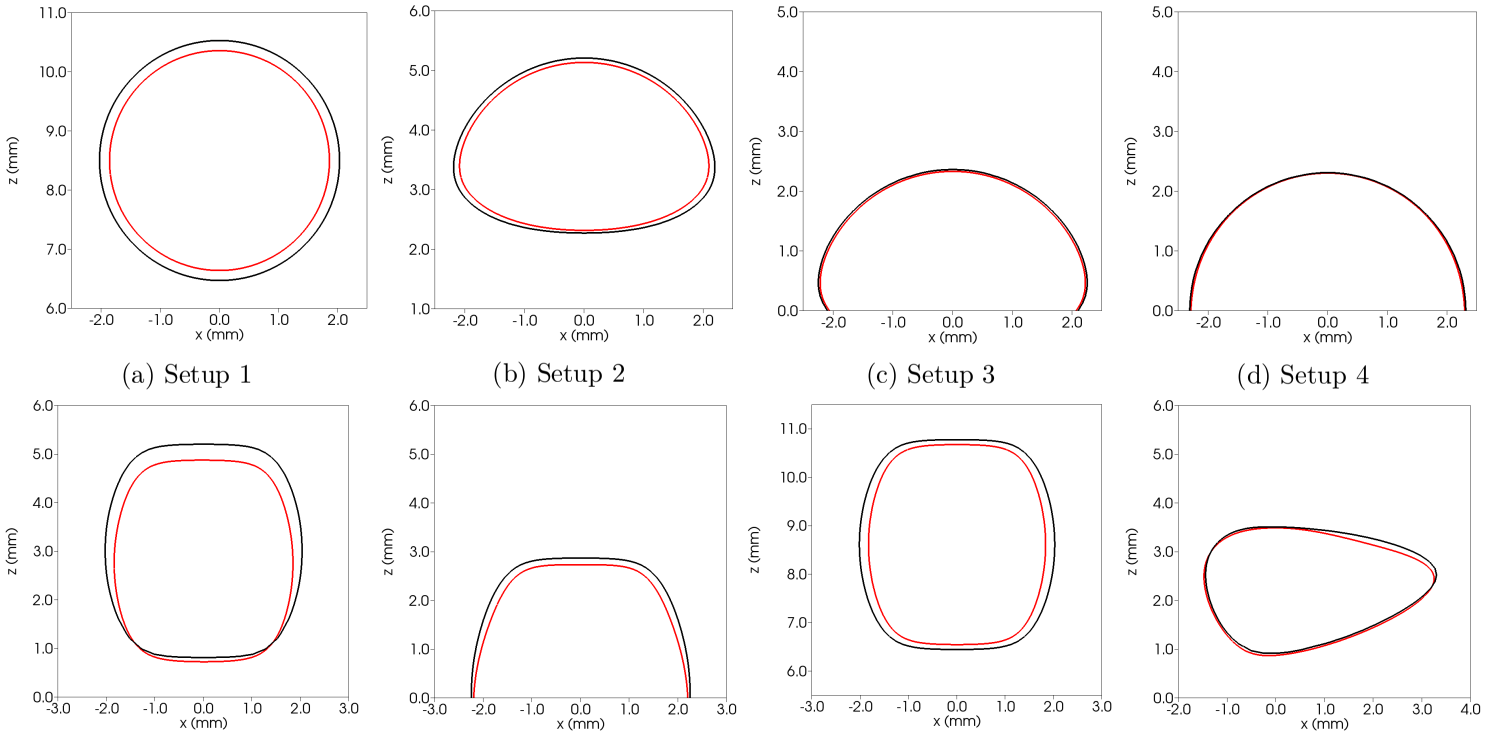

(a) Setup 1 (b) Setup 2 (c) Setup 3 (d) Setup 4

(e) Setup 5 (f) Setup 6 (g) Setup 7 (h) Setup 8

Figure 7.10: Contours illustrating the edge of the cell phase to show how the cell phase moves over the first six hours of dimensional time. The black and red lines illustrate the $\theta_C = 0.005$ contour line initially and after 6 hours respectively. Stimulated loading conditions are considered and parameters are given in Table 7.1.

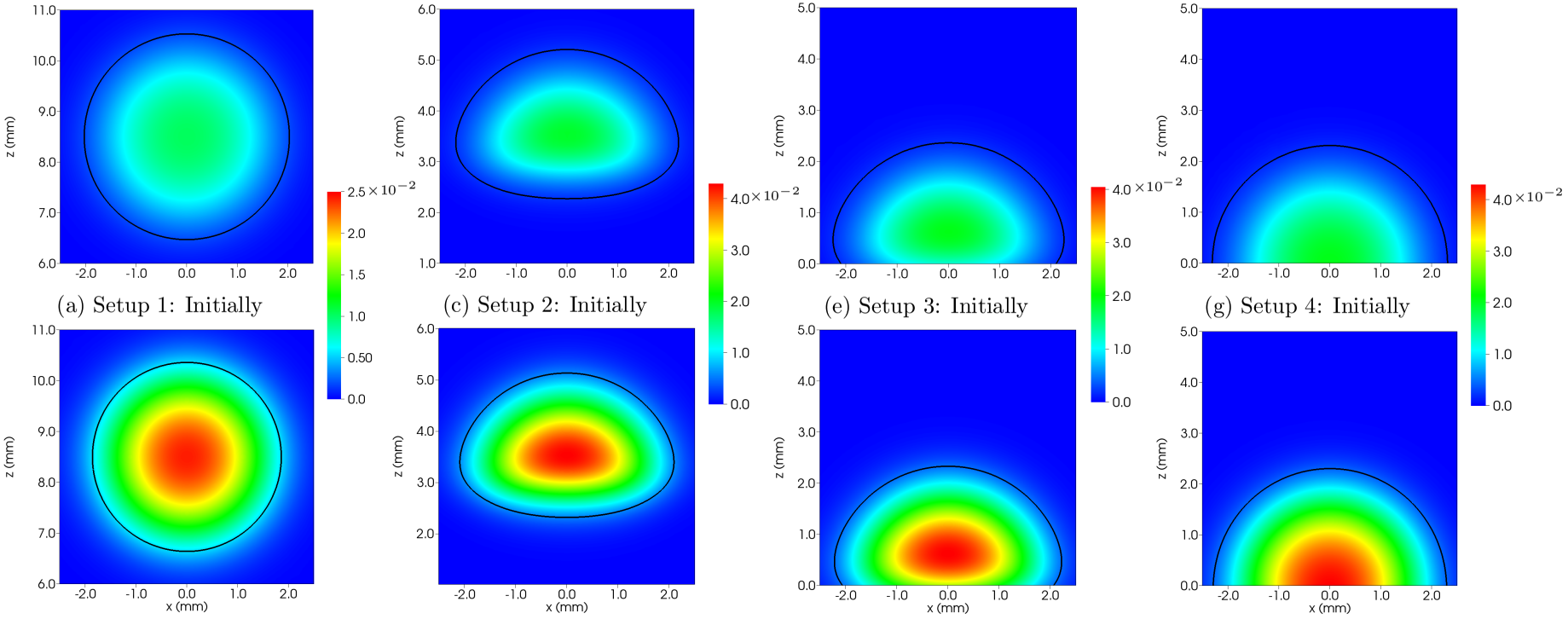

(a) Setup 1: Initially (c) Setup 2: Initially (e) Setup 3: Initially (g) Setup 4: Initially

(b) Setup 1: 6 hours (d) Setup 2: 6 hours (f) Setup 3: 6 hours (h) Setup 4: 6 hours

Figure 7.11: Substrate volume fraction, θ_J, in the regions around the constructs for Setups 1 – 4, initially and after six hours. The figures on the top row, (a), (c), (e) and (g), show the spatial distribution at the initial time point. The figures on the bottom row, (b), (d), (f) and (h), show the spatial distribution after six hours of dimensional time. Stimulated loading conditions are considered and parameters are given in Table 7.1. The black contour lines indicate the "edge" of the constructs, where the threshold $\theta_C = 0.005$ is employed.

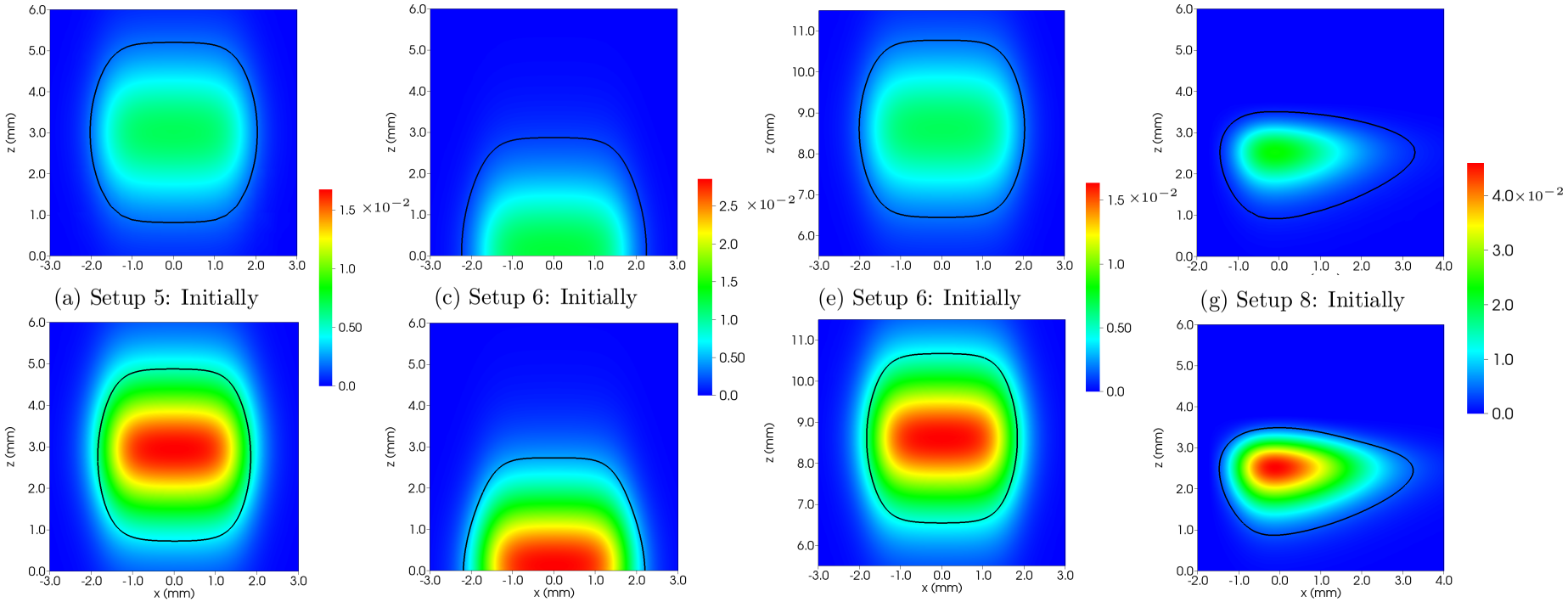

(a) Setup 5: Initially (c) Setup 6: Initially (e) Setup 6: Initially (g) Setup 8: Initially

(b) Setup 5: 6 hours (d) Setup 6: 6 hours (f) Setup 6: 6 hours (h) Setup 8: 6 hours

Figure 7.12: Substrate volume fraction, θ_J, in the regions around the constructs for Setups 5 – 8, initially and after six hours. The figures on the top row, (a), (c), (e) and (g), show the spatial distribution at the initial time point. The figures on the bottom row, (b), (d), (f) and (h), show the spatial distribution after six hours of dimensional time. Stimulated loading conditions are considered and parameters are given in Table 7.1. The black contour lines indicate the "edge" of the constructs, where the threshold $\theta_C = 0.005$ is employed.

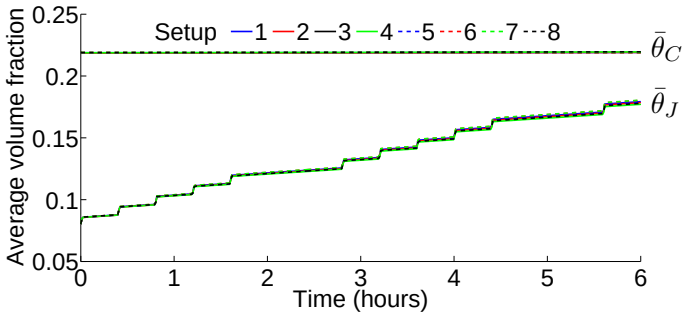

Figure 7.13: Average cell, $\bar{\theta}_C(t)$, and substrate, $\bar{\theta}_J(t)$, volume fraction through time for the eight different setups considered, with the setup number indicated in the legend. The average volume fraction of phase k is given by Equation (7.1). Stimulated loading conditions are considered and parameters are given in Table 7.1.

Table 7.3: The mean FSSM initially and after six hours and the percentage change between the two time points for the eight different experimental setups considered, in the region where $\theta_C \geq 0.005$. Stimulated loading conditions are considered and parameters are given in Table 7.1.

Setup number	**Mean FSSM**		
	Initial (Pa) (2 d.p.)	**After six hours** (Pa) (2 d.p.)	**Percentage change** 1 (d.p.)
Setup 1	1.04×10^{-6}	1.18×10^{-6}	13.2 %
Setup 2	7.19×10^{-7}	6.77×10^{-7}	−5.7 %
Setup 3	8.38×10^{-7}	6.92×10^{-7}	−17.5 %
Setup 4	1.13×10^{-6}	8.69×10^{-7}	−23.0 %
Setup 5	1.90×10^{-6}	1.96×10^{-6}	3.4 %
Setup 6	9.68×10^{-7}	1.08×10^{-6}	11.8 %
Setup 7	7.68×10^{-7}	1.21×10^{-6}	57.8 %
Setup 8	2.58×10^{-6}	1.23×10^{-6}	−52.4 %

substrate phase volume fraction.

The spatial distributions of the FSSM, initially and after six hours for the eight setups considered, are plotted in Figures 7.14 and 7.15. The mean and the standard deviation of the FSSM at the initial and end time points and the percentage change over this time period for the eight different setups are given in Tables 7.3 and 7.4 respectively. Those setups (1, 2, 5, 6 and 7) that have a cell phase decreasing in area over the first six hours show an increase in both the mean and the standard of the FSSM over the same period, except for Setup 2, the setup with a semicircular–shaped construct in the transwell insert, which shows a small decrease in the mean shear stress. Table 7.5 gives the maximum value of the FSSM predicted by the model for the eight setups, and the percentage change over time, and demonstrates that these setups also show an increase in the maximal FSSM over the six hour time period. In contrast, Setups 3,

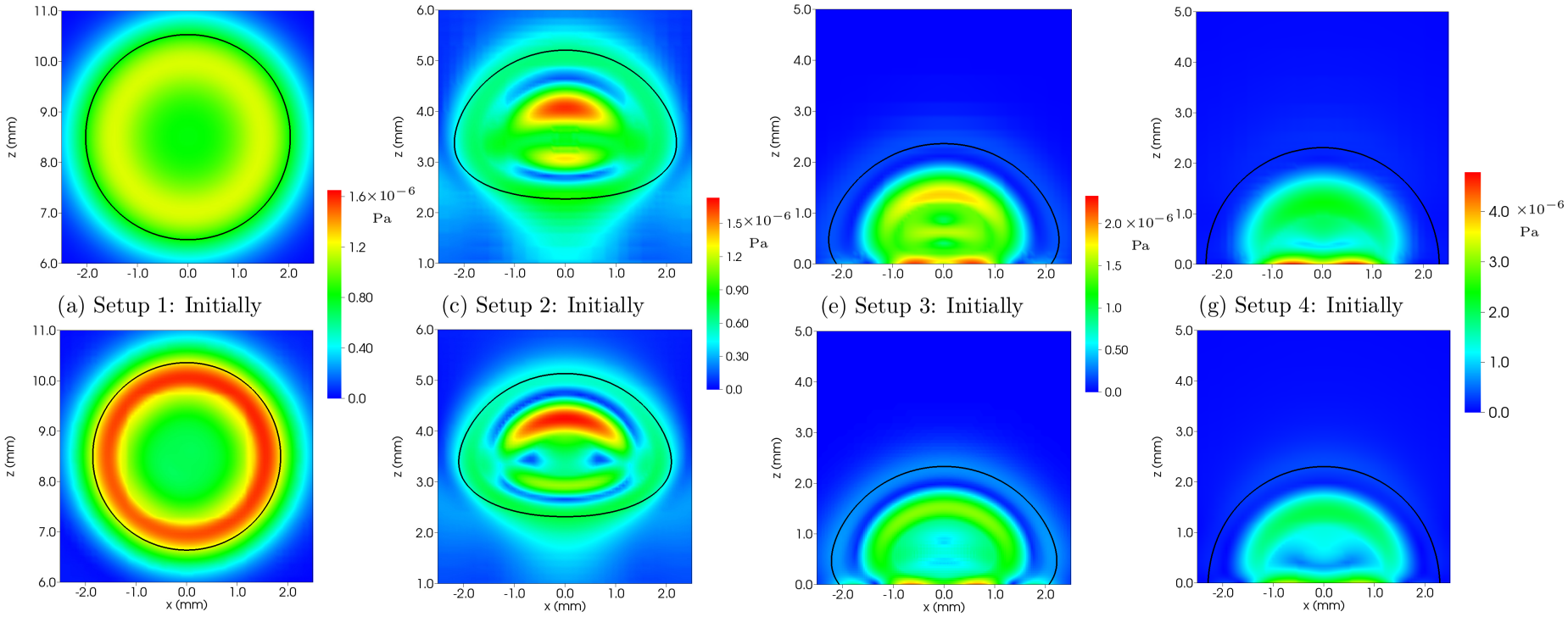

Figure 7.14: Magnitude of the fluid shear stresses (FSSM), measured by the maximum absolute eigenvalue of the deviatoric part of the fluid stress tensor, in the regions around the constructs for Setups 1 – 4, initially and after six hours. The figures on the top row, (a), (c), (e) and (g), show the spatial distribution at the initial time point. The figures on the bottom row, (b), (d), (f) and (h), show the spatial distribution after six hours of dimensional time. Stimulated loading conditions are considered and parameters are given in Table 7.1. The black contour lines indicate the "edge" of the constructs, where the threshold $\theta_C = 0.005$ is employed.

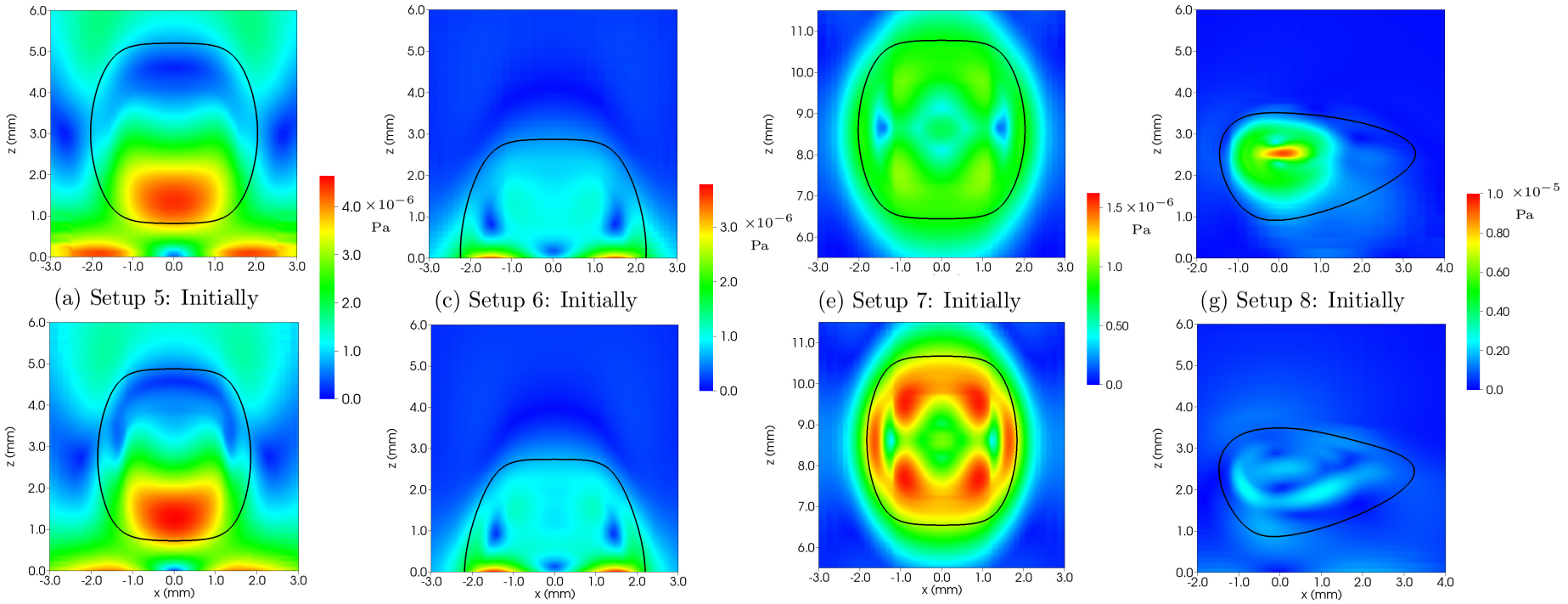

(a) Setup 5: Initially

(c) Setup 6: Initially

(e) Setup 7: Initially

(g) Setup 8: Initially

(b) Setup 5: 6 hours

(d) Setup 6: 6 hours

(f) Setup 7: 6 hours

(h) Setup 8: 6 hours

Figure 7.15: Magnitude of the fluid shear stresses (FSSM), measured by the maximum absolute eigenvalue of the deviatoric part of the fluid stress tensor, in the regions around the constructs for Setups 5 – 8, initially and after six hours. The figures on the top row, (a), (c), (e) and (g), show the spatial distribution at the initial time point. The figures on the bottom row, (d), (b), (f) and (h), show the spatial distribution after six hours of dimensional time. Stimulated loading conditions are considered and parameters are given in Table 7.1. The black contour lines indicate the "edge" of the constructs, where the threshold $\theta_C = 0.005$ is employed.

Table 7.4: The standard deviation of the FSSM initially and after six hours and the percentage change between the two time points for the eight different experimental setups considered, in the region where $\theta_C \geq 0.005$. Stimulated loading conditions are considered and parameters are given in Table 7.1.

Setup number	**Standard deviation in FSSM distribution**		
	Initial (Pa) (2 d.p.)	**After six hours** (Pa) (2 d.p.)	**Percentage change** (1 d.p.)
Setup 1	1.61×10^{-7}	2.92×10^{-7}	81.5 %
Setup 2	2.87×10^{-7}	3.43×10^{-7}	19.5 %
Setup 3	6.25×10^{-7}	4.19×10^{-7}	−33.0 %
Setup 4	8.83×10^{-7}	6.20×10^{-7}	−29.8 %
Setup 5	1.25×10^{-6}	1.33×10^{-6}	6.7 %
Setup 6	4.64×10^{-7}	4.65×10^{-7}	0.3 %
Setup 7	1.56×10^{-7}	2.19×10^{-7}	40.2 %
Setup 8	1.84×10^{-6}	5.08×10^{-7}	−72.5 %

Table 7.5: Comparison of the maximal value of the FSSM distributions initially and after six dimensional hours for the eight different experimental setups considered, in the region where $\theta_C \geq 0.005$. Stimulated loading conditions are considered and parameters are given in Table 7.1.

Setup number	**Maximum FSSM**		
	Initial (Pa) (2 d.p.)	**After six hours** (Pa) (2 d.p.)	**Percentage change** (1 d.p.)
Setup 1	1.27×10^{-6}	1.60×10^{-6}	20.1 %
Setup 2	1.66×10^{-6}	1.71×10^{-6}	2.9 %
Setup 3	2.33×10^{-6}	1.97×10^{-6}	-18.3 %
Setup 4	4.78×10^{-6}	3.10×10^{-6}	-54.3 %
Setup 5	4.43×10^{-6}	4.64×10^{-6}	4.5 %
Setup 6	3.49×10^{-6}	3.78×10^{-6}	7.7 %
Setup 7	1.08×10^{-6}	1.62×10^{-6}	50.0 %
Setup 8	9.49×10^{-6}	2.65×10^{-6}	-258.1 %

4 and 8, which show a cell phase increasing in area over this time period, show a decrease in the mean, the maximal value and the standard deviation of the FSSM predicted by the model. This can be explained thus: for the setups that show the area occupied by the cell phase getting smaller, the volume fraction of the cell phase increases in region of the construct. This causes the gradient of the cell phase volume fraction to increase in magnitude, which increases the magnitude of the forcing terms. As a result the magnitude of the cell and fluid fluxes and, consequently, the FSSM increase. Conversely, those setups that show the area occupied by the cell phase getting larger also show a decrease in the volume fraction of the cell phase, and a decrease in the magnitude of the cell volume fraction gradients. This causes the magnitude of the forcing terms and, as a consequence, the cell and fluid fluxes and the fluid shear stresses, to decrease in magnitude.

The spatial distribution of the cell and substrate phases volume fractions for Setups 5 and 7 are similar, both being rectangular in shape and surrounded by fluid, the main difference being the position of the construct in the well. However, the spatial distribution and the FSSM for the eight different setups are markedly different, Figures 7.15(a) – (b) and (e) – (f). This is due to the proximity of the construct in Setup 5 to the base of the well, and the no–flux and no–slip boundary condition employed there, given by Equation (5.37). In particular, this causes maximal FSSMs at the base of the construct in Setup 5, whereas the fluid shear stresses predicted for Setup 7 are maximal in magnitude around the whole periphery of the construct. Such results indicate the importance of placing the construct away from the well walls to allow sufficient flow around all sides of the developing construct and prevent such edge effects occurring.

Tables 7.3 and 7.5 indicate that mean and maximal FSSM are highest initially in Setup 8, the setup with the asymmetric–shaped construct. However, the fluid shear stresses show the largest decrease in the maximal value and the mean over the six hour experiment for this setup, as can be seen by comparing Figures 7.15(g) and (h). In contrast, the mathematical model predicts that Setup 5, the setup of a rectangular–shaped construct held in the transwell insert, has the highest mean and maximal values of FSSM after six hours, and Setup 7, the setup of a rectangular–shaped construct held in the centre of the well, shows the greatest increase in both the mean and the maximal values of FSSM over the six hour time period. Further, the setup of the rectangular–shaped construct placed in the centre of the well (Setup 7) shows the

lowest standard deviation in the FSSM after 6 hours, which could result in a more homogeneous spatial distribution of mineralisation than for the other setups.

7.3 Conclusions

In this chapter we have presented numerical results through time for the model introduced in Chapter 5 for a six hour experiment, which is a long enough period of time to see a change in the results. In Section 7.1 we considered the effect the loading conditions have on the spatial distribution of the quantities of interest over time. We demonstrated that both the maximal and average FSSM are higher under stimulated loading conditions after 6 hours than under control loading conditions. In particular, there are two regions of higher FSSM, above and below the centre of the construct. A spatial distribution in FSSM similar to this could explain the heterogeneous spatial patterning in the mineralisation seen experimentally.

In Section 7.2 we considered eight different sets of initial conditions and investigated the effect the position and shape of the construct has on the constituent phase volume fractions and the FSSM over the first six hours. We demonstrated that the initial conditions have little effect on the average volume fraction of the cell and substrate phases, and, as a consequence, the total quantity of cells and substrate, as time progresses. In contrast, Figures 7.14 and 7.15 illustrate that the initial conditions have a substantial effect on the distribution of the FSSM as time evolves. Of those setups considered, a setup of a rectangular–shaped gel in the centre of the well gives the greatest increase in the maximal value of the FSSM over the first six hours, as well as the lowest standard deviation of the FSSM after six hours. However, this setup also shows one of the highest percentage increases in standard deviation over the six hour time period and so over a longer time period the distribution of FSSMs predicted by the model may be one of the more heterogeneous of the setups considered. In contrast, a setup of a rectangular–shaped gel on the base of the well, Setup 6, shows the most constant standard deviation of fluid shear stresses over time. In particular, we have demonstrated that placing the construct close to the sides of the well can result in non–symmetric spatial distributions of FSSMs. As a consequence, we suggest that the construct be placed as centrally in the well as possible.

7.4 Discussion

In addition to the assumptions discussed in Section 5.8, we highlight here those assumptions that are relevant to the time–dependent results in this chapter.

The kind of investigation performed in Section 7.2 could be used to optimise the shape and position of the construct in the well in order to either maximise the magnitude of the fluid shear stresses, or minimise the spatial variation in the substrate phase volume fraction and FSSM distributions. In the above investigations we have set the substrate phase volume fraction initially to be a multiple of the initial cell phase volume fraction. In addition, we have investigated initial conditions for the cell and substrate phase volume fractions that are maximal in the centre of the constructs. For clinical applications the shape and size of the construct would normally be determined by the desired shape of the implant. Future work could involve altering the seeding strategy and initial ratio of cells to substrate for a given construct shape in order to investigate the optimal seeding strategy and construct placement.

In these chapters we have chosen the cell aggregation, substrate affinity, intraphase and interphase repulsion parameters, ν, χ, δ_a and δ_b, to illustrate behaviour rather than basing their values on experimental data. Furthermore, we increased the size of the fluid phase macroscale viscosity and used an averaged form of the substrate deposition rate in order to aid numerical simulation. In order to allow quantitative predictions to be made, experimentally relevant parameters and experimental validation of the mathematical model need to be made. This would enable us to examine whether the magnitude of the fluid shear stresses predicted by the model are within the range recorded experimentally (10^{-4} – 1.2 Pa [McCoy and O'Brien, 2010]) as inducing osteogenesis and increasing mineralisation *in vitro*. We have demonstrated that the FSSM distribution can explain a patchy spatial distribution of mineralisation. However, the model does not predict higher FSSMs at the rim of the construct for the setup with a semicircular–shaped gel placed in the transwell insert, which is similar to that used experimentally. Therefore, it cannot, alone, explain the particular distribution in mineralisation seen experimentally. In contrast, a rim of increased FSSM is seen in the circular–shaped construct held in centre. Future work could involve expanding this model to allow for a FSSM–dependent substrate deposition term and using experimentally relevant parameters. This would allow an

investigation of how the fluid shear stresses alter the spatial distributions of the constituent phase volume fractions. In this work we have run numerical simulations on a 2D domain, the cross section of the well. Running simulations in three spatial dimensions could predict an alternative spatial distribution of FSSM. However, due to the number of degrees of freedom, this would require substantial code development, and is discussed in Chapter 8.

Chapter 8

Conclusions and discussion

8.1 Contributions of this thesis

The aim of this thesis was the development of mathematical models and the use of numerical simulation in order to further understand the experimental setup of an adult human MSC seeded collagen gel placed in a hydrostatic bioreactor, with hydrostatic pressure stimulus used to develop the construct into a bone–like material.

As discussed in Chapter 1, there are no known mathematical models for investigating the effects of hydrostatic pressure on tissue engineered bone. We developed a suite of three related mathematical models of increasing complexity, each investigating different aspects of the experimental setup.

The first step in this thesis was to characterise the response of bone–producing cells to hydrostatic pressure quantitatively in order to answer the first question posed in Chapter 1: "given that bone–producing cells respond to elevated levels of hydrostatic pressure by increasing mineralisation, are the effects of the cell memory of the loading history important?" In Chapter 3 we developed the mass transfer terms that are used throughout the thesis. These included the effects of cell birth, cell death, substrate deposition and substrate degradation, where the substrate deposition rate was pressure–dependent. We demonstrated in Section 3.2 that including the effects of cell memory is important to prevent an overestimation of the quantity of substrate deposition when the developing construct is exposed to pressures above the pressure threshold

for extended periods of time. In order to determine which experimental strategy produces the best end product, measured by the quantity of substrate at the end time under stimulated over control loading conditions, the parameterised model was then used to test different seeding strategies and the frequency and amplitude of the intermittent cyclic loading conditions. Suggestions for further development of the mass transfer terms are proposed in Section 8.2.1. This would enable other experimentally variable parameters, such as the length of each session of loading within the bioreactor, to be optimised. Further potential validation of the results of the mathematical model is discussed in Section 8.2.2.

The spatial distribution of the solid substrate within a tissue engineered bone product is highly important in determining its quality. Bone is load–bearing within the body and for a bone implant to be useful and to carry weight the mineralised matrix cannot be too heterogeneous.

To address the second and third questions posed in Chapter 1: "does the loading strategy influence the spatial distribution of cells and ECM deposition and mineralisation?" and "what factors, biochemical or biomechanical, contribute to the heterogeneous spatial distribution of mineralisation seen experimentally?" we considered two separate spatio–temporal models.

1. The first of the spatial models, considered in Chapter 4, was a reaction–diffusion model where cell birth and substrate deposition were dependent on the concentration of a nutrient to investigate biochemically–induced spatial variation. Oxygen was chosen as the rate–limiting nutrient and it was demonstrated that, as time evolves, a heterogeneous substrate phase develops qualitatively similar to that seen experimentally.

   The model demonstrated that the intermittent cyclic loading strategy produced more substrate than the control loading conditions overall, but that the control conditions produced a more uniform substrate phase.

2. In the second of the spatial models, a multiphase model, we tested the hypothesis that the magnitude of the fluid shear stresses is related to the heterogeneous spatial distribution of mineralisation seen experimentally. The model was introduced in Chapter 5 and the results were presented in Chapters 6 and 7. It was demonstrated that flow is driven by the additional pressures produced by cell–cell interactions and cell–scaffold interactions along gradients in the constituent phase volume fractions. The effect of the parameters

describing the behaviour of these two terms on the initial velocity and pressure solutions was investigated in Chapter 6. In Chapter 7 numerical simulations through time were presented. Results indicated that the mean and maximal magnitude of the fluid shear stresses are higher under stimulated than control loading conditions. In addition, eight different experimental setups were considered to illustrate the effect of the position and shape of the construct on the spatial distribution of the quantities of interest over time.

These results indicated that, although the quantity of substrate is increased under stimulated loading conditions, it is more spatially heterogeneously distributed than under control conditions. Taken together, these two models demonstrated that both nutrient gradients and magnitudes of fluid shear stresses could be separately responsible for a spatially patchy substrate phase. However, for the initial conditions and parameters investigated, the spatial distribution of the magnitude of fluid shear stress was not sufficient to predict the spatial distribution in the mineralisation seen experimentally.

We now proceed to a discussion of ways in which this work could be extended in order to improve the above models and address outstanding questions.

8.2 Future work

There are significant areas for further development of the research presented in this thesis. We propose some avenues for future work, including the relaxation of some of the assumptions made in the formulations of the models. The future work is split into three sections: mathematical modelling, experimental and numerical developments. These are discussed in Sections 8.2.1, 8.2.2 and 8.2.3 respectively.

8.2.1 Model development

We propose some model developments which could be included in future to improve the accuracy of the mathematical models presented in this thesis. We first discuss increasing the number of phases before proposing possible improvements to the mass transfer terms and the material assumptions.

Increasing the number of phases

In this thesis we made the assumption that the constituents in the experimental setup can be represented by three separate phases: cells, substrate and fluid. Because the collagen gel is seeded with MSCs, which are multipotent cells, there will be several different types of cells due to their varying degrees of differentiation within the construct. These different cell types will include MSCs, preosteoblasts, osteoblasts and osteocytes and could be modelled by separate cell populations. This would allow various cell attributes (such as particular cell birth, cell death, substrate deposition and substrate degradation rates) to be associated with different cell populations. In addition we could account for interactions between the different cell types; for example, differentiation from one cell type into another, and the communication between the osteocytes, the main mechanosensors, and the osteoblasts, which deposit bone. Furthermore, the time delays needed for differentiation, as in Carlier *et al.* [2011], and the asymmetry of stem cell division could be included [MacArthur, 2004, Sengers *et al.*, 2007b].

The substrate phase in the models in this thesis encompassed the initial collagen scaffold and any deposited mineralised ECM. In order to compare the mathematical and experimental results we assumed that any increase in substrate volume fraction from the initial condition was equal to the mineralised volume, as discussed in Chapter 2. Future work could involve modelling the deposition of the matrix and its mineralisation as separate processes, as in Carlier *et al.* [2011]. Inclusion of such a distinction between ECM and mineralisation could lead to more precise predictions. However, it is not currently possible to distinguish experimentally between the initial scaffold and ECM, and so it is difficult to quantify the amount of ECM deposition. Consequently experimental validation of such inclusions is not currently possible.

Mass transfer terms

In Chapter 3 we hypothesised that the substrate deposition rate took the form presented in Equation (3.36). This included a decay term so that the rate of substrate deposition decreases with the length of time for which the applied pressure has been above a threshold. An extension of this to include spatial effects, as given in Equation (4.6), was considered in Chapter 4. As discussed in Section 3.4, the form of the substrate deposition term given in Equations (3.36)

and (4.6) assumes that cells respond instantly to any pressure changes. In addition, no recovery period is included and we assume that there is no limit to the amount of stimulation to which the cells will respond positively. For that reason, the mathematical model predicted that the best loading strategy would be to apply cyclical loading constantly to the construct. In addition the model predicted that increasing the frequency of loading results in ever–increasing gains of the volume fraction of substrate under stimulated when compared with control loading conditions, as shown in Figure 3.23. Including a stimulation saturation and recovery term would mean that we could optimise the quantity of substrate deposited under stimulated compared to control loading conditions, for the length of the time of loading within the bioreactor. The inclusion of a small delay to allow for the cellular sensing of pressure changes would result in more accurate results at high frequencies of loading. We note that an averaged form of the substrate deposition rate with memory effects, as given in Equation (5.5), was used in the temporal simulations in Chapter 7 in order to aid numerical computation. Here the rate of substrate deposition for the times the construct is in the bioreactor, k_4, is dependent on the frequency and amplitude of the cyclic loading employed. This could be extended to a form including memory effects in future work, to enable an investigation of the effects of the amplitude and frequency on the quantities of interest for the multiphase model.

As the applied pressure exerted by the bioreactor is within physiological ranges we did not include pressure–dependent cell apoptosis. This is known to occur at very high hydrostatic pressures as discussed in Section 1.1.4. A consequence of this is that the model predicted that an increase of the amplitude of cyclic loading always results in an increase in the quantity of substrate deposited for stimulated samples compared to control samples, as can be seen in Figure 3.22. Future work could include pressure–dependent cell apoptosis and also an investigation of a pressure–dependent cell birth rate.

It is known that fluid shear stress stimulates the cellular differentiation of preosteoblasts into osteoblasts and increases both osteoblast proliferation and mineralisation [Lee *et al.*, 2011, Yeatts and Fisher, 2011, McCoy and O'Brien, 2010]. These effects were not included in the mass transfer terms proposed in this thesis. Future work could include the examination of the dependence of growth on the fluid shear stress magnitude by altering the substrate deposition rate in the multiphase model in Chapter 7, in a similar manner to Osborne *et al.* [2010], O'Dea

et al. [2010] and Shakeel *et al.* [2013]. This would enable the effect of fluid shear stress magnitude on construct development and spatial distribution through time to be investigated.

In Chapters 6 and 7, in order to examine the qualitative effects of biomechanically–induced spatial patterning in isolation, we assumed that all nutrients were well perfused in the fluid phase, and waste products were adequately removed to prevent their build up and adverse effects. The results presented in Chapter 4 demonstrated that the inclusion of a diffusible nutrient with nutrient–dependent mass transfer terms influences the spatial distribution of the constituent phases. It would be interesting to include the effects of nutrient depletion and waste product build–up in the multiphase model in future work to see whether inclusion of nutrient–dependent mass transfer terms significantly influences the spatial distribution of the fluid shear stress magnitudes predicted by the model. It is relatively straightforward to add the diffusion of chemicals in solution into a multiphase framework, for example as in Breward *et al.* [2002] and Lemon and King [2007a], although such inclusions would result in a decrease in the speed of the numerical simulations. The effects of osteogenic growth factors on the quantity of substrate deposition could also be investigated in future work.

Rheological/material properties

In Chapters 5 – 7 we assumed that the cell and fluid phases act as viscous fluids and that the substrate is a stationary rigid body. The macroscale viscosity parameters in the literature suggested that there is a very large difference in magnitude between the cell and fluid phases (7×10^6). We sought to represent the experimental setup qualitatively and, in order to aid numerical computation, we increased the fluid phase viscosity so that the difference between the two values was of the order of 10^3. Future work could include asymptotic analysis in order to exploit the difference in scales between the macroscale viscosity parameter for the cell and the fluid phases.

The form of the conservation of momentum equation, Equation (5.7), in the multiphase framework gave stress tensors in general form. We could, therefore, investigate different material assumptions for the phases. Tissues contain solid, fluid and elastic elements, show complex, non–linear responses to stresses, shears and biochemical signals [Verdier *et al.*, 2009] and do not

follow Hooke's law [Humphrey, 2003]. While it is obviously appropriate to model the culture medium as a viscous fluid, it may be more suitable to model the cell and substrate phases as different materials. Modelling the substrate as an elastic or poroelastic material may be more suitable because of the elastic and porous properties of the substrate. This would allow us to consider the effect of pressure–induced compression and deformation. The theory of porous media has been used to model a wide variety of biological tissues [Kapellos *et al.*, 2010]. Several works consider the effects of compression on cartilage including Mow *et al.* [1980], Klisch *et al.* [2003], Sengers *et al.* [2004] and Lai *et al.* [1991]. However, little work has been done on the effects of compression on bone tissue.

In order to derive the conservation of mass equations we assumed that each of the constituent phases has the same constant density. This is a commonly used assumption in the mathematical modelling of tissue growth and allows the system of equations to be reduced. The density of the cell and fluid phases may stay constant. However, this is unlikely to be true for the substrate phase because of the mineralisation of the ECM. Future work could allow for a substrate phase with an evolving density. This would also allow further experimental validation, using density information from the μCT scanner, as shown in Figure 2.6.

8.2.2 Experimental development

Validation and testing of the mathematical models presented in this thesis is necessary before they can be used in a quantitatively predictive manner. This will require the repetition of the experiments, presented in Chapter 2, for a larger number of samples. This should include experiments performed under different loading regimes in order to test the robustness of the model. Our experimental collaborators will perform further experiments in future in order to allow this to happen. In addition we have not compared the cell volume fraction with experimental data. So that this can be achieved, future experimental work could include the measurement of cell numbers.

We did not model the contraction process of the gel and assumed that it has contracted by "day 0". Further experimental and modelling work is needed in order to understand what factors, such as initial cell numbers and collagen density, affect the contraction of the gel. This

would also enable experimentalists to produce a gel with the initial conditions suggested as optimal in Section 3.3.

As demonstrated in Chapter 4, because of the lack of perfusion in the current experimental setup there are insufficient oxygen and nutrients at the centre of the construct. Future work could include an investigation of the use of hydrostatic pressure along with fluid perfusion or other methods to increase the mass transport to the centre of the construct. Strategies for developing larger constructs, stimulating angiogenesis and vascularisation, are important areas of development in tissue engineering.

All the parameters within this thesis were assumed to be temporally and spatially constant. Parameters such as the cell birth rate and cell death rate are difficult to estimate. They vary according to cell type, degree of cell differentiation and the age of the donor, as well as several other factors such as cell density [Stolzing *et al.*, 2008]. Future experimental work could focus on understanding how cell and substrate properties vary through time.

8.2.3 Numerical development

Within this thesis we have attempted to use experimentally realistic parameters where possible, and have sought a qualitative description of the experimental setup in Chapters 4 – 7. In order to make quantitative predictions, validation of the mathematical models is needed. This would require further development and optimisation of the numerical code, and possibly for the code to be written in parallel so that it can be run on multiple processors. However, writing code in parallel successfully requires significant expertise and is far from straight forward. Running code on multiple processors would also enable parameter searches and further optimisation of experimentally changeable parameters and loading conditions to be performed.

We have presented all spatial results in two dimensions. Simulations in three spatial dimensions, to include full geometry effects, could be performed in future work. The numerical code for spatial computations is written in deal.II [Bangerth *et al.*, 2013, 2007], as discussed in Appendix A, and is developed in such a way as to be dimensionally independent. However, running three dimensional simulations would result in a considerable increase in the number of degrees of freedom. Consequently, for accurate simulations, code may need to be developed to run on

multiple processors.

The modelling improvements suggested in Section 8.2.1 would also require further development of the numerical code.

8.3 Final thoughts

The development of a clinically relevant tissue engineered bone construct is still some way in the future. As demonstrated in this thesis, mathematical modelling and numerical simulation can inform experimentalists of underlying mechanisms that cannot be measured experimentally. It can also inform experimentalists of better experimental strategies. The work presented in this thesis is a preliminary investigation into the effect of hydrostatic pressure stimulation on tissue engineered bone. We have developed a suite of three related models that investigate separate aspects of the experimental setup, from looking at global quantities to the local spatial distribution. Using these we have demonstrated that the cell memory of loading is important and that there are conflicting experimental design constraints, with samples under stimulated loading conditions producing more substrate but with a more heterogeneous distribution than samples under control loading conditions. Future work, as outlined above, could help experimentalists to start to produce tissue engineered bone constructs with a more uniform substrate spatial distribution in order to pave the way to the production of clinically useful products in the future.

Appendix A

Computational methods

The focus of this thesis is on the development of mathematical models, to describe tissue engineered bone growth in a hydrostatic bioreactor, using existing numerical methods to give an approximate solution to these. Throughout this thesis we solve the dimensionless systems of equations, but, to allow comparison to the experimental results and data, we rescale all numerical results so that they are in dimensional quantities. Furthermore, in order to compare results, we use a visual inspection. In this appendix we give details of the numerical methods employed additional to those set out in the body of the thesis. This includes a brief description of theoretical results for the approaches used in the thesis.

First order finite difference methods (semi–implicit for the cell phase and implicit for the substrate phase) are employed in Chapter 3 to solve the system of ODEs and give the numerical solutions presented. As such, the numerical method has error of order $\max(\Delta t)$, the maximum timestep size.

In Chapters 4 – 7 we use the deal.II framework [Bangerth *et al.*, 2007, 2013] in preference to developing our own code. Deal.II is an open source, object–orientated, C++ library, specifically developed to solve PDEs using FEMs [Bangerth *et al.*, 2013]. It is an established piece of software that has been used to compute numerical approximations to a wide variety of mathematical problems and it won the 2007 J. H. Wilkinson Prize for Numerical Software. The advantages of deal.II include that it allows for code development independent of the spatial dimension, it is able to handle adaptive mesh refinement and hanging nodes, discontinuous and continuous Galerkin

elements, curved boundaries and parameterisation of the shape function degree. Additionally, it is tested and reliable, has an established user base, is open–source software, is under active development and has the facility to consider non–standard problems. There exist several other libraries capable of implementing FEMs. However, we choose deal.II over others due to the advantages listed above.

The numerical simulations in Chapters 4 – 7 are performed in a two–dimensional Cartesian coordinate system by considering the cross section of the experimental setup. This is equivalent to ignoring derivatives in the y–coordinate direction. Code is developed in Cartesian coordinates (as opposed to cylindrical coordinates with radial symmetry) as this allows for non–radially symmetric initial conditions.

As discussed in Sections 4.1.3 and 4.2.2, finite difference methods are used to discretise the time derivative, and continuous Galerkin FEMs with linear basis elements are used to give an approximate spatial solution of the cell phase volume fraction and nutrient concentration at each timestep for the models presented in Chapter 4. The evolution equation for the substrate phase volume fraction is an ODE at each spatial point and is solved using the implicit Euler method. For both models considered in Chapter 4, when nutrients are assumed to be well–perfused and where oxygen concentration as a representative nutrient is explicitly tracked, the linear system describing the discretised spatial problem is solved using a conjugate gradient linear solver without preconditioning at each timestep. Solver tolerances of the order 10^{-16} and 10^{-8} for the dimensionless cell phase volume fraction and for the nutrient concentration respectively are used, which are orders of magnitude below the dimensionless solutions. Under standard assumptions on the governing equations, error analysis states that the optimal $\mathcal{L}_2$ spatial convergence rate for the standard diffusion equation, solved using continuous Galerkin FEMs with linear basis functions, is of the order h^2, where h is a characteristic length of the element [Chen, 2005, Elman *et al.*, 2005]. As such, one would expect the numerical solutions presented in Chapter 4 to show spatial convergence of the order h^2 and temporal convergence of the order $\max(\Delta t)$. This could be verified in future work.

In order to seek a numerical solution to the multiphase model, investigated in Chapters 5 – 7, the system of equations is decoupled in two separate systems; a *velocity–pressure* system and a *volume fraction* system. Further details on the numerical implementation are given in Sec-

tion 5.7. The velocity–pressure system, a generalised Stokes flow, is solved at each time point using a $\mathcal{Q}_2 - \mathcal{Q}_1$ approximation, which uses continuous Galerkin rectangular elements of order two for the velocity and order one for the pressure. The dimensionless discretised linear system is solved using a generalised minimal residual method with a tolerance of 10^{-12} and preconditioned using a Schur compliment [Elman *et al.*, 2005] in a similar manner to that described in the twenty–second deal.II tutorial [Step-22]. It is known that the optimal $\mathcal{L}_2$ order of convergence for the standard Stokes flow using a $\mathcal{Q}_2 - \mathcal{Q}_1$ approximation is of the order h^2 [Elman *et al.*, 2005] if the solutions are smooth enough, where h may here be taken to be the characteristic length of the largest element as we use an unstructured mesh (see Figure 5.5). However, the required smoothness of the velocity and pressure solutions may not hold in practice, in which case the order of convergence could be reduced. The volume–fraction system consists of a hyperbolic PDE for the conservation of mass for the cell phase and an ODE for the substrate phase. Euler methods are used to discretise the temporal derivatives in these two equations thus yielding an expected temporal $\mathcal{L}_2$ convergence of order Δt. Discontinuous Galerkin finite elements with quadratic basis functions are used to solve the resulting discretised system. The resultant linear system is solved using a conjugate gradient method with tolerance of the order 10^{-8}. The optimal $\mathcal{L}_2$ spatial convergence of a quadratic discontinuous Galerkin FEM scheme for a standard first order hyperbolic problem is known to be of the order $h^{2+\frac{1}{2}}$, although in practice the full order of convergence is often not achieved[a]. Future work would be required to determine what the convergence of the numerical solution for the multiphase model examined in Chapters 5 – 7 is in practice.

A number of checks were performed in order to confirm that the numerical algorithms used were giving the correct results. Throughout the thesis, the timestep size and mesh refinement are chosen such that a decrease in size of the timestep or an increase in the mesh refinement does not lead to any visually distinguishable change in the presented numerical results. Checks were performed for both of these. The tolerances of the linear solvers used were set to be orders of magnitude below the $\mathcal{L}_2$ norm of the dimensionless solution. In addition, in order to validate the numerical algorithm, the numerical solutions in Chapter 3 were compared to results from the stability analysis. For the models presented in Chapter 4, checks were made

[a]Private communication with deal.II developers.

against a one spatial dimension reduction solved using both finite element and finite difference methods, as well as varying the values of the pressure threshold, diffusion coefficients and growth rates. The numerical algorithm for the multiphase model was validated, by altering the domain and boundary conditions, against results for the perfusion bioreactor in Osborne *et al.* [2010]. The results in Osborne *et al.* [2010] were, in turn, validated against a one spatial dimension reduction exploiting the long–wavelength limit, for which the equations were obtained in O'Dea *et al.* [2010]. Furthermore, consideration of a first order hyperbolic PDE with a known analytical solution allowed us to check the part of the code responsible for solving the conservation of mass equation for the cell phase. Additionally, the velocity–pressure system solver was checked by solving Pouiselle flow with a known analytical solution. Finally, results through time and space were compared to a one spatial dimension reduction, and the effect of parameter variation on the numerical solution was checked. These checks confirmed the accuracy of numerical algorithms used to give the numerical solutions presented in this thesis.

Appendix B

Initial conditions

Here we detail the additional initial conditions used in Section 7.2. These describe three rectangular–shaped constructs, and one asymmetric–shaped construct. As for the circular–shaped and semicircular–shaped initial conditions, functions of hyperbolic tangent are used to give continuous initial conditions, for the reasons discussed in Section 5.4.

Setup 5 : Rectangular–shaped construct placed in the transwell insert

Here we set the initial cell and substrate phase volume fractions to be

$$\begin{aligned}\theta_k(x,z,0) = A_k^{r_t}\left(\tanh\left(C_k\left(x-2r_c\right)\right)-\tanh\left(C_k\left(x+2r_c\right)\right)\right)\\ \times\left(\tanh\left(D_k\left(z-s_h-\frac{r_c}{4}\right)\right)-\tanh\left(D_k\left(z-s_h\right)\right)\right), \qquad k=C,J. \quad \text{(B.1)}\end{aligned}$$

As for the initial conditions given in Section 5.4, we require this expression to satisfy Equation (5.19). Nondimensionalisation is performed as in Section 5.6, where we denote the dimensionless variables by the caret notation and set $\mathbf{x} = H\hat{\mathbf{x}}$ where H is the height of the culture medium in the well. In dimensionless variables, the initial conditions are given by

$$\begin{aligned}\theta_k(\hat{x},\hat{z},0) = A_k^{r_t}\left(\tanh\left(\hat{C}_k\left(\hat{x}-2\hat{r}_c\right)\right)-\tanh\left(\hat{C}_k\left(\hat{x}+2\hat{r}_c\right)\right)\right)\\ \times\left(\tanh\left(\hat{D}_k\left(\hat{z}-\frac{\hat{s}_h}{2}-\frac{\hat{r}_c}{4}\right)\right)-\tanh\left(\hat{D}_k\left(\hat{z}-\frac{\hat{s}_h}{2}\right)\right)\right), \qquad k=C,J, \quad \text{(B.2)}\end{aligned}$$

where $\hat{r}_c = \dfrac{r_c}{H}$, $\hat{s}_h = \dfrac{s_h}{H}$, $\hat{C}_k = C_k H$ and $\hat{D}_k = D_k H$. These initial conditions must satisfy Equation (5.42).

Setups 6 and 7 : Rectangular–shaped constructs placed on the base and in the centre of the well

Here we use similar initial conditions for the rectangular–shaped gel placed in the transwell insert (Setup 5). In dimensionless variables the initial conditions for Setup 6, a rectangular–shaped gel place on the base of the well, are given by

$$\theta_k(\hat{x},\hat{z},0) = A_k^{r_b}\left(\tanh\left(\hat{C}_k\left(\hat{x}-2\hat{r}_c\right)\right) - \tanh\left(\hat{C}_k\left(\hat{x}+2\hat{r}_c\right)\right)\right) \times \left(\tanh\left(\hat{D}_k\left(\hat{z}-\frac{\hat{r}_c}{4}\right)\right) - \tanh\left(\hat{D}_k\hat{z}\right)\right), \qquad k = C, J, \quad \text{(B.3)}$$

and the initial conditions for the rectangular–shaped gel in the centre of the well, Setup 7, are given by

$$\theta_k(\hat{x},\hat{z},0) = A_k^{r_c}\left(\tanh\left(\hat{C}_k\left(\hat{x}-2\hat{r}_c\right)\right) - \tanh\left(\hat{C}_k\left(\hat{x}+2\hat{r}_c\right)\right)\right) \times \left(\tanh\left(\hat{D}_k\left(\hat{z}-\frac{\hat{H}}{2}-\frac{\hat{r}_c}{4}\right)\right) - \tanh\left(\hat{D}_k\left(\hat{z}-\frac{\hat{H}}{2}\right)\right)\right), \qquad k = C, J. \quad \text{(B.4)}$$

As before, $\hat{C}_k = C_k H$ and $\hat{D}_k = D_k H$, and these initial conditions must satisfy Equation (5.42).

Setup 8 : Assymetric–shaped construct

To describe an asymmetric–shaped construct, we set the initial cell and substrate volume fractions to be

$$\theta_k(x,z,0) = A_k^{q}\left(\tanh\left(D_k\left(x-r_c\right)\right) - \tanh\left(B_k\left(x+r_c\right)\right)\right) \times \left(\tanh\left(E_k\left(z-s_h\right)\right) - \tanh\left(F_k\left(z-s_h+\frac{r_c}{2}\right)\right)\right), \qquad k = C, J. \quad \text{(B.5)}$$

Table B.1: Dimensionless parameters describing the initial conditions for the additional rectangular–shaped and asymmetric–shaped constructs used in Section 7.2.

$A_C^{r_t}$	=	0.07466	$A_J^{r_t}$	=	$0.11A_C^{r_t}/0.3$
$A_C^{r_b}$	=	0.1363	$A_J^{r_b}$	=	$0.11A_C^{r_b}/0.3$
$A_C^{r_c}$	=	0.07256	$A_J^{r_c}$	=	$0.11A_C^{r_c}/0.3$
A_C^{a}	=	0.07063	A_J^{a}	=	$0.11A_C^{a}/0.3$
$\hat{C}_C = \hat{C}_J$	=	30	$\hat{D}_C = \hat{D}_J$	=	10
$\hat{E}_C = \hat{E}_J$	=	10	$\hat{F}_C = \hat{F}_J$	=	20
$\hat{s}_h$	=	2.9/17	$\hat{r}_c$	=	0.8681/17

Nondimensionalisation as before yields

$$\theta_k(\hat{x},\hat{z},0) = A_k^a\left(\tanh\left(D_k\left(\hat{x}-\hat{r}_c\right)\right) - \tanh\left(\hat{B}_k\left(\hat{x}+\hat{r}_c\right)\right)\right) \times\left(\tanh\left(\hat{E}_k\left(\hat{z}-\hat{s}_h\right)\right) - \tanh\left(\hat{F}_k\left(\hat{z}-\hat{s}_h+\frac{\hat{r}_c}{2}\right)\right)\right), \qquad k=C,J. \quad \text{(B.6)}$$

where $\hat{C}_k = C_k H$, $\hat{D}_k = D_k H$, $\hat{E}_k = E_k H$ and $\hat{F}_k = F_k H$, and the initial conditions satisfy Equation (5.42).

Parameters

In addition to those parameters prescribed previously (see Section 5.6.1), we set $\hat{D}_k = 10$, $\hat{E}_k = 10$, $\hat{F}_k = 20$ for $k = C, J$. The parameters $A_k^{r_t}$, $A_k^{r_b}$, $A_k^{r_c}$ and A_k^a for $k = C, J$ are chosen to satisfy the initial experimental volumes through Equation (5.42). This yields the parameters given in Table B.1.

Appendix C

Abbreviations

- **ECM** — ExtraCellular Matrix ..... 3.
- **MSC** — Mesenchymal Stem Cells ..... 4.
- **ODE** — Ordinary Differential Equation ..... 28.
- **FEM** — Finite Element Method ..... 33.
- **PDE** — Partial Differential Equation ..... 33.
- **ISTM** — Institute for Science & Technology in Medicine ..... 34.
- **μCT** — Micro Computerised Tomography ..... 38.
- **FSSM** — Fluid Shear Stress Magnitude ..... 91.
- **2D** — Two–Dimensional ..... 95.

Mathematical notation and nomenclature

Here we list the symbols used in this thesis along with the first page of their occurrence. The symbols are split into seven separate sections: general variables and parameters; spatial parameters; variables and parameters describing the pressure loading; parameters describing the initial quantities; parameters used to describe the mass transfer between the phases; and parameters specific to the three separate models developed in this thesis. In general, non–bold characters, *e.g.* n, are used to denote scalars, boldface Roman characters, *e.g.* $\mathbf{x}$, are used for vectors, and boldface Greek characters, *e.g.* $\boldsymbol{\sigma}$, are used for tensors. The list below shows the dimensional quantities, where applicable. Where additional notation is used to donate dimensionless quantities, these are indicated in brackets.

General variables and parameters

$\boldsymbol{\mathcal{I}}$ Rank–2 identity tensor, page 125.

$\mathbf{n}$ Outward pointing normal, page 98.

$\mathbf{x}$ Cartesian coordinates, page 41.

Ω Whole well spatial domain, page 40.

Ω_C Semicircular construct–only domain, page 95.

θ_k Volume fraction of phase k, page 51.

p_0 Dimensionalisation constant for pressure, page 54.

t Time, page 41.

Spatial parameters

H Height of the surface of the culture medium, page 40.

R Radius of the well, page 40.

r_c Radius of the construct, page 45.

s_h Height of transwell insert above well base, page 40.

Pressure loading variables and parameters

ω Frequency of cyclic loading (Υ), page 42.

a Amplitude of cyclic loading (A), page 42.

p_{app} Applied pressure, page 41.

p_{atm} Atmospheric pressure, page 42.

Parameters describing initial quantities

C_0 Initial volume of cells, page 53.

J_0 Initial volume of collagen, page 53.

N_0 Initial number of cells, page 44.

V_0 Initial volume of the construct, page 45.

Mass transfer parameters

α Measure of the length of cell memory, page 72.

τ The length of time applied pressure has been above the threshold, Equation (3.35), page 72.

k_1 Substrate deposition rate at atmospheric pressure (K_1), page 52.

k_2 Substrate deposition rate above pressure threshold, model without memory (K_2), page 52.

k_3 Substrate deposition rate above pressure threshold, model with memory (K_3), page 72.

k_4 Average substrate deposition rate during loading periods (K_4), page 124.

k_b Cell birth rate, page 51.

k_d Cell death rate (K_d), page 51.

k_p Pressure–dependent substrate deposition rate (K_p), page 52.

k_{jd} Substrate degradation rate (K_{jd}), page 52.

p_1 Pressure threshold value (P_1), page 53.

t_1 The last time applied pressure was equal to the threshold with increasing gradient, Equation (3.34), page 71.

Ordinary differential equation model

γ Relationship between substrate deposition and substrate degradation rates, Equation (3.20), page 56.

Diffusion model

η Cell oxygen uptake term, page 109.

D_C Cell diffusion coefficient, page 96.

D_n Oxygen diffusion coefficient, page 108.

n Oxygen concentration, page 108.

n_0 Oxygen concentration in culture medium, page 109.

Multiphase model

β_{kl} Coefficient for the Darcy–type viscous drag exerted on phase k by phase l, page 125.

$\boldsymbol{\sigma}_k$ Stress tensor of phase k, page 124.

χ Substrate affinity parameter, page 126.

δ_a Intraphase repulsion parameter, page 126.

δ_b Interphase repulsion parameter, page 126.

$\mathbf{f}_{kl}$ Interphase force exerted on phase k by phase l, page 124.

$\mathbf{v}_k$ Velocity of phase k, page 123.

μ_k Macroscale viscosity of phase k, page 125.

ν Cell aggregation parameter, page 126.

ψ_{CJ} Additional pressure produced by cell–substrate interactions, Equation (5.13), page 126.

Σ_C Additional pressure produced by cell–cell interactions, Equation (5.12), page 126.

m Repulsion scaling parameter, page 126.

p_k Intraphase pressure, the pressure in phase k, page 125.

p_{kl} Interphase pressure, the pressure exerted on phase k by phase l, page 125.

In addition to the above, the caret notation, *e.g.* $\hat{t}$, is used to denote dimensionless quantities unless otherwise stated, except for those specified above. A bar, *e.g.* $\bar{\theta}_C$, is used to donate the average volume fraction through time and a star, *e.g.* θ_C^*, is used in Chapter 3 to donate the equilibrium point.

Bibliography

D. J. Acheson. *Elementary fluid dynamics*. Oxford Applied Mathematics and Computing Science Series. Clarendon press, Oxford, 1990.

S. Astanin and L. Preziosi. *Selected topics in cancer modeling; genesis, evolution, immune competition, and therapy*, chapter Multiphase models of tumour growth. Birkhauser, 2008.

G. A. Ateshian. On the theory of reactive mixtures for modeling biological growth. *Biomechanics and Modeling in Mechanobiology*, 6(6):423–445–445, 2007.

S. F. Badylak, D. Taylor, and K. Uygun. Whole-organ tissue engineering: decellularization and recellularization of three-dimensional matrix scaffolds. *Annual Review of Biomedical Engineering*, 13:27–53, 2011.

W. Bangerth, R. Hartmann, and G. Kanschat. deal.II – a general purpose object orientated finite element library. *Association for Computing Machinery Transactions on Mathematical Software*, 33(4):24/1 – 24/27, 2007.

W. Bangerth, T. Heister, L. Heltai, G. Kanschat, M. Kronbichler, M. Maier, B. Turcksin, and T. D. Young. The `deal.ii` library, version 8.1. *arXiv preprint* `http://arxiv.org/abs/1312.2266v4`, 2013.

N. Basso and J. Heersche. Characteristics of in vitro osteoblastic cell loading models. *Bone*, 30(2): 347–351, 2002.

G. K. Batchelor. *An introduction to fluid dynamics*. Cambridge Mathematical Library. Cambridge University Press, 1973.

A. Boccaccio, A. Ballini, C. Pappalettere, D. Tullo, S. Cantore, and A. Desiate. Finite element method (FEM), mechanobiology and biomimetic scaffolds in bone tissue engineering. *International Journal of Biological Sciences*, 7(1):112–132, 2011.

C. J. W. Breward, H. M. Byrne, and C. E. Lewis. Modelling the interactions between tumour cells

and a blood vessel in a microenvironment within a vascular tumour. *European Journal of Applied Mathematics*, 12(05):529–556, 2001.

C. J. W. Breward, H. M. Byrne, and C. E. Lewis. The role of cell-cell interactions in a two-phase model for avascular tumour growth. *Journal of Mathematical Biology*, 45(2):125–152, 2002.

C. J. W. Breward, H. M. Byrne, and C. E. Lewis. A multiphase model describing vascular tumour growth. *Bulletin of Mathematical Biology*, 65(4):609–640, 2003.

D. W. Buck and G. A. Dumanian. Bone biology and physiology: part I. The fundamentals. *Plastic and Reconstructive Surgery*, 129(6):1314–1320, 2012a.

D. W. Buck and G. A. Dumanian. Bone biology and physiology: part II. Clinical correlates. *Plastic and Reconstructive Surgery*, 129(6), 2012b.

H. M. Byrne. Dissecting cancer through mathematics: from the cell to the animal model. *Nature Reviews Cancer*, 10(3):221–230, 2010.

H. M. Byrne and M. A. J. Chaplain. Free boundary value problems associated with the growth and development of multicellular spheroids. *European Journal of Applied Mathematics*, 8(06):639–658, 1997.

H. M. Byrne and L. Preziosi. Modelling solid tumour growth using the theory of mixtures. *Mathematical Medicine and Biology*, 20(4):341–366, 2003.

H. M. Byrne, J. R. King, D. L. S. McElwain, and L. Preziosi. A two-phase model of solid tumour growth. *Applied Mathematics Letters*, 16(4):567–573, 2003.

H. M. Byrne, T. Alarcon, M. R. Owen, S. D. Webb, and P. K. Maini. Modelling aspects of cancer dynamics: a review. *Philosophical Transactions of the Royal Society A: Mathematical, Physical and Engineering Sciences*, 364(1843):1563–1578, 2006.

A. Carlier, Y. C. Chai, M. Moesen, T. Theys, J. Schrooten, H. Van Oosterwyck, and L. Geris. Designing optimal calcium phosphate scaffold-cell combinations using an integrative model-based approach. *Acta Biomaterialia*, 7(10):3573–3585, 2011.

S. H. Cartmell and A. J. El Haj. *Mechanical bioreactors for bone tissue engineering*, chapter 8, pages 193 – 208. Springer, 2005.

J. Chen, C. Liu, L. You, and C. A. Simmons. Boning up on Wolff's law: mechanical regulation of the cells that make and maintain bone. *Journal of Biomechanics*, 43(1):108–118, 2010.

Z. Chen. *Finite element methods and their applications*. Springer, 2005.

G. Cheng, B. B. Youssef, P. Markenscoff, and K. Zygourakis. Cell population dynamics modulate the rates of tissue growth processes. *Biophysical Journal*, 90(3):713–724, 2006.

B. Clarke. Normal bone anatomy and physiology. *Clinical Journal of the American Society of Nephrology*, 3(Supplement 3):S131–S139, 2008.

N. G. Cogan and Robert D. Guy. Multiphase flow models of biogels from crawling cells to bacterial biofilms. *Human Frontier Science Program Journal*, 4(1):11–25, 2010.

F. Coletti, S. Macchietto, and N. Elvassore. Mathematical modeling of three-dimensional cell cultures in perfusion bioreactors. *Industrial and Engineering Chemistry Research*, 45(24):8158–8169, 2006.

S. C. Cowin and S. B. Doty. *Tissue mechanics*. Springer, 2007.

E. M. Czekanska, M. J. Stoddart, R. G. Richards, and J. S. Hayes. In search of an osteoblast cell model for in vitro research. *European cells and materials*, 24:1–17, 2012. ISSN 1473-2262.

V. Díaz-Zuccarini and P. V. Lawford. An in-silico future for the engineering of functional tissues and organs. *Organogenesis*, 6(4):245–251, 2010.

P. Diehl, J. Schauwecker, W. Mittelmeier, and M. Schmitt. High hydrostatic pressure, a novel approach in orthopedic surgical oncology to disinfect bone, tendons and cartilage. *Anticancer Research*, 28(6B): 3877–3883, 2008.

R. Dimitriou, E. Jones, D. McGonagle, and P. Giannoudis. Bone regeneration: current concepts and future directions. *BioMed Central Medicine*, 9(1):66+, 2011.

M. Doblaré, J. M. Garcıa, and M. J. Gómez. Modelling bone tissue fracture and healing: a review. *Engineering Fracture Mechanics*, 71(13-14):1809–1840, 2004.

T. J. Eggum and C. J. Hunter. Development and validation of a system for the growth of cells and tissues under intermittent hydrostatic pressure. *Journal of Biomechanical Engineering*, 130(6):064501+, 2008.

A. El Haj and S. Cartmell. Bioreactors for bone tissue engineering. *Journal of Engineering in Medicine*, 224(12):1523–1532, 2010.

B. D. Elder and K. A. Athanasiou. Hydrostatic pressure in articular cartilage tissue engineering: from chondrocytes to tissue regeneration. *Tissue Engineering. Part B, Reviews*, 15(1):43–53, 2009.

M. J. Ellis and J. B. Chaudhuri. Poly(lactic-co-glycolic acid) hollow fibre membranes for use as a tissue engineering scaffold. *Biotechnology and Bioengineering*, 96(1):177–187, 2007.

H. C. Elman, D. J. Silvester, and A. J. Wathen. *Finite elements and fast iterative solvers: with applica-*

tions in incompressible fluid dynamics. Numerical Mathematics and Scientific Computation. Oxford University Press, 2005.

B. Flanagan and G. Nichols. Bone matrix turnover and balance in vitro. I. The effects of parathyroid hormone and thyrocalcitonin. *The Journal of Clinical Investigation*, 48(4):595–606, 1969.

A. C. Fowler. *Mathematical Models in the Applied Sciences*. Cambridge Texts in Applied Mathematics. Cambridge University Press, 1997.

S. J. Franks and J. R. King. Interactions between a uniformly proliferating tumour and its surroundings: uniform material properties. *Mathematical Medicine and Biology : A Journal of the Institute of Mathematics and its Applications*, 20(1):47–89, 2003.

S. J. Franks, H. M. Byrne, J. R. King, J. C. E. Underwood, and C. E. Lewis. Modelling the early growth of ductal carcinoma in situ of the breast. *Journal of Mathematical Biology*, 47(5):424–452, 2003a.

S. J. Franks, H. M. Byrne, H. S. Mudhar, J. C. E. Underwood, and C. E. Lewis. Mathematical modelling of comedo ductal carcinoma in situ of the breast. *Mathematical Medicine and Biology*, 20(3):277–308, 2003b.

D. Furlani, M. Ugurlucan, L. Ong, K. Bieback, E. Pittermann, I. Westien, W. Wang, C. Yerebakan, W. Li, R. Gaebel, R. Li, B. Vollmar, G. Steinhoff, and N. Ma. Is the intravascular administration of mesenchymal stem cells safe? *Microvascular Research*, 77(3):370–376, 2009.

J. Gardinier, S. Majumdar, R. Duncan, and L. Wang. Cyclic hydraulic pressure and fluid flow differentially modulate cytoskeleton re-organization in MC3T3 osteoblasts. *Cellular and Molecular Bioengineering*, 2(1):133–143, 2009.

F. A. Gerhard, D. J. Webster, G. H. van Lenthe, and R. Müller. In silico biology of bone modelling and remodelling: adaptation. *Philosophical Transactions of the Royal Society A: Mathematical, Physical and Engineering Sciences*, 367(1895):2011–2030, 2009.

L. Geris, J. Vander Sloten, and H. Van Oosterwyck. In silico biology of bone modelling and remodelling: regeneration. *Physical and Engineering Sciences*, 367(1895):2031–2053, 2009.

L. Geris, R. Schugart, and H. Van Oosterwyck. In silico design of treatment strategies in wound healing and bone fracture healing. *Philosophical Transactions of the Royal Society A: Mathematical, Physical and Engineering Sciences*, 368(1920):2683–2706, 2010.

J. R. Henstock, M. Rotherham, J. B. Rose, and A. J. El Haj. Cyclic hydrostatic pressure stimulates enhanced bone development in the foetal chick femur in vitro. *Bone*, 53(2):468–477, 2013.

R. Hess, T. Douglas, K. A. Myers, B. Rentsch, C. Rentsch, H. Worch, N. G. Shrive, D. A. Hart, and D. Scharnweber. Hydrostatic pressure stimulation of human mesenchymal stem cells seeded on collagen-based artificial extracellular matrices. *Journal of Biomechanical Engineering*, 132(2): 021001+, 2010.

M. E. Hubbard and H. M. Byrne. Multiphase modelling of vascular tumour growth in two spatial dimensions. *Journal of Theoretical Biology*, 316:70–89, 2013.

J. D. Humphrey. Review paper: continuum biomechanics of soft biological tissues. *Proceedings of the Royal Society of London. Series A: Mathematical, Physical and Engineering Sciences*, 459(2029):3–46, 2003.

H. Isaksson. Recent advances in mechanobiological modeling of bone regeneration. *Mechanics Research Communications*, 42:22–31, 2012.

H. Isaksson, C. C. van Donkelaar, R. Huiskes, and K. Ito. Corroboration of mechanoregulatory algorithms for tissue differentiation during fracture healing: comparison with in vivo results. *Journal of Orthopaedic Research*, 24(5):898–907, 2006.

M. Jamnongwong, K. Loubiere, N. Dietrich, and G. Hébrard. Experimental study of oxygen diffusion coefficients in clean water containing salt, glucose or surfactant: consequences on the liquid-side mass transfer coefficients. *Chemical Engineering Journal*, 165(3):758–768, 2010.

R. L. Jilka, R. S. Weinstein, T. Bellido, A. M. Parfitt, and S. C. Manolagas. Osteoblast programmed cell death (apoptosis): modulation by growth factors and cytokines. *Journal of Bone and Mineral Research : The Official Journal of the American Society for Bone and Mineral Research*, 13(5):793–802, 1998.

E. O. Johnson, T. Troupis, and P. N. Soucacos. Tissue-engineered vascularized bone grafts: basic science and clinical relevance to trauma and reconstructive microsurgery. *Microsurgery*, 31(3):176–182, 2011.

G. E. Kapellos, T. S. Alexiou, and A. C. Payatakes. Theoretical modeling of fluid flow in cellular biological media: an overview. *Mathematical Biosciences*, 225(2):83–93, 2010.

J. Kestin, M. Sokolov, and W. A. Wakeham. Viscosity of liquid water in the range $-8\,^{\circ}\mathrm{C}$ to $150\,^{\circ}\mathrm{C}$. *Journal of Physical and Chemical Reference Data*, 7(3):941–948, 1978.

H. Khayyeri, S. Checa, M. Tägil, and P. J. Prendergast. Corroboration of mechanobiological simulations of tissue differentiation in an in vivo bone chamber using a lattice-modeling approach. *Journal of Orthopaedic Research*, 27(12):1659–1666, 2009.

S. H. Kim, Y. Rak R. Choi, S. Park, M. S, Jung W. W. Shin, K. D. D. Park, S. J. Kim, and J. W. W. Lee.

ERK 1/2 activation in enhanced osteogenesis of human mesenchymal stem cells in poly(lactic-glycolic acid) by cyclic hydrostatic pressure. *Journal of Biomedical Materials Research. Part A*, 80(4):826–836, 2007.

J. Klein-Nulend, J. Paul V., M. E. Van Strien, M. D. Jong, and E. H. Burger. Inhibition of osteoclastic bone resorption by mechanical stimulation in vitro. *Arthritis and Rheumatism*, 33(1):66–72, 1990.

J. Klein-Nulend, R. G. Bacabac, and M. G. Mullender. Mechanobiology of bone tissue. *Pathologie-biologie*, 53(10):576–580, 2005.

S. M. Klisch, S. S. Chen, R. L. Sah, and A. Hoger. A growth mixture theory for cartilage with application to growth-related experiments on cartilage explants. *Journal of Biomechanical Engineering*, 125(2): 169–179, 2003.

E. Kreyszig. *Advanced engineering mathematics*. John Wiley & Sons, Inc., New York, NY, USA, 8th edition, 2000.

W. M. Lai, J. S. Hou, and V. C. Mow. A triphasic theory for the swelling and deformation behaviors of articular cartilage. *Journal of Biomechanical Engineering*, 113(3):245–258, 1991.

D. A. Lee, M. M. Knight, J. J. Campbell, and D. L. Bader. Stem cell mechanobiology. *Journal of Cellular Biochemistry*, 112(1):1–9, 2011.

G. Lemon and J. R. King. Multiphase modelling of cell behaviour on artificial scaffolds: effects of nutrient depletion and spatially nonuniform porosity. *Mathematical Medicine and Biology*, 24(1):57–83, 2007a.

G. Lemon and J. R. King. Travelling-wave behaviour in a multiphase model of a population of cells in an artificial scaffold. *Journal of Mathematical Biology*, 55(4):449–480–480, 2007b.

G. Lemon, J. R. King, H. M. Byrne, O. E. Jensen, and K. M. Shakesheff. Mathematical modelling of engineered tissue growth using a multiphase porous flow mixture theory. *Journal of Mathematical Biology*, 52(5):571–594, 2006.

G. Lemon, S. L. Waters, F. R. A. J. Rose, and J. R. King. Mathematical modelling of human mesenchymal stem cell proliferation and differentiation inside artificial porous scaffolds. *Journal of Theoretical Biology*, 249(3):543–553, 2007.

M. C. Lewis, B. D. MacArthur, J. Malda, G. Pettet, and C. P. Please. Heterogeneous proliferation within engineered cartilaginous tissue: the role of oxygen tension. *Biotechnology and Bioengineering*, 91(5): 607–615, 2005.

C. Liu, Y. Zhao, W. Y. Cheung, R. Gandhi, L. Wang, and L. You. Effects of cyclic hydraulic pressure on osteocytes. *Bone*, 46(5):1449–1456, 2010.

J. Liu, Z. Zhao, L. Zou, J. Li, F. Wang, X. Li, J. Zhang, Y. Liu, S. Chen, M. Zhi, and J. Wang. Pressure-loaded MSCs during early osteodifferentiation promote osteoclastogenesis by increase of RANKL/OPG ratio. *Annals of Biomedical Engineering*, 37(4):794–802, 2009.

J. S. Lowengrub, H. B. Frieboes, F. Jin, Y. L. Chuang, X. Li, P. Macklin, S. M. Wise, and V. Cristini. Nonlinear modelling of cancer: bridging the gap between cells and tumours. *Nonlinearity*, 23(1): R1–R91, 2010.

S. R. Lubkin and T. Jackson. Multiphase mechanics of capsule formation in tumors. *Journal of Biomechanical Engineering*, 124(2):237–243, 2002.

B. MacArthur. Mathematical modelling of skeletal repair. *Biochemical and Biophysical Research Communications*, 313(4):825–833, 2004.

I. Martin. The role of bioreactors in tissue engineering. *Trends in Biotechnology*, 22(2):80–86, 2004.

R. J. McCoy and F. J. O'Brien. Influence of shear stress in perfusion bioreactor cultures for the development of three-dimensional bone tissue constructs: a review. *Tissue Engineering. Part B, Reviews*, 16(6):587–601, 2010.

S. M. Morgan, S. Tilley, S. Perera, M. J. Ellis, J. Kanczler, J. B. Chaudhuri, and R. O. C. Oreffo. Expansion of human bone marrow stromal cells on poly-(dl-lactide-co-glycolide) (PDLLGA) hollow fibres designed for use in skeletal tissue engineering. *Biomaterials*, 28(35):5332–5343, 2007.

V. C. Mow, S. C. Kuei, W. M. Lai, and C. G. Armstrong. Biphasic creep and stress relaxation of articular cartilage in compression: theory and experiments. *Journal of Biomechanical Engineering*, 102(1):73–84, 1980.

M. Mullender, A. J. El Haj, Y. Yang, M. A. van Duin, E. H. Burger, and J. Klein-Nulend. Mechanotransduction of bone cells in vitro: mechanobiology of bone tissue. *Medical and Biological Engineering and Computing*, 42(1):14–21, 2004.

J. D. Murray. *Mathematical biology: I. An introduction.* Springer, third edition, 2002.

J. Nagatomi, B. P. Arulanandam, D. W. Metzger, A. Meunier, and R. Bizios. Frequency- and duration-dependent effects of cyclic pressure on select bone cell functions. *Tissue Engineering*, 7(6):717–728, 2001.

J. Nagatomi, B. P. Arulanandam, D. W. Metzger, A. Meunier, and R. Bizios. Cyclic pressure affects osteoblast functions pertinent to osteogenesis. *Annals of Biomedical Engineering*, 31(8):917–923, 2003.

S. P. Neuman. Theoretical derivation of Darcy's law. *Acta Mechanica*, 25(3):153–170, 1977.

H. Ockendon and J. R. Ockendon. *Viscous Flow*. Cambridge Texts in Applied Mathematics. Cambridge University Press, 1995.

R. O'Dea. *Multiphase modelling of tissue growth in dynamic culture conditions*. PhD thesis, The University of Nottingham, 2007.

R. D. O'Dea, S. L. Waters, and H. M. Byrne. A two-fluid model for tissue growth within a dynamic flow environment. *European Journal of Applied Mathematics*, 19(06):607–634, 2008.

R. D. O'Dea, S. L. Waters, and H. M. Byrne. A multiphase model for tissue construct growth in a perfusion bioreactor. *Mathematical Medicine and Biology*, 27(2):95–127, 2010.

R. D. O'Dea, H. M. Byrne, and S. L. Waters. Continuum modelling of in vitro tissue engineering: a review. In L. Geris, editor, *Computational Modeling in Tissue Engineering*. Springer, 2012.

R. D. O'Dea, J. M. Osborne, A. J. El Haj, H. M. Byrne, and S. L. Waters. The interplay between tissue growth and scaffold degradation in engineered tissue constructs. *Journal of Mathematical Biology*, 67 (5):1199–1225, 2013.

R. J. O'Keefe and J. Mao. Bone tissue engineering and regeneration: from discovery to the clinic–an overview. *Tissue engineering. Part B, Reviews*, 17(6):389–392, 2011.

G. Orlando, K. J. Wood, R. J. Stratta, J. J. Yoo, A. Atala, and S. Soker. Regenerative medicine and organ transplantation: past, present, and future. *Transplantation*, 91(12):1310–1317, 2011.

D. Orr and K. Burg. Design of a modular bioreactor to incorporate both perfusion flow and hydrostatic compression for tissue engineering applications. *Annals of Biomedical Engineering*, 36(7):1228–1241, 2008.

J. M. Osborne. *Numerical and computational methods for simulating multiphase models of tissue growth*. PhD thesis, Computational Biology Research Group, The University of Oxford, 2009.

J. M. Osborne and J. P. Whiteley. A numerical method for the multiphase viscous flow equations. *Computer Methods in Applied Mechanics and Engineering*, 199(49-52):3402–3417, 2010.

J. M. Osborne, R. D. O'Dea, J. P. Whiteley, H. M. Byrne, and S. L. Waters. The influence of bioreactor geometry and the mechanical environment on engineered tissues. *Journal of Biomechanical Engineering*, 132(5):051006+, 2010.

V. Parikka, A. Väänänen, J. Risteli, T. Salo, T. Sorsa, H. K. Väänänen, and P. Lehenkari. Human mesenchymal stem cell derived osteoblasts degrade organic bone matrix in vitro by matrix metalloproteinases. *Matrix Biology*, 24(6):438–447, 2005.

V. Podrazký and V. Sedmerová. Densities of collagen dehydrated by some organic solvents. *Cellular and Molecular Life Sciences*, 22(12):792, 1966.

L. Preziosi and A. Tosin. Multiphase modelling of tumour growth and extracellular matrix interaction: mathematical tools and applications. *Journal of Mathematical Biology*, 58(4):625–656, 2009.

V. Quaranta, A. Weaver, P. Cummings, and A. Anderson. Mathematical modeling of cancer: the future of prognosis and treatment. *Clinica Chimica Acta*, 357(2):173–179, 2005.

J. Rauh, F. Milan, K. P. Günther, and M. Stiehler. Bioreactor systems for bone tissue engineering. *Tissue Engineering. Part B, Reviews*, 17(4):263–280, 2011.

Y. Reinwald, K. H. L. Leonard, J. R. Henstock, J. P. Whiteley, J. M. Osborne, S. L. Waters, P. Levesque, and A. J. El Haj. Evaluation of the growth environment of a hydrostatic force bioreactor for preconditioning of tissue-engineered constructs. *Tissue Engineering Part C: Methods — published online ahead of print version*, 2014.

K. A. Rejniak and L. J. McCawley. Current trends in mathematical modeling of tumor-microenvironment interactions: a survey of tools and applications. *Experimental Biology and Medicine*, 235(4):411–423, 2010.

R. C. Riddle and H. J. Donahue. From streaming-potentials to shear stress: 25 years of bone cell mechanotransduction. *Journal of Orthopaedic Research*, 27(2):143–149, 2009.

N. Rivalain, J. Roquain, and G. Demazeau. Development of high hydrostatic pressure in biosciences: Pressure effect on biological structures and potential applications in Biotechnologies. *Biotechnology Advances*, 28(6):659–672, 2010.

J. Roelofsen, J. Klein-Nulend, and E. H. Burger. Mechanical stimulation by intermittent hydrostatic compression promotes bone-specific gene expression in vitro. *Journal of Biomechanics*, 28(12):1493–1503, 1995.

T. Roose. Solid stress generated by spheroid growth estimated using a linear poroelasticity model. *Microvascular Research*, 66(3):204–212, 2003.

T. Roose, S. J. Chapman, and P. K. Maini. Mathematical models of avascular tumor growth. *Society for Industrial and Applied Mathematics Review*, 49(2):179–208, 2007.

F. R. A. J. Rose and R. O. C. Oreffo. Bone tissue engineering: hope vs hype. *Biochemical and Biophysical Research Communications*, 292(1):1–7, 2002.

E. Salter, B. Goh, B. Hung, D. Hutton, N. Ghone, and W. L. Grayson. Bone tissue engineering bioreactors: a role in the clinic? *Tissue engineering. Part B, Reviews*, 18(1):62–75, 2012.

J. Sanz-Herrera, J. Garcia-Aznar, and M. Doblare. A mathematical model for bone tissue regeneration inside a specific type of scaffold. *Biomechanics and Modeling in Mechanobiology*, 7(5):355–366, 2008.

J. A. Sanz-Herrera, J. M. García-Aznar, and M. Doblaré. A mathematical approach to bone tissue engineering. *Physical and Engineering Sciences*, 367(1895):2055–2078, 2009.

J. E. Schroeder and R. Mosheiff. Tissue engineering approaches for bone repair: concepts and evidence. *Injury*, 42(6):609–613, 2011.

M. A. Schwartz and R. K. Assoian. Integrins and cell proliferation: regulation of cyclin-dependent kinases via cytoplasmic signaling pathways. *Journal of Cell Science*, 114(Pt 14):2553–2560, 2001.

B. G. Sengers, C. W. J. Oomens, and F. P. T. Baaijens. An integrated finite-element approach to mechanics, transport and biosynthesis in tissue engineering. *Journal of Biomechanical Engineering*, 126(1):82–91, 2004.

B. G. Sengers, H. K. Heywood, D. A. Lee, C. W. Oomens, and D. L. Bader. Nutrient utilization by bovine articular chondrocytes: a combined experimental and theoretical approach. *Journal of Biomechanical Engineering*, 127(5):758–766, 2005.

B. G. Sengers, C. P. Please, and R. O. C. Oreffo. Experimental characterization and computational modelling of two-dimensional cell spreading for skeletal regeneration. *Journal of The Royal Society Interface*, 4(17):1107–1117, 2007a.

B. G. Sengers, M. Taylor, C. P. Please, and R. O. C. Oreffo. Computational modelling of cell spreading and tissue regeneration in porous scaffolds. *Biomaterials*, 28(10):1926–1940, 2007b.

B. G. Sengers, C. P. Please, M. Taylor, and R. O. C. Oreffo. Experimental-computational evaluation of human bone marrow stromal cell spreading on trabecular bone structures. *Annals of Biomedical Engineering*, 37(6):1165–1176, 2009.

M. Shakeel, P. C. Matthews, R. S. Graham, and S. L. Waters. A continuum model of cell proliferation and nutrient transport in a perfusion bioreactor. *Mathematical Medicine and Biology*, 30(1):21–44, 2013.

R. J. Shipley and S. L. Waters. Fluid and mass transport modelling to drive the design of cell-packed

hollow fibre bioreactors for tissue engineering applications. *Mathematical Medicine and Biology*, 29 (4):329–359, 2012.

R. J. Shipley, G. W. Jones, R. J. Dyson, B. G. Sengers, C. L. Bailey, C. J. Catt, C. P. Please, and J. Malda. Design criteria for a printed tissue engineering construct: a mathematical homogenization approach. *Journal of Theoretical Biology*, 259(3):489–502, 2009.

R. J. Shipley, S. L. Waters, and M. J. Ellis. Definition and validation of operating equations for poly(vinyl alcohol)-poly(lactide-co-glycolide) microfiltration membrane-scaffold bioreactors. *Biotechnology and Bioengineering*, 107(2):382–392, 2010.

R. J. Shipley, A. J. Davidson, K. Chan, J. B. Chaudhuri, S. L. Waters, and M. J. Ellis. A strategy to determine operating parameters in tissue engineering hollow fiber bioreactors. *Biotechnology and Bioengineering*, 108(6):1450–1461, 2011.

B. R. Simon. Multiphase poroelastic finite element models for soft tissue structures. *Applied Mechanics Reviews*, 45(6):191–218, 1992.

N. G. Singer and A. I. Caplan. Mesenchymal stem cells: mechanisms of inflammation. *Annual Review of Pathology: Mechanisms of Disease*, 6(1):457–478, 2011.

Step-22. *The deal.II tutorial: step-22*. URL `http://www.dealii.org/developer/doxygen/deal.II/step_22.html`.

Step-30. *The deal.II tutorial: step-30*. URL `http://www.dealii.org/developer/doxygen/deal.II/step_30.html`.

A. Stolzing, E. Jones, D. McGonagle, and A. Scutt. Age-related changes in human bone marrow-derived mesenchymal stem cells: consequences for cell therapies. *Mechanisms of Ageing and Development*, 129 (3):163–173, 2008.

D. N. Sun, W. Y. Gu, X. E. Guo, W. M. Lai, and V. C. Mow. A mixed finite element formulation of triphasic mechano-electrochemical theory for charged, hydrated biological soft tissues. *International Journal for Numerical Methods in Engineering*, 45(10):1375–1402, 1999.

M. A. Swartz and M. E. Fleury. Interstitial glow and its effects in soft tissues. *Annual Review of Biomedical Engineering*, 9(1):229–256, 2007.

E. Takai, R. L. Mauck, C. T. Hung, and X. E. Guo. Osteocyte viability and regulation of osteoblast function in a 3D trabecular bone explant under dynamic hydrostatic pressure. *Journal of Bone and Mineral Research : The Official Journal of the American Society for Bone and Mineral Research*, 19 (9):1403–1410, 2004.

S. Tan, W. Pan, G. Ma, N. Cai, K. Leong, and K. Liao. Viscoelastic behaviour of human mesenchymal stem cells. *BioMed Central Cell Biology*, 9(1):40+, 2008.

G. A. Truskey. *Transport phenomena in biological systems*. Pearson, 2009.

C. H. Turner. Three rules for bone adaptation to mechanical stimuli. *Bone*, 23(5):399–407, 1998.

C. Verdier, J. Etienne, A. Duperray, and L. Preziosi. Review: theological properties of biological materials. *Comptes Rendus Physique*, 10(8):790–811, 2009.

S. Whitaker. Flow in porous media II: the governing equations for immiscible, two-phase flow. *Transport in Porous Media*, 1(2):105–125, 1986.

R. Whittaker, R. Booth, R. Dyson, C. Bailey, L. Parsonschini, S. Naire, S. Payvandi, Z. Rong, H. Woollard, and L. Cummings. Mathematical modelling of fibre-enhanced perfusion inside a tissue-engineering bioreactor. *Journal of Theoretical Biology*, 256(4):533–546, 2009.

D. J. Wilson, J. R. King, and H. M. Byrne. Modelling scaffold occupation by a growing, nutrient-rich tissue. *Mathematical Models and Methods in Applied Sciences*, 17(Supp):1721+, 2007.

V. W. Wong, K. C. Rustad, M. T. Longaker, and G. C. Gurtner. Tissue engineering in plastic surgery: a review. *Plastic and Reconstructive Surgery*, 126(3):858–868, 2010.

A. B. Yeatts and J. P. Fisher. Bone tissue engineering bioreactors: dynamic culture and the influence of shear stress. *Bone*, 48(2):171–181, 2011.

D. Zhang, S. Weinbaum, and S. C. Cowin. Estimates of the peak pressures in bone pore water. *Journal of Biomechanical Engineering*, 120(6):697–703, 1998.